YEARBOOK
2020

INSTITUTE OF TECHNICAL PHYSICS AND MATERIALS SCIENCE
CENTRE FOR ENERGY RESEARCH
PART OF EÖTVÖS LORÁND RESEARCH NETWORK

http://www.mfa.kfki.hu/

Published by
Institute of Technical Physics and Materials Science
Centre for Energy Research
Part of Eötvös Loránd Research Network

EK MFA Yearbook 2020

Director: Prof. Béla Pécz, D.Sc.

Address: Konkoly-Thege Miklós út 29-33,
H-1121 Budapest, Hungary
Postal: P.O.Box 49, H-1525 Budapest, Hungary
Phone: +36-1-392 2224
E-mail: info@mfa.kfki.hu
URL: http://www.mfa.kfki.hu/

Editor: Krisztina Szakolczai, Ph.D.
Published by: EK MFA, Budapest, Hungary, 2021

Content

GENERAL INFORMATION

Director's foreword

As the director of MFA, it is my pleasure to welcome the reader. I recommend browsing the present yearbook which continues the series of the former ones and contains results achieved in 2020.

2020 was the first whole year what we spent as the member of Eötvös Loránd Research Network (ELKH). One year ago I complained that the salaries remained low. However, I also had reported that ELKH also requested an increased budget for the network from the state. Now it is my pleasure to report that in the second half of 2020 our budget was already substantially increased and as part of that the salaries were increased by 30% as the average.

The COVID-19 pandemic caused a lot of turbulence in the life of our institute. According to the various government rules people had to stay at home and work online, what was actually beneficial from the point of view of new publications. However, we had to keep run the whole technology and equipment facility of MFA, in which we succeeded. Some of the running projects were prolonged by our supporting agencies. Especially our leaders of the scientific departments had to spend more time with the planning of the group activity keeping up with the new medical rules. Also many colleagues had to attend at home the learning/teaching of their young children as the education also went digital online. Despite all the above difficulties I am on the opinion that MFA closed a successful year in 2020.

The 18th International Conference on Thin Films (ICTF) jointly organized by 18th Joint Vacuum Conference (JVC) took place between 22-26 November, 2020. The conference was scheduled originally in June but due to the worldwide Covid case it was postponed to November. MFA members participated actively in the organisation of the event giving the chair (J. Gyulai) and the co-chair (B. Pécz) of the conference. The conference was attended by more than 150 participants from 31 countries. We had 3 plenary, 15 invited, 59 oral lectures and 80 posters presented in on-line form. Despite the pandemic situation the series of the ICTF and JVC conferences were not broken and the participants had a lot of possibility to report on their new results and even change ideas and plans.

ICTF is a conference series organised by IUVSTA (International Union for Vacuum Science Technique and Applications) an organisation which represents about 30 000 engineers/scientists worldwide. The acting president of IUVSTA announced that a new prize for young scientist s giving the best talks on ICTF conference is founded by IUVSTA and named after our Professor Péter B. Barna. The first two prizes were announced at the end of the conference. Moreover, Peter B. Barna was nominated as honorary president of IUVSAT for his extremely successful scientific carrier. When I am writing this forward it is a fact that the general assembly of IUVSTA agreed on his nomination.

The Advanced Functional Materials for Autonomous Sensor Networks (KoFAH, www.kofah.hu) project was successfully finished in 2020. The aim of the KoFAH research project is to solve energy issues of Wireless Sensor Networks using advanced energy harvesting materials, low-power MEMS/NEMS devices, smart energy management, and highly efficient communication protocols. In the framework of KoFAH program we initiated the development of novel autonomous sensors and upgrade our ongoing systems. The consortium was composed from the Microtechnology/Nanosensors Department of MFA (www.mems.hu, www.nems.hu) and BHE Bonn Hungary Electronics Ltd., an RF/Microwave system manufacturing company (www.bhe-mw.eu) and coordinated by our János Volk. Some of the details especially on piezoresistive energy harvest systems are included in the present yearbook. The project was supported by the National Research, Development and Innovation Fund of the Hungarian Government (NVKP_16-1-2016-0018).

I congratulate to my colleagues: János Lábár, who was awarded by the Officer's Cross of the Hungarian Order of Merit, and Lajos Tóth, who was awarded by the Knight's Cross of the Hungarian Order of Merit. I am also please to inform you that our Miklós Serényi received the Academic-Patent Award.

We are very proud of our PhD students (Radó János, Király Balázs, Soukaina Lamnini, Farkas Enikő and Pálinkás András) who were supervised by colleagues at MFA and defended their thesis successfully in 2020 and got the PhD degree from different universities.
We are also proud of the scientific results achieved by our colleagues, I hope you will enjoy learning them in this book.

Here I note that the former MFA Yearbooks are available electronically at https://www.mfa.kfki.hu/yearbooks/

Béla Pécz, D.Sc., Director

Organizational structure

Director: Dr. Béla Pécz, D.Sc.

Scientific departments	
Thin Film Physics Department	Katalin BALÁZSI, Ph.D.
Complex Systems Department	Géza ÓDOR, D.Sc.
Photonics Department	Péter PETRIK, D.Sc.
Nanosensorics Laboratory	János VOLK, Ph.D.
Microsystems Department	Péter FÜRJES, Ph.D.
Nanostructures Department and "Lendület" group - 2D Materials	Levente TAPASZTÓ, Ph.D.
"Lendület" group - Topological Nanostructures	Péter NEMES-INCZE, Ph.D.
"Lendület" group - NanoBioSensorics	Róbert HORVÁTH, Ph.D.

Directly supervised functions	
Head of Scientific Advisory Council	Levente TAPASZTÓ, Ph.D.
Scientific secretary, projects and PR	Krisztina SZAKOLCZAI, Ph.D.
Quality control, patents, MTMT, REAL admin	Andrea BOLGÁR
Technical support	Károly BODNÁR
Financial administration	Zsuzsanna KELEMEN
Informatics	Gergely TAMÁS
Technology transfer (IPR)	Antal GASPARICS, Ph.D.

Key Financial Figures of MFA

The turnover realised by the institute always reflect the national and international political and financial system and also the efforts of the institute.

The domestic subsidies did not change for about a decade. But after the research centre network has been reorganizes in 2019 and the centre left the MTA network and became part of the Eötvös Loránd Research Network a slow correction started on the subsidy. It has been adjusted partly to the number and salary of the researchers as well as excellence and output of the centre. The overhead of the institute is still around 35% of the annual budget.

The number of researchers together with the research supporting staff dropped from ca. 140 to 100 in the last 10-12 years. Due to the correction of the subsidy in 2020, we hope we can provide a more predictable research career with an acceptable (although still not competitive) salary and stabilize that number. If the number of staff reduced at this rate in the future that would jeopardize the implementation of the grants.

The recent projects – apart from the fundamental research grants – arise from industrial and application driven ideas. Despite all the efforts of colleagues R&D grants require stable strong and research motivated SMEs, which is hard to find in Hungary. The large domestic projects (VEKOP) and also the H2020 grant are running out, making the fiscal year 2022 more uncertain. Nevertheless the institute and its administration handles over 40 grants and 20 other R&D contracts each year.

Since 2015 MFA is part of the Centre of Energy Research. The financial operation is only partly transparent, therefore the data shown here for 2015-20120 for MFA are based upon our own estimates.

MFA budget 2003-2020 (million HUF)

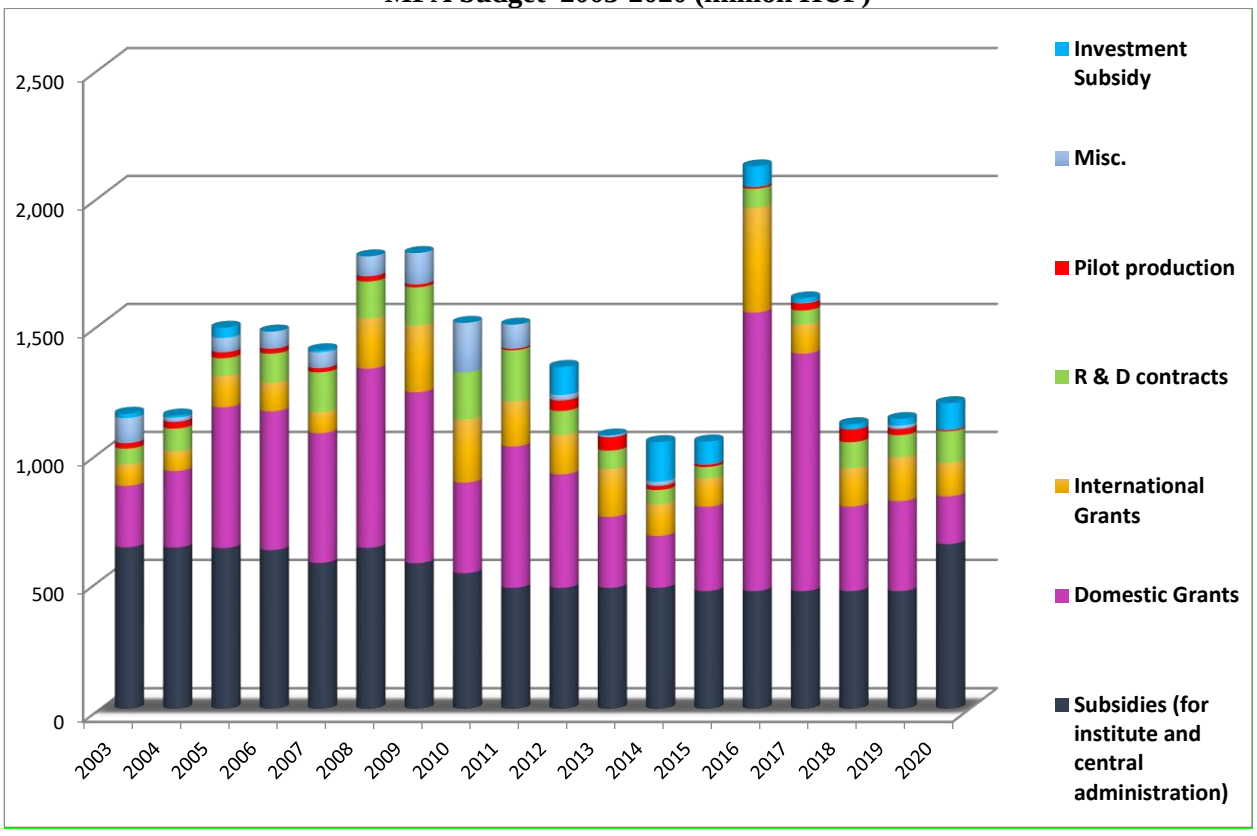

MFA 2003-2020 restoration and investment spendings (million HUF)

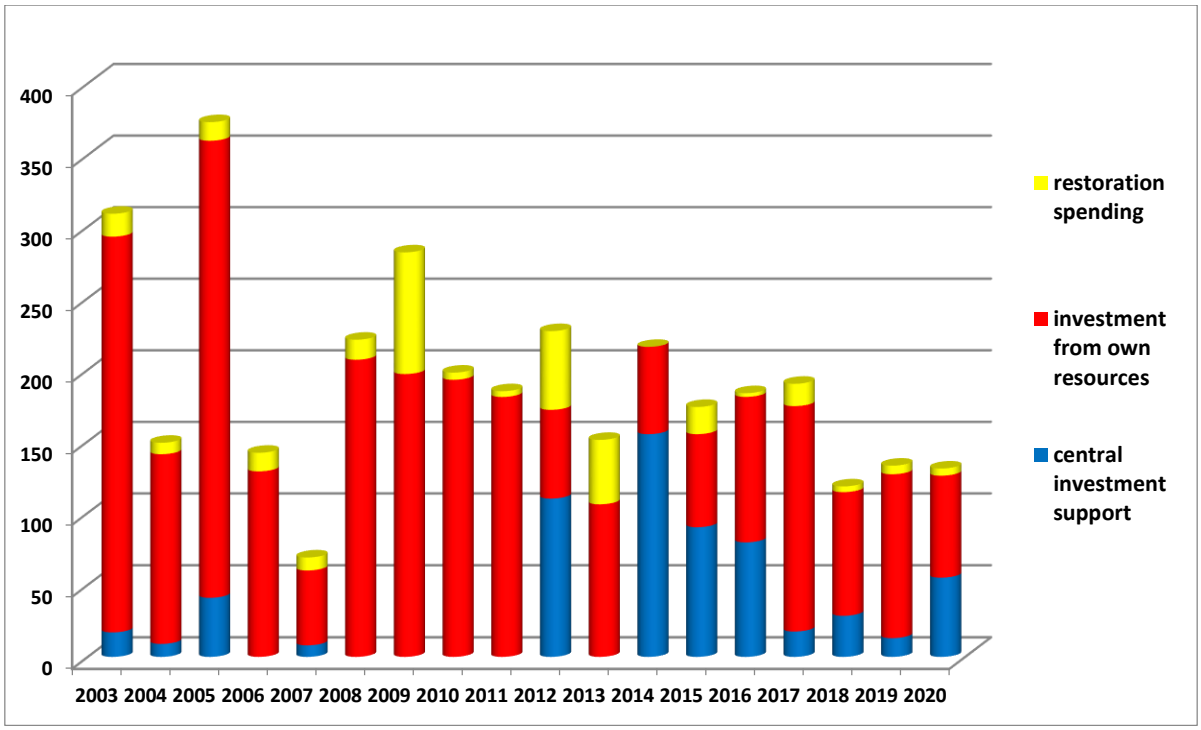

Publication and Citation statistics of MFA

According to the Thomson-Reuters ISI "Web of Knowledge", and MTMT2 databases, the Institute has an average publication activity of ca. 100 scientific papers in IF journals a year. The number decreased a bit in the last years, but recently MFA researchers publich in journals with higher impact factor.

MFA and its predecessor's publications

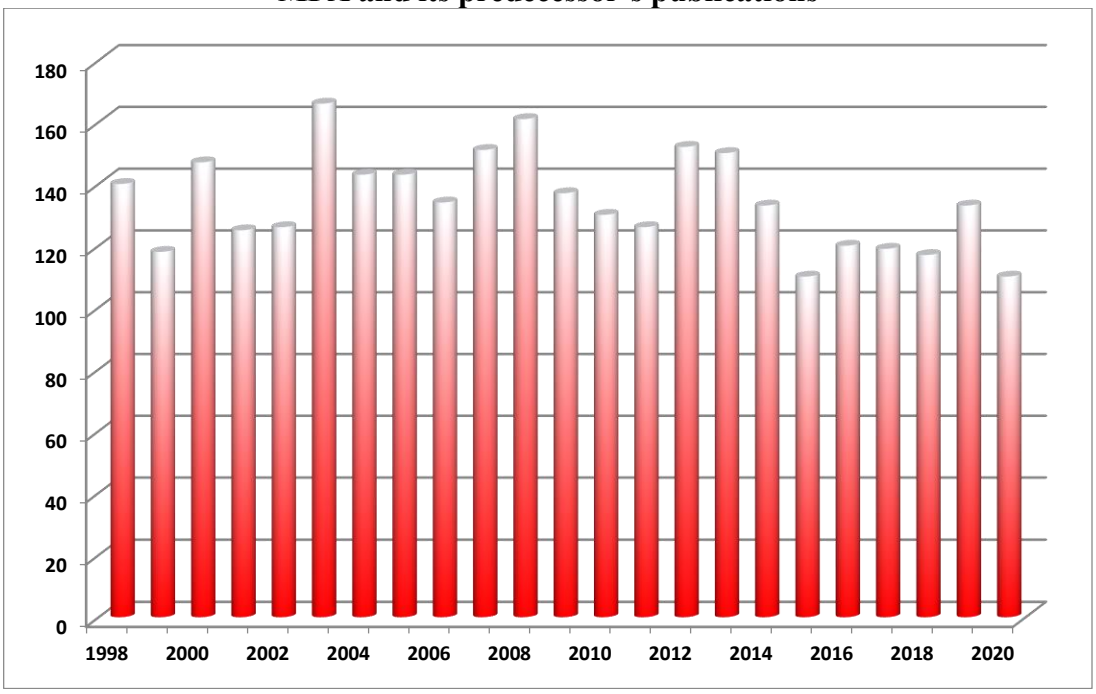

MFA and its predecessor's citations

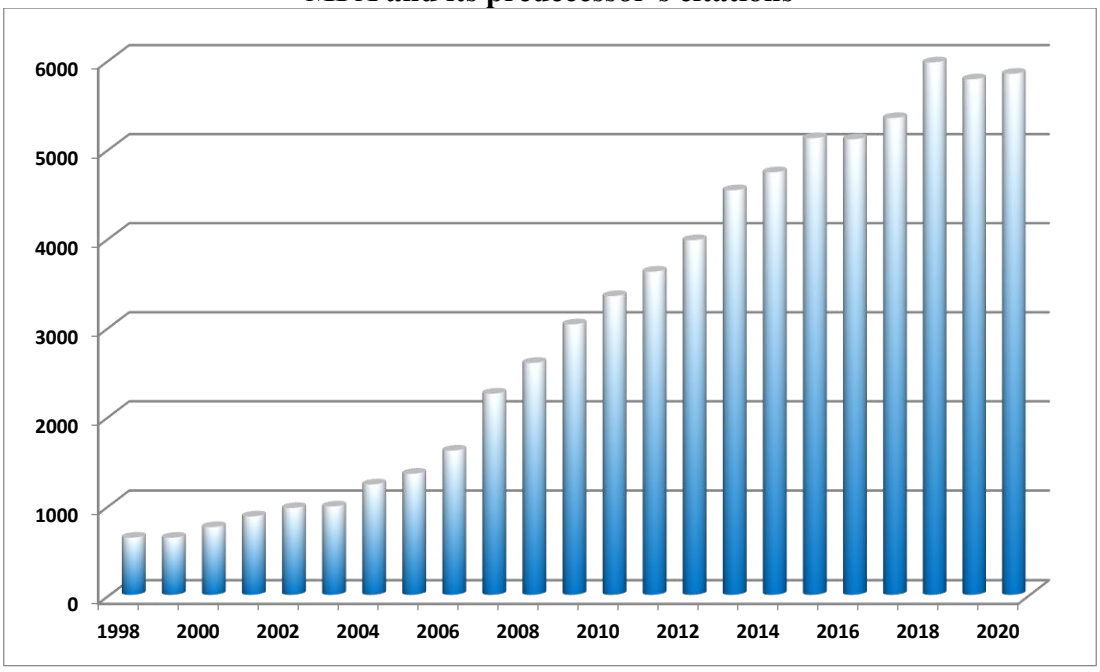

Prizes and Distinctions

	**LÁBÁR, János**	Order of Merit of the Republic of Hungary Officer's Cross
	**TÓTH, Lajos**	Order of Merit of the Republic of Hungary Knight's Cross
	**SERÉNYI, Miklós**	MTA Patent Award
	**BALÁZSI, Katalin**	ACERS Global ambassador award
	**BALÁZSI, Katalin**	Acta Materialia, Mary Fortune Global Diversity Medal

	**SZOLNOKI, Attila**	MFA prize (institute)
	**PÉTER, Beatrix**	MFA prize (postdoctoral)
	**KALAS, Benjámin**	MFA prize (young researcher)
	**KELEMEN, Imréné**	MFA prize (research support)
	**PÁLINKÁS, András**	Ferenczi György prize

Dr. János Lábár (top) and Dr. Lajos Tóth (bottom) receives Hungarian Order of Merit from Tamás Schanda Deputy Minister of Innovation and Technology Ministry

Dr. Miklós Serényi (second from left) receives Patent award at the Hungarian Academy of Sciences

Important events in 2020

Due to the SARS-COV-2 (COVID-19) pandemic, all of out planned conferences and workshops had to be postponed or cancelled. Organizers of the ICTF JVC 2020 finally moved the whole event online. Professor Péter B. Barna was nominated as IUVSTA honorary president.

SCIENTIFIC REPORTS

Nanostructures Laboratory

Head: Dr. Levente TAPASZTÓ, Ph.D., research fellow

Research Staff:

- Zsolt Endre HORVÁTH, D.Sc., Deputy Head of Laboratory
- Prof. László Péter BIRÓ, Member of the HAS
- Gergely DOBRIK, Ph.D.
- Krisztián KERTÉSZ, Ph.D.
- Antal Adolf KOÓS, Ph.D.
- Géza István MÁRK, Ph.D.
- Péter NEMES-INCZE, Ph.D.
- Zoltán OSVÁTH, Ph.D.
- Gábor PISZTER, Ph.D.
- Péter SÜLE, Ph.D.
- Péter VANCSÓ, Ph.D.

Ph.D. students:

- Péter KUN, Ph.D. student
- András PÁLINKÁS, Ph.D. student
- János PETŐ, Ph.D. student
- Márton SZENDRŐ, Ph.D. student

The research activity of the Nanostructures Laboratory is based on the two-decade-long expertise in the synthesis, characterization and engineering of various nanostructures using scanning probe microscopy as the main experimental technique. Since more than a decade, our research efforts are focused on the investigation of two-dimensional materials. Besides graphene, in the last couple of years, novel 2D materials, mainly form the family of transition metal chalcogenides (TMC) have been intensely studied. Recently, we have further extended our activity with the investigation of layered topological insulator crystals. We have also successfully continued our research on bioinspired photonic nanoarchitectures.

The most notable scientific achievement during 2020 were the publication of a Nano Letters paper on observation of a quantum spin-Hall state in a novel topological insulator, the realization of graphene based Quantum Point Contact device published in npj 2D Materials & Applications, as well as a patent on the nanocorrugated graphene based SERS substrate. András Pálinkás has successfully (summa cum laude) defended his PhD thesis at Budapest University of Technology, and also received the Ferenczi György prize.

Robust quantum point contact operation of narrow graphene constrictions patterned by AFM cleavage lithography

680263-NanoFab2D-ERC-2015-STG, LP2014-14 Lendület , LP2017-9 Lendület, Korea-Hungary Joint Laboratory

P. Kun, B. Fülöp (BME), G. Dobrik, P. Nemes-Incze, I. E. Lukács, Sz. Csonka (BME), L. Tapasztó

Due to its outstanding electronic quality, manifesting itself in particularly high charge carrier mobility and long coherence lengths, considerable efforts have been invested into realizing graphene-based quantum devices. One of the basic building blocks of nanoelectronics is a quantum point contact (QPC) – a narrow constriction between two extended electrically conducting areas. In the case of graphene, only the physical removal of material provides a viable solution to realize leakage-free confinement, but the problem of the induced edge disorder must be solved. We have developed a novel AFM-based nanofabrication technique, which enables patterning high edge-quality graphene constrictions with an unmatched precision down to 10 nm feature size. Constrictions can be formed by cutting two lines with one of their ends in close proximity, and the other ends reaching the edges of the flake. To demonstrate the precision of this technique we show the topography of an approximately 10 nm wide constriction (Fig. 1.1). By performing lattice resolution imaging in contact mode, before patterning, we set the precise crystallographic orientation of the cutting direction. Our finding was that the edge quality can be significantly improved when cutting (cleaving) graphene along its high symmetry (armchair/zigzag) lattice directions. In this case the edge roughness can be reduce to ~ 2 nm.

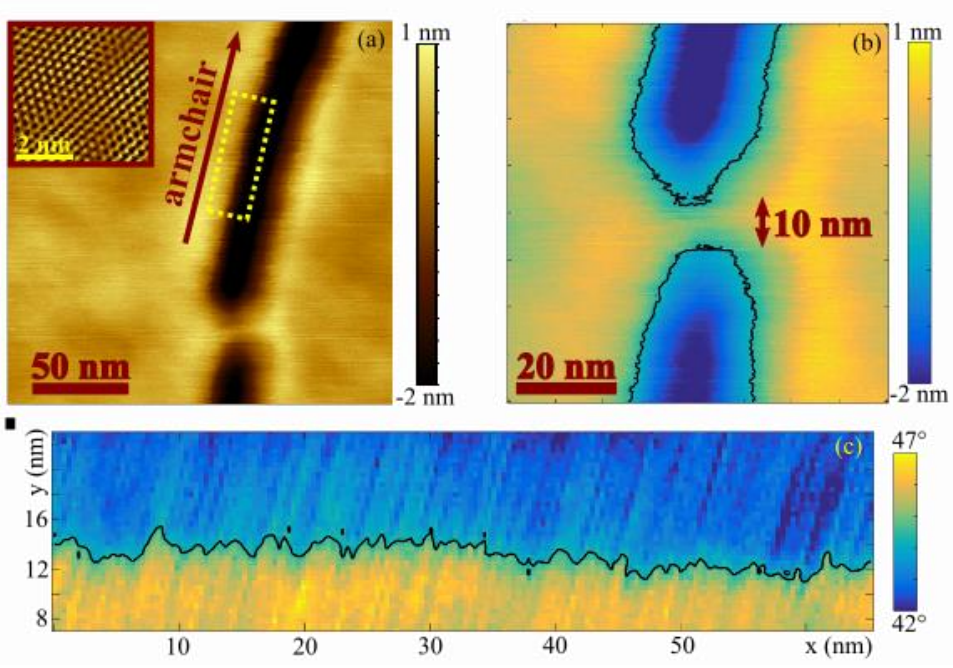

Figure 1.1. *(a-b) Topographic tapping-mode AFM image of a 10 nm wide graphene constriction, inset: lattice resolution revealing the main crystallographic directions (c) edge roughness from the phase image of the dashed rectangular area of (a).*

Transport measurements in two-probe configuration have been performed at low temperature (1.5 K), on the graphene QPC devices contacted by Ti/Au (5/70 nm) electrodes and using the heavily doped Si

substrate as back-gate electrode. Plotting the conductance as a function of the applied backgate voltage (Fig. 1.2) for a ~ 75 nm wide constriction reveals well-defined plateaus around G values of 3, 5, 7, 9, and 11 e^2/h, evidencing the conductance quantization with 2 e^2/h step heights, on top of the square root gate-dependence. This is attributed to lifting the valley degeneracy. In externally applied magnetic field (8 T) conductance steps with roughly e^2/h steps can be seen due to as the spin degeneracy is also lifted in addition to the valley degeneracy.

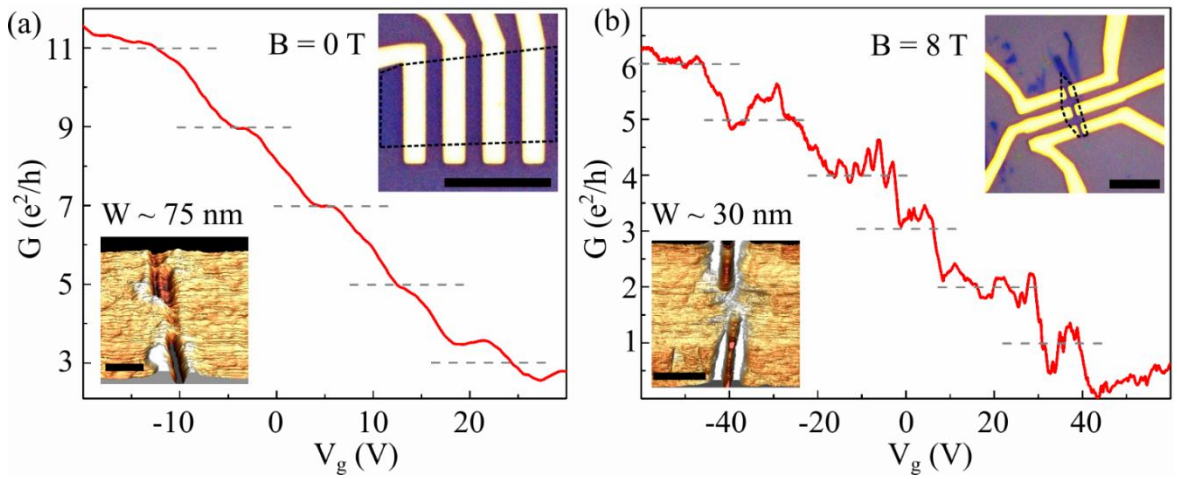

Figure 1.2. *Conductance measurements (1.5 K) of graphene QPCs patterned by AFM cleavage lithography (trenches running along zigzag directions). (Upper insets: optical images of the devices. Lower insets: 3D topographic AFM images of the constrictions, scale bars: 100 nm.) (a) a ~75 nm wide constriction revealing conductance quantization separated by 2 e^2/h steps. (b) a ~30 nm wide constriction in magnetic field (8 T) displaying quantization steps with e^2/h spacing.*

By investigating the temperature dependence of the QPC characteristics, conductance plateaus could be clearly observed up to 20 K, and signatures of conductance quantization could be detected even at 40 K. This is in accordance with the estimated energy separation of transversal modes (~5 meV for 60 nm width), expected to persist up to ~3 k_BT (~5 meV at 20 K) thermal energy.

Our AFM based nanopatterning technique enables the fabrication of robust graphene QPCs, lifting the highly demanding requirements for the device quality, prohibitive for most applications. This technique has the advantage of avoiding energetic beams and aggressive chemical etching that can induce additional disorder extending tens of nanometers inwards from the nominal edges. Moreover, the quality of the edges is further preserved, since after the mechanical cleavage, constriction edges never come into contact with resist material or wet chemistry. Such devices can be employed as cheap resistance standards, providing precise resistance plateaus without requiring externally applied magnetic fields or very low temperatures for their reliable operation.

Correlated insulator in the surface state of multilayer rhombohedral graphite

Lendület LP2017-9, H2020-SGA-FET-GRAPHENE-2019-881603 Graphene Flagship Core3

M. S. Mohd Isa, I. Hagymási (Wigner, Max Planck), Z. Tajkov, K. Márity, O. László (BME), J. Koltai (ELTE), P. Kun, K. Kandrai, A. Pálinkás, P. Vancsó, L. Tapasztó, P. Nemes-Incze

In the last few years, 2D electron systems with flat electronic bands have become a new platform to study the behavior of strongly correlated electrons. Flat bands can arise in van der Waals crystals, if the charge carriers are subjected to a well-defined, long-range periodic potential. At various carrier concentrations in the flat band, they host emergent many-body phenomena, such as ferromagnetism, Mott insulating and superconducting states [Ref. 1.1]. Another example of a 2D electron system with a flat band is in the surface states of rhombohedral graphite (RG).

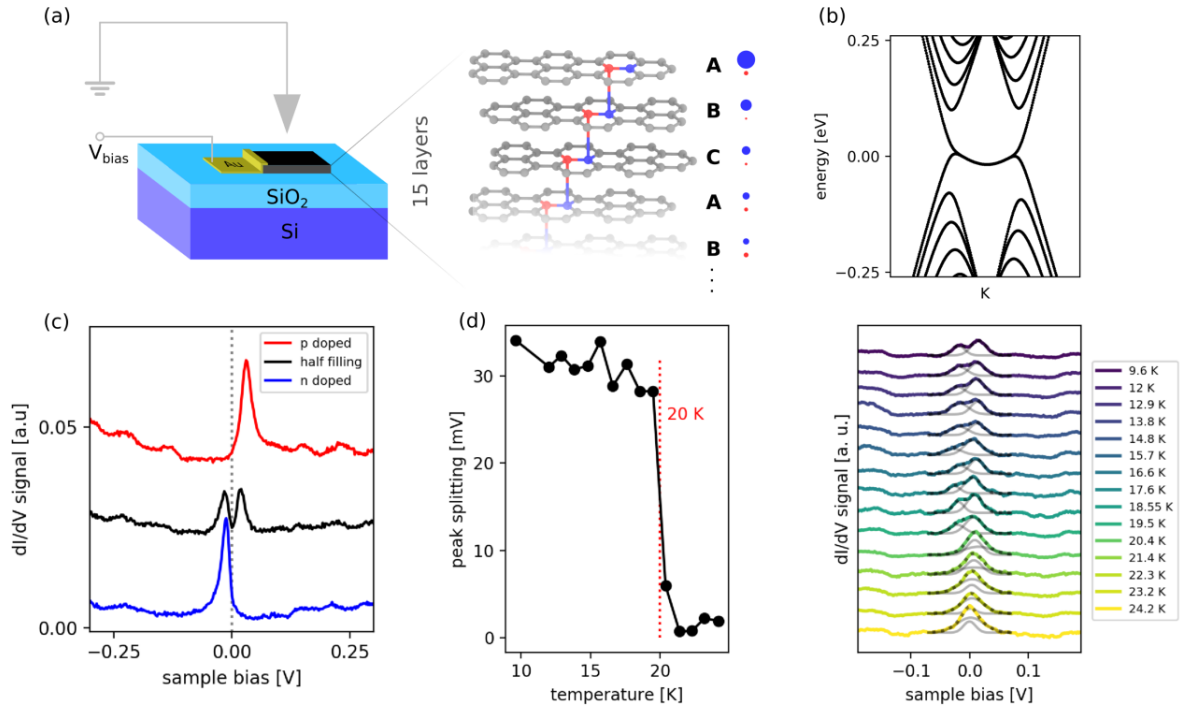

Figure 1.3. ***(a)*** *Schematic of the STM measurement. The letters ABC, denote the stacking sequence of graphene in RG. The size of blue and red circles is proportional to the electronic density on the similarly colored sublattices.* ***(b)*** *Band structure of RG, showing the flat surface state.* ***(c)*** *Tunneling conductance of the RG surface at various charge densities. When the surface state is half filled, it shows a splitting indicative of the gap opening of a correlated insulating state.* ***(d)*** *The gap closes at a temperature above 20 K.*

RG is a metastable form of graphite, which is a topological, nodal line Dirac semimetal in the bulk. It hosts flat surface states of topological origin [Ref. 1.2] in the top and bottom graphene layers (see Fig. 1.3 a,b). In this case one does not need to precisely engineer a periodic superlattice to achieve a flat band system. Instead, the larger the number of graphene layers in the RG, the larger the electronic density in the surface state and the smaller the dispersion.

Since RG is a metastable form of graphite it is quite rare in exfoliated samples and there is no known method to grow this material in a controlled way. Our group has managed to identify thick (more than 10

layers) RG samples among exfoliated graphite crystals, using Raman spectroscopy. For the first time we have been able to identify and study the surface state in thick samples by low temperature (9 K) STM measurements (see Fig. 1.3). In tunneling conductance measurements, the flat band is visible as a pronounced peak near the Fermi level, around 0 bias voltage. Comparing measurements at different charge densities (Fig. 1.3.c), we find that the peak shows a splitting at the Fermi level, when partially filled. This behavior is consistent with a correlated insulating state, having a gap of the order of 30 meV. Furthermore, we measure a critical temperature of 20 K, above which the gap closes. Using the Hubbard model and density matrix renormalization group calculations we have reproduced the observed splitting and identify the gapped state as a sublattice antiferromagnetic insulator.

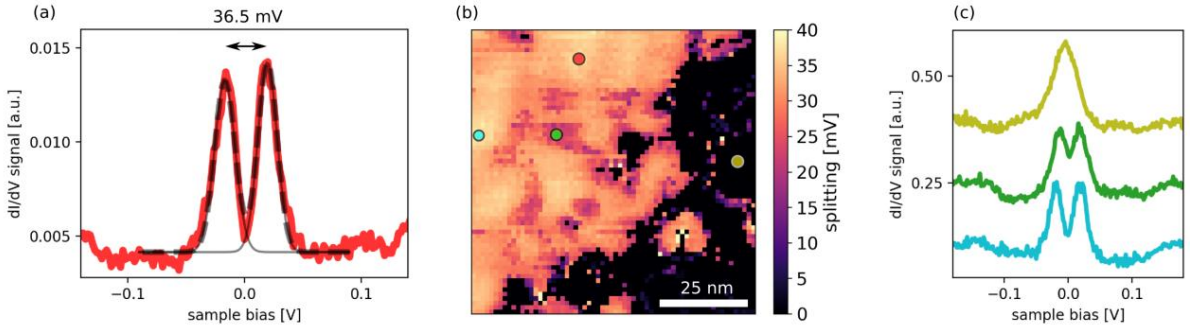

Figure 1.4. ***(a)*** *Double gaussian fit to the split surface state.* ***(b)*** *Mapping the local splitting, as revealed by gaussian fitting across an 80x80 nm^2 area of the RG.* ***(c)*** *Selected tunneling conductance spectra at the positions shown by the appropriately colored markers in (b).*

Surprisingly, if we map the splitting over a large area (80x80 nm^2), we find that it shows a domain structure. Areas of large splitting neighbor areas with no observable splitting (Fig. 1.4 b,c). This behavior is indicative of competing many-body ground states, such as in high T_c superconductors [Ref. 1.3]. More investigation is needed to elucidate the origin of these domains and of the precise nature of the ground state. Our work establishes RG as a new platform to study many-body interactions in a topological 2D electron system, at surprisingly high temperatures, up to 20 K.

Synthesis and characterization of graphene-silver nanoparticle hybrid materials

OTKA K119532, OTKA KH129587, OTKA K134258

Z. Osváth, A. Pálinkás, G. Piszter, Gy. Molnár

Noble metallic nanoparticles (NPs) are extensively applied for chemical and biological sensing due to their local surface plasmon resonance (LSPR) and surface-enhanced Raman scattering (SERS) properties. Nanostructured Ag is the best material for plasmonics due to the absence of interband absorptions and low optical loss at optical frequencies. However, silver has poor stability under ambient conditions, forming Ag_2S on its surface. Graphene seems to be the ideal protective coating, since it is atomically thin and impenetrable to standard gases, including helium. In this work, we present a simple method for the preparation of Ag NPs and graphene–silver nanoparticle hybrids directly onto highly oriented pyrolytic graphite (HOPG) substrates.

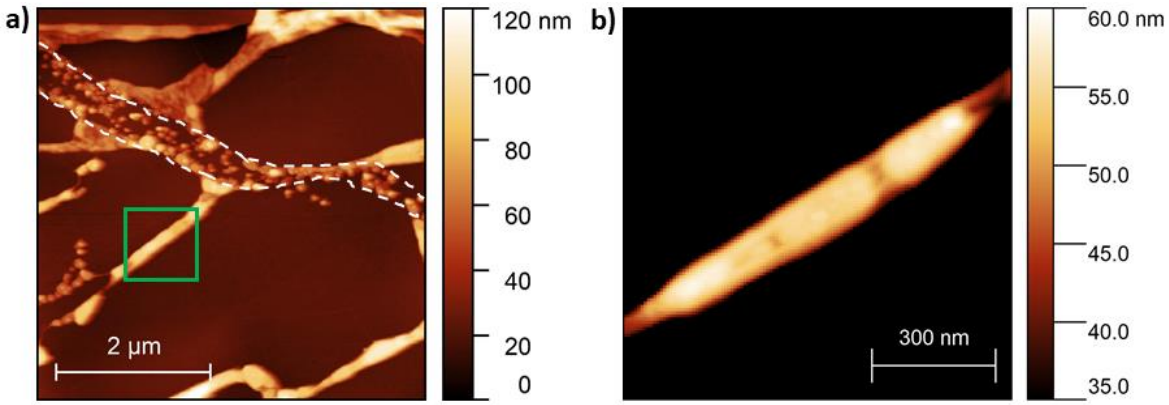

Figure 1.5. *(a) AFM image of graphene-covered Ag nanostructures formed on HOPG substrate during annealing at 400 °C. Bare nanoparticles are also observed between the two white dashed lines, which mark a discontinuity of the graphene overlayer. (b) Larger magnification AFM image corresponding to the square marked with green line in a), showing graphene–Ag NP–HOPG sandwich structure.*

Immediately after silver deposition and opening of the vacuum chamber, the thin silver films were covered with CVD graphene. The transfer process yielded a graphene coverage of 40-50%. A subsequent annealing at 400 °C resulted in flat silver nanoparticles on the non-covered areas, while on graphene-covered regions various hybrid structures formed. Typical AFM images of the obtained graphene–Ag hybrid nanostructures are shown in Figure 1. Elongated structures, as well as large, nanoparticle-free graphene/HOPG areas, are also observed (Figure 1.5.a). Closer investigation of the elongated structures reveals graphene-covered groups of Ag NPs, as shown in Figure 1b (graphene–Ag NPs–HOPG sandwich structure). Using Tunneling Spectroscopy, we revealed charge transfer between Ag NPs and the graphene overlayer, resulting in slight *n*-doping of graphene.

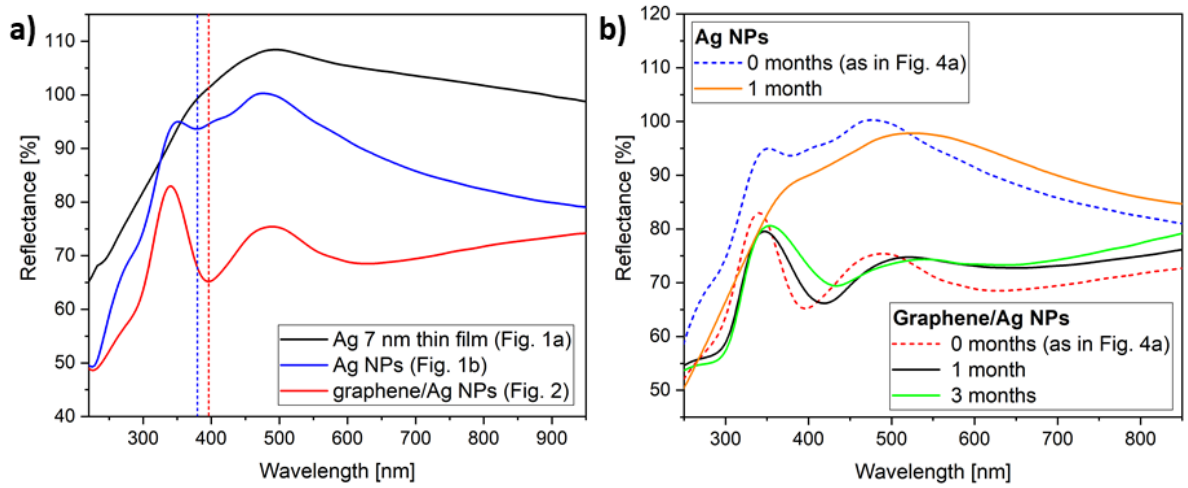

Figure 1.6. *(a) Optical reflectance spectra of the as-deposited Ag thin film (black), the Ag NPs produced by annealing (blue), and the graphene-covered Ag NPs (red). The LSPR of Ag NPs (blue dashed line) is redshifted when covered with graphene (red dashed line). (b) Optical spectra measured after one month on bare Ag NPs (orange) and on graphene/Ag NPs (black). For better comparison, the initial spectra from a) are also shown (blue dashed and red dashed lines, respectively). The spectrum of graphene/Ag NPs measured after 3 months is also plotted (green).*

The reflectance spectra of the as-deposited Ag thin film, bare Ag NPs, and graphene-covered Ag NPs are shown in Fig. 1.6.a. While the spectrum of the as-deposited Ag thin film is featureless, we observe a reflectance minimum at 379 nm for the sample with bare Ag NPs, which is attributed to the LSPR of the nanoparticles. The LSPR is more pronounced for the graphene-covered Ag NPs, which is redshifted to 396 nm. We investigated how the optical properties of Ag NPs and graphene/Ag NPs kept under ambient conditions vary in time. We performed the same reflectance measurements on the same samples one month and three months after preparation. The corresponding spectra are shown in Fig. 1.6.b. It can be clearly observed that due to spontaneous sulfurization, the optical reflectance spectrum of bare Ag NPs already loses its features after one month. In contrast, graphene-covered Ag NPs have well-defined LSPR, even after three months. Nevertheless, the amplitude of the resonance decreases and the LSPR gradually shifts towards larger wavelengths, i.e., the reflectance minimum is observed at 418 and 433 nm after one and three months, respectively. A more detailed study of the graphene/Ag NPs was performed by SEM and EDX. The EDX analysis of aged non-covered nanoparticles revealed the presence of sulfur, a spectroscopic signature of spontaneous sulfurization from air. Importantly, no sulfur was observed on graphene-encapsulated Ag NPs, even after 14 months, which demonstrates the long-term protective capability of the graphene coating. Thus, a way to improve the stability in time of the LSPR could be to increase significantly the total graphene coverage of the Ag NPs. Such protection can be very useful for example in LSPR shift-based sensor applications, photocatalysis, or the preparation of advanced SERS substrates. [Ref. 1.4]

Reconstruction-free magic-angle flat-bands with ultra-long interlayer distances

680263-NanoFab2D-ERC-2015-STG, LP2014-14 Lendület , Korea-Hungary Joint Laboratory

M. Szendrő, P. Vancsó, G. Dobrik, L. Tapasztó

Twisted bilayer graphene (TBG) hosts extremely flat bands extended all over the superlattice Brillouin-zone near the Fermi-level at the twist angles of the so-called 'magic-angles'. Therefore, TBG is thought to be an excellent candidate to accommodate exotic quantum phases. Indeed, superconducting and Mott-insulating phases have already been identified near the first magic angle (~1.1°) . Although there are several other magic angles below 1.1°, however, at such small twist angles a special surface reconstruction sets on, which disperses the flat-bands significantly, hindering its desirable property.
Here we studied both the mechanical and electronic decoupling of the graphene layers with increasing interlayer distance (ID) for these very small twist angles. We found using classical molecular (CMD) simulations that a moderate mechanical decoupling (~4.5Å) is sufficient to prevent the formation of the reconstruction (Fig. 1.7).

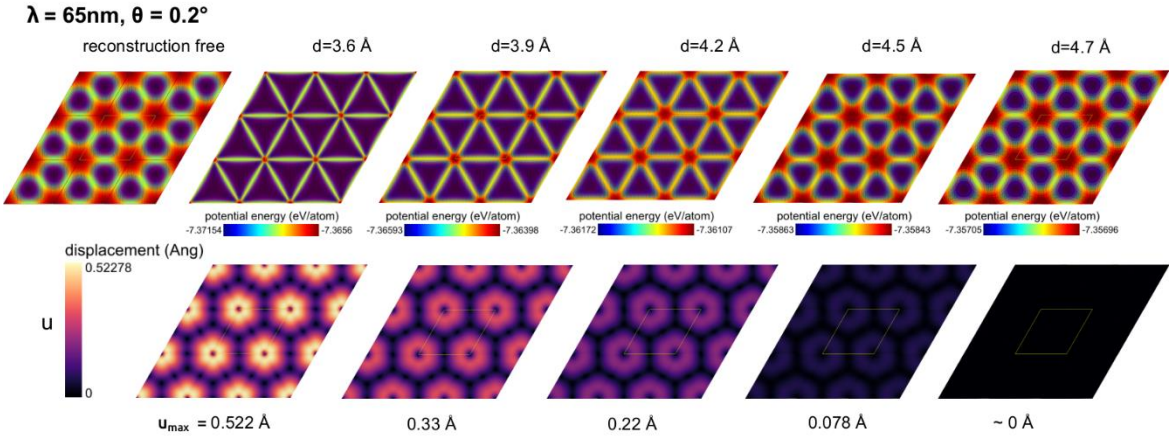

Figure 1.7. *Surface reconstruction of small-angle TBG during mechanical decoupling. In-plane geometrical relaxation of a 65nm x 65nm Moiré-superstructure using CMD simulations. Top row: potential energy surface of the relaxed top layer with different interlayer distances. Bottom row: displacement magnitude of the atoms in the top layer with different interlayer distances.*

However, the system remains electronically coupled enough to maintain the flat-bands. The latter was studied by DFT, tight-binding (TB), and continuum models. We showed that DFT calculations predict a much slower decay of the coupling strength with increasing ID than existing TB methods do. Based on our DFT calculations we proposed a new TB parametrization to accommodate this effect. With our new TB parameters, we also implemented the continuum model of the TBG. Using these models, we showed, that the position of the first magic angle decreases slower with increasing ID than is expected, and at ID of 4.5Å a magic angle of 0.1° still persists with a prominent flat band (Fig. 1.8).

These tendencies were also supported by experiments. We have prepared TBG samples by back folding one layer of graphene onto itself on an amorphous silica substrate. It has been previously reported, that the ID of backfolded TBG on amorphous SiO2 can be much larger (up to 6 Å) than the equilibrium distance (3.35 Å).

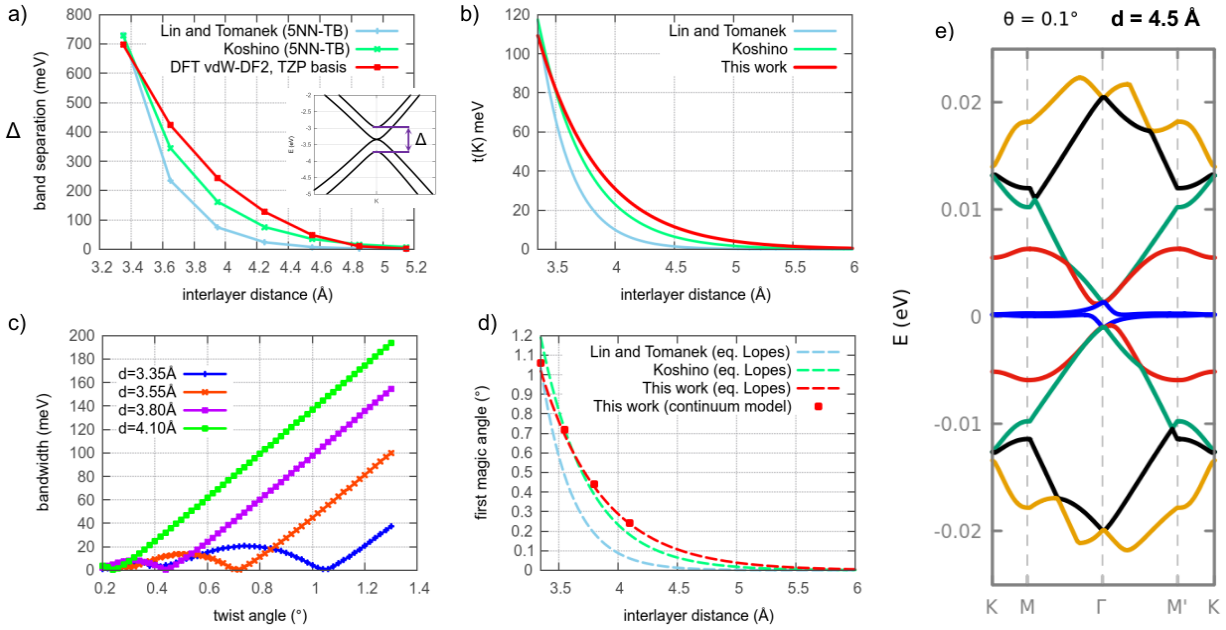

Figure 1.8. *Electronic decoupling of small-angle TBG. a) Band separation at the K point of an AB bilayer graphene calculated from 5-NN Tight-binding models and compared to DFT calculations. b) Decay of the coupling strength at the K point of our TB parametrization compared to other models. c) Bandwidth of the lowest conduction band for different twist angles and interlayer distances calculated from continuum model band-structures. d) Position of the first magic-angle with increasing interlayer distance calculated from theory and continuum model. e) Continuum model band-structure of TBG at increased ID with an apparent flat-band.*

Indeed we have found samples with an ID of about 5 Å and a very large Moiré-periodicity (65 nm), which corresponds to a twist angle of about 0.2°. Moreover, in agreement with our calculations, the Moiré-patterns revealed the absence of the surface reconstruction. Also, these samples showed significant LDOS peaks in STM spectra at the Fermi-level indicating an intact flat-band even at large interlayer distances (~5 Å).

Selective vapor sensing of structurally colored lepidopteran wings under humid conditions

OTKA K115724

G. Piszter, K. Kertész, Zs. Bálint, L. P. Biró

The efficient detection of volatile organic compounds (VOCs) is crucial, as in our everyday indoor activities and living environments their presence is inevitable. Therefore, it is important to develop sensors that may work in atmospheric humidity similar to our everyday living and working conditions, can endure repeated vapor exposures, and can be used for real-time analysis while remaining sensitive and chemically selective. The biological photonic nanoarchitecture-based sensors are excellent candidates for this task as they are cheap and ready-made devices available at a macroscopic size in high quality, therefore they can be used in the potential applications instantly.

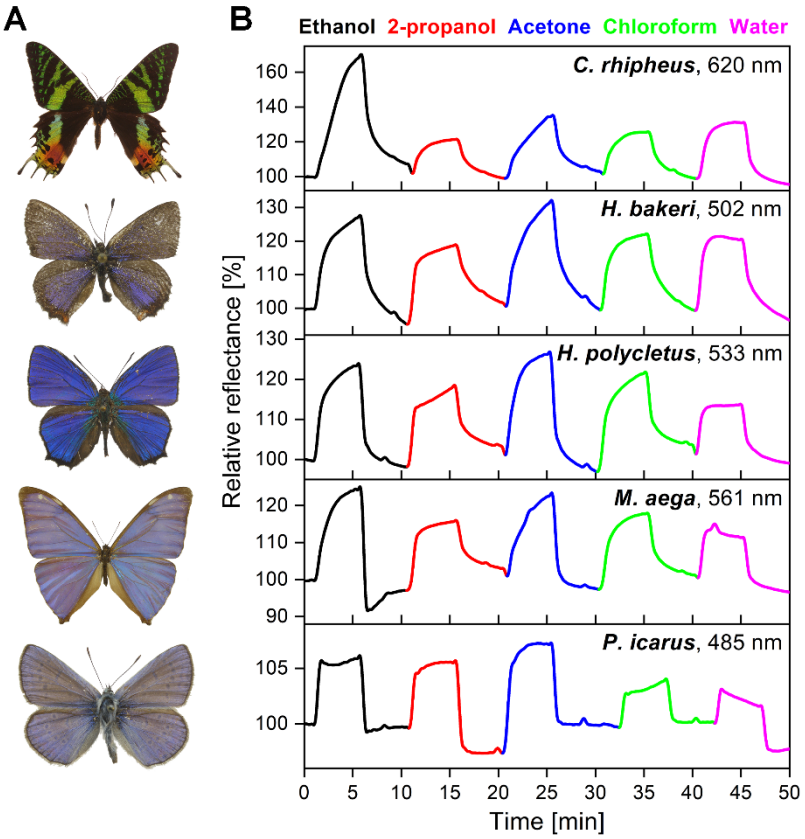

Figure 1.9. *(**A**) Photographs of the investigated specimens. (**B**) Test substances were exposed to the sensors for 5 min, with 5-min purging in between. The measured time-dependent intensity of the spectral changes was plotted as a function of time. Different volatile organic compounds (VOCs) are noted by different colors. Each of the wings showed specific time-dependent optical responses for the five test substances. The nanometer values (upper right corners) show the wavelengths of the spectral responses from which the time-dependent signals were generated.*

In this study, the vapor-sensing properties of butterfly and moth wings were investigated by optical spectroscopy in the presence of water vapor. Due to the open structure of the nanoarchitectures, the color of these chitin–air nanocomposites changed rapidly when the vapor composition of the ambient atmosphere changed. The long-term color changes were affected by the swelling of the chitin.

To investigate the time-dependence of the color change signal, five test substances were used for 5-min vapor exposures on the wings in 50% dilution (Fig. 1.9). The vapor flows were separated by 5-min purging of the cell with synthetic air. The optical responses of the different test substances are indicated with different colors for all five samples. There are clearly visible differences in the shapes of the substance-specific signals between the VOCs, showing that the time-dependent color change signal can be used in real-time substance-selective vapor sensing.

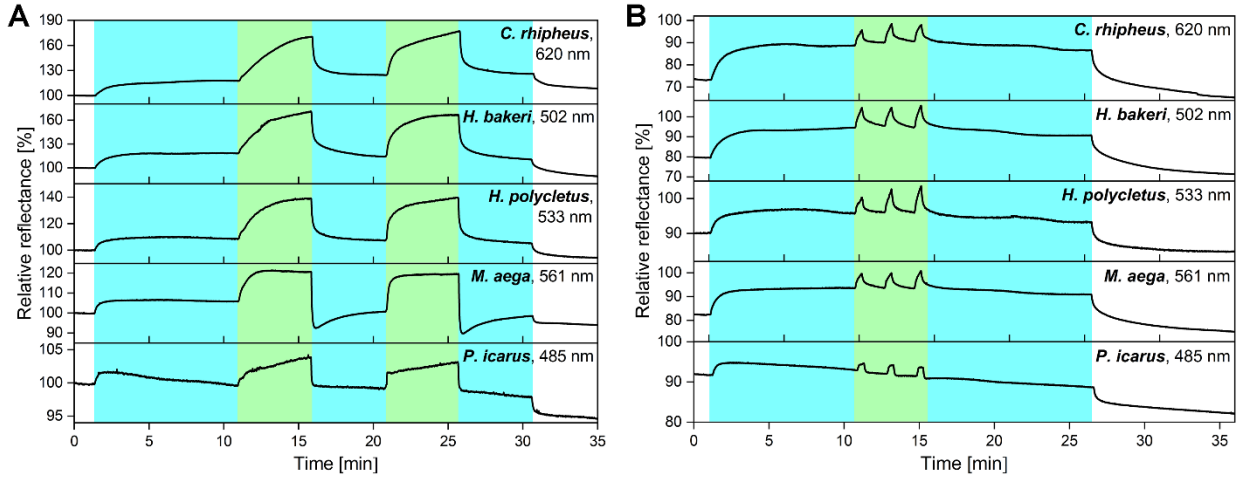

Figure 1.10. *The VOC-sensing properties of the samples were tested in the presence of humidity. Therefore, a constant 25% water vapor background was applied, and it was followed by* ***(A)*** *two 5-min-long 50% ethanol vapor exposures or* ***(B)*** *three 30 s 50% ethanol pulses. In both cases, the response signal was separated from the background of the humidity, and the intensity of the time-dependent signal was preserved compared to the humidity-free case.*

The vapor-sensing properties in the presence of water vapor were investigated to simulate a real-world environment in the laboratory. Thus, the environment was designed to reproduce room temperature, atmospheric pressure, and in this case 25% relative humidity. The maximal intensity of the spectral change was plotted as a function of time in Figure 1.10.A, while 5-min-long 50% ethanol pulses (green) were added to the constant water vapor background (blue). In the second measurement (Fig. 1.10.B), 30 s ethanol pulses (green) were applied to investigate whether the sensors preserved their short response times and relatively high sensitivities for VOCs in the presence of water vapor. The measurements show that by choosing a suitable reference level, the effect of continuously present water vapor can be taken into account and the concentration of the test substances can be deduced. This provides an opportunity not only to analyze pre-measured data sets, but also to perform real-time measurements in atmospheric humidity based on the substance-specific time-dependent color change signal which can be measured on the structurally colored wings of butterflies or moths.

Additive and subtractive modification of butterfly wing structural colors

OTKA K115724

K. Kertész, Zs. Baji, A. Deák, G. Piszter, Zs. Rázga (SZTE), Zs. Bálint (MTTM), L. P. Biró

Functional nanostructures in insect cuticle can generate structural colors. These photonic nanoarchitectures exhibit highly diverse structures: from lamellar multilayers, through inverse opal-like and gyroid structures, to photonic amorphous, many examples can be found. The structural color of the butterfly wings is determined by the characteristic sizes of the photonic nanoarchitecture and the refractive indices of the materials building up the wing scales. As the structural properties of these biological materials are exciting for materials scientists for replication, modeling, and finding potential applications, it is useful to get a deeper insight into how the physical properties of these often sophisticated nanoarchitectures can be affected by modifying their structural and material properties.

Controlled modifications were performed on two kinds of photonic nanoarchitectures: (1) of biological origin, built mainly from chitinous materials; and (2) of bioinspired samples fabricated using ordered layers of silica spheres built by Langmuir-Blodgett (L-B) method. Two distinct methods were used, thinning by oxygen plasma etching and thickening by atomic layer deposition (ALD), to obtain a series of optically modified samples. Scanning and transmission electron micrographs were taken of the sample series thus obtained. The samples were subjected to optical reflectance spectrometry, and the results were compared to optical simulations.

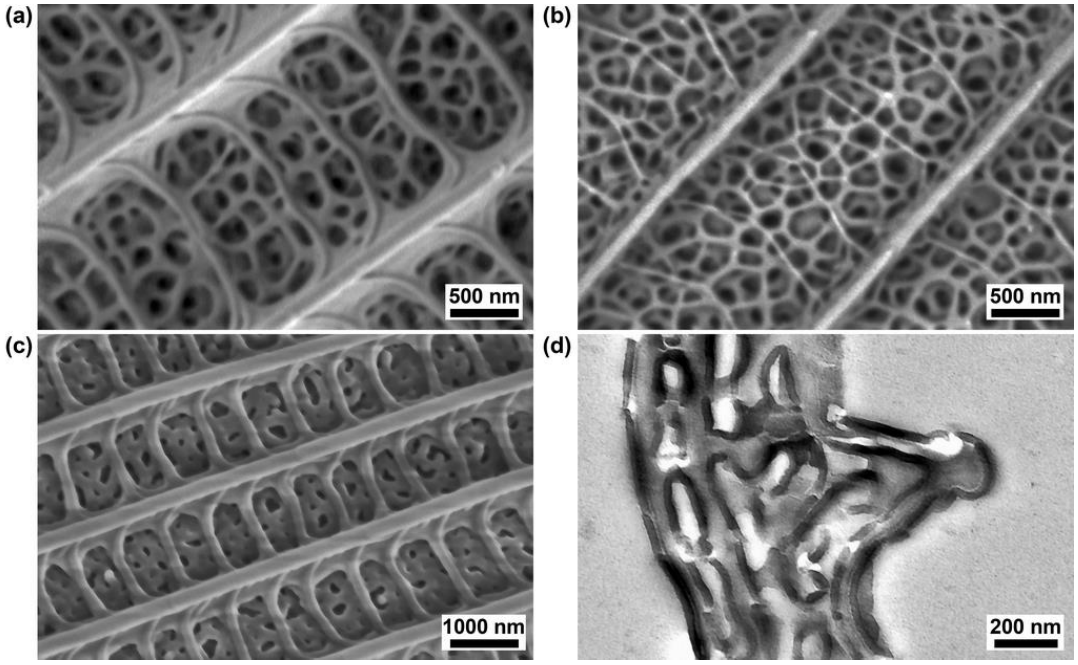

Figure 1.11. *Scanning and transmission electron micrographs of Polyommatus icarus cover scales on the dorsal wing surface. (a) pristine; (b) after 2 min of oxygen plasma etching; (c) with a 40 nm ALD layer of Al_2O_3; (d) a TEM image of sample (c).*

In a typical butterfly wing scale, the spongy structure in the area between the ridges and the cross-ribs determines the blue color. Because it is a highly permeable structure, the ALD precursors entered the deepest areas in the pores and resulted in conformal thickening of the chitin nanostructures. The size of the holes, filled by air in natural conditions, determines how thick the ALD layer can be. By contrast, oxygen plasma treatment erodes and thins the chitin: the ridges become narrower and the cross-ribs are hardly visible on SEM images. Inside the porous nanostructure, the ratio of chitin to air voids is reversed (see Fig. 1.11). This process has a limit, as after a certain level the material completely disappears, the integrity of the structure vanishes, and the wing scale nanoarchitecture collapses. For artificial L-B samples the ALD coating covers the silica spheres in a homogeneous and conformal manner in all layers of spheres, narrowing the free space between them, which is similar to the closure of the pores observed in the photonic nanoarchitecture of the wing scales.

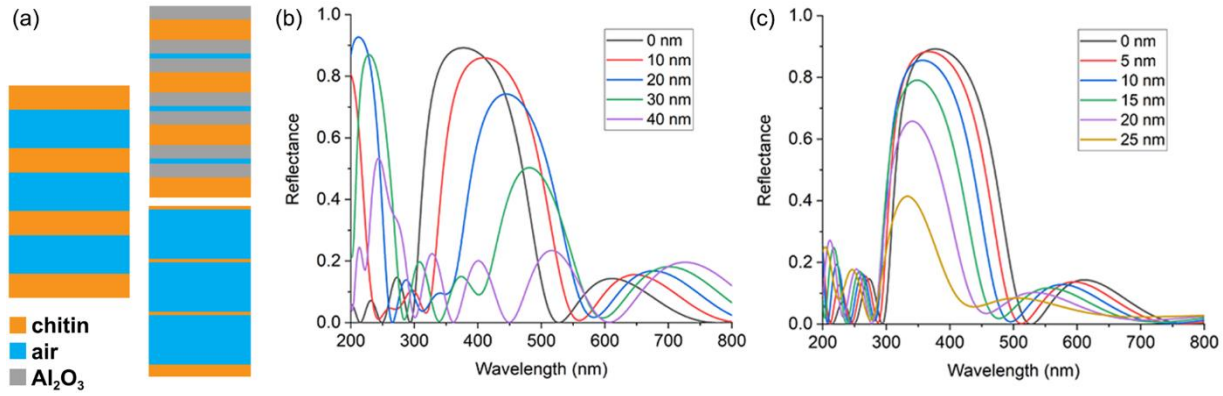

Figure 1.12. *(a) Multilayer model of Polyommatus icarus wing scale: thickening both sides of the chitin layer by Al_2O_3 addition at the expense of air layers (top); thinning of the chitin by oxygen plasma etching (bottom). (b) Calculated normal incidence reflectance spectra on a structure from (a) with deposited Al_2O_3 layers of 10–40 nm on both sides. (c) The same calculation while thinning the chitin layers by 5–25 nm on both sides.*

The change in the optical reflectance spectrum was measured by means of an integrating sphere for all samples. We found that the ALD shifted the reflected spectrum towards longer wavelengths, while oxygen plasma etching towards shorter wavelengths. The magnitude of the shifts was around 80 nm with both treatments which means a remarkable 160 nm range of tuning possibility, promising for practical applications. Transfer matrix method was used to calculate the reflectance spectra of the modified samples, and it predicted spectral shift values and peak intensity trends similar to those found experimentally (Fig. 1.12). Whether from the thickening or thinning side, until the reflectance peak begins to collapse, these modifications can be used to precisely tune the reflectance of porous photonic structures both with biological and artificial bioinspired origin. As on porous 3D structures, the entire volume of the samples can be accessed, therefore the surface modification techniques have stronger effects on optical and chemical properties which may be a benefit in potential applications.

Photonics Department

Head: Dr. Peter PETRIK, D.Sc., scientific advisor

Research Staff:

- Miklós FRIED, D.Sc., Head of Ellipsometry Laboratory
- András DEÁK, Ph.D., Head of Chemical Nanostructures Laboratory
- Miklós SERÉNYI, D.Sc.
- Gábor VÉRTESY, D.Sc.
- Antal GASPARICS, Ph.D.
- Norbert NAGY, Ph.D.
- Zoltán LÁBADI, Ph.D.
- Ferenc RIESZ, C.Sc.
- Dániel ZÁMBÓ, Ph.D. on leave
- Emil AGÓCS, Ph.D., on leave
- György KÁDÁR, D.Sc., Prof. emeritus
- Tivadar LOHNER, D.Sc., Prof. emeritus
- János MAKAI, C.Sc., retired
- András HÁMORI, dr. univ., retired
- György JUHÁSZ, dr. univ., retired

Students:

- Benjamin KALAS, Ph.D.
- Szilárd POTHORSZKY, Ph.D.
- Alekszej ROMANENKO, M.Sc., Ph.D.
- Dániel SZEKRÉNYES, Ph.D.
- Dávid KOVÁCS, M.Sc.
- Rita NÉMEDI, B.Sc.

The Photonics Department develops unique methods and tools for non-destructive optical and magnetic measurement of surface nanostructures and materials (spectroscopy; magnetic material testing; biosensors; surface curvature measurement; surface testing; water contamination). One of the most important tasks of the Department is patenting and application of the methods in international projects with partners representing the industry and the high technology.

Optical detection of molecules on liquid and gas surfaces by membrane-based in-situ mid infrared spectroscopic ellipsometry

OTKA K131515

A. Romanenko, B. Kalas, P. Hermann, O. Hakkel, L. Illés, M. Fried, P. Fürjes, G. Gyulai, P. Petrik

We have shown that infrared ellipsometry (IRSE) flow cells (with membrane thicknesses of 2 and 5 μm) can be prepared from SOI wafers. The process includes lithography and microfabrication on commercially available SOI wafers (Fig. 2.1 and 2.2). We have shown that the size of the 5 mm x 20 mm (50μL volume) size cells can be realized without damaging the membranes during fluid flow. Unfortunately, the use of ribs in reinforcing the membranes is not advantageous, they further increase the fragility of the structure, as cracks may form in the edges between the ribs and the membrane. Fitted ellipsometry spectra revealed high-quality single-crystal membranes (c-Si), The average roughness of the top and buried sides of the membrane was ≈ 0.4 ± 0.1 nm (Fig. 2.1). Although those with a thickness of 2 μm were laterally inhomogeneous and bent due to their thinness.

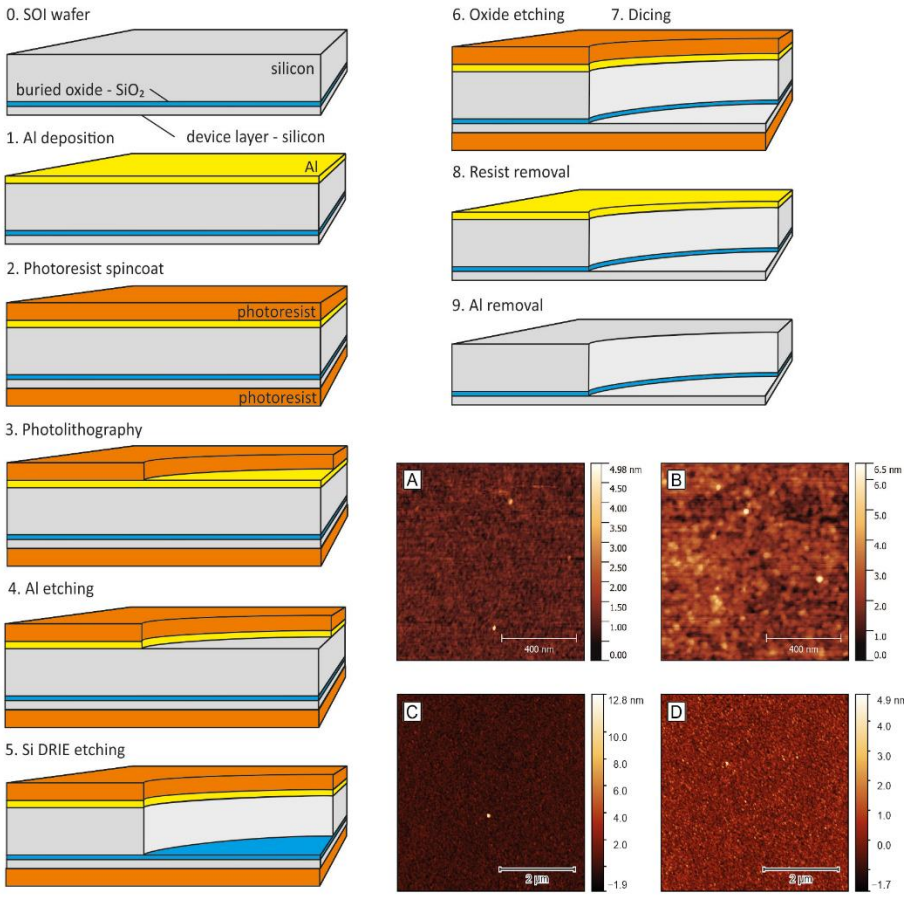

Figure 2.1*. Steps of fabrication of the silicon flow cell by 3D micromachining of SOI wafer resulting in a few micrometer thin crystalline silicon membrane transparent in the IR spectral range. Surface maps of the top [A] and inner side of the silicon membrane of the flow cell measured by AFM. [Ref 2.1]*

The applicability of the configuration was demonstrated by in-situ analysis of polylactide-co-glycolide (PLGA) nanoparticles adsorption of the membrane surface (Fig. 3). The characteristic performance of the method was demonstrated by calculating both the chemical (bonding states) and physical (layer thickness) properties of the nanoparticle layer.

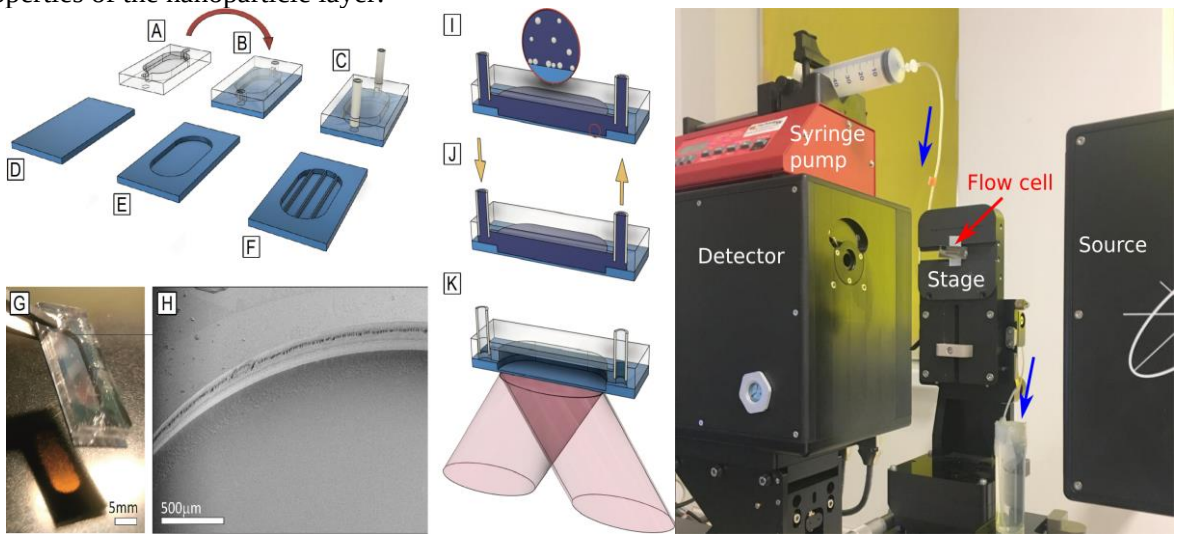

Figure 2.2. *[A–F] Steps of the fabrication of a sealed chamber and the assembled flow cell with the thin silicon membrane. [G] and [H] show the cell and the edge of the membrane. [I–K] Design and application of the membrane-based IRSE cell. The photograph on the right shows the measurement setup. The cell was mounted on the vertical stage of the IR ellipsometer.* [Ref 2.1]

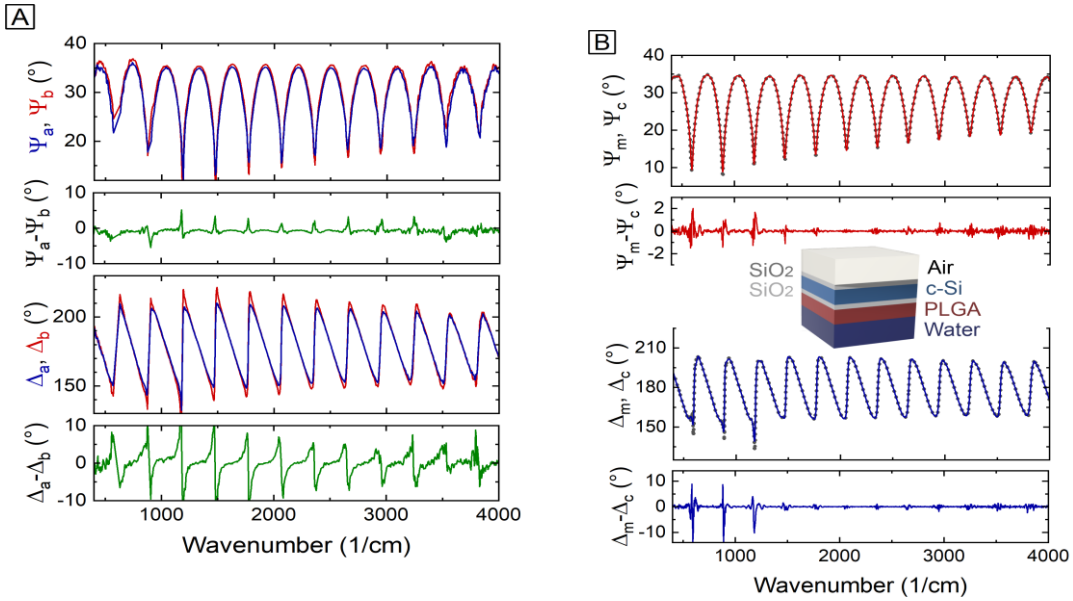

Figure 2.3. *[A] Ψ and Δ IR spectra measured on the 5 µm membrane before (red lines and index "b") and after (blue lines and index "a") the PLGA nanoparticle adsorption in water. [B] the measured (black lines) and fitted (colored lines) spectra after PLGA nanoparticle adsorption. The differences are plotted below the graphs.* [Ref 2.1]

The completed concept opens up new possibilities in which the membrane thickness of thematic cells, the use of different new sublayers, size, and many other parameters can be further optimized to further increase sensitivity and speed. In addition, we have the ability to perform measurements and simulations to find the most appropriate parameter ranges for both optical design and materials. As a result, the optical design can be optimized and the best configurations can be identified, allowing simple and inexpensive sensors to be built for specific purposes.

Optical spectroscopy studies on nanoparticles

NKFIH FK128327, KH129578, 2018-2.1.13-TÉT-FR-2018-00002

D. P. Szekrényes, Zs. Zolnai, A. Deák

In our recent work we investigated how changes in the plasmon linewidth of individual gold nanorods upon thiol binding to the particles' surface can be used to investigate the ligand exchange in detail. We used positively and negatively charged small molecule thiols to *in situ* study the spectral changes of individual particles' (Fig. 2.4.a). While for cysteamine almost complete ligand coverage can be achieved, the accumulation of the negatively charged mercaptopropionic acid is inhibited by the original CTAB capping molecules (Fig. 2.4.b). By evaluating the thiol-induced plasmon linewidth changes at different bulk CTAB concentration levels, it was concluded that the molecular interaction between the adsorbing thiol, and the CTAB that is physically bound to the particle surface, results in completely different final composition and structure of the surface ligand layer (Fig. 2.4.c).

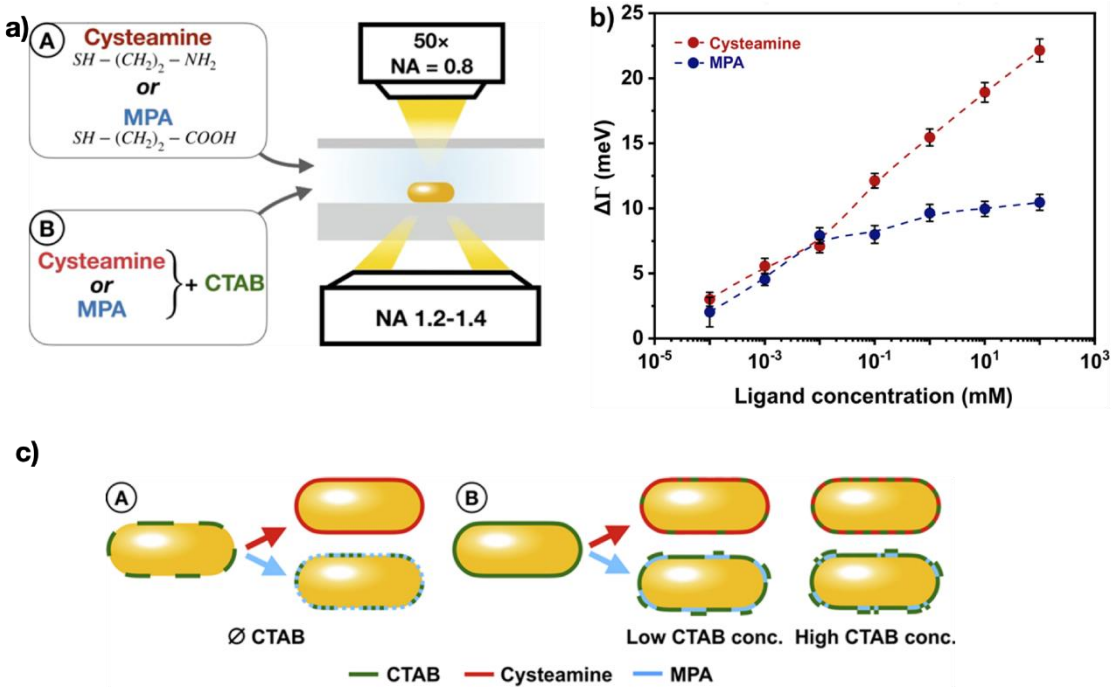

Figure 2.4*. a) Schematics of the measurement. b) Changes in the plasmon resonance linewidth as a function of the thiol concentration (no CTAB added). c) Schematics of the derived ligand exchange scenarios.*

We continued our work in the controlled preparation of nanosphere dimers at solid/liquid interface with the specific aim to investigate their arrangement and surface separation in-situ in the aqueous environment by optical microspecroscopic measurements. As the coupled spectrum of such dimers is well known change sensitively with the surface-to-surface separation, it could provide a platform to study in the colloidal interaction between nanoparticles. The model system is depicted on Fig 2.5.a. The colloidal interaction between the particles can be taken into account by considering the double-layer, dispersion and steric terms in the expression for the total interaction energy. The simulation predicts that the formation of dimers is possible in our system and the preferential arrangement of the second particle will be ontop of the substrate located one's (Fig. 2.5.b). In situ microspectroscopy measurements on individual particles (Fig. 2.5.c)

corfirm the dimer formation (see ex-situ SEM inset). The next step will be the detailed in-situ, polarisation resolved investigation of the spectra, that could be used for the determination of the equilibrium particle separations by comparingthe data with simulation results (Fig. 2.5.d).

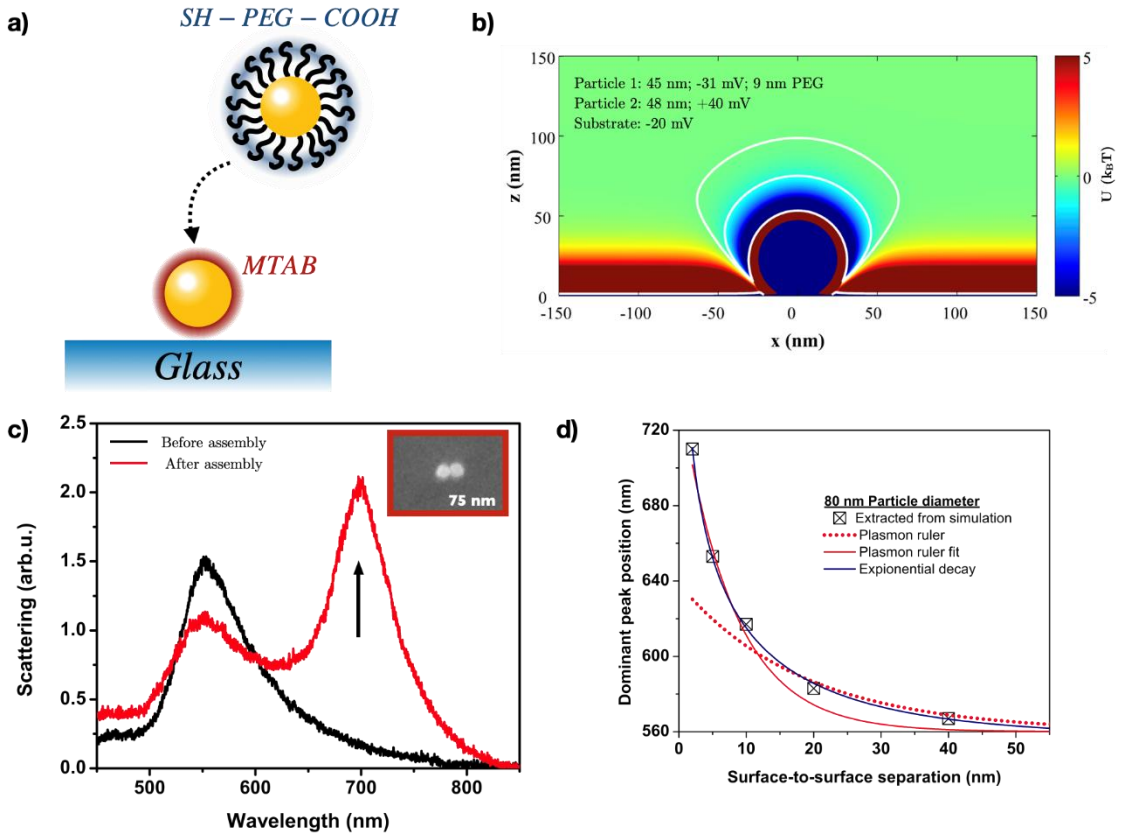

Figure 2.5*. a) Schematics of the model system for the controlled dimer formation. b) Simulation data showing the net colloidal interaction energy (U) in k_BT units between the substrate anchored positively charged, and the approaching negatively charged nanoparticle (double layer, dispersion and steric interactions were taken into account). c) Example showing the spectral change of an individual nanosphere's spectrum upon dimer formation (inset shows the correlative SEM image of the given dimer). d) Theoretical change in the dimer's dominant peak position (marked by an arrow in c) as a function of the separation distance as extracted from optical simulations.*

In the framework of a bilateral project we also work with our French partner, Doru Constantin from the Laboratoire de Physique des Solides (Orsay) on the detailed SAXS investigation of our PEGylated gold nanoparticles, that we used earlier with great success to demonstrate the ionic strength and temperature triggered clustering of nanoparticles. We successfully determined the nanoparticle cluster structure ftom the SAXS measurements, that are in agreement with the optical data on the same systems (Fig. 2.6). From the results the the surface grafted PEG chain collapse and the clusterformation process can be better understood. [Ref. 2.2]

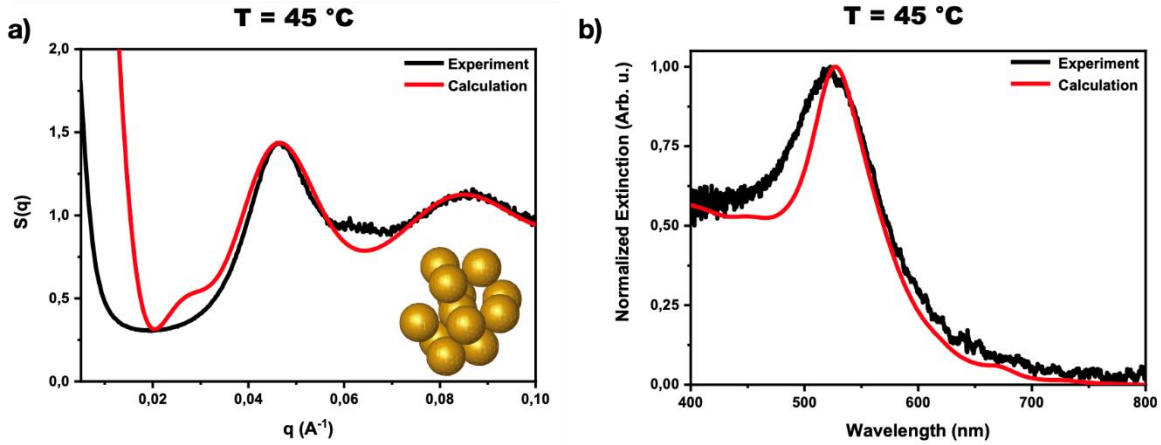

Figure 2.6. *a) Small angle X-ray scattering spectra of the PEGylated (750 Da) gold nanospheres (14 nm) measured at 45°C in the presence of 0.125 M K_2SO_4. The inset shows the derived characteristic nanoparticle cluster structure and size (12 particle, 2 nm separation of average with a Gaussian noise of 0.1). b) The optical extinction spectrum of the same system; the red curve corresponds to the optical simulation result based on the derived nanoparticle cluster structure.*

Non-destructive evaluation (NDE) system for the inspection of operation-induced material degradation in nuclear power plants

EU H2020 NOMAD 755330

G. Vértesy, A. Gasparics, I. Borsos

The long-term operation (LTO) of existing nuclear power plants (NPPs) has already been accepted in many countries as a strategic objective to ensure adequate supply of electricity over the coming decades. In order to estimate the remaining useful lifetime of NPP components, LTO requires reliable tools. The objective of NOMAD project is the development, demonstration and validation of a non-destructive evaluation (NDE) tool for the local and volumetric characterisation of the embrittlement in operational reactor pressure vessels (RPVs). In order to address these objectives, the following steps should be taken: Development and demonstration of an NDE tool for the characterisation of RPV embrittlement; Extension of the existing database of RPV material degradation by adding correlations of mechanical, microstructural and NDE parameters; and application of the developed tool to Charpy geometry samples and also to cladded material block type specimens resembling the actual RPV inspection scenario.

The MFA contributes to the NOMAD project with own micromagnetic testing method: so called Magnetic Adaptive Testing (MAT). MAT is a recently developed method for nondestructive characterization of ferromagnetic materials which is based on systematic measurement and evaluation of minor magnetic hysteresis loops. This method is being tested and evaluated regarding its applicability for the determination of the material changes and the variation of the material properties during exposure to neutron irradiation. As shown in our several previous research activities, MAT provides more sensitivity for material degradation than the major hysteresis loop and has an improved feature of measurement error suppression. An additional significant advantage of this method is that there is no need for magnetic saturation of the measured samples, which eases the practical application.

MAT measurements were performed on reactor steel material before and after neutron irradiation and the nondestructively determined magnetic parameters were compared with the destructively measured ductile-to-brittle transition temperature (DBTT) values and with other available mechanical test results, such as the Upper Shelf Energy, Vicker Hardness and Yield strength were provided by Belgian Nuclear Research Centre (SCK•CEN). Within the framework of the project five different electro-magnetic, electric and acoustic non-destructive measurement techniques were applied on the common specimen set and their results are processed and evaluated individually. A common data-base has been established on the outcomes of the individual non-destructive, as well as, on the destructive test results in order to evaluate the performances of the different NDE methods, but also to be able to recognize their possible synergies. The different ouput parameters of each competing methods have been ranked by the Wilcoxon signed rank test, and the MAT was classified as 'excellent candidates' accordingly.

The possible synergies, that can be utilized, are studied by different statistical methods, but also by different types of machine learning approaches. Our group was devoted to the study of the applicability of the 'Support Vector' (SV) method, as well as of the 'Neural Networks' (NN). Although the fact, that the total number of the available physical experimental cases are rather limited, and also taking into account, that the determination of the transition temperature in destructive way can not be carried out individualy on each test specimens, but on their groups, the machine learning methods could provide quite promising results that forecasts the success of the project. The results of our evaluation were published in joint papers with the consortium members.

The surface conditions can affect the magnetic coupling between the sample surface and the probes of magnetic type NDE methods, and this phenomenon, as a side effect can degrade the performance. Therefore, a joint study on the effect of the surface roughness was performed by comparing the MAT and the Barkhausen Noise (BN) results. Charpy speciemen set of 22NiMoCr37 nuclear reactor pressure vessel steel material with different surface roughness paramteres (like R_a) were developed by SCK•CEN and measured by the group of the Coventry University and by our one. In case of the MAT, the sample set was measured with two different "speeds" settings i.e. with two different slopes of the reverse magnetization. The obtained results were compared with the outcomes of the BN method. A direct quantitative, monotonic correlation between the magnetic behaviour and the surface roughness was obtained by applying two different types of magnetic measurements. The two measurements gave similar results (Fig. 2.7.). It was an important observation that by increasing the speed of change of the magnetizing current, the dependence of MAT descriptors on the surface roughness parameter can be reduced or in opposite direction: this creates the possibility to derive the surface roughness from magnetic parameters. This result is new, compared with previous measurements [Ref 2.3].

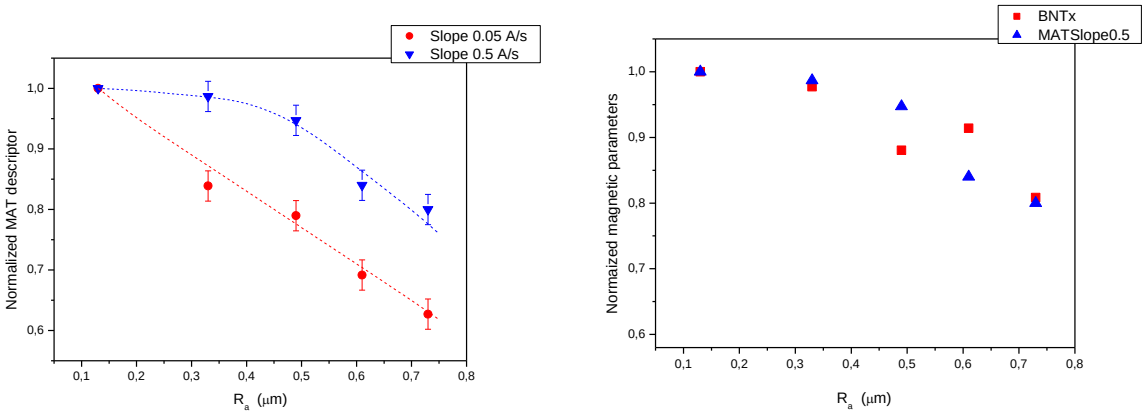

Figure 2.7. *Left: the normalized MAT descriptor for characterizing the correlation with R_a surface roughness parameter with two different slopes of magnetizing current; Right: Comparison of transversal BN signal and MAT descriptor with 0.5 A/s slew rate of magnetizing current as functions of surface roughness R_a. (slew)*

As soon as the Belgian partner could make available the desctructive test results: i.e. the determined transition temperature (DBTT) values, it was possible to compare them with our experimental results obtained in the hot cell measurement campaign. Charpy specimens made of four different types of materials are studied: 18MND5-W, 22NiMoCr37, A508-B and HSST-03. In spite of the large scatter of points a good correlation was obtained between these characteristics and the MAT method was found a promising candidate of the project (Fig. 2.8.). This conclusion was approved also by the Wilcoxon signed rank test, later on. The machine learning studies could highlight also, that significant source of the observed scattering can be related to 'noise' of the DBTT determination: since the NDE methods can observe the differences between each specimens, while the formal Charpy Impact Test could providejust an averaged data for their groups.

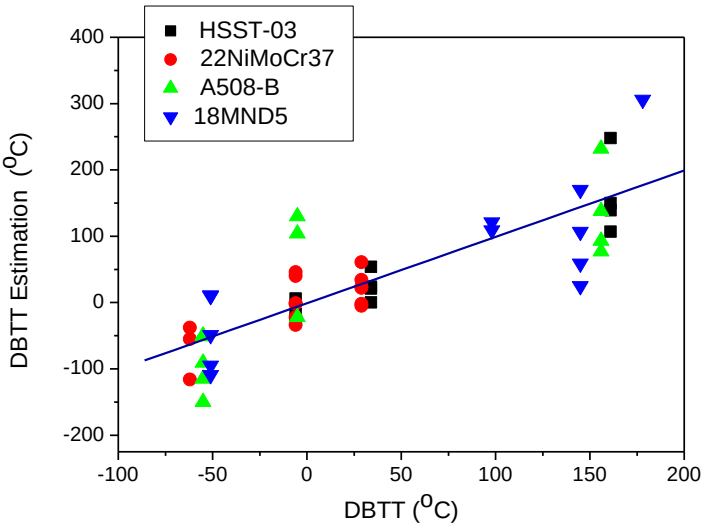

Figure 2.8. *Estimated DBTT values as functions of measured DBTT values for all investigated materials.*

Neural Network based analysis was performed on the established common data base. The database comprizes of all output values of the five different NDE methods that were measured in the hotcell campaings, as well as, before the irradiation of the specimens. The determination of the DBTT was targeted, and the achieved resolution of the combined methods was studied. The results are quite encouraging (Fig. 2.9.). The real and successful application demands to be able to distingish unambiougusly 50° of DBTT shift [Ref 2.4]. Actually, the recent destructive methods could reach this resolution only by performing numerous Charpy Impact Tests and averaging the results. However the scatterig of the NN test results are approximately +/-20°. There are some outlying points, which one relate to the problem of the extraordinary low number of train set elements.

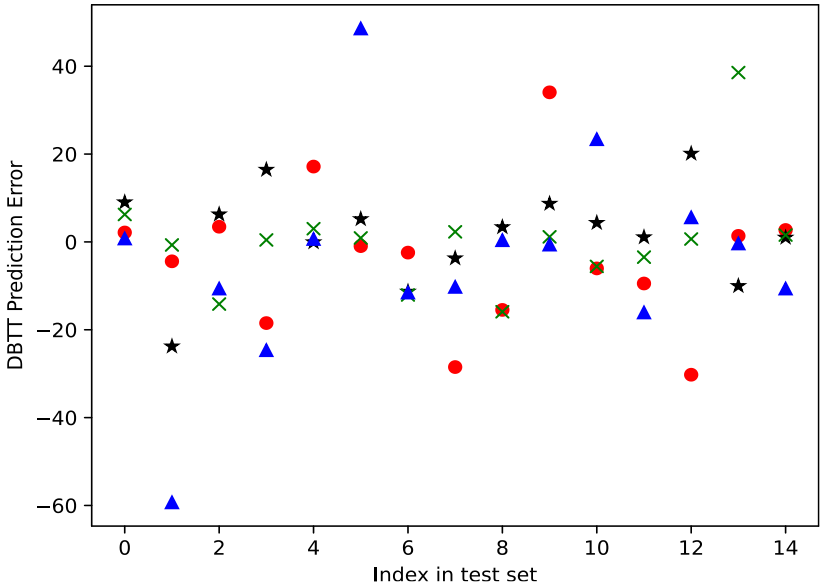

Figure 2.9. *DBTT prediction error of the Neural Networks: tested by four sets (marked with different symbols) of randomly selected 15 elements data sets.*

Complete state space for Capillary Bridge Probe method and its use in evaluation of measurements

OTKA FK 128901

N. Nagy

The developed indirect Capillary Bridge Probe method combines the accuracy of the Wilhelmy method and the general usability of the sessile drop method without their limitations. The method is based on the use of a liquid bridge as a probe: the capillary bridge of the test liquid is stretched between the rim of the base of a cylinder and the investigated surface under equilibrium conditions. The advancing contact angle on the sample can be measured during the stepwise decrease of the bridge length. The receding contact angle is determined during the retraction of the cylinder. The contact angle is calculated from Delaunay's analytical solution, while the necessary parameters are obtained from the measured capillary force and from the automated analysis of the captured image of the liquid bridge. The bridge is formed from a pendant drop. This unique feature ensures that the advancing contact line finds dry (not prewetted) surface.

Look-up tables were calculated for the relevant parameter space, where the possible neck/haunch- (r_0) and surface radius (r_c), and capillary force (F_c), values were used as input parameters with the resolution of 5 μm and 0.1 μN, respectively. The resulted Plateau-class, bridge length, volume, and contact angle on the lower surface (ϑ) were tabulated. The possible equilibrium states of water capillary bridges are shown in Fig. 2.10.

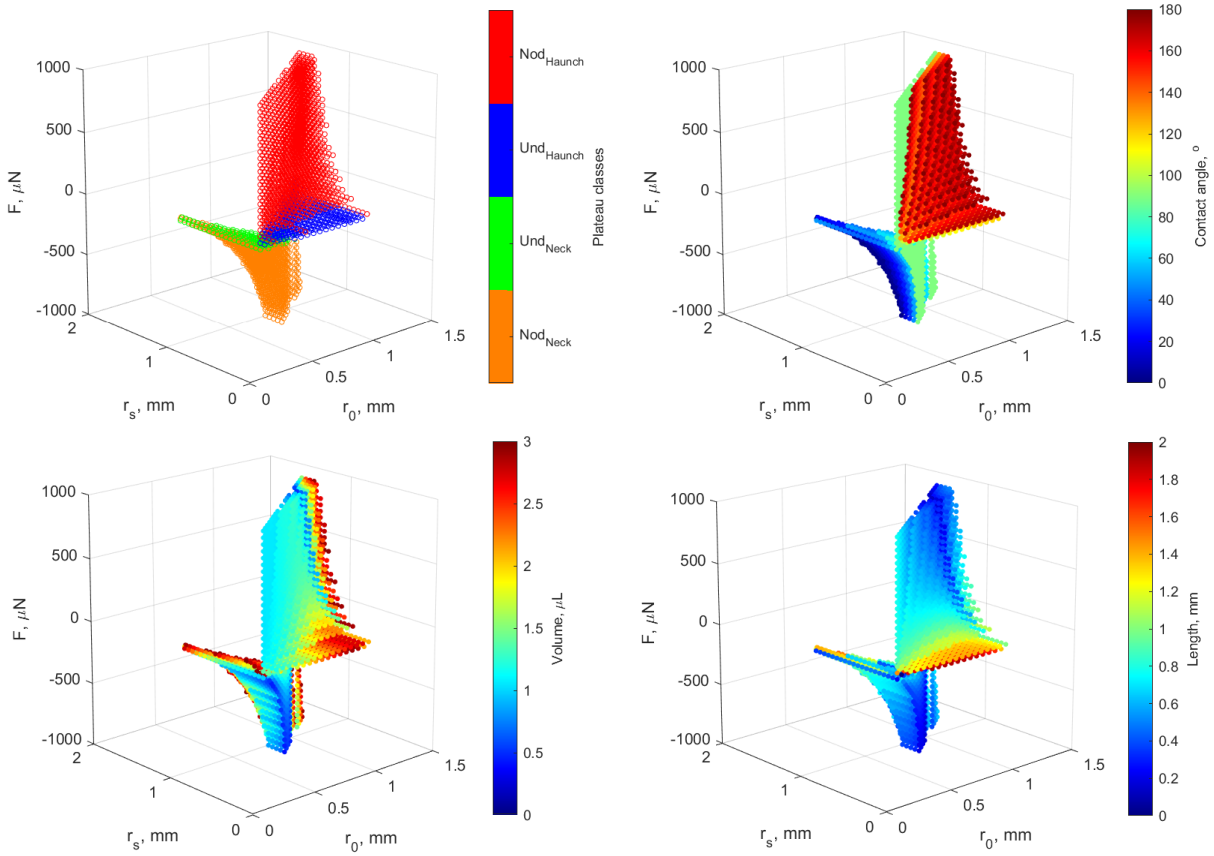

Figure 2.10. *Visualization of equlibrium state space of water capillary briges.*

This novel kind of visualization allows us to investigate the relations of different parameters, as well as the density of states. Obviously, there are two major planes. The $r_0 = r_s$ plane contains the cylindrical states (not shown) and separates strictly the bridges with neck ($\vartheta < 90°$) and the bridges with haunch ($\vartheta > 90°$). The other major plane is the $F_c = 0$. Its surroundings represent long bridges and contains mainly unduloid states. The regimes of positive and negative capillary forces are not symmetrical to this plane: there are states which represent bridges with haunch ($\vartheta > 90°$) but with negative F_c values.

One of the advantages of the precalculated look-up tables appears in the evaluation process. The applied equations are valid only in axisymmetric case. Therefore, a second camera would be needed to verify the symmetry of the bridge perpendicularly to the axis of the goniometer. This verification can be done by applying the look-up tables: significant difference between the measured and the tabulated value of capillary force and bridge length refers to asymmetric or non-equilibrium state. Therefore, measured points with higher deviation than 4% are neglected during the evaluation. (The great majority of the measured points show deviation less than 2% from the equilibrium values.)

The use of these three-dimensional matrices has further advantages. The modelling of equilibrium states of liquid bridges and the investigation of the sensitivity of the given parameters are quick and relatively convenient. Here the difficulty of the inverse calculations can be avoided.

Images and image series imitating the results of real measurement cycles can be generated having these tables. As an example, Fig. 2.11 shows a generated image with the actual CMOS resolution (left), supposing reflective substrate. Magnified image parts from a measured image (middle) and a generated image with added blur and noise (right) are also shown in Fig. 2.11.

Several hundred images were generated and evaluated to investigate and improve the image analysis during the evaluation. In the improved version, the difference in coordinates of contact points is zero in the most cases and never exceeds 2 pixels. Furthermore, the uncertainty of the contact angle determination originating from the camera resolution can be also determined for different contact angles. This value (the mean of absolute difference between the determined and the real contact angle values) is 0.2° in the 0.5°–85° contact angle range. As well as the behavior of different edge find algorithms can be investigated under different conditions (*i.e.* with different contrast, blur, and noise levels). In those cases, when not small details are interesting, the Sobel algorithm was proved to be the most precise and robust. [Ref. 2.5]

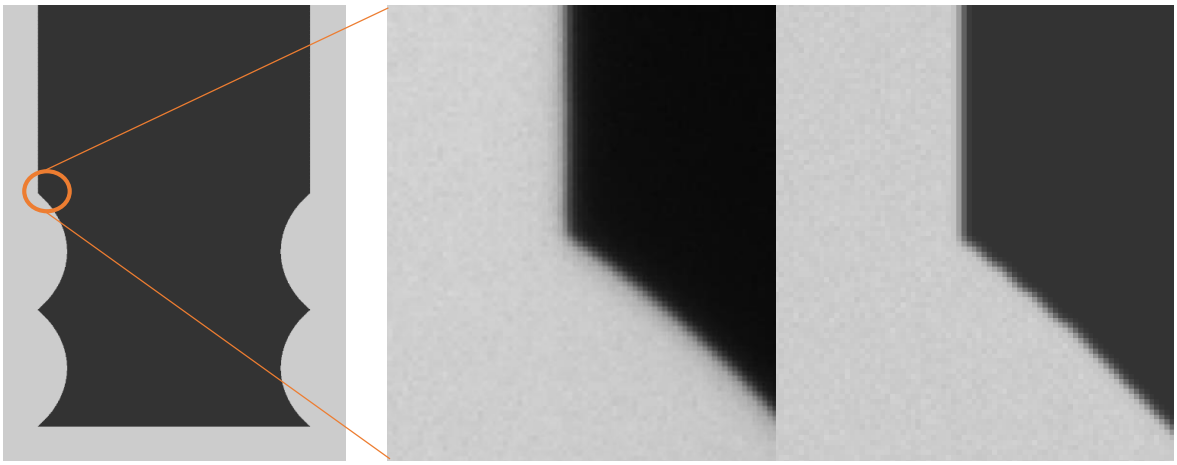

Figure 2.11. *Generated image of a water capillary bridge with the actual camera resolution (left). Magnified part of a measured image (middle) and a generated image (right) with blur and noise.*

Sensing layer for Ni detection in water created by immobilization of bio-engineered flagellar nanotubes on gold surfaces

OTKA NN117847, NN117849, K131515

Z. Labadi, B. Kalas, A. Saftics, L. Illes, H. Jankovics, É. Bereczk-Tompa, A. Sebestyén, É. Tóth, B. Kakasi, C. Moldovan, B. Firtat, M. Gartner, M. Gheorghe, F. Vonderviszt, M. Fried, P. Petrik

The environmental monitoring of Ni is targeted at a threshold limit value of 0.34 μM, as set by the World Health Organization. This sensitivity target can usually only be met by time-consuming and expensive laboratory measurements. There is a need for inexpensive, field-applicable methods, even if they are only used for signaling the necessity of a more accurate laboratory investigation. In this work, bioengineered, protein-based sensing layers were developed for Ni detection in water. Two bacterial Ni-binding flagellin variants were fabricated using genetic engineering, and their applicability as Ni-sensitive biochip coatings was tested. Nanotubes of mutant flagellins were built by in vitro polymerization.

A large surface density of the nanotubes on the sensor surface was achieved by covalent immobilization chemistry based on a dithiobis(succimidyl propionate) cross-linking method. The formation and density of the sensing layer was monitored and verified by spectroscopic ellipsometry and atomic force microscopy. Cyclic voltammetry (CV) measurements revealed a Ni sensitivity below 1 μM. It was also shown that, even after two months of storage, the used sensors can be regenerated and reused by rinsing in a 10 mM solution of ethylenediaminetetraacetic acid at room temperature. [Ref. 2.6]

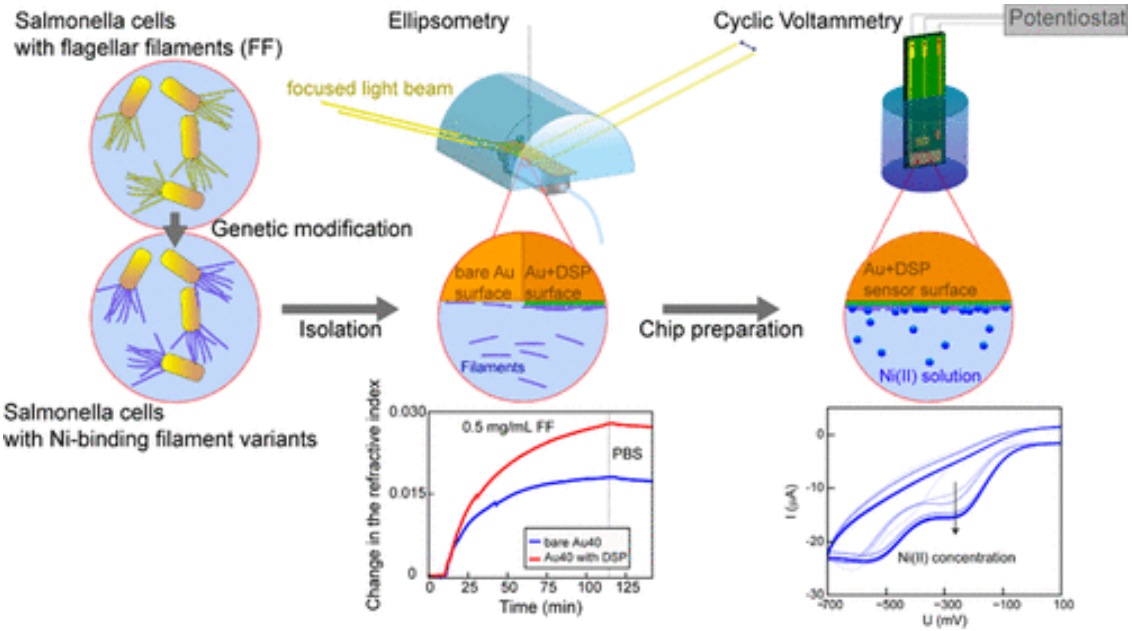

Figure 2.12*. Bioengineered bacterial flagellar filaments (left) were covalently immobilized onto gold surface (middle) and the Ni sensitivity was measured by cyclic voltammetry (right)*

Bragg structure design for investigating protein adsorption by real-time Kretschmann-Raether ellipsometry

OTKA K120785

B. Kalas, K. Ferencz, A. Saftics, Z. Czigany, M. Fried, P. Petrik

Optical biosensors are of fundamental role in their field of label-free characterization of various processes related to biomolecules due to the outstanding sensitivity and non-destructive characteristic [Ref. 2.7, Ref. 2.8]. Among the numerous optical sensing approaches surface plasmon resonance (SPR) spectroscopy [Ref. 2.9, Ref. 2.10] is one of the most widely used technique for capturing the typically minute changes in the signal, related to e.g., protein adsorption or conformation changes of biomolecules.

It is also possible to realize a biosensor surface without a thin Au layer and the absence of any SPR related material (usually metal) in a sensing structure has already been proposed [Ref. 2.11, Ref. 2.12]. As an example, a new configuration has been introduced recently for biosensing applications, the so-called Bragg-mirror structure (BMS) [Ref. 2.13, Ref. 2.14]. Similar to SPR, electromagnetic waves (the so-called Bloch surface waves) are confined to the surface of the layer structure which show an exponential decay of the field inside the liquid ambient.

In this work we utilize a Bragg mirror structure with an SiO_2 top layer to create a resonance in the ultraviolet wavelength range, near the absorption peak position of various proteins. We demonstrate that the wavelength of enhanced sensitivity can be adjusted by proper design of the multilayer structure. The possibility to design the wavelength of enhanced sensitivity supports measurements of better selectivity, optimized for the absorption of the target material. Since the width of the resonant peak in the reflectance spectra can be sharper than those of plasmonics, and they can be positioned at more favorable regions of the instrument and material (e.g., in terms of intensity or selectivity), the sensitivity can exceed those of plasmon-enhanced measurements. In this study we demonstrate the main features of the concept at the example of in situ spectroscopic ellipsometry of fibrinogen adsorption in the Kretschmann-Raether configuration. We realized a resonant peak with a full width at half maximum of 3 nm near the wavelength of 280 nm, which coincides with the absorption maximum of fibrinogen.

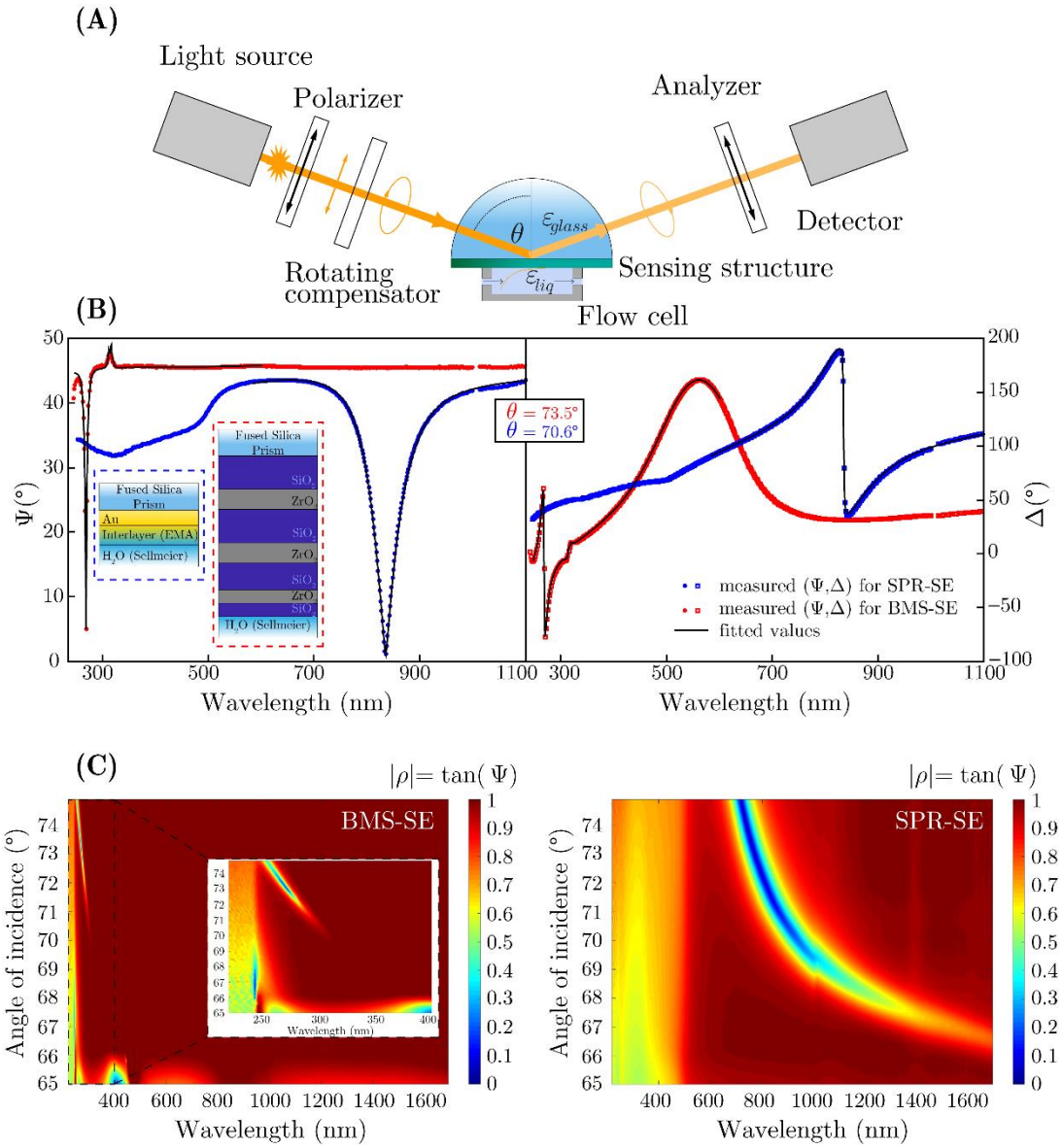

***Figure 2.13**. The schematic arrangement for an ellipsometric measurement in the Kretschmann-Raether configuration utilizing BMS-SE and SPR-SE (A). (B) Typical measured Ψ and Δ spectra for both BMS-SE (red symbols) and SPR-SE (blue symbols). The solid lines show fitted values by using the optical models presented in the insets (left hand-side). (C) tan(Ψ), i.e., $|r_p/rs|$, measured on the BMS (left hand-side) and Au (right hand-side) layer in the whole wavelength range in the Kretschmann-Raether configuration. The inset in BMS-SE shows the spectra closer to the BMS resonance wavelength.*

Preparation and Characterization of Mixed Metal Oxide Layers using Reactive Combinatorial Sputtering

VOC-DETECT M-ERA-Net, OTKA NN131269, OTKA K129009

Z. Labadi, C. Moldovan, B. Firtat, M. Gartner, M. Gheorghe, P. Petrik, M. Fried

Combinatorial DC sputtering method of metal oxides is presented onto a 30x30cm substrate. Specifically, tungsten and molybdenum oxides were deposited and characterized for electrochromic and sensoric purposes. Mapping ellipsometry combined with RBS proves the presence of the continuous composition range in the layers. Samples of amorphous character were tested for electrochromic properties in organic electrolyte. Combinatorial deposition of non-stoichiometric suboxides for VOC gas sensing also presented.

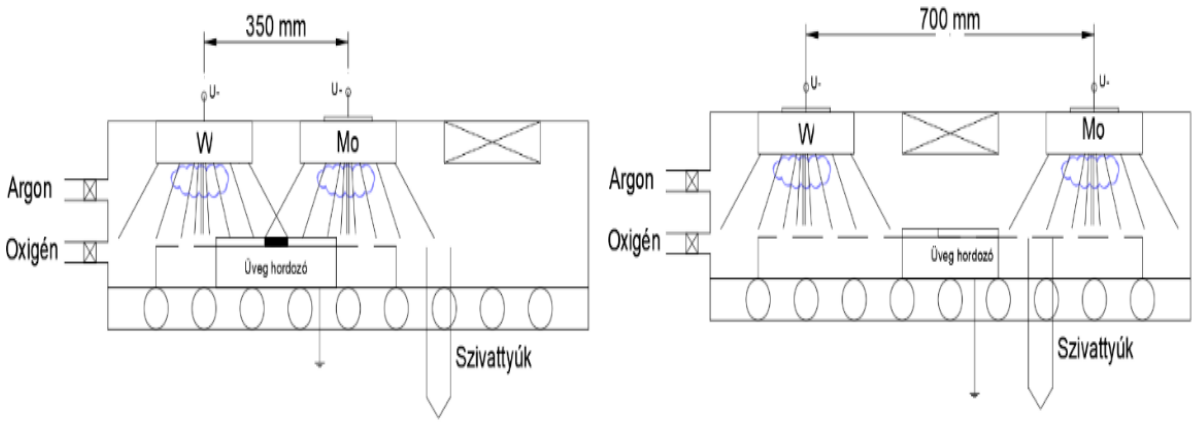

Figure 2.14. *Idea of ‚combinatorial' sputtering:Proper cyclic movement of substrate allows mixed (left) or superlattice-type (right) layers with lateral composition gradient*

Fig. 2.15. shows the ellipsometric mapping of the combinatorial layer (a) together with the schematic optical model (b), while Figure 2c shows the composition of the layer alongside the substrate movement axis. It can be seen from these figures that the layer contains the full compositional range of the MoO_3-WoO_3 binary oxide system.

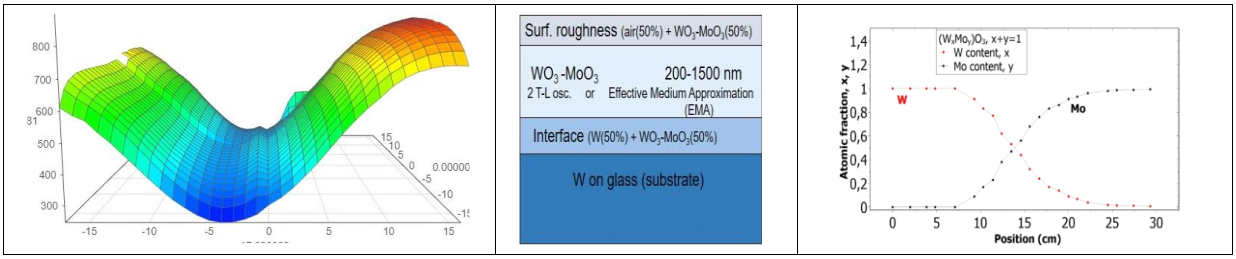

Figure 2.15. *Ellipsometry mapping and optical model of the combinatorial layer (a,b) and lateral composition curves taken by RBS (c)*

Fig. 2.16. shows the coloured and bleached state of the (Mo,W) oxide layer in 0,1M LiClO4 – propylene carbonate solution. The colorization efficiency can be measured in the full visible wavelength range, and the combinatorial approach allows 2% composition resolution.

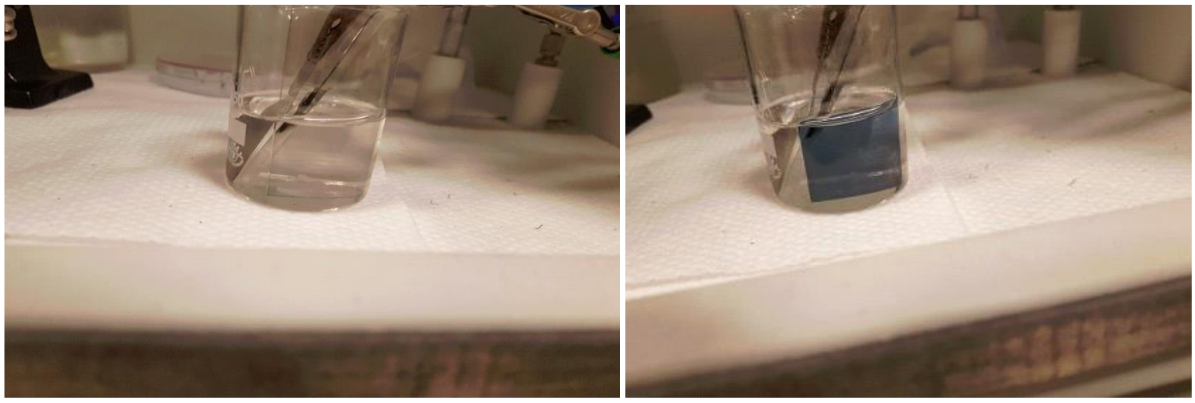

Figure 2.16. *Coloured and bleached state of the (W,Mo) oxide film*

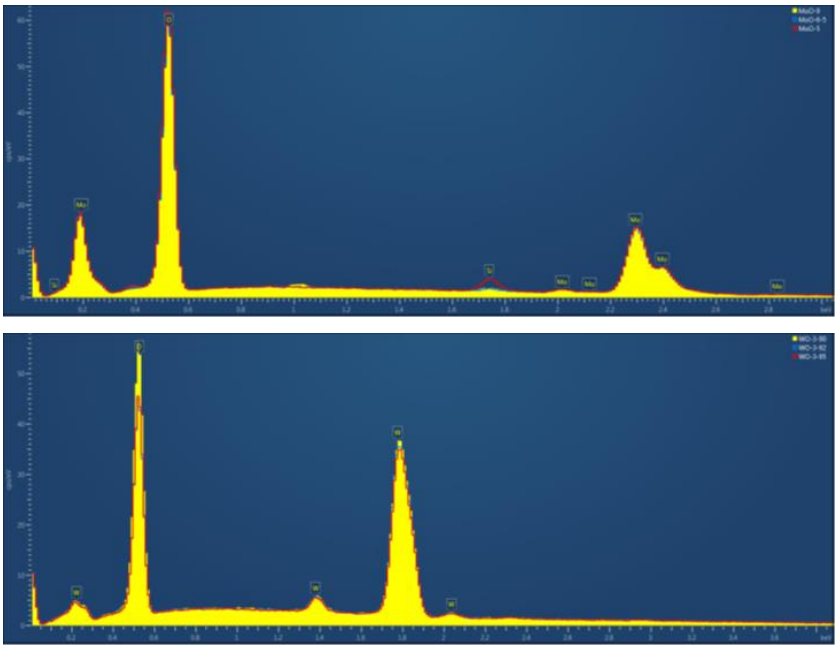

Figure 2.17. *EDS spectra of stoichiometric oxides and suboxides of W and Mo Semi-quantitative analysis shows 10% oxygen vacancy*

Combinatorial samples were also deposited under oxygen depleted conditions. Fig. 2.17. shows the electron dispersive spectrum of the suboxides. The non-stoichiometric samples are tested for VOC gas sensing properties (benzene and formaldehyde sensing). [Ref. 2.15]

In-situ control of defect dynamics by ellipsometry during ion implantation – evolution of disorder and cavity structure in single-crystalline Ge during implantation of Sb ions

OTKA K131515 and K129009

T. Lohner, A. Németh, Z. Zolnai, B. Kalas, A. Romanenko, N. Q. Khánh, E. Szilágyi, E. Kótai, E. Agócs, Z. Tóth, J. Budai, P. Petrik, M. Fried, I. Bársony, and J. Gyulai

Ion implantation has been a key technology in microelectronics and generally, for the controlled surface modification of materials for tribology, biocompatibility, corrosion resistance and many more. In this work in-situ spectroscopic ellipsometry was used for accurately tracking and on-line evaluating the accumulation of voids and damage in crystalline Ge during implantation of 200-keV Sb+ ions at a total fluence of 10^{16} cm^{-2} using an ion flux of 2.1×10^{12} $cm^{-2}s^{-1}$. The phases of damage accumulation were identified using unique optical multi-layer models describing the layer structure and composition. The formation of initial partial disorder was followed by complete amorphization and void formation occurring at the fluence of 1×10^{15} cm^{-2}, reaching a high volume fraction of voids and a layer thickness of ≈200 nm by the end of the process. This agrees with numerical simulations and results of complementary measurements including ion beam analysis and electron microscopy. The developed in-situ method for controlling the dynamics of structural damage accumulation is a versatile ion-implantation tool for avoiding adverse void formation and for controlled evolution of subsurface nanocavities or cellular surface texture alike.

The above work has been summarized in a manuscript (Lohner Tivadar, Németh Attila, Zolnai Zsolt, Kalas Benjamin, Romanenko Alekszej, Khanh Nguyen, Szilágyi Edit, Kótai Endre, Agócs Emil, Tóth Zsolt, Budai Judit, Petrik Péter, Fried Miklós, Bársony István, Gyulai József: In-Situ Control of Defect Dynamics By Ellipsometry During Ion Implantation – Evolution of Disorder and Cavity Structure in Single-Crystalline Ge During Implantation of Sb Ions). The manuscript was accepted by the journal SCIENTIFIC REPORTS. It will be published in 2021.

The work was presented as a poster also (Tivadar Lohner, Edit Szilágyi, Zsolt Zolnai, Attila Németh, Péter Petrik, Zsolt Fogarassy, Levente Illés, Endre Kótai, Miklós Fried: Determination of complex dielectric function of ion-bombarded amorphous germanium by spectroscopic ellipsometry) in the 18th International Conference on Thin Films and 18th Joint Vacuum Conference (https://akcongress.com/ictf-jvc/), (ICTF-JVC-2020, Budapest, 2020.11.22-26.) .

Makyoh topography and related methods

F. Riesz

Makyoh topography is an optical tool for the qualitative flatness testing of specular surfaces, based on the defocused detection of a collimated light beam reflected from the tested surface (Fig. 2.18). By inserting a square grid into the path of the illuminated beam, the height map can be calculated by integrating the gradients obtained from the distortion of the grid's reflected image (quantitative extension).

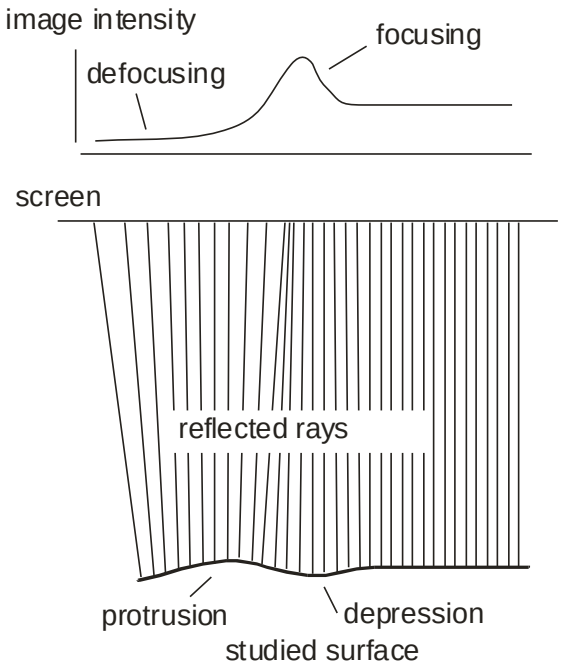

***Figure 2.18**. The scheme of Makyoh-topography*

In the past year, activities were concentrated both on methodology and applications.

It was shown earlier that utilising the existing Makyoh setup under certain geometrical conditions, a schlieren-like measurement can be realised where the imaging lens' aperture plays the role of the schlieren knife edge. This leads to a useful tool complementing the traditional Makyoh scheme. This year, the traditional knife-edge set-up was alo implemented and compared to the aperture based one. The effect of finite source size and mirror (spherical) aberrations were observed.

The swirl defects in *p*-type Si wafers were studied further using Makyoh topogrphy and the schlieren-like method describe above. High amount of data was collected whose analysis and interpretation is in progress.

Thin Film Physics Department

Head: Dr. Katalin BALÁZSI, Ph.D., senior scientist

Research Staff

- Ildikó CORA, Ph.D. (maternity leave from August)
- Zsolt CZIGÁNY, D.Sc.
- Zsolt FOGARASSY, Ph.D.
- Mónika FURKÓ, Ph.D.
- Viktória KOVÁCSNÉ-KIS, Ph.D.
- János LÁBÁR, D.Sc, (retired from July)
- Béla PÉCZ, D.Sc., deputy general director of Centre for Energy Research, director of MFA
- Adél RÁCZ , Ph.D.
- György Zoltán RADNÓCZI, Ph.D.
- György SÁFRÁN, C.Sc.
- Attila SULYOK, Ph.D.
- Orsolya TAPASZTÓ, Ph.D.
- Árpád BARNA, D.Sc., Prof. emeritus
- Péter B. BARNA, D.Sc., Prof. emeritus
- Miklós MENYHÁRD, D.Sc., Prof. emeritus
- György RADNÓCZI, D.Sc., Prof. emeritus

Ph.D. students

- Erzsébet DÓDONY
- Klára HAJAGOS-NAGY (maternity leave until November)
- Nikolett HEGEDŰS
- Tamás KOLONITS
- Soukaina LAMNINI (Stipendium Hungaricum scholarship)
- Mohamed AFROIU (Stipendium Hungaricum scholarship)
- Kaoua H. Maroua (Stipendium Hungaricum scholarship from September)

Technical Staff

- Andrea J. FENYVESINÉ
- Valéria OSVÁTH (maternity leave)
- Noémi SZÁSZ
- Sándor GURBÁN
- Andor KOVÁCS
- Viktor VARGA

The scientific results of the Thin Film Physics Department are related to thin film and ceramic fields. The main research topics are in line with modern trends of material science with the respect to a 50 years long history of the department. In 2020, the important base research field was the development of the 2D semiconductor and multicomponent thin films supported by several international basic scientific projects and collaborations.

The second research line, the development of different ceramics supported by the basic and applied projects, was continued. Gradient sandwich ceramics (Si_3N_4- Si_3N_4 / multilayered graphene) and different calcium phosphate based bioceramics were developed framework of the international cooperations. The last line and uniqueness of the Department (in national and international level) was the transmission electron microscopy. The effect of the structure on the developed material´s properties was demonstrated by this TEM study and they showed that the optimal structure can be directed in a controlled way. All topics was supported by methodical developments based on electron diffractions.

In 2020, 61 papers appeared in refereed journals with a cumulative impact factor of 273. In addition, 5 papers in conference proceedings were published with no impact factor. Members of the group presented 1 plenary and 2 invited lectures, 6 oral talks and 3 posters at national and international conferences and 1 patent. The group received 2280 independent citations in the examined interval of the last two years. The online International 18th International Conference on Thin Films &18th Joint Vacuum Conference (ICTF-JVC2020) – the event of the IUVSTA - was organized in Budapest between November 22 and 26 by members of Thin Film Physics Department.

Research members of the group lectured three courses at universities and four members held laboratory practices. All courses were for full semester (Eötvös Lóránd University - ELTE, and Budapest University of Technology and Economics - BME, and University of Pannonia- UP and Óbuda University - OE). In addition, 7 PhD students were supervised. 1 PhD student successfully defended her PhD degree.

Social activity of the group is landmarked by 15 memberships in different committees of the Hungarian Academy of Sciences and in boards of societies, giving one elected representative to the General Assembly of the Hungarian Academy of Sciences.

2D InN thin films between graphene and SiC grown by MOCVD via intercalation

VEKOP-2.3.3-15-2016-00002, OTKA NN118914, Flag-Era JTC 2015-005 'Grifone", MTA Italian –Hungarian bilateral Programme

B. Pécz (EK MFA), G. Nicotra (CNR), F. Giannazzo (CNR), R. Yakimova (IFM), A. A Koos (EK MFA), A. Kakanakova-Georgieva (IFM)

Wide band gap semiconductors with a direct band gap are capable of emitting light. This is something that many people learned when the Nobel Prize was awarded for LEDs in 2014. The researchers had already worked for about two decades on materials such as GaN, AlN and InN. The last of these materials (indium nitride) was slightly unusual, given its forbidden band gap of 0.7 eV, which is not very wide. However, the above three materials can easily be grown in a ternary form and InN played a crucial role in the preparation of light emitting diodes (LED) and lasers in the form of InxGa1-xN. The band gap and the wavelength of the emitted light can be tuned with indium content. The exploration of 2D materials together with valuable theoretical papers predicted that the nitrides will also possess novel properties. Researchers supposed that the band gap of the bilayer InN will widen and can be used as a light emitting layer in the visible range.

The work which resulted in a bilayer of indium nitride formed in the closed space of hydrogenated epitaxial graphene on SiC was carried out in a FLAG ERA project called GRIFONE, with cooperation between Sweden, Italy and Hungary. The coordinator of the project with overall conceptualization and course of research is Anelia Kakanakova (Linköping University, Sweden), while the partners are Filippo Giannazzo (CNR Catania, Italy) and Béla Pécz (EK MFA). The project aimed the development of a general platform that provides the possibility to develop 2D semiconductors by (Metalorganic Vapour Deposition). Successful examples are 2D AlN (published earlier in Nanoscale) and indium nitride. The successful outcome of the research on 2D InN was led by Béla Pécz [Ref. 3.1].

The buffer layer of epitaxial graphene on SiC turns to an additional graphene layer, with a weekly bond to the substrate, which means we can let metal atoms into the space of graphene-SiC by intercalation. This was used in the present experiments as well to provide indium atoms and nitrogen from ammonia by MOCVD (by AK, Linköping University, Sweden). The results clearly show that the formed layer was successfully stabilized.

The whole surface of the sample was investigated by conductive AFM (by F.G, CNR Catania, Italy), which showed that more than 90% of the sample surface is covered by InN (below the graphene). Occasionally thicker inclusion of InN (5-7 layer thick) was also traced still under the graphene. Fig. 3.1.a) in the next figure shows the bilayer InN in the aberration corrected THEMIS 200 microscope of MFA (HAADF image in STEM mode). The intensity is proportional with the square of the atomic number and one can see clearly the two rows of the indium atoms. Fig. 3.1b) shows the rear-observed 3D InN, which actually shows a cubic layer sequence. Fig. 3.1.c) shows an (annular bright field) image which provides the possibility to observe the light elements as well. Indeed, on the right side one can observe the nitrogen bond to indium as well as the carbon in SiC.

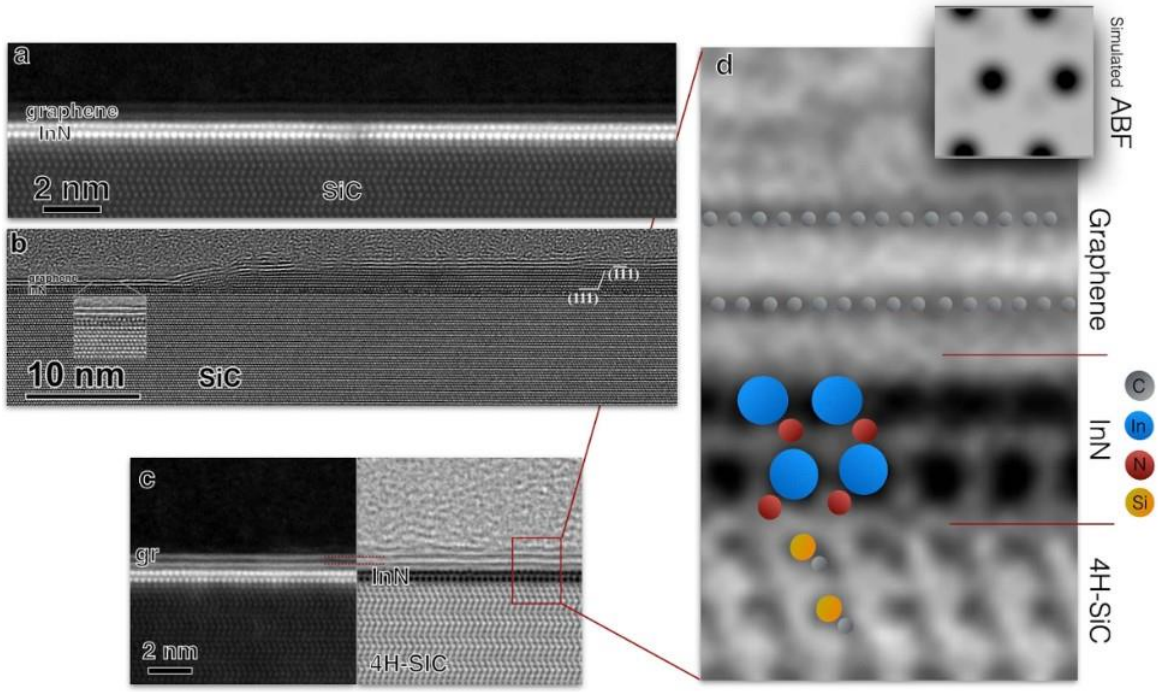

Figure 3.1. *Images taken for the bilayer of InN: a) STEM HAADF image of graphene/SiC template intercalated with trimethylindium and ammonia. Two sub-layers of intercalated In with high-intensity Z contrast underneath bilayer of graphene are clearly seen. b) HREM image of the same specimen taken in TEM mode at 200 keV. c) ABF/HAADF STEM overview image of the intercalated InN on SiC. d) Magnified from the same image with an insert of simulated image calculated by JEMS software.*

The final proof for the chemical composition of the bilayer was provided by EELS (Electron Energy Loss Spectroscopy) carried out by Giuseppe Nicotra CNR-IMM Beyond Nano laboratory. The results clearly showed the fine structure of Nitrogen K edge and that the layer is oxygen free.

The importance of the new findings was enhanced by the work of Antal Koós (EK MFA) when he took I-V characteristics place by place on the sample by STS (Scanning Tunnelling Spectroscopy). The results showed a band gap of 2±0.1 eV instead of the 0.7 eV for the bulk case. With this synthesis, the 2D InN took its place among the real wide band gap semiconductors.

Scratch resistance of SiC-rich composite nano-coatings produced by noble gas ion mixing

A.S. Rácz (EK MFA), D. Dworschak, M. Valtiner, M. Menyhárd (EK MFA)

Recently we have shown that it is possible to produce SiC nano-coating at room temperature by applying IBM (ion beam mixing) on C/Si multilayer structures; the layers exhibit excellent corrosion resistive properties. From the viewpoint of protective coatings besides the corrosion resistance the good mechanical behavior of the layer is important, as well. As the thickness of the produced SiC-rich coatings was only some tens of nanometers conventional hardness tests are generally not suitable for testing.

Alternatively a scratch test with AFM in which a tip is indented into the substrate and then moved at a fixed depth along the surface is applied for studying extreme thin layers. Therefore the scratching resistance of the ion mixed samples has been measured by standard scratch test applying an atomic-force microscope with a diamond- coated tip (radius < 15 nm) and they were compared to that measured on Si single crystal. The applied load varied in the range of 4-18 μN. The scratching resistance of the samples correlated with the effective areal density of the SiC; with increasing effective areal density the scratch depth decreases (Fig. 3.2). Above sufficiently high effective areal density of SiC the scratch resistance (hardness) of the produced layer was somewhat higher than that of single crystal silicon. Previously it has been shown that such layers have excellent corrosion resistive properties as well. These findings allow to tune and design the mechanical and chemical properties of the SiC protective coatings. [Ref. 3.2]

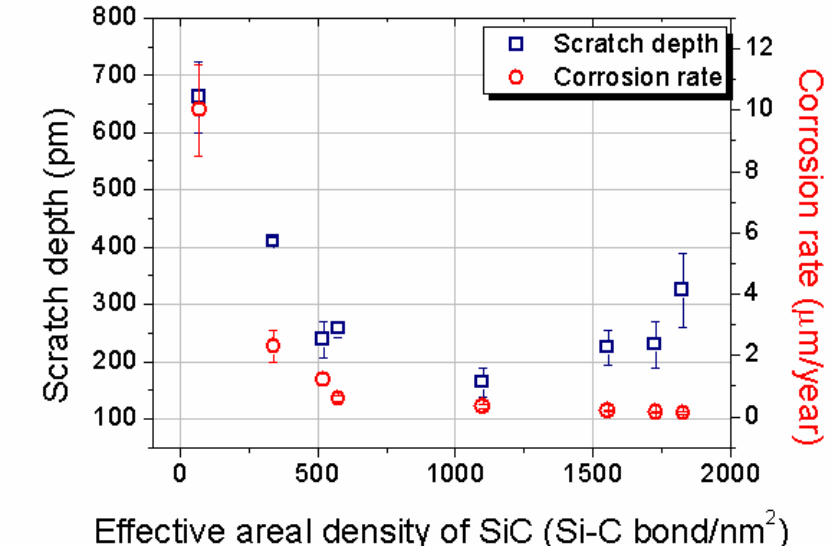

Figure 3.2. *Scratch depth and corrosion rate vs the effective areal density of SiC for all samples for normal load 15.8 μN.*

Spinodal decomposition in reactively sputtered $(V_{0.64}Al_{0.36})_{0.49}N_{0.51}$ and cathodic arc evaporated $Ti_{0.27}Al_{0.21}N_{0.52}$ formation of secondary phases

VEKOP-2.3.3-15-2016-00002

Zs. Czigány (EK MFA), M. Hans (Aachen), D.M. Holzapfel (Aachen), A.O. Eriksson (Balzers), M. Arndt(Balzers), H. Ruess(Aachen), J. Krause(Aachen), P. Ondračka (Aachen), D. Music (Aachen), S. Evertz (Aachen), D. Primetzhofer (Uppsala) and J. M. Schneider (Aachen)

The stability of VAlN and TiAlN hard coatings at high temperatures (900-1100°C) is inevitable in applications aiming at increasing the lifetime of tools. The cooperation between MFA and Aachen University started in 2019. The VAlN and TiAlN layers were deposited by reactive sputtering and cathodic arc evaporation, respectively, at Aachen University. The TEM/STEM investigations were made on the C_S corrected THEMIS 200 microscope of MFA.

Spinodal phase separation can be expected in both material systems on thermodynamic basis. In this process V (Ti) and Al rich fcc nitride phases form, which may even improve the mechanical properties. Such phase separation was revealed by EDS elemental maps on 8-20nm scale and by electron diffraction for TiAlN due to 3.7% lattice parameter difference between AlN and TiN. (The difference between the lattice parameters of VN and AlN phases is only 0.5%.) In VAlN the hexagonal AlN phase was observed above 900°C which forms at the grain boundaries according to HRTEM and dark field images (Fig. 3.3).

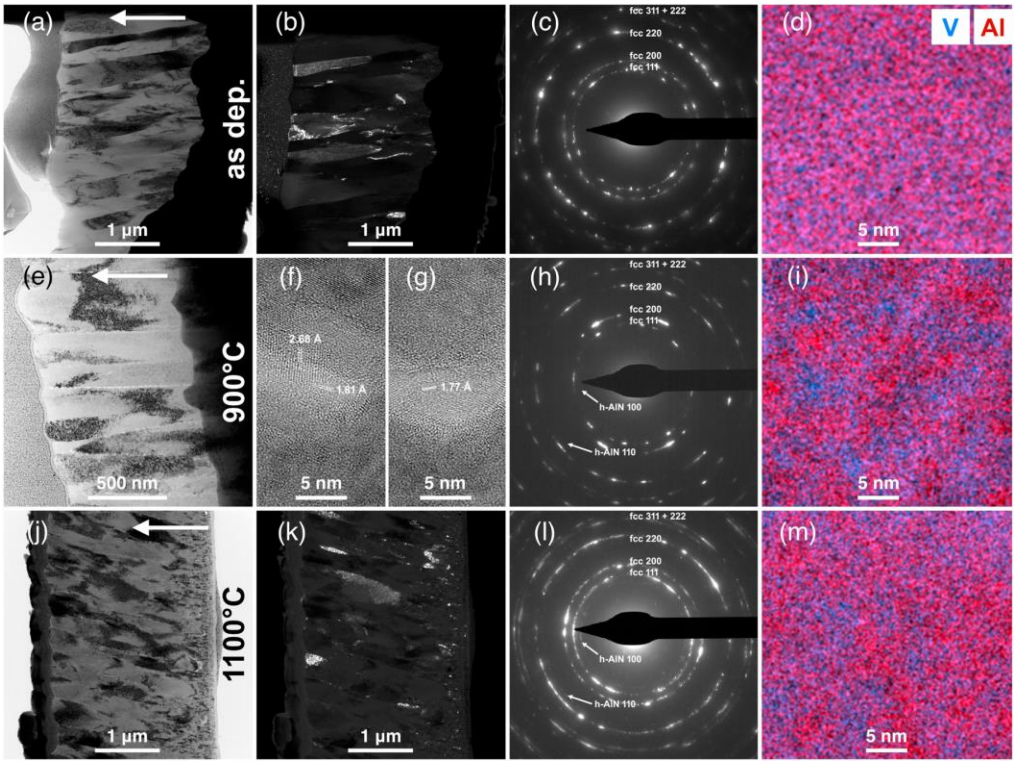

Figure 3.3*. TEM characterization of as deposited and annealed $(V_{0.64}Al_{0.36})_{0.49}N_{0.51}$ thin film flakes at different temperatures. The combined V and Al elemental maps show the spinodal decomposition above 900°C. SAEDs indicate the appearance of hexagonal AlN in the films above 900°C. HR images (f and g) and DF image at 1100°C (k) demonstrate the occurrence of nanocrystals of hexagonal AlN phase at grain boundaries. Columns from left to right: BF, DF, SAED and Elemental map images*

The presence of macroparticles in cathodic arc evaporated coatings is considered one of the greatest drawbacks of this synthesis method. We demonstrated with transmission electron microscopy (TEM) and atom probe tomography (APT) that the thermal stability of a macroparticle in the industrial benchmark coating (Ti,Al)N does not limit the overall coating thermal stability up to 1000 C because metal-rich macroparticles exhibit a higher thermal stability than the c-(Ti,Al)N matrix. It is shown that the superior stability of the macroparticle upon annealing is enabled by the self-organized formation of a c-TiN based diffusion barrier shell around the macroparticle (Fig. 3.4). One paper was published in 2020 about VAlN coatings [Ref. 3.3] and one manuscript was submitted about TiAlN [Ref. 3.4]

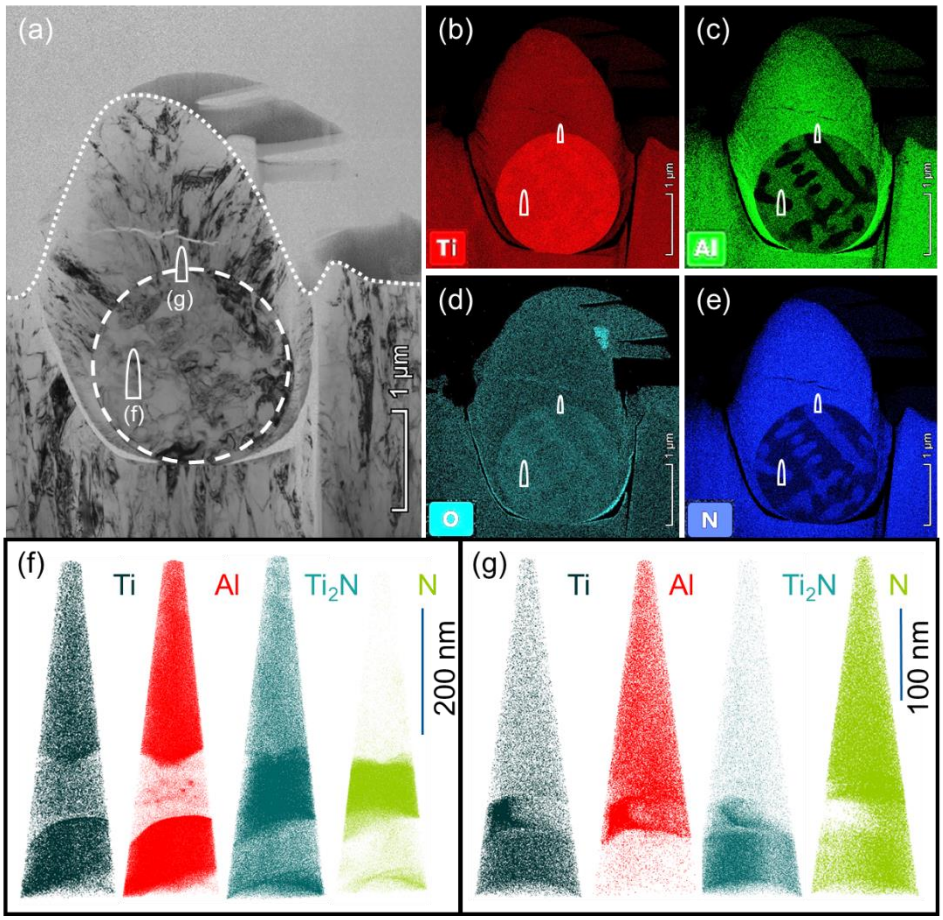

Figure 3.4. *(a) BF image of as deposited $(Ti_{0.56}Al_{0.44})_{0.48}N_{0.52}$ cross-sections; embedded spherical macroparticle and sample surface are marked with dashed and dotted lines, respectively, (b) (c), (d) and (e) display elemental maps for Ti, Al, O and N respectively, (f) and (g) APT characterization of tip taken from the centre of a macroparticle at the position indicated in (a) showing Ti, Al, Ti_2N and N ions.*

The effect of additive cysteine on the nanostructure, hardness and thermal stability of electrodeposited nickel

T. Kolonits (EK MFA, ELTE), L. Péter (Wigner), I. Bakonyi (Wigner), J. Gubicza (ELTE), Zs. Czigány (EK MFA)

In the present study the effect of cysteine on the nanostructure (grain size, dislocation density and twin fault probability), mechanical properties and thermal stability of electrodeposited nickel was investigated. The main methods were X-ray diffraction line profile analysis (XRD-LPA) and transmission electron microscopy (TEM). First, the effect of different concentrations of cysteine in the bath was investigated. Later, the thermal stability of the layers produced by a certain concentration of cysteine was measured.

The nickel layers were a few tens of micrometres thick and were deposited at room temperature by low current density onto copper substrate (which was removed later by electrochemical dissolution). The initial electrolyte contained mainly nickel-sulfate ($NiSO_4 \cdot 7\ H_2O$) and boric acid (H_3BO_3); this electrolyte was doped by cysteine in the concentration of range 0-0.4 g/L. Phase and microstructural analysis was performed by XRD and TEM. The mechanical properties were characterized by the indentation hardness. These micro- and macro properties were investigated after heat treatments at different temperatures (400, 500, 600, 750 and 1000 K).

Similar to some other additives like saccharin, even a small amount of cysteine (0.1 g/L) eliminated the columnar grain growth and resulted a polycrystalline layer with a grain size about 20 nm. Increasing the concentration of cysteine in the bath, the grain size, dislocation density, twin fault probability and hardness tend to a saturation value. Over a cysteine concentration of 0.4 g/L there were no notable changes of the micro- and macro- parameters observed. However, it is remarkable, that between concentrations of 0.2 and 0.3 g/L there was a jump in the dislocation density, the twin fault probability (Fig. 3.5.) and also the texture of the sample changed from type (111) out of plane fiber texture to a type (200) one.

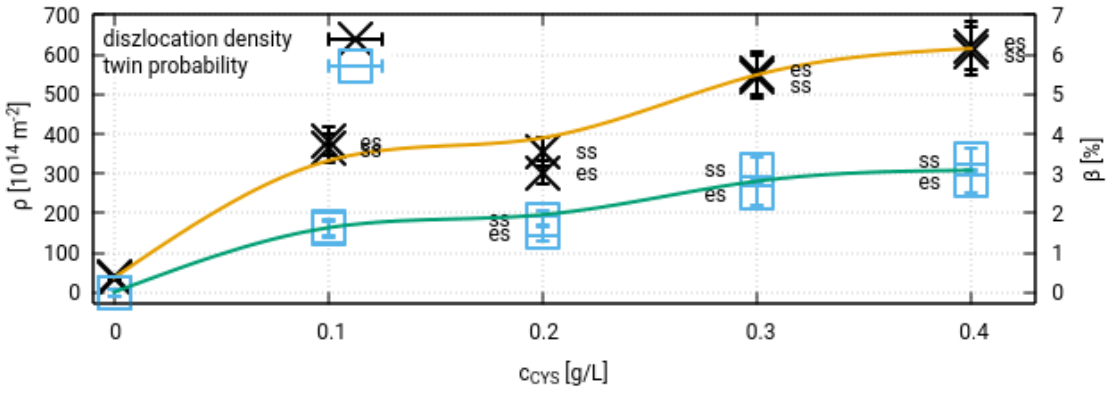

Figure 3.5. *Dislocation density and twin fault probability of samples deposited from bath with different concentration of cysteine*.

The highest hardness (~6800 MPa) was reached when 0.4 g/L cysteine was applied in the bath, which value is higher than was ever observed in the literature (<6000 MPa). Therefore, this sample was selected to thermal stability measurements between 400 and 1000 K.

Samples produced with cysteine had similar response to the heat treatment like those produced with saccharin. The microstructure was stable between 300 and 400 K. After a heat treatment at 500 K the hardness increased (~8400 MPa) due to the microstructural changes (like segregation of impurities and

grain boundary relaxation). Total re-crystallisation was observed at 1000 K. However, significant difference to saccharin is that the limit of thermal stability increased from 600 K to 750 K (Fig. 3.6). It is also remarkable, that the grain and crystallite size decreased to the half of the original value after a heat treatment at 500 K. [Ref. 3.5]

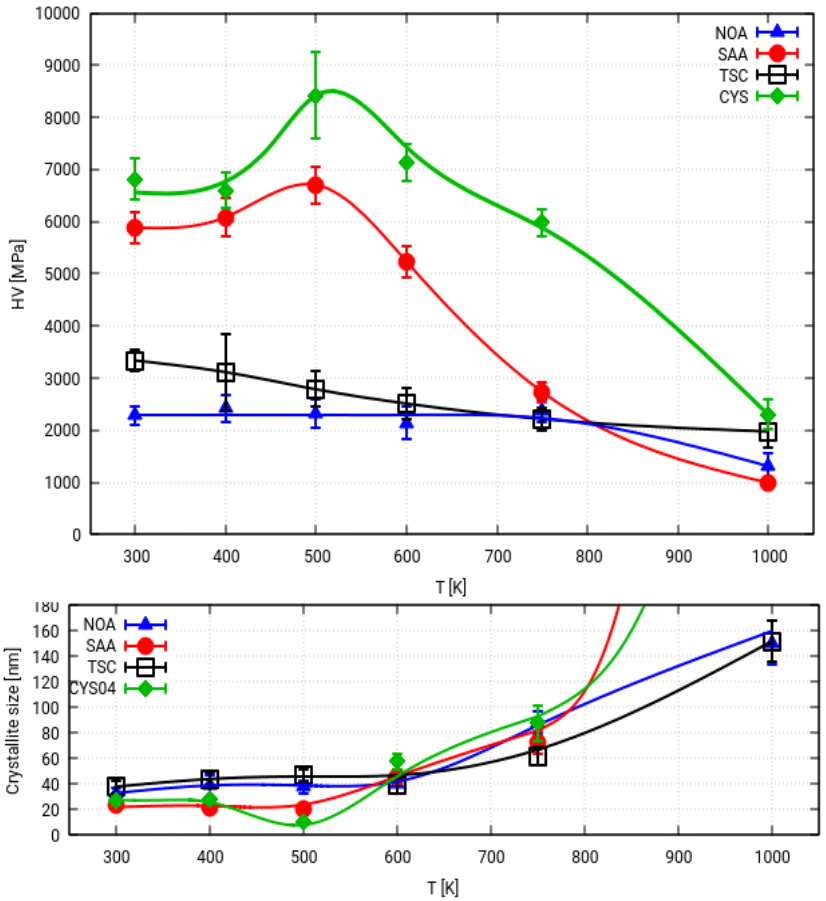

***Figure 3.6**. Hardness (top) and crystallite size (bottom) of nickel layers deposited with different additives versus different heat treatments.*

The effect of growth temperature and background pressure on the structure of CoCrCuFeNi alloy films

OTKA NN112156, VEKOP-2.3.3-15-2016- 00002

K. Hajagos-Nagy, F. Misják, Gy. Radnóczi

In this work, we give a brief review of the structure of CrCoCuFeNi alloy films as a function of growth parameters. These multicomponent films are often used as protective coatings, therefore their mechanical and anticorrosion properties are of main interest. The structure and morphology of the films fundamentally determines their mechanical properties, so mapping the effect of growth on them is of outmost importance.

The structure formation of thin films is studied through the structure zone model [Ref. 3.6, Ref. 3.7]. The model divides the growth morphologies of one component, one phase films into three categories based upon the relative growth temperature T_S/T_M, where T_S is the substrate temperature and T_M is the melting point. In zone I ($0< T_S/T_M <0.1$) the films have fibre-like structure without texture. In the T zone ($0.1< T_S/T_M<0.3$) as a result of competitive growth V-shaped crystals grow and texture develops. In zone II ($T_S/T_M>0.3$) the film is composed of columnar crystals with a restructuration growth texture. Zone III can only form in case of two-phase films. This zone is characterized by globular crystals without texture [Ref. 3.7]. The globular crystals form through repeated nucleation when the second phase grows around the crystals of the first phase and covers them. Then the first phase nucleates again on the surface of the second phase.

CoCrCuFeNi films were deposited by DC magnetron sputtering on thermally oxidized Si wafers. We varied the background pressure and films were grown at selected values of $5x10^{-8}$, $5x10^{-7}$ and $5x10^{-6}$ mbar and for these experiments the substrate temperature was kept constant at room temperature (300 K). In addition, another layer was grown at higher temperature (650 K) where the background pressure was $5x10^{-6}$ mbar.

Fig. 3.7.a-c shows the structure of CoCrCuFeNi films grown at room temperature and different background pressure. 300 K corresponds to $T_s/T_M\approx0,17$ and predicts the formation of a zone T structure. The layer which was grown at $5x10^{-6}$ mbar (shown in Fig. 3.7.a) has inhomogeneous structure along the film thickness. The part closer to the substrate has globular structure, while in the part closer to the film surface short fibre-like morphology is visible. There fibre-like grains are formed due to a mild competitive growth but texture has not formed yet. The growth corresponds to the boundary between zone III and T zone, where impurities cause repeated nucleation. The grain size is around 10-15 nm.

The film grown at $5x10^{-7}$ mbar has T zone structure, and has a strong <111> texture. The competitive growth takes place during the growth of the first 100 nm. After that only the <111> orientation crystals grow parallel to each other as these are the crystals with optimal orientation. They are densely packed with planar defects on {111} planes, normal to the direction of growth. Fig. 3.7.e shows that the distance of these planar defects can be as small as 0.1-1 nm.

By lowering the background pressure further to $5x10^{-8}$ mbar the structure and morphology of the film remains the same (shown in Fig. 3.7.c). Therefore, the change in growth morphology takes place between $5x10^{-7}$ and $5x10^{-6}$ mbar background pressure and there is no need to use a better vacuum than $5x10^{-7}$ mbar. The change in growth process is due to the change in the quantity of impurities. At $5x10^{-6}$ mbar background pressure the impurities (mainly oxygen) form a thin second phase layer on the growth surface of the growing crystals and it is able to cover them in a form of a 2D layer. Therefore, repeated nucleation happens and a globular structure and later during growth a fibre-like structure forms. If we calculate the ratio of O_2

molecules and metallic atoms that arrive to the growth surface at various background pressures, we find that for the $5x10^{-6}$ mbar value this ratio is around 1:2. This ratio is probably enough for the formation of a Metal-O type (e.g. CrO) 2D covering layer. If we lower the pressure by one order of magnitude, less impurities arrive to the growth surface and even if a second phase is able to form, its growth rate is slower, so it cannot interrupt the growth of the alloy crystals.

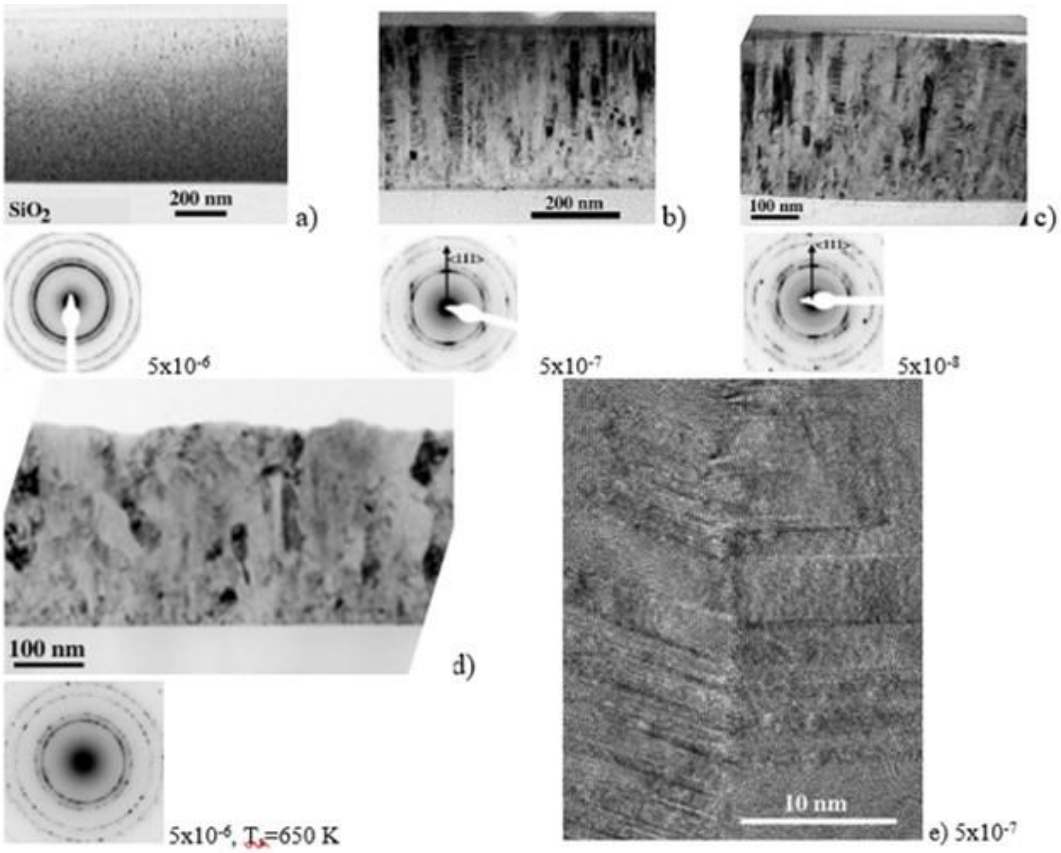

Figure 3.7. *Cross-sectional TEM images of CoCrCuFeNi alloy films grown at different background pressures at 300K (a-c) and at 650 K and $5x10^{-6}$ mbar (d). (e) is a magnified part of image (c).*

Fig. 3.7.d shows the effect of higher temperature on growth. 650 K corresponds to $Ts/T_M=0.38$ which projects the formation of a zone II layer. However, the film shown in Fig. 3.7.d has a globular structure with only columnar-like crystals. This structure implies the presence of a 2D or even a 3D second phase. The second phase was able to form due to the background pressure which was $5x10^{-6}$.

In conclusion, the structure of multicomponent but one phase CoCrCuFeNi alloy films greatly depends on the ratio of the metallic and impurity atoms arriving at the surface. We can influence this ratio by changing the background pressure and the deposition rate. Thus, by adjusting these sputtering parameters we can grow a film with desired - columnar of globular - structure.

This study was supported by the Hungarian National Research, Development and Innovation Office through the OTKA NN112156 project. The authors also acknowledge the VEKOP-2.3.3-15-2016-00002 project of the European Regional Investment Funds.

In-situ TEM investigation of high entropy CoCrCuFeNi alloy films

OTKA NN112156, VEKOP-2.3.3-15-2016-00002, János Bolyai Fellowship, ÚNKP-19–4, Stipendium Hungaricum

M. Arfaoui, V. Kis, Gy. Radnóczi

The high entropy alloys (HEA) are composed from at least five main components each contributing a 5-30 at % fraction to the alloy. They can be characterised by high mixing entropy, making also possible the formation of simple crystal structures (FCC or BCC e.g.). The stability of HEA structures is an important parameter of their technological application. The HEA films and bulk materials are excellent structural materials, their investigation started around 2005 and is intensively continued since then. In this work we investigate the structural transformations in HEA thin films during annealing.

40-50 nm thick single phase FCC CoCrCuFeNi HEA thin film samples were produced by DC magnetron sputtering and annealed in-situ in an electron microscope. The structural changes were followed both by bright field images and selected area diffraction (Fig. 8). The structure of the film is stable up to about 400ºC. Around 450ºC a newly formed BCC phase was detected in them, having certain crystallographic relation ($d(111)_{FCC}=d(110)_{BCC}$) with the host FCC phase.

The formation of the BCC phase crystallites took place without measurable morphological and compositional changes in the film so, it was considered to be a diffusionless transformation [Ref. 3.8].

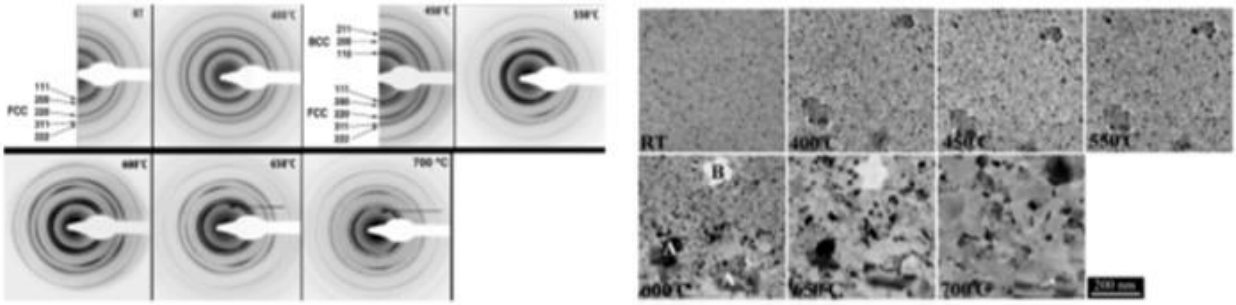

Figure 3.8. *Structural changes in HEA films during in-situ TEM annealing followed by selected area electron diffraction (left) and bright field TEM images (right).*

Above 550 ºC further new phases occur, these changes are, however, already connected to bulk diffusion processes in the films. As a result of intensive material transport processes thickness fluctuations, Fe-Co, and Ni-Cu intermetallic compounds as well as Cu or Co rich alloys form and grow rapidly (Fig. 3.9). The continuity of the film is maintained by a surface Cr-oxide layer, a few nm thick. This oxide layer can play important role in corrosion-resistance of CoCrCuFeNi alloy films [Ref. 3.9].

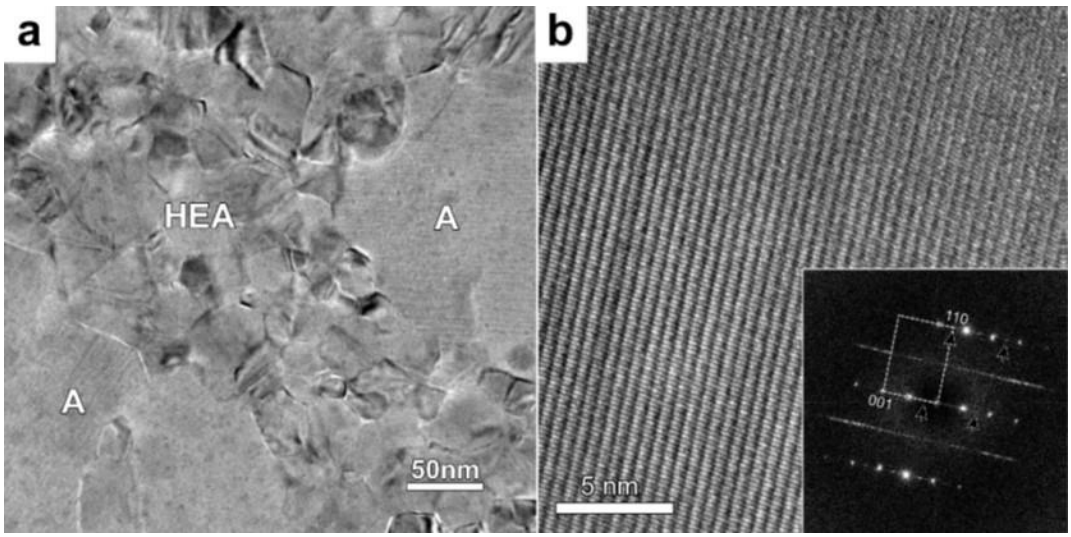

Figure 3.9. *Low magnification TEM (a), and high resolution lattice image (HRTEM) of a Cr-rich intermetallic phase (sample annealed at 700 ºC) (b). In the Fourier transform diffraction (insert to (b)) the unit cell of the BCC phase is outlined. The superlattice reflections (00½) point to the ordering process taking place in the BCC lattice (2x2x4 BCC cells), the diffuse scattering shows the presence of planar defects on (00l) planes. These grains (A) can be the precursor phases of the sigma phase forming at 700 ºC.*

Investigating the diffusionless FCC to BCC transformation the samples were subjected to (ex-situ or post annealing) HRTEM. Orientation relationships specific for martensitic transformation were found between the two phases (Fig. 3.10).

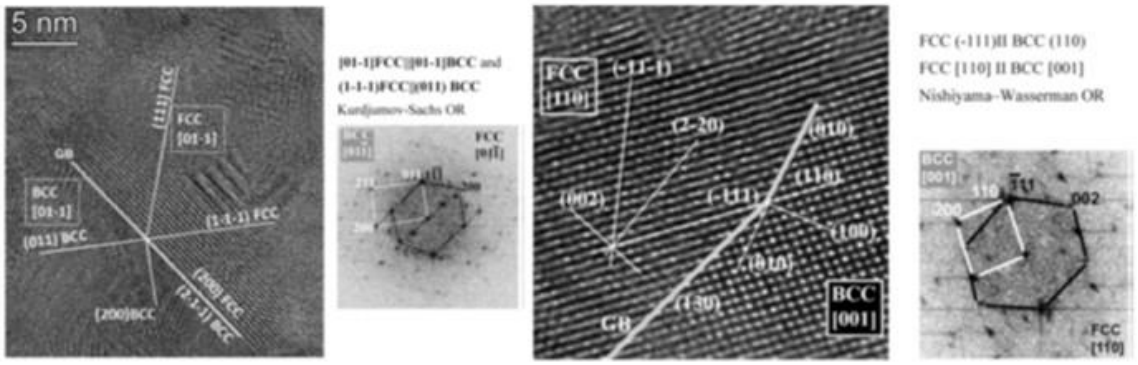

Figure 3.10*. Two orientation relationships, specific for martensitic transformation between the host FCC and the newly formed BCC grains appearing around 450 ºC.*

The observed structural changes around 450 ºC accompanied by morphological stability show that the first step of transformation takes place by martensitic mechanism. Then, in the newly formed BCC structure, in which larger free volume facilitates atom movement, diffusion processes start leading to further compositional and phase changes in CoCrCuFeNi HEA films.

This study was supported by the Hungarian National Research, Development and Innovation Office through the OTKA NN112156 project. The authors also acknowledge the VEKOP-2.3.3-15-2016- 00002 project of the European Structural and Investment Funds. V. K-K. is indebted to the János Bolyai Fellowship of the Hungarian Academy of Sciences and the ÚNKP-19–4 New National Excellence Program of the Ministry for Innovation and Technology. M. Arfaoui also acknowledges the Tempus Public Foundation according to the decree 285/2013 (26.07) of the Hungarian government on Stipendium Hungaricum scholarship programme.

Ion exchange processes on human dental enamel surface

OTKA K125100

V. Kis (EK MFA), Zs. Kovács (ELTE) M. Hegedűs (ELTE), A. Sulyok (EK MFA), D. Takács (Óbuda Univ.), A. Jakab (EK MFA), L. Illés (EK MFA), K. Hajagos-Nagy (EK MFA), N. Rózsa (SOTE), G. Radnóczi (EK MFA)

Dental enamel, a special hard tissue made up by biological apatite, is able to fulfill its biological function during lifetime. It is exposed to severe chemical and mechanical environmental effects without the ability of remodeling and with only very restricted capacity of remineralizing and repairing. A deep knowledge of ion exchange processes on the surface of dental enamel are essential both from the point of view of enamel degradation and tooth retention treatments. Dental enamel is made up of bioapatite nanocrystals which are cca. 20–50 nm wide and up to micrometer long, which, similarly to bone, are organized in a hierarchical structure over several orders of magnitude: enamel rods or prisms on the micrometer scale build up the compact enamel. Minor volume fraction of inorganic interprismatic and intergranular materials enhance ion migration providing channels for faster diffusion. The organic component, enamel protein and water (ca. 5w% altogether) is located between the nanocrystals and have crucial role in the stiffness of dental enamel. It allows a viscoelatic behaviour of dental enamel [Ref. 3.10], which, together with the gradually changing misorientation of the adjacent nanocrystals [Ref. 3.11] contributes to an effective blocking ability of crack propagation.

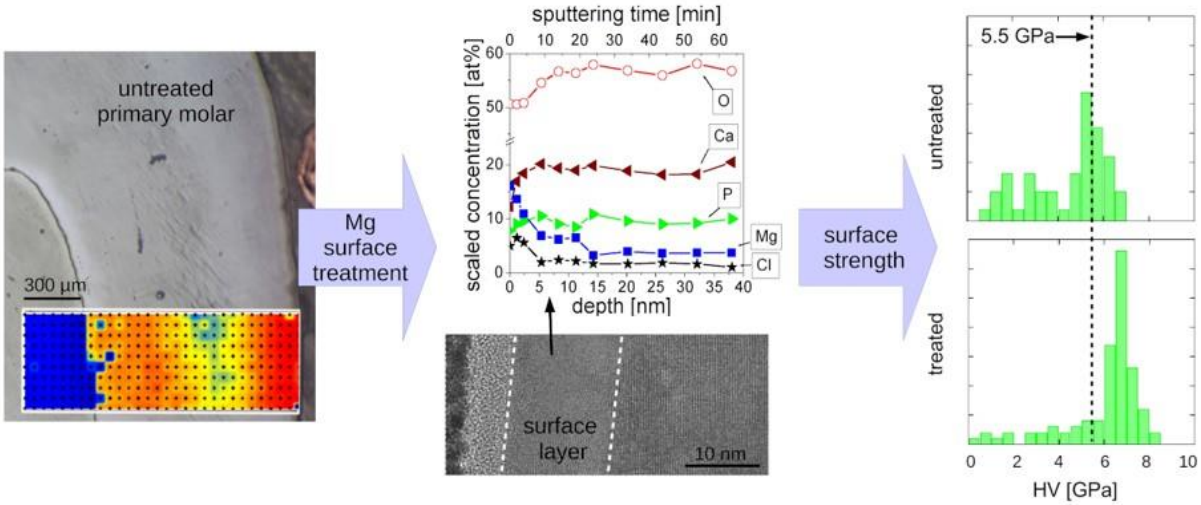

Figure 3.11. *(left) Untreated primary dental enamel , optical micrograph. The colour scale shows the result of nanoindentation tests made in a 10x30 matrix (decreasing HV red > yellow> blue). (middle) After ion exchange, XPS and HRTEM both reveal two distinct zones on the enamel surface. (right) Surface HV before and after ion exchange experiment [Ref. 3.12].*

In the study [Ref. 3.12] we report on Mg incorporation into the outer surface of primary dental enamel by ion exchange experiments under controlled conditions, focusing on changes of the concentration, microstucture and strength characterized by nanohardness. After Mg treatment of dental enamel, depth profile analysis and HRTEM allowed to distinguish two zones near the enamel surface. A surface layer of approximately 10–15 nanometer thickness proved to be strongly enriched in Mg with nonapatitic atomic environment. Below this surface layer the apatite crystal structure of enamel preserved with a moderately increased (in average 3 at%) Mg content. By comparing these changes with compositional changes of the abiogenic reference samples, two parallel processes, namely (1) incorporation via dissolution and

reprecipitation and (2) direct incorporation by diffusion, were concluded in nanostructured apatites. Amorphous intergranular phase facilitates Mg diffusion. Mg can be trapped in the intergranular phase and also can incorporate into the bioapatite nanocrystals, as indicated by the measured ionic ratio which, after ion exchange approximates the value characteristic of stoichiometric apatite.

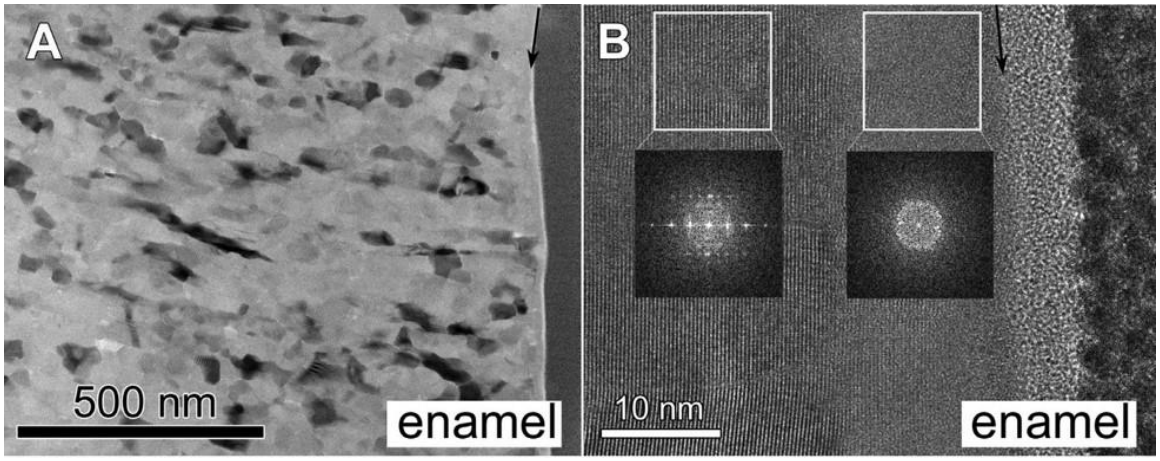

Figure 3.12. *Cross sectional TEM (a) and HRTEM (b) image of Mg exchanged primary dental enamel. On the HRTEM image a ca. 10 nm thick poorly crystalline layer can be seen, which corresponds to the zone containing >5at% Mg, according to the XPS. Below this surface layer dental enamel apatite crystals are seen (Fourier transform) where the Mg content is ca. 3 at% (XPS). Black arrow indicates the outer surface of the enamel.* [Ref. 3.12].

The increased Mg concentration in the dental enamel surface was followed by a notable increase of nanohardness (cca. 20%). Hardness increase was explained in part by the decreased crystal- lite size in the thin surface layer due to the inhibitory effect of Mg on reprecipitation and additionally by the effect of Mg, which diffused into larger depths and incorporated both into the apatite nanocrystals and the intergranular layers in between them. Based on first-principles plane-wave calculations, the elastic moduli of the Ca-vacancy containing apatite are about 10–60% lower than those of the vacancy free apatite crystals, depending on the crystallographic position of the vacancy [Ref. 3.13]. This anticipates that lower number of vacancies, i.e. composition approaching to stoichiometry, can increase hardness in enamel apatite.

Preparation of CaP and multi element doped hydroxyapatite (mCaP) powders and coatings

OTKA PD131934

M. Furkó (EK MFA), K. Balázsi (EK MFA), C. Balázsi (EK)

The aim of our research work is to prepare and examine ionic doped bioceramic – biopolymer composite powders as potential coatings for implant surfaces. Calcium phosphate (CaP) powders were prepared by wet chemical precipitation using different calcium and phosphorus sources and the ionic doped calcium phosphate powders were deposited by co-precipitating different bioactive ions such as Mg, Sr, Zn along with the base CaP. In addition, the micro and nanostructure of base CaP powders were studied with regard to different sources used and how the change of their structure was dependent on the deposition parameters and substituting ions.

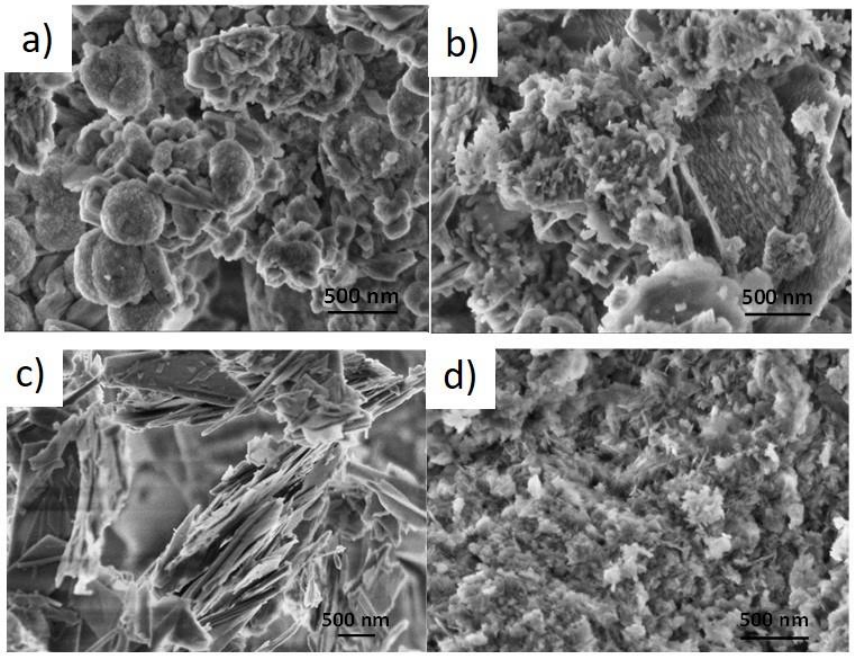

Figure 3.13. *SEM images on CaP powders prepared with different Ca precursors (a) $Ca(NO_3)_2$, (b) $CaCl_2$, (c) $Ca(Ac)_2$ as well as (d) Ca gluconate.*

The structural observations revealed, that the smallest grain size with almost amorphous structure was obtained when calcium gluconate was used as Ca source (Fig. 3.13.d), while in the case of nitrate and chloride salt of Ca, the crystallinity was higher. In the case of calcium nitrate precursor, the size of particles was higher and larger spherical agglomerates can also be observed in the size of several hundred nanometres (Fig. 3.13.a). In the case of $CaCl_2$ precursor, the size and form of resulting precipitate were very various. It consisted of small rod-like particles in nanosize and also of larger blocks (Fig. 3.13.b), while for $Ca(Ac)_2$, the resulting particles were in mainly thin, large plate-like form that were parallelly oriented (Fig. 3.13.c).

Effect of ionic substitution: the addition of different bioactive ions into the starting solution has also changed the morphology of the precipitated powders. The substituting ions were also deposited in the form of low soluble phosphate precipitates along with different CaP phases. The forms and sizes of particles

were very diverse, the powders contained large plate-like, rod-like grains in 0.5 – 5 µm sizes and small, needle-like particles as well as agglomerated spherical and flake-like particles. The elemental distribution of substituting elements was homogeneous within the CaP matrix according to the SEM elemental mapping (Fig. 3.14).

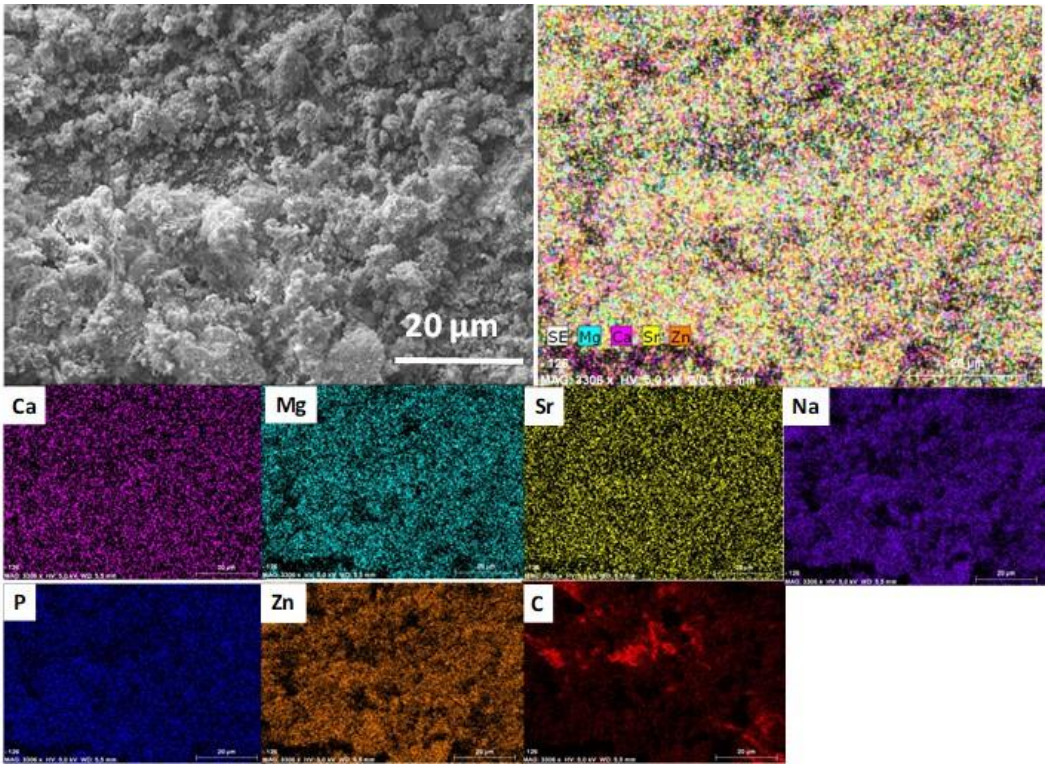

Figure 3.14. *SEM image and elemental mapping on ionic doped CaP powder prepared from Ca gluconate precursor.*

CaP/biopolymer (polyvinyl pyrrolidon, PVP) composites were prepared by electrospinning technique (Fig. 3.15). The bioactive ions were added to the base CaP suspension in the form of their chloride salts. The incorporation of added ions occurred during the co-precipitation with CaP phases.

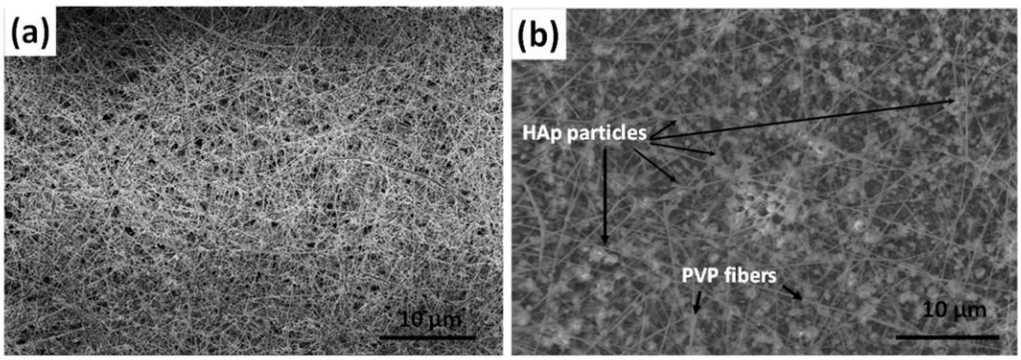

Figure 3.15. *SEM image of (a) PVP fibers and (b) CaP loaded PVP fibers.*

The suspension was mixed with biopolimer solution in appropriate concentrations and ratio in ethanol media. The fiber generation was performed by electrospinning apparatus, using high voltage difference between the two electrodes (needle and collector). According to SEM analyses, the CaP particles (white agglomerates, nodules) were sufficiently incorporated between the polymer fibers.

Examination of the hydrogen incorporation in radio frequency-sputtered hydrogenated SiN_x thin films

N. Hegedüs (EK MFA, Guardian), R. Lovics, M. Serényi (EK MFA), Zs. Zolnai (EK MFA), P. Petrik (EK MFA), J. Mihály (TTK), Zs. Fogarassy (EK MFA), C. Balázsi (EK MFA) and K. Balázsi (EK MFA)

Hydrogenated silicon nitride films (SiN_x:H) are widely used in microelectronics industry to enhance the efficiency of silicon based light emitters or to improve the efficiency of silicon solar cells as antireflective and passivation layer on the front surface of such device structures. SiN_x:H films have been reported to show a good surface and bulk passivation effect after annealing due to atomic hydrogen diffusion to the surface.

The most common techniques for deposition of the silicon nitride films with or without hydrogen addition are different types of Chemical Vapor Depositon (CVD) or Magnetron Sputtering (MS). In case of different sputtering techniques, it is possible to directly control the amount of hydrogen by means of adjusting the applied hydrogen gas flow. The deposited film always contains hydrogen. On the other hand, its amount can´t be controlled directly during the preparation process. Due to this fact, sputtering techniques could be interesting as alternative fabrication methods for controlled hydrogen concentration in direct way from zero by adjusting the applied hydrogen gas flow to the chamber.

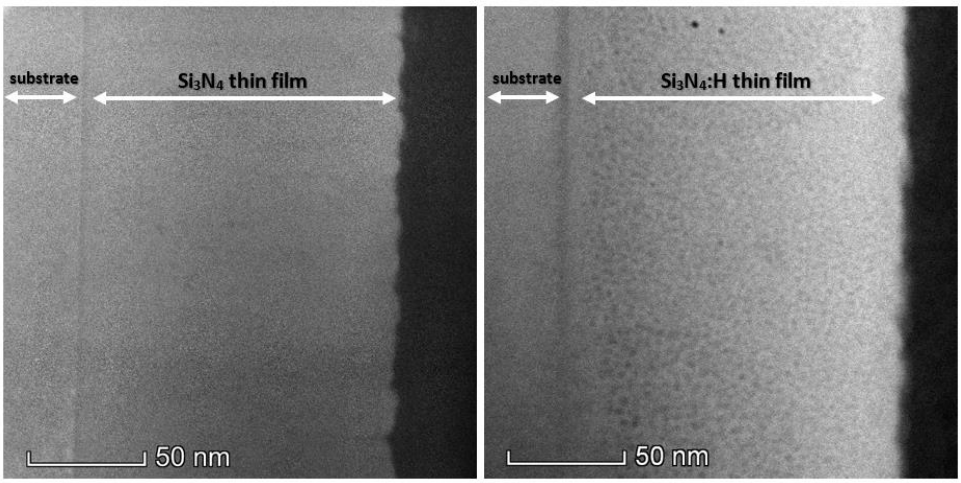

Figure 3.16. *TEM images of hydrogen-free (left) and hydrogenated (right) silicon nitride thin films.*

In this work, hydrogen-free and hydrogenated silicon nitride films were deposited by Radio Frequecy (RF) sputtering applying various amount of hydrogen gas. Optical properties were investigated as a function of hydrogen concentration of the plasma. Structural characterization revealed that the porosity of the film can be significantly influenced by hydrogenation (Fig. 3.16).

a-SiN_x:H films were sputtered at various H_2 flow with average thickness of 150 nm and the effect of hydrogen incorporation on structural and optical properties was studied. The detailed structural characterization confirmed the formation of a dense thin films at hydrogen-free sputtering and porous structure with homogenously distributed nanometer-scale porosities caused by hydrogen addition. The refractive index of 1.96 was characteristic for hydrogen-free SiN_x thin films.

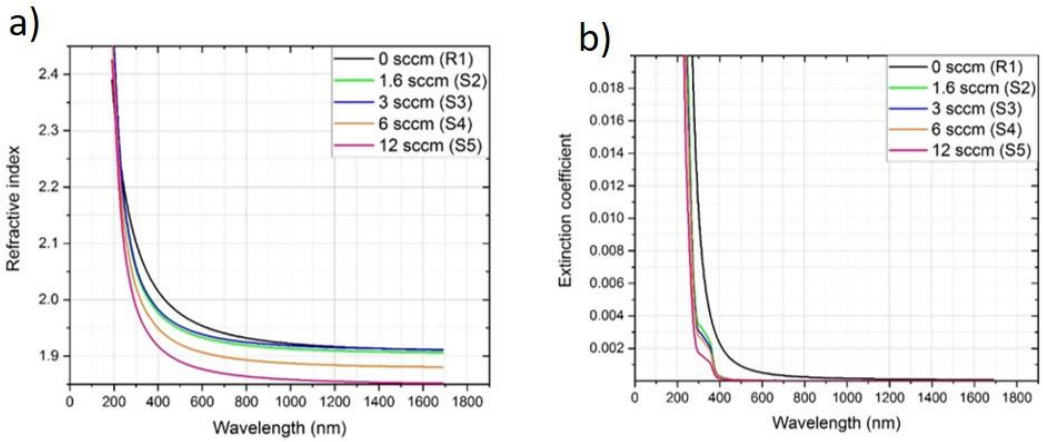

Figure 3.17. *Effect of hydrogen flow on the optical properties of a-Si_3N_4 thin films. a) refractive index, b) extinction coefficient.*

Hydrogen flows up to 3 sccm have been found to have no or minimal effect to refractive index, for flows from 6 to 12 sccm the refractive index decreased from 1.96 to 1.89 which can be explained by the hydrogen and nitrogen incorporation in the thin films (Fig. 3.17). The calculations from FTIR spectra showed that a-SiN_x:H sputtered at 6 sccm H_2 flow presented the concentration of bound hydrogen ~ 4 at.%. The ERDA measurements confirmed a total hydrogen content of 10 at.%. This means that 6 at.% hydrogen was incorporated in a molecular form during the layer growth, which explained the lower density of the thin films. The out-diffusion of hydrogen due to annealing plays a prominent role in the densification of thin films. The molecular form of hydrogen released at a temperature of ~ 65°C from the film. Blisters with 100 nm diameter are created on the surface of the thin films. The low activation energy calculeted by the Arrhenius-method refers to significant diffusion of hydrogen molecules. [Ref. 3.14]

Porous sandwich ceramic of layered silicon nitride-zirconia composite with various multilayered graphene content

OTKA NN127723, FLAG-ERA "Ceranea"

K. Balázsi (EK MFA), M. Furkó (EK MFA), Zs. Fogarassy (EK MFA), Varga Viktor (EK MFA), Z. Liao (IKTS), J. Dusza (IMR SAS), E. Zschech (IKTS), C. Balázsi (EK MFA)

The silicon nitride (Si_3N_4) is the widely used high-temperature ceramic material (up to 1500 °C). Due to it's extreme high hardness and toughness in a wide range of temperatures, potential applications include reciprocating engine components, turbo chargers, bearings, metal cutting and shaping tools as well as hot metal handling. Silicon nitride has better mechanical properties at high temperatures compared to most metals, and it's low coefficient of thermal expansion (CTE) results in a higher thermal shock resistance than for most ceramic materials. These ceramics can be prepared in different forms, sintered bulk or layered. Multilayer ceramic composites (MCC) consist of two ceramic materials. These ceramics are consisting of insoluble parts in each other and sequentially piled in a symmetric manner.

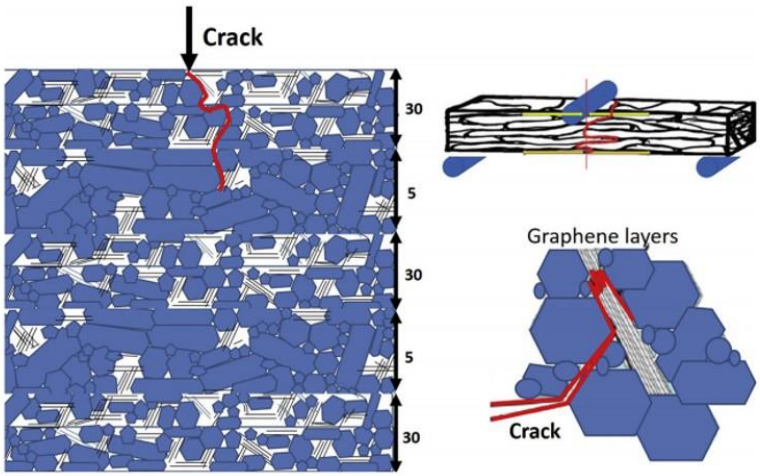

Figure 3.18. *Schematic view of multi-layered ceramic composite with the crack propagation mechanism in the structure*.

Multilayered ceramic composites have attracted attention due to their excellent mechanical properties like high damage tolerance, ablation resistance, impact resistance or high thermal conductivity the gradient structure allowed the crack to propagate along a variety of paths, and thus, to absorb more energy (Fig. 3.18).

In this work, we are firstly produced the gradient-structured Si_3N_4 ceramics with few layers graphene by attritor milling and hot isostatic pressing. Development was a part of the "Graphene Flagship" FLAG-ERA Joint Transnational Call 2017 partnership for graphene innovation developments supported by the European Commission. The partners of consortium leading by Dr. Csaba Balázsi (EK MFA) are researchers from the Fraunhofer Institute of Ceramic Technology and Systems (Fraunhofer IKTS, Germany) and the Institute of Materials Science of the Slovak Academy of Sciences (IMR SAS, Slovakia). Graphene Flagship Partnering Project „CERANEA" develops graphene-filled ceramic sandwiches that deliver materials with enhanced properties and functionalities.

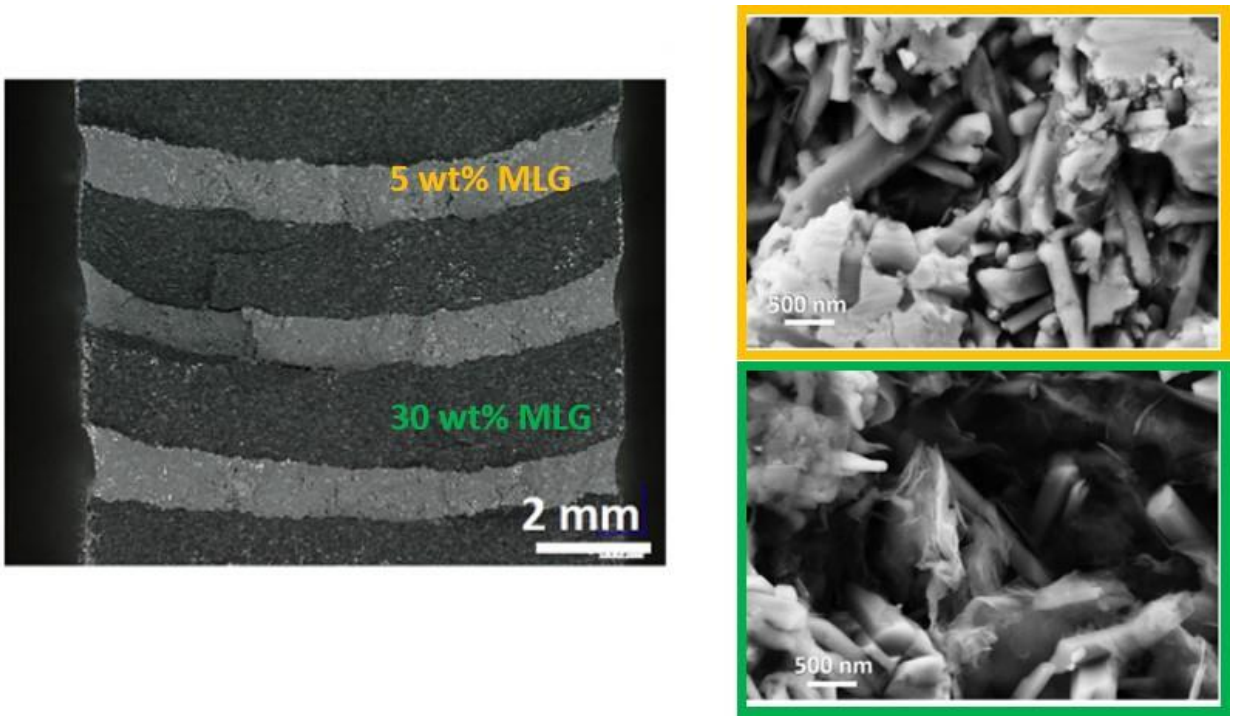

Figure 3.19. *Morphology of multilayered Si_3N_4/ graphene (left) with 5 wt% and 30 wt% graphene addition (right).*

The porosity of the samples increased by around two times with increasing of the multilayer graphene content (MLG) content. The density values were lower for samples with high MLG content owing to their very porous microstructure. The mechanical test confirmed that sandwich structure with combination of 5-30-5 wt% MLG layers showed 2 or 3 times better properties than structure with 30-5-30 wt% MLG. The main effect on mechanical properties had the layer with 30 wt% MLG with porosity of ~66% and high α/β-Si_3N_4 ratio of sintered ceramic matrix. [Ref. 3.15-17]

Al_2O_3-AlN composite and AlON ceramic development using the powder technology

OTKA NNE129976

K. Balázsi (EK MFA), M. Furkó (EK MFA), V. Varga (EK MFA),
S. Gurbán (EK MFA), F. Cinar (ITU), C. Balázsi (EK)

Aluminum oxynitrides (AlON) is a relatively hybrid ceramic system of aluminum oxide and aluminum nitride (Al_2O_3-AlN). Currently commercially available AlON materials exhibit average grain sizes in the order of 150–200 μm; however, development of new methods to control the grain size, especially at the nano-scale could create materials with improved properties. The most promising techniques for AlON preparation are the hot isostatic pressing (HIP) or spark plasma sintering (SPS).

The currently available and used techniques are still all expensive, as well as being energy and time consuming. We intend to develop an eco-friendly preparation method of AlON in which we develop a novel way to reduce the temperature and/or time thus requiring lower energy.

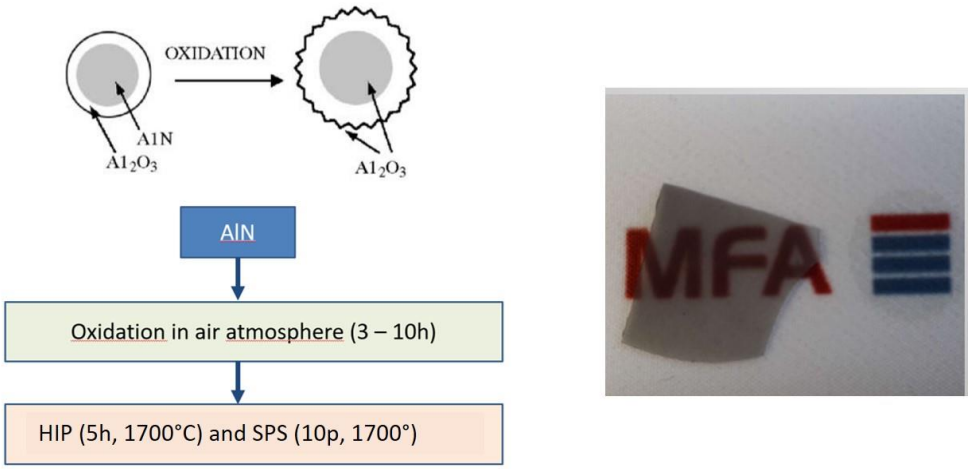

Figure 3.20. *Schematic view of preparation process (left) and final semi-transparent AlON (right).*

The aim of our work was the preparation of cheap Al_2O_3-AlN composites and transparent AlON by eco-friendly technology. The oxidization of base AlN powder with specific surface area and an average particle size of 0.80 -1.8 μm for 3, 6 and 10h at 900°C in air atmosphere was the first step (Fig. 3.20, left). HIP and SPA were used for sintering of oxidized powders. The increasing the oxidation time significantly improved the tensile strength of sintered samples compared to the reference. The nanosize composition and homogenity of sintered powders resulted the semi-transparent nanomaterial (Fig. 3.20, right). The results are under publication. [Ref. 3.18]

Self-regulating gas inlet system for reactive RF sputtering of composition spread Hf oxy-nitride layers

OTKA K129009

G. Sáfrán, N. Szász, G. Dobrik, B. Kalas and M. Serényi

Thin layers of metal-oxy-nitrides (MeON) are widely used (Me denotes e.g. Al, Ti, Hf, Si) for wavelength selective coatings of optical elements, smart windows and laser diodes [Ref. 3.19]. Their advantageous feature is the tunable refractive index by the proportion of the oxide and nitride components. Our aim was the synthesis of a single, concentration spread combinatorial sample in order to reveal the optical properties of various radiofrequency (RF)-sputtered metal-oxy-nitride layers in a wide range of O/N ratios. The composition-spread layer is deposited from a single Me target by RF sputtering through a moving slit, meanwhile the ratio of the reactive components (O and N) in the plasma gas is varied. As we want to cover a composition range of the deposited film from Me-oxide to nitride the oxygen partial pressure has to be varied well below $1\cdot10^{-4}$ mbar. Unfortunately, the common gas dispensers cannot provide both the required low flow rates and fine control of partial pressures. We propose a self-regulating assembly for gas inlet: Oxygen is introduced to the chamber by a peristaltic pump emptying a finite volume reservoir. The pressure in the reservoir gradually decreases resulting in a decrease of the partial pressure of oxygen while that of argon and nitrogen is kept constant by using conventional flow meters. A continuous depletion of the Ar-O-N reactive gas mixture in oxygen, during deposition, enables the deposition of composition spread oxy-nitride combinatorial samples.

According to our experiments an oxygen partial pressure change between $1\cdot10^{-4}$ and $1\cdot10^{-5}$ mbar is suitable to cover a composition range of the deposited layer between Hf-oxide and Hf-nitride. The setup of the proposed self-regulating gas inlet assembly is represented by Fig. 3.21.a. Prior to reactive RF sputter deposition of combinatorial samples a dedicated experiment was carried out. For this test, our RF sputtering chamber (Leybold Z400) was used. The vial of 48 cm^3 volume was filled with 1 bar oxygen and the volume rate of the peristaltic pump was set to 1 cm^3/min. As the sputtering chamber was evacuated, by a turbo molecular pump, to its base pressure of about $6\cdot10^{-7}$ mbar the peristaltic pump was started and it began to deliver O_2 from the vial into the chamber. As oxygen appeared in the chamber, the pressure suddenly increased to $9\cdot10^{-5}$ mbar followed by a continuous decay due to a decrease of the delivered gas from the gradually emptied vial. The variation of the pressure in the chamber as a function of pumping time is plotted with full circles, in Fig. 3.21.b.

Peristaltic pumping from a finite volume vial can be modeled by repetitive application of the general gas equation. Let p_{N2} be the pressure of the vial in the n^{th} minute:

$$p_{N2}=p_0(1-v/V)^n \qquad (1)$$

where p_0 is the manifold pressure of the V-volume vial and v volume of the O_2 gas pumped out during one minute. The p_{O2} partial pressure change at 1sccm O_2 inlet into the vacuum system was determined by the dedicated measurement. It was found to be $0.9\cdot10^{-4}$ mbar right after the start of the peristaltic pump, and with a sudden transient it dropped to $0.8\cdot10^{-4}$ mbar which is considered the initial value. The final pressure of the system was chosen to be 10^{-6} mbar, hence p_{O2} can be estimated as follows:

$$p_{O2}=0.1+8(1-1/V)^n \qquad (2)$$

(n is the elapsed time in minutes).

The pressure change as a function of time, modeled according to equation (2), is plotted with a solid line in Figure 1 (b). It starts at of $8\cdot10^{-5}$ mbar and shows an asymptotic decrease towards $1\cdot10^{-6}$ mbar, within 105 minutes.

The HfON composition spread layer was deposited onto a 25x10 mm^2 Ge wafer through a shutter with a 1 mm slot that was swept along the substrate. The stepping motor moved the slot by 25 µm per step controlled by a microcontroller. Sputtering was performed under 10:1 mixture of high purity nitrogen and argon at a plasma pressure of $2.5 \cdot 10^{-2}$ mbar. O_2 gas was introduced from the 48 cm^3 vial with 1 bar initial pressure, and peristaltic pumping was maintained for 110 min at a volume rate of 1cm^3/min.

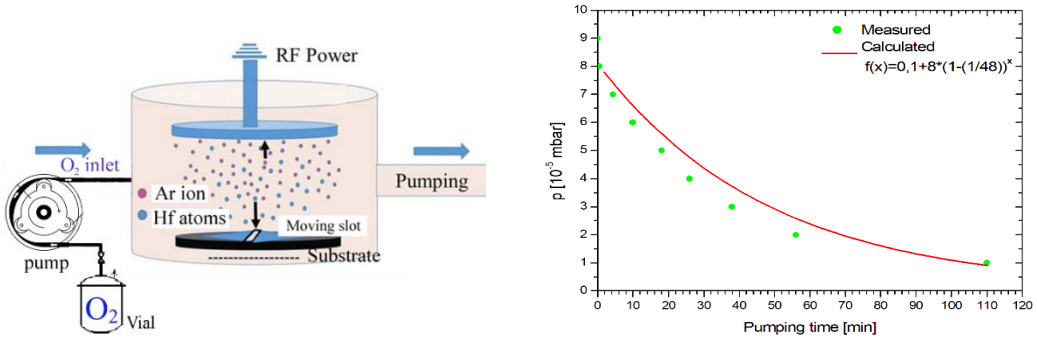

Figure 3.21. *(a) Setup of the self-regulating gas inlet. (b) Variation of oxygen partial pressure in the sputtering chamber during an oxygen inlet experiment: the peristaltic pump was operated at a rate of 1cm^3/min emptying the 48 cm^3 vial of 1 bar initial pressure. Measured pressure decay during the experiment (●). Calculated pressure decay according to equation 2 (–).*

Sputtering the Hf target in an Ar-O-N reactive gas mixture from which oxygen was gradually depleted resulted in a continuous drop of the O/N ratio in the deposited HfON. The deposit was laterally distributed along the substrate by the sweeping slot, so that a composition spread film was formed covering the range of transition from Hf-oxide to Hf-nitride. The properties of the combinatorial Hf-oxy-nitride sample prepared as above were investigated by EDS and ellipsometry. For to reveal the effects of the variation of oxygen inlet on the oxygen and nitrogen proportion of the layer the composition was determined along the sample by EDS in a FEI Scios scanning electron microscope using 3 keV probe with 13 nA current The O/O+N ratio as a function of distance along the combinatorial layer is plotted in Fig. 3.22.

The optical properties of the combinatorial sample along the substrate were investigated by means of a spectroscopic ellipsometer with a rotating compensator configuration (Woollam-2000DI). The variation of refractive index revealed as a function of distance along the sample is plotted in Fig. 3.22. According to the dedicated test the assembly for variable oxygen gas inlet has worked properly.

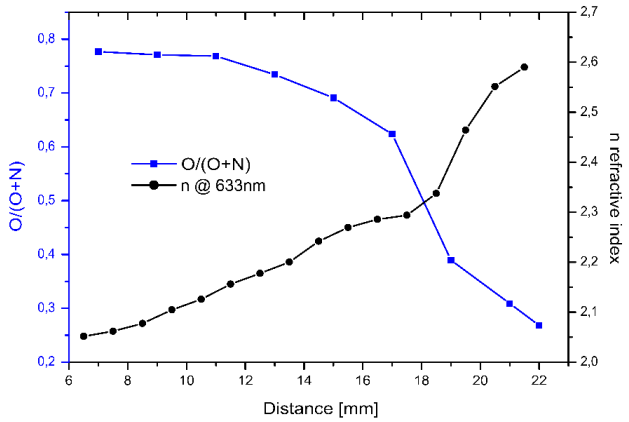

Figure 3.22*. Variation of O/O+N and refractive index along the combinatorial Hf-O-N sample revealed by EDS (■), and* ***n*** *by ellipsometry at 632.8 nm wavelength (●), respectively.*

The correlations of composition of sputtering gas and that of deposited film, as well refractive index variation are presented in Fig. 3.22. as a function of position along the combinatorial sample. The O/(O+N) ratio measured by EDS, depicted with full squares, shows monotonous decrease along the sample. It is due to the gradual oxygen depletion of plasma gas during reactive sputtering. O/(O+N) values extending between 0.78 and 0.27 indicates that the combinatorial layer covers a wide composition range of HfON. The correlated refractive index values measured by ellipsometry and evaluated by the methods and parameters of [Ref. 3.20-21] are depicted with full circles. It shows a monotonous transition of n-values between 2.05 and 2.6. Obviously, refractive index variation of the combinatorial sample covers about the entire composition range between stoichiometric HfO2 [Ref. 3.22-23] and HfN [Ref. 3.24-25]. The results shown in Fig. 3.22. are illustrating that one sample concept combinatorial technique was successfully adapted to reactive RF sputtering and that the synthesized combinatorial sample is suitable to a comprehensive characterization of Me-oxy-nitrides in a wide composition range [Ref. 3.26].

Nanosensors Laboratory

Head: Dr. János VOLK, Ph.D., senior research fellow

Research Staff:
- Gábor BATTISTIG, D.Sc., Deputy Head of Department (part time)
- Zsófia BAJI, Ph.D.
- Nguyen Quoc KHÁNH, Ph.D.
- István Endre LUKÁCS, Ph.D.
- György MOLNÁR, Ph.D.
- László PÓSA, Ph.D.
- János RADÓ, Ph.D.
- Zsolt ZOLNAI, Ph.D.

Technical Staff:
- János Márk BOZORÁDI, M.Sc. student
- Tamás CSUKÁS, engineer
- János FERENCZ, engineer
- Levente ILLÉS, engineer
- Attila NAGY, technician
- Miklós SZAPPANOS, engineer
- Erika TUNYOGI, engineer

Ph.D. students / Diploma workers:
- Binderiya Oyunbolor, M.Sc. student
- Máté SÜTŐ, M.Sc./Ph.D. student

Nanosensors Laboratory was established at the beginning of 2019 from the former Department of Microtechnology. The core infrastructure, having two semiconductor clean rooms, is shared and operated together with the Microsystems Laboratory. The mission of the Lab is to utilize the emerging results of nanotechnology and materials science for novel physical sensors, particularly for micro- and nanometer sized electromechanical systems (MEMS/NEMS). The activity of the research group relates to five domestic projects and several scientific collaborations with national and international partners. In the most significant project of the group, titled ‘Advanced Functional Materials for Autonomous Sensor Networks’, the work was divided into three levels: i) research of CMOS compatible functional thin films; ii) development of MEMS energy harvester and sensor devices; iii) development of wireless proof-of-concept (PoC) sensor nodes.

ScAlN is one of the investigated functional materials. Because of its high piezoelectric coefficient, it is a promising candidate for next generation piezo-MEMS devices. The aim of the group is to optimize the properties of the layers by changing their stoichiometry during the reactive co-sputtering. The deposited piezoelectric layers are characterized by several ion-beam, electron-beam, and scanning probe techniques (RBS, EDS, PFM). VO_2 is another functional material, which is studied by the group. It attracts considerable interest because of its semiconductor-to-metal transition at relatively low temperature (67 °C), which is beneficial both for electronic and thermochromic applications. We have pointed out that a rational and up scalable synthesis can be done by post-annealing of metallic vanadium under ambient air atmosphere.

The main motivation of device related research is to study novel vibrational energy harvesters for autonomous sensor nodes and novel frequency sensitive vibration sensors for middle-ear human implants. Besides, the group performs research in the field of novel tactile sensors and artificial skins where AlGaN/GaN heterostructure based membranes can play a significant role. The developed wireless sensor systems include an autonomous vibration analyzer, a 3D force sensor based integrated tire sensor, as well as a mobile gamma-radiation detector.

Nanotechnology related research was carried out mainly in collaboration with Physics Department of BME. On the one hand, the group continued the work on spintronic devices in the framework of National Quantumtechnology Program (HunQuTech), on the other hand, they have progress in the field of memristors.

Piezoresponse Force Microscopy on Pulse DC Deposited AlN for Energy Harvesting

NVKP_16-1-2016-0018 "KoFAH"

N.Q.Khánh, S. Soleimani, and J. Volk

Tremendous amount of sensors to be used over the world necessitate zero-energy, as well as self-supporting sensor concept. Piezoelectric AlN, a good candidate for such purpose is generally applied in the form of thin layer deposited on different substrates by mean of ion sputtering. We have applied Piezoresponse Force Microscopy (PFM) to study the effect of the substrate bias voltage on the piezoelectric properties of the pulse DC sputtered AlN layer in nanoscale. Fig. 4.1 shows the electromechanical (EM) displacement as a function of exciting AC voltage on non-piezoelectric SiO_2 sample. It is clearly seen that using probe with high stiffness, the electrostatic force, i.e. the non-piezoelectric contribution to the PFM response, which could cause a significant error in the piezoelectric properties determination from the measured data, can be eliminated. Taking into account the clamping effect of the substrate as well as using proper calibration sample (c-cut $LiNbO_3$), the piezoelectric coefficient (d_{33}) map of the nitride layer can be obtained by PFM (Fig. 4.2).

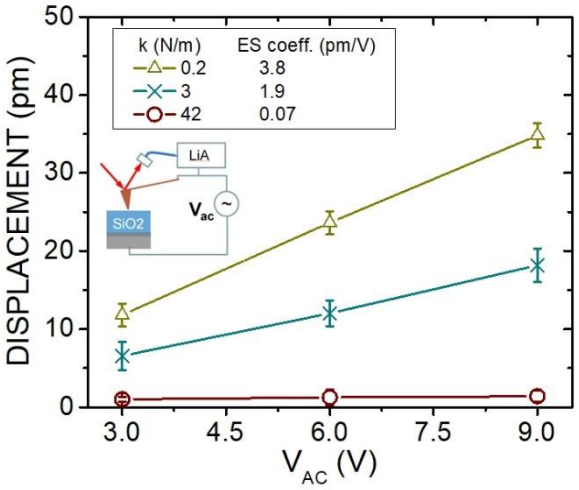

Figure 4.1. *PFM displacement responses due to electrostatic force on non-piezoelectric SiO_2 blank sample. ES contribution is almost negligible using a high stiffness (42N/m) probe.*

The PFM results reveal the improving effect of substrate bias on the piezoelectric properties of the sputtered AlN layer, among others (Fig. 4.3). The ratio of the areas having no piezoelectric character, i.e. the dead zones, decreases with increasing substrate bias (Fig. 4.3.d). As a result, the average value of d_{33} increases, which is in fair agreement with that measured by macro method, i.e. the Berlincourt piezotester (Fig. 4.3.e).

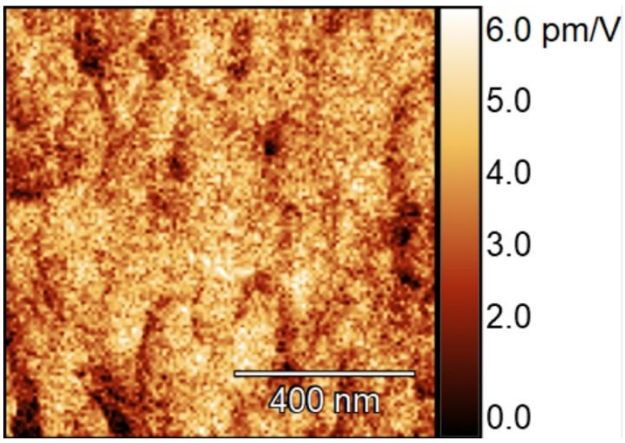

Figure 4.2. *d_{33} piezoelectric constant map of the AlN layer deposited at 5 mTorr with V_{bias}=-100V.*

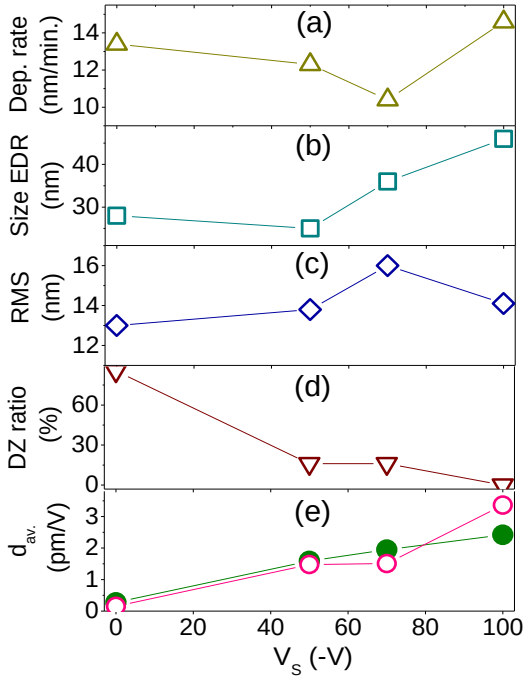

Figure. 4.3. *Effect of substrate bias on the properties of AlN thin film deposited at 5 mTorr with 20% N_2 gas ratio, and Al target power of 450W: deposition rate (a), grain size (equivalent disc radius) (b), surface roughness (RMS) (c), dead zone ratio (d), and corrected average piezoelectric coefficient (e) as a function of substrate bias voltage. Piezoelectric coefficient measured by macroscopic method (Piezometer) also shown in (e) for comparison (green dots).*

Piezoelectric Improvement of Aluminum Nitride Layer Deposited by Pulse DC Reactive Ion Sputtering for Energy Harvesting

NVKP_16-1-2016-0018 "KoFAH"

N.Q.Khánh, B. Oyunbolor, Z. Horváth, and J. Volk

Piezoelectric aluminum nitride thin layer is a good candidate for energy harvesting applications, which can support sensors, and their network, among others. Its advantages manifest in its compatibility to MEMS technology, and stability in harsh environment. For its applications in the form of thin film, the key features are good piezoelectric coefficient (d_{33}) and smooth film surface. We have attempted to improve the piezoelectric, and morphologic properties of the nitride layer deposited on Si substrate using our pulse DC reactive ion sputtering system (VAKSIS – MiDAS).

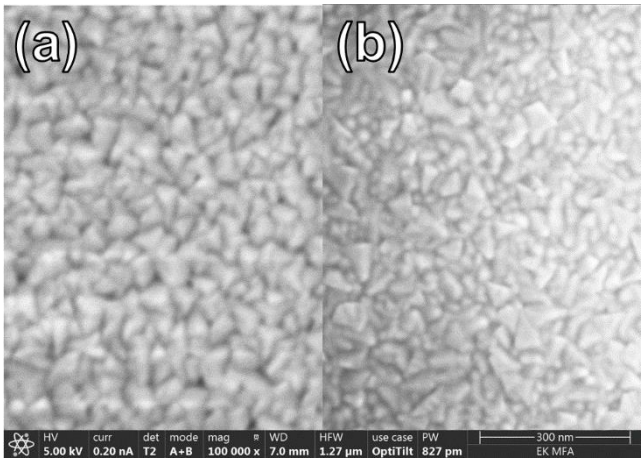

Figure 4.4. *FESEM images of layer deposited with 450W, 30% N_2 gas ratio at 5 mTorr (a), and 1.5 mTorr (b).*

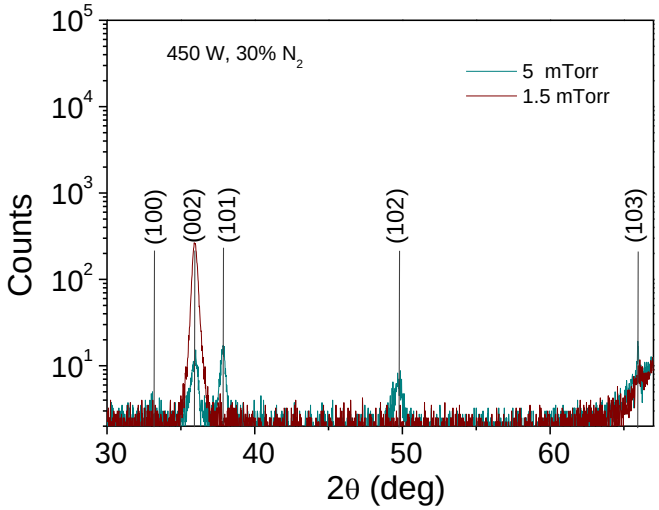

Figure 4.5. *XRD pattern of layer deposited with 450W, 30% N_2 gas ratio at different gas pressures*

Fig. 4.4 shows the FESEM images of the samples deposited at 1.5 and 5 mTorr. The grain size seems the same for both. However, the surface roughness (RMS) measured by AFM is better for low process

pressure, namely, it is 1.7 nm compared to 8.1 nm for 5 mTorr. Low pressure is also proven to be favorable regarding the piezoelectric coefficient of the layer measured by PiezoTest (Berlincourt method), i. e. 1.0, and 0.02 pC/N, respectively. The reason is that the lower the pressure, the longer the mean free path (MFP) of the sputtered particles, the higher kinetic energy, i. e. enhanced surface diffusion of the adatoms which promotes the growth of AlN crystal in (002) preferential direction as shown by XRD (Fig. 4.5). At 5 mTorr pressure the 002 peak is weak, and there are also other weak peaks revealing that the growth is insufficient in this case, resulting in non-piezoelectric film.

The most effective way to improve the piezoelectric properties of nitride layer, however, is the alloying AlN with scandium. Our deposition system enables co-sputtering, so desired concentration of Sc can be achieved via control of sputtering power ratio of Al and Sc as presented in Fig. 4.6, where good agreement can be observed between RBS and EDS data. The improvement of d_{33} with Sc concentration in $Al_{1-x}Sc_xN$ nitride film can be followed in Fig. 4.7. The magnitude of the measured d_{33} monotonously increases with Sc content up to ca. x=0.4, where the highest value of 4.9 pC/N was achieved, then it decreases to quasi zero at x~0.51. The benefit of the introduction of Sc is associated with the stress the hexagonal ScN phase induces in the AlN crystal structure making it more asymmetric. However, at high Sc concentration ScN crystal gradually transforms to cubic structure, thus the nitride film is losing it piezoelectric character.

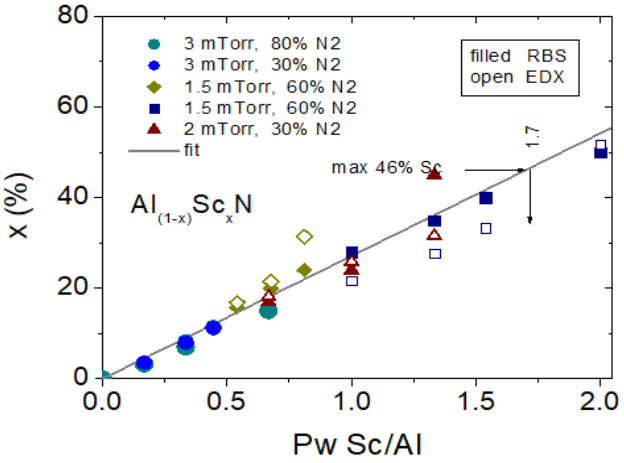

Figure 4.6. *Sc content determined by RBS, and EDS as a function of targets' power ratio*

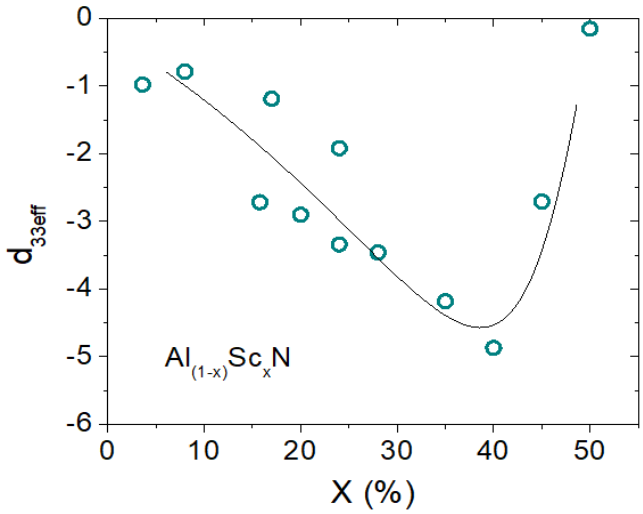

Figure 4.7. *Piezoelectric coefficient (d_{33eff}) measured by Piezotester as a function of Sc content (x in $Al_{1-x}Sc_xN$). Line for guiding eye.*

A rational fabrication method for low switching-temperature VO_2

L. Pósa, Gy. Molnár, B. Kalas, Zs. Baji, Zs. Czigány, P. Petrik and J. Volk

Most of the vanadium oxides show semiconductor to metal transition (SMT), due to external stimuli, i.e., temperature or electric field, while their electrical conductance changes several orders of magnitude. Among the series of oxides, VO_2 is the most studied material due to its transition close to room temperature at 68 °C, where the crystalline structure of the material reorganizes from monoclinic to tetragonal rutile structure. In bulk VO_2 beside the five orders of magnitude change in the electrical conductivity, the optical transmission also undergoes a substantial reduction, especially in the near-infrared regime.

Due to the several oxidation states of vanadium, preparation of VO_2 film is highly challenging. There are numerous thin film deposition techniques to prepare VO_2 layer, however, all methods suffer from narrow process windows, i.e., minor changes in the growth parameters can cause significant degradation in the performance of electrical/optical switching. Oxidation of metallic vanadium films by thermal annealing provides a cheap and simple method for preparing vanadium-oxides; however, it also requires a precise control of the parameters to achieve the appropriate phase. Since V_2O_5 is the thermodynamically most stable stoichiometry at high O_2 partial pressure, the VO_2 is only an intermediary phase with many other oxides towards the formation of V_2O_5. This phenomenon is pronounced during oxidation in air, which would offer a temptingly simple approach for VO_2 synthesis.

During our work we focused on the preparation of VO_2 films with thermal oxidation of evaporated vanadium films in air [Ref. 4.1]. This method, combined with the measurement of electrical resistance, provides a simple and sensitive optimization procedure. We found that a slightly lower than conventionally applied annealing temperature (400 °C) results in a 30 min wide process window in respect to the oxidation time. Moreover, the result of the oxidation was not sensitive to the initial quality of the metal layer; we got the same switching behavior even if the vanadium film was exposed to air for seven months. This preparation approach offers a highly flexible and cost-effective method to synthesize vanadium-dioxide films.

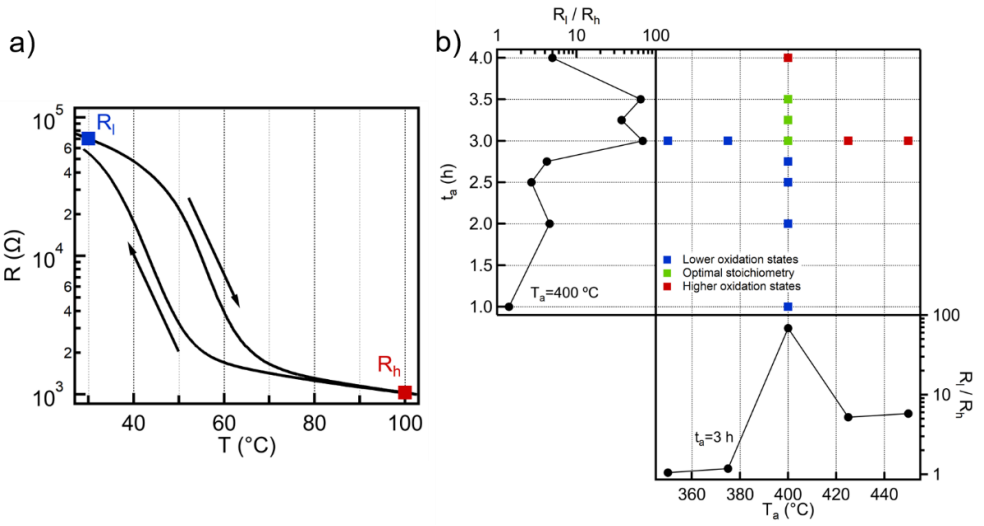

Figure 4.8. *a) Typical temperature dependent resistance curve of VO_x film annealed at T_a = 400 °C for t_a = 3.0 h. The blue/red dot marks the resistance at 30/100 °C on the heating branch (R_l and R_h, respectively), whereas the arrows indicate the direction of the hysteresis curve. b) The applied annealing time and temperature combinations (middle panel), the colors of the dots indicate the oxidation state of the vanadium according to the electrical property. The resistance switching ratios (R_l/R_h) are also shown as a function of the annealing temperature (bottom panel) and annealing time (left panel).*

Fig. 4.8.a shows a typical temperature dependent electrical resistance trace of an oxidized V film. The nearly two orders of magnitude changes in resistance close to room temperature anticipates VO_2 rich content. The transition temperature (T_c) is 56 °C during the heating and 43 °C during the cooling branch. Compared to the similar preparation method in the literature, it means about 10 °C lower transition temperature. The hysteresis width is around 10-13 °C, which is a typical value for polycrystalline thin films, while the magnitude of the transition (R_l/R_h) for this particular sample is 68. This resistance switching ratio is in the same regime or higher than the other layers which were prepared by oxidation of metallic V under atmospheric pressure. Although the T_c is still too high for smart window application, maybe it can be further reduced by using W doped V layer or V-W alloy.

To study the sensitivity of the SMT to the annealing parameters, we varied both the annealing temperature (T_a) and the time (t_a), separately. The applied annealing temperature-time combinations during the optimization process are summarized in Fig. 4.8.b, whereas the corresponding resistance switching ratios (R_l/R_h) are shown in side panels as a function of the annealing parameters. When we increased the annealing temperature, the resistance switching feature appeared only at T_a=400 °C, while below/above this temperature the layer showed metallic/insulating behavior (see bottom panel of Fig. 4.8.b). This tendency demonstrates well the narrow process window. In contrast, phase transition occurs in wider parameter range, when the oxidation time (t_a) was tuned (see left panel of Fig. 4.8.b). The quality of the VO_x films does not change significantly between the annealing times of 3.0 and 3.5 h. This finding refers to a wider process window, which significantly promotes the reliable production of the VO_2 content. Cross sectional TEM pictures also confirmed the presence of VO_2 and identified two VO_x layers (approximately 100–100 nm) with different (50 and 100 nm) average grain sizes.

In order to confirm that a similar low temperature switching occurs also in the near infrared optical properties, an in situ spectroscopic ellipsometry study was carried out. During the temperature dependent spectroscopic ellipsometry (SE) measurement we monitored the complex reflection coefficient (ρ) by collecting the Ψ and Δ ellispometric angles. The annealed VO_x layer shows a reversible SMT during the heating cycle (see Fig. 4.9.a), the change in the ellipsometric angle Ψ has a maximum around 60° in the infrared wavelength range, in good agreement with previous reports. The parameters of the hysteresis loop are in good accordance with the electrical characterization. Based on the TEM pictures, the optical model was set up by a semi-infinite Si substrate, a SiO_2 layer and two VO_x thin layers. The model fit identifies the top VO_x layer as V_2O_5 phase since the two interband transitions of pentoxide can be clearly seen near 3.0 and 4.5 eV. The bottom VO_x layer corresponds to the VO_2, the optical constants of which at the wavelength of 1540 nm at low and high temperature are (n_l, k_l) = (2.62, 0.47) and (n_h, k_h) = (2.16, 3.04), respectively.

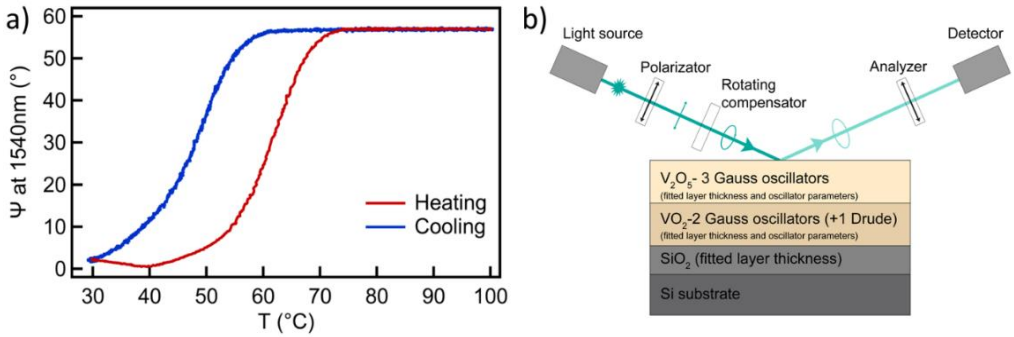

Figure 4.9 *(a) Temperature dependent variation of Ψ during the heating cycle at a wavelength of 1540 nm. (b) Schematic of the applied optical model and the SE measurement arrangement.*

In conclusion, a rational technique was demonstrated to fabricate VO_2 coatings. Since the oxidation of metallic vanadium is carried out at atmospheric air at a relatively low annealing temperature (400 °C), it is prosperous for mass production. Moreover, the low temperature phase transition of 49±7 °C makes it a promising candidate as an infrared transmission blocking layer.

Continuous monitoring of the tire side wall deformation for advanced vehicle control systems

NVKP_16-1-2016-0018 "KoFAH"

J. Radó, A. Nagy, G. Battistig, and J. Volk

Advanced vehicle control systems, especially self-driving vehicles, are gathering more and more information to increase efficiency, reduce emissions, and increase safety. A set of sensors are installed today in the engine and placed in different locations in the car to monitor the vehicle's movement and the environment. A process that determines the movement of a vehicle, the interaction between the tire and the road surface, is not yet or only barely monitored. Currently, only the ABS sensor provides information during breaking, but it contains little information about the slipping of the vehicle and its direction. The slip of the vehicle is detected by a sensor that monitors the lateral acceleration and detects the rotation of the vehicle.

Part of the rotating tire in contact with the road surface is constantly deformed. The most significant deformation occurs on the sidewall of the tire. The elastic deformation of the sidewall counteracts the forces acting between the tire and road surface from the friction and adhesion. If the deformation of the sidewall can be measured continuously while the vehicle is moving, it can be used to determine the forces between the tire and the road surface, and even the load on the given wheel. It would be a significant advantage to measure the adhesion conditions separately for each wheel, so that each wheel would provide continuously independent measurement data on its contact with the road surface. When the traction conditions differ significantly wheel by wheel, the vehicle control electronics can intervene to increase stability and safety. Even an early warning can be generated when the adhesion may have dropped below a critical level for only one wheel, but the whole vehicle has not slipped yet and the side accelerations are still within limits.

A proof-of-concept sensor developed in the Nanosensors Laboratory of MFA is suitable for continuously measuring the deformation of a vehicle tire while the vehicle is in motion. The sensor is mounted inside the tire and consist of the following units: in-house developed silicon-based 3D force microsensor with housing, wireless communication for continuous transmission of measurement data, as well as a battery-powered power supply with wireless charging (Fig. 4.10.).

Figure 4.10. *Integrated tire monitoring sensor system: 3D force sensor, read-out electronics with RF unit and charging coil*

Tire with the developed sensor system was mounted on a test vehicle and measurements were carried out at Zalazone and kick plate test facilities (Fig. 4.11) in cooperation with the Institute for Computer

Science and Control (SzTAKI). Driving on the test track, during various maneuvers, all parameters of the vehicle's movement (longitudinal and lateral accelerations, rotation, etc.) and signals from the tire sidewall deformation were measured and recorded continuously (Fig. 4.12). In case of sudden changes, when even just one wheel loses traction, the deformation signals change drastically.

Figure 4.11. *Tire deformation sensors in action*

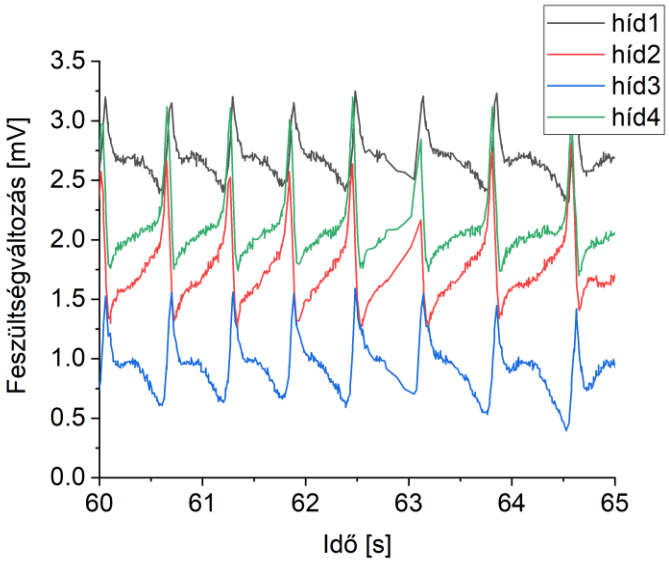

Figure 4.12. *Tire deformation signals during run*

The development of a 3D microsensor housing and an industrial process for incorporation into a tire would be possible only with the involvement of a partner from tire industry. The optimization of wireless communication and its connection into the vehicle control system can be envisaged with the involvement of a car manufacturer partner. The power supply of the measuring / data processing and communication unit integrated in the tire requires an energy harvesting technology, which is currently under development. The deformation, that occur in the tire during movement, provides enough energy to supply the entire unit.

Autonomous vibration monitoring wireless sensor network

NVKP_16-1-2016-0018 "KoFAH"

M. Szappanos, E. Tunyogi, G. Novotnik (Ante kft), J. Földes (BHE), Gy. Mikó (BHE), P. Harmat (Ante kft), J. Volk

Though wireless sensor networks can be used for various applications their usage is often limited by the finite lifetime of the battery or the high cost of electrical cabling. Therefore, there is a high demand for self-powered sensor nodes. In this work we demonstrated an autonomous wireless sensor network for vibration monitoring and diagnosis. In this application changing of the resonance spectrum can predict several failures, such as unbalance in rotating machinery, bearing wear, cogwheel imperfections etc. The design principle was to power the sensor node by an energy harvester and minimize the electrical consumption of the sensors, microcontroller, and RF transmitter (Fig. 4.13). The sensor node consists of three printed circuit boards (PCB). The lowest PCB has a thermometer, a humidity sensor and three capacitive 3D MEMS accelerometers covering the frequency range of 1 Hz-3200 Hz at a maximum sensitivity of 78 μG. A low power consumption microcontroller, which processes the obtained data, performs Fast Fourier Transformation (FFT) and switches the system between active, idle, and sleeping modes.

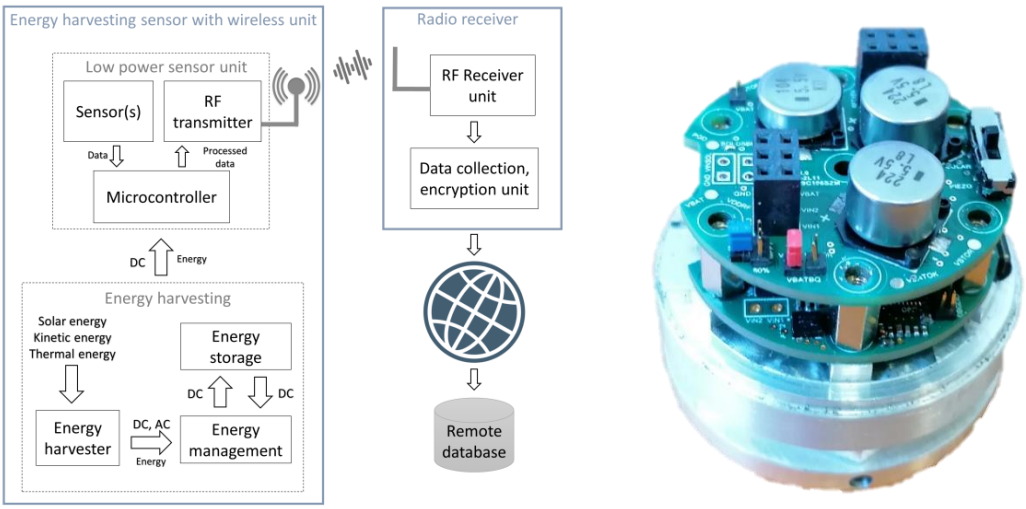

Figure 4.13. *Block diagram of the autonomous sensor node and the path of the data toward the remote database (left panel). Implemented sensor node without cap (right panel).*

The second PCB level is dedicated to energy management and storage having three supercapacitors on-board (Fig. 4.13, right panel). It can accept electrical power of both low and high impedance energy harvesters (hybrid harvesting) such as thermoelectric generator (TEG), vibrational energy harvester (VEH), or micro photovoltaic cell (PV). The energy harvester can be either connected externally or integrated in the house of the node. So far, we have tested the following EH solutions: external piezoelectric VEH (Midé), metal- and Si-substrate-based MEMS VEHs developed in our lab, external electromagnetic (EM) VEH (Revibe), external TEG, and integrated micro-TEG (TEC-Microsystems). We have found that the applicability of the energy harvesters depends on the working environment. In case of a vibrating sensor location, having a fix characteristic resonance frequency and sufficient acceleration (a>100 mG), EM-VEH is a reasonable choice. At lower peak acceleration but sufficient temperature gradient between a hot surface and the ambient (e.g T_{surf}-T_{amb}=60-20 °C) deployment of a TEG, even an integrated one, is a feasible option

to cover the average power need of 1 mW for the sensor node. In bright external locations and even in well illuminated indoor places PV cells overperform all other EH solutions.

The third PCB level is responsible for the RF communication. In consists of a purpose designed RF circuit and a PCB antenna. In order to minimize the ratio of the required energy and the bit size of the transmitted data, we have developed a new RF communication protocol. In our patent pending solution the transmitted data and the sensor identifiers are encoded in the time delay between short on-state pulses. Hence, very low average power can be obtained at a reasonable broadcasting intensity.

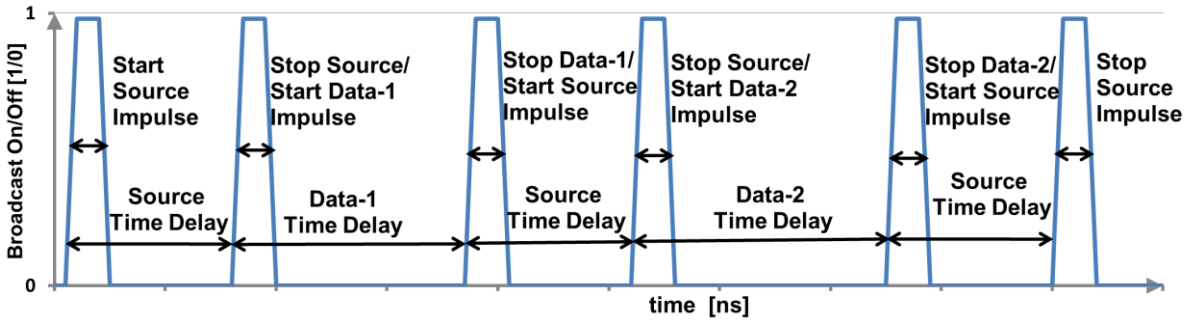

Figure 4.14. *Schematic illustration of the time-domain encoded transmission of two data items.*

The obtained sensor data are collected and encrypted by a receiver which was design by BHE Bonn Hungary Electronics. Here, the power consumption is not critical anymore and covered by the Power over Ethernet (PoE) line of the UTP cable. In our network configuration one receiver can collect data from 32 sensor nodes and transmits the encrypted signals into the cloud through a PC.

The validation of the system was carried out by an electromagnetic shaker setup in our lab and will be continued in operational environment (TRL7) in the near future. We think that developed system can be a useful stand-alone solution for long-term monitoring of machine condition. Moreover, it can trigger new applications for condition monitoring of various civil infrastructures such as highways and bridges.

Wireless environmental radiation monitoring system – DOZINET 2.0 - Recent developments

NVKP_16-1-2016-0018 "KoFAH"

E. Tunyogi, J. Volk, A. Hirn

In the frame of the DoziNet project, initiated in 2019, it was demonstrated that the radiation detector system, developed by the Space Research Laboratory for sounding rocket experiments, can be combined with the communication protocol developed by the Nanosensors Lab. The primary objectives of the 2nd phase of the project (DoziNet 2.0) in 2020, were to make the DoziNet unit more compact, to extend the existing network of Geiger-Müller (GM) probes of the KFKI Campus with 5 new relocatable DoziNet units and to optimize the system for radiation protection vehicle (DoziMobile).

The concept behind the development was to provide uniform mechanical design for the different applications and also uniform electronic design with optional modules to be implemented when required. Requirements were to be compatible with passive/active GPS antenna, communication through USB (laptop connected directly to the unit), GSM or LoRaWAN, power supply from batteries, optionally solar cells, or mains electric power, integral data storage with subsequent data download and real-time data visualization.

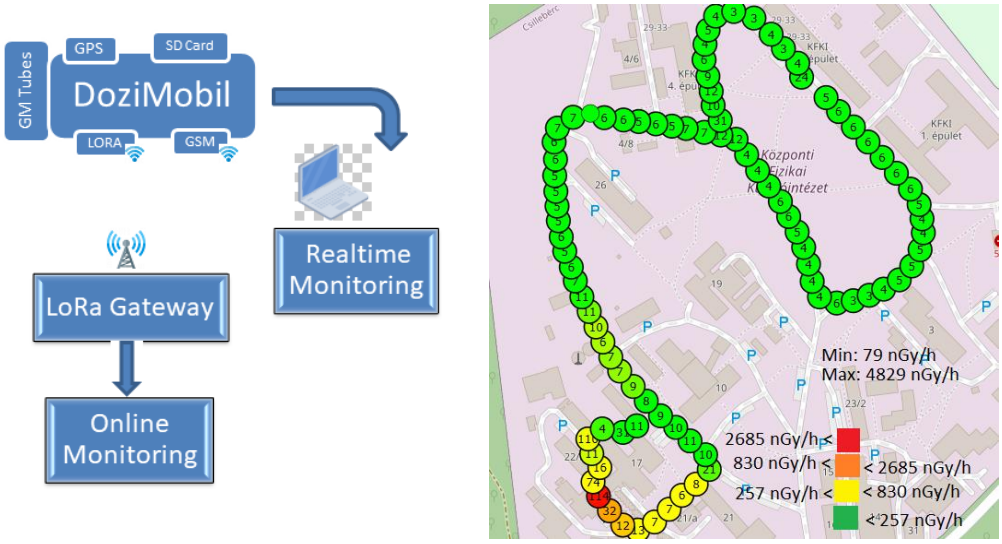

Figure 4.15. *DoziMobile/DoziNet system design (left) and the dose rate mapping measurement at the KFKI Campus using the DoziMobile unit – autoscaling visualization mode*

The prototype of the DoziNet/DoziMobile instrument was manufactured. Operation of the DoziMobile was demonstrated in an environmental dose rate measurement at the KFKI Campus (Fig. 4.15). The results of the car borne survey were in good agreement with former measurements carried out by manual measurements on site. Sampling rate, data collection frequency and alarm levels could be set by the user. Preset color coding and autoscaling are both implemented in the visualization module of the software. Results of the study on the use of DoziMobile in Nuclear Accident Prevention and Protection are documented.

Substrate effects on gold nanoparticle plasmon resonance scattering intensity and radiative damping

OTKA FK128327

Zs. Zolnai, D.P.Szekrényes, D. Zámbó, A. Deák

Substrate properties might significantly influence the scattering spectra of supported plasmonic nanoparticles (NPs) because of different radiative and non-radiative damping mechanisms. In general, the material of the underlying substrate highly affects different damping terms and scattering intensity. Besides nonradiative surface damping and chemical interface damping, to date less attention was paid to radiative damping, despite the fact that it may have significant contribution to overall damping of the surface plasmon resonance (SPR). Also this term strongly depends on the local environment of the NPs, e.g., the dielectric properties of the underlying substrate, and has fundamental impact on the far-field scattering intensity of SPR. The scattering intensity of NPs is important factor in different applications like nanosensorics and surface enhanced Raman scattering (SERS). In this work we investigate radiative damping and scattering intensity of the SPR of individual gold nanorods (NRs) and nanospheres (NSs) deposited on silicon and glass surfaces to follow substrate mirror charge induced changes to plasmon resonance properties. We apply dark-field single-particle scattering spectroscopy correlated with field emission scanning electron microscopy (FESEM) as characterization technique.

Fig. 4.16. shows single particle scattering spectra of a gold NS and a gold NR deposited on Si substrate. The scattered intensities for each SPR peak can be well fitted with a Lorentzian oscillator model with three characteristic parameters, the FWHM, resonance peak position, and spectrum height (scattered peak intensity).

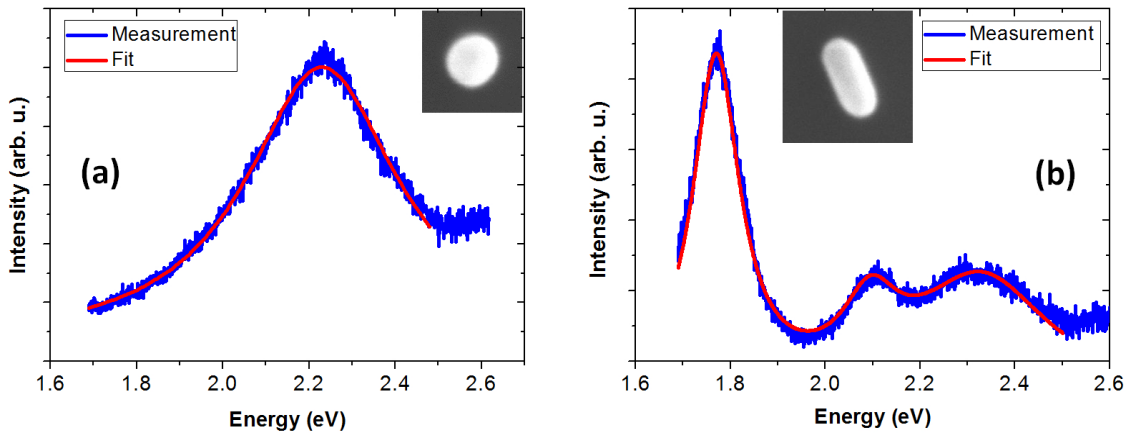

Figure 4.16. *Single particle dark-field scattering spectra of (a) a gold nanosphere with diameter of 53 nm and (b) a gold nanorod with size of 85×38 nm, deposited on Si substrate, respectively. Red lines show Lorentzian fits for the transversal surface plasmon resonance mode of the NS and for the longitudinal (at 1.78 eV) and transversal (at 2.25 eV) modes of the NR. Insets: FESEM micrographs of the nanoparticles.*

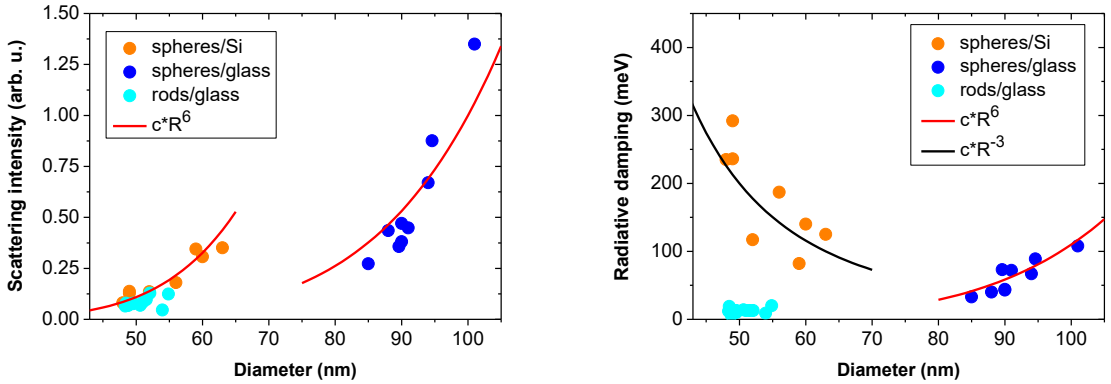

Figure 4.17. a (left) *Dark field scattering intensity of the SPR of individual gold nanospheres and nanorods deposited on Si and glass substrates vs. particle diameter.* ***b (right)*** *Radiative damping of the SPR of individual gold nanospheres and nanorods deposited on Si and glass substrates vs. particle diameter. For nanorods an effective particle diameter is considered*

As Fig. 4.17.a shows, for NSs on both Si and glass substrate the scattering intensity follows the expected R^6 trend, where R is particle radius. In case of the Si substrate almost an order of magnitude higher scattering intensity can be observed compared to glass. This is because in Si, thank to its high dielectric constant, a much stronger mirror charge dipole appears than in glass. Also, for Si NSs a constructive interference, due to strong surface reflection from the Si/air interface, amplifies the local polarizing electric field at the position of the particle, and thus the overall scattering intensity is enhanced. For glass the poor reflection plays minor role in scattering intensity. Note, for NRs an effective radius is considered as $(R_1R_2^2)^{1/2}$, where R_1 and R_2 are the major and minor radii of the NR. NRs on glass substrate gives comparable scattering intensity as NSs on Si. However, for NRs the efficiency for detection is higher because in this case the dipole far-field scattering pattern is originated from the longitudinal SPR mode and its intensity maximum appears perpendicular to the sample surface, while for NSs on Si the transversal SPR mode maximum scattering intensity is oriented parallel to the substrate plane.

In Fig. 4.17.b the radiative damping term vs. particle size as evaluated from Lorentzian spectrum fits and FESEM analysis are shown. For NSs on glass, $\sim R^6$ dependence appears, similarly to the size dependence of scattering intensity. For the Si substrate, however, a decreasing trend can be observed which was semi-empirically approximated with an $\sim R^{-3}$ function. Such trend may be understood with detailed analysis of the strong distance (NP size) dependence of the mirror charge induced dipole–dipole interaction and surface reflection induced interference effects.

In conclusion, for large dielectric constant substrates, like Si, a much higher radiative damping and, consequently, higher far-field scattering intensity of the SPR resonance can been observed. Our experiments provide valuable information when noble metal NPs are applied in different plasmonic applications.

Microsystems Laboratory

Head: Dr. Péter FÜRJES, Ph.D., senior research fellow

Researchers:

- István BÁRSONY, member of HAS,
- Orsolya BÁLINT-HAKKEL, Ph.D., maternity leave
- Ferenc BÍRÓ, Ph.D.
- Csaba DÜCSŐ, Ph.D.
- Péter FÖLDESY, Ph.D.
- Péter FÜRJES, Ph.D.
- Zoltán HAJNAL, Ph.D.
- István RÉTI, Ph.D.
- Zoltán SZABÓ, PhD.

PhD Students:

- Anita BÁNYAI (ÓE Univ. Óbuda)
- Anita Zátonyi (University Pannonia)
- János RADÓ (ÓE Univ. Óbuda)

Engineers / technicians:

- György ALTMANN, technician
- Gabriella BÍRÓ, technician
- Tibor CSARNAI, electrical engineer
- Magda ERŐS, technician
- Petra HERMANN, bioengineer
- Róbert HODOVÁN, mechatronic engineer
- Csaba LÁZÁR, electrical engineer
- Margit PAJER, technician
- Zsuzsanna Brigitta SIK, bioengineer

The main goal of the Microsystems Laboratory is to research and develop integrated sensors and sensor systems, MEMS and BioMEMS devices fabricated by silicon or polymer micro- and nanomachining technology. The activity covers the characterisation, materials systems and technology solutions and the development of sensing principles. The application of micromachining technology enables the miniaturisation of sensing and analytical systems and integration of various functions of sample preparation, sensing, readout, actuation or communication, respectively. The laboratory is focusing on the development of mechanical, physical, chemical (and biochemical) sensors, functional micro- and nanofluidic devices, implantable microsystems and infrared LED.

Our medium-term goal is to broaden the spectra of perspective research topics of MEMS systems and to develop a systematic organisation and form a dynamic and growing research group in the Microsystems Laboratory. Considering the financial environment our research directions fit to the European and Hungarian strategic roadmaps and directives (S3 - National Smart Specialisation Strategy) by the following research topics:

- Healthy society & wellbeing: BioMEMS, Lab-on-a-Chip, Organ-on-a-Chip, microfluidic systems, implantable, wearable devices, personal medicine, continuous monitoring, etc.
- Vehicle technologies: Driving safety sensors
- Clean and renewable energies: Low consumption electronics, sensors for energy industry, characterisation photovoltaic systems,
- Sustainable environment: Environment safety sensors (water monitoring), gas sensors (smart home, smart clothes)
- Healthy food: Food safety sensors, spectroscopy

Research group structure in the Microsystems Laboratory

The development of MEMS devices requires solid design capacity and advanced cooperation among the research and technical staffs for precise operation of the full micromachining fabrication line. Actually, 9 researchers, 7 engineers / PhD student and 4 technicians work for the Laboratory with close and flexible cooperation with the colleagues of the Nanosensors Laboratory.

- **MEMS / smart sensors (Csaba Dücső, Ferenc Bíró, János Radó):** The team's primary expertise is traditional MEMS sensor development, such as gas, environmental and mechanical sensors with an emphasis on the technology of 3D microstructure implementation.
- **BioMEMS, medical applications (Péter Fürjes, Csaba Dücső, János Radó):** Silicon based sensor development and their electro-mechanical integration, specifically for medical applications, are the long-term goals in this topic. The medical field demands the development of tools in low numbers that have extensive added value, which also aligns with the European strategic directives. The topic includes Si and flexible integrated microstructure development as subcontractors in the National Brain Programme.
- **Lab-on-a-Chip / Organ-on-a-Chip (Péter Fürjes, Anita Bányai, Orsolya Hakkel):** The Lab-on-a-Chip and Organ-on-Chip systems are essential building blocks of Point-of-Care diagnostic tools in the medical field. We have vast experience in this topic, especially in microfluidics. Accordingly, we actively collaborate with companies in this field (77 Elektronika Kft., Diagnosticum Zrt.) as well.
- **IRLED (Zoltán Szabó, Ferenc Bíró, István Réti):** We fabricate and develop a few thousand infrared LEDs per year (partners: Anton Paar, Senop). Additionally, we envisaged a larger scope spectroscopic development and application in the frame of an actual ECSEL grant. Environmental analytics and food safety applications could be important goals for IR spectroscopy and other optical developments.
- **Integrated systems / Heterogeous integration /IoT (Péter Földesy, János Márk Bozorádi):** Research grants ask for a certain level of preparedness, which usually includes demo systems (sometimes prototypes). Therefore, the requirements of developed instruments and their electro-mechanical integration are becoming a greater task.
- **Technology, FEM / Multiphysics Modelling (Zoltán Hajnal):** Modelling, such as digital twin, is a widely applied method in engineering practice. It speeds up development and manufacturing time of prototypes while also lowering costs. The application of these methods is not as straight forward for the development of microstructures due to the effects of microenvironments. However, the use of these simulations is indispensable. The group is effectively corroborating the research and development tasks.

Infrastructure and technological competencies

This is a unique infrastructure in Hungary accordingly its sustainable operation and development is strategic goal. The infrastructure is open for academic and industrial partners to realize complex, purpose-designed microsystems, nanocircuits, as well as Lab-on-a-Chip devices.

The high-tech microtechnology related fabrication and characterisation systems work in a class 10 cleanroom facility. The laboratory is dedicated for 3D processing of 3" and 4" Si / glass / polymer substrates with maximal resolution of 1μm, together with lithographic mask manufacturing. Electron beam lithography and focused ion beam (FIB) milling are also available with resolution of 20nm. The structural design and development are also supported by multi-domain Finite-Element Modelling (FEM), and process simulation. Wide spectra of characterisation techniques are also available: optical (fluorescent) and electron microscopy (SEM and EDS), atomic force microscopy (AFM), profilometry, optical and electrical measurements, electrochemical impedance spectroscopy, microfluidic characterisation, mechanical vibration and climate test chambers, UV / VIS / IR / FTIR spectroscopy, etc.

Available micromachining techniques:

- Patterning – mask design, laser pattern generator, photolithography, (double side) alignment, electron beam lithography (E-Beam), Focused Ion Beam processing – FIB milling, nanoimprinting

- Structured polymer layers – PMMA, PI, SU8 patterning, micromoulding, soft lithography – PDMS
- Wet chemistry – chemical wafer cleaning, isotropic and anisotropic etching techniques
- Dry etching – deep reactive ion etching, plasma etching techniques (DRIE, RIE)
- High temperature processes – thermal oxidation, diffusion, annealing, rapid thermal annealing (RTA)
- Physical thin film depositions – Thermal and electron beam evaporation, DC and RF Sputtering
- Chemical thin film depositions – Atmospheric and Low Pressure Chemical Vapour Deposition (CVD, LPCVD, LTO), thermal and plasma enhanced Atomic Layer Deposition (ALD)
- Liquid Phase Epitaxy of III-V compound semiconductors (LED manufacturing)
- Wafer bonding – Si-glass, glass-glass, polymer-glass anodic and thermal bonding
- Chip dicing, wire bonding especially for sensor applications
- Special packaging techniques and methods

In the frame of the project grant "VEKOP-2.3.3-15 – Modernisation of the microtechnological infrastructure to achieve European compatibility" a new oxidation / diffusion furnace was installed in the cleanroom. The Thermco TT2000 J155 furnace is equipped with four tubes and enable to elaborate high quality processes to deposit electronic grade silicon-oxides.

Figure 5.1. *Thermco TT2000 J155 oxidation / diffusion furnace system was installed in the cleanroom.*

Cooperations

Apart from the European and bilateral international R&D projects wide cooperative and knowledge network was established by the large number of joint research projects with Hungarian research centres (ATOMKI, BME, PPKE, SE, SZBK, PTE, WIGNER, SZTAKI) and research groups to perform interdisciplinary research. We are supporting the National Quantum Technology Programme (HunQuTech) and the National Brain Programme by our infrastructural background. Besides the scientific projects, the Lab offers technology development services, with these industrial partners (SEMILAB, Diagnosticum, 77 Elektronika, CellSorter, Mirrotron, Z-Microsystems (Austria), Anton Paar (Austria), Senop (Finland), FRK (Poland), Philips (The Netherlands)) the higher technology readiness levels are also achievable (TRL 2 → 6).

The technological and scientific results are directly transferred into the higher education, by means of several lectures, laboratory practices, TDK, diploma and PhD works. Our researchers give lectures at various departments of BME, PPKE, ÓE, DE, ELTE.

Major research projects

The researchers of the Microsystems Laboratory are involved in development, fabrication and integration micro- and nanosystems, sensor structures to open new perspectives in the field of medical diagnostics, Minimal Invasive Surgery techniques, energy-efficient autonomous systems (sensor networks, autonomous driving). Our interest covers the topics of optical analytics (spectroscopy), environmental and safety (gas detectors) sensors.

- A pilot line for the next generation of smart catheters and implants – POSITION-II, ECSEL 2017-2-783132
- Accelerating Innovation in Microfabricated Medical Devices – Moore4Medical, ECSEL Innovation Actions (IA), Call ECSEL-2019-1-IA
- Low power consumption-type nano-sensors for gas detection in harsh environment – Hungarian-Russian Collaborative Research Program - 2017-2.3.4-TéT-RU-2017-00006
- Development of the microtechnology infrastructure to achieve European compatibility - VEKOP-2.3.3-15-2016-00010
- Development of Rapid Urine Bacteria Analyzer – VEKOP-2.2.1-16-2017-00001 – „Versenyképességi és Kiválósági Együttműködések"
- Investigation of novel implant materials for high-resolution, multiparametric imaging of cortical activity, OTKA K 120143
- Understanding the impact of nanostructuring to control neural cell - solid surface interactions at brain-machine interfaces, OTKA NN 116550 (participant)
- Low-dimensional nanomaterials for the optical sensing of organic molecules on liquid and gas interfaces - OTKA K 131515 (participant)
- IR spectroscopy of extracellular vesicles: from exploratory study towards IR-based diagnostics – OTKA K 131594 (participant)
- Thin film integrity check by capillary bridge test – OTKA FK 128901 (participant)

Scientific cooperation:

- Development and manufacturing microfluidic systems in the project "Application chiptechnology for improvement the success of human in vitro fertilisation – GINOP-2.3.2-15 Stratégiai K+F műhelyek kiválósága" for University of Pécs
- Manufacturing optrode devices applied in the NKP_17 „National Brain Programme" - 2017_1.2.1-NKP-2017-00002 for Pámány Péter Catholic University

Industrial cooperation:

- Development and optimisation polymer based autonomous microfluidic cartridge, its production technology and measurement methodology for high sensitive Point-of-Care detection of cardiovascular blood biomarkers for 77 ELEKTRONIKA Ltd. (subcontraction)
- Development CVD technology and equipment for deposition low roughness polycrystalline Silicon layers for MIRROTRON Ltd. (subcontraction)
- Development and maufacturing microstructured Silicon injection moulding insert for Z-MICROSYSTEMS GmbH (subcontraction)
- Development and manufacturing specific calibration test samples for characterisation methods of semiconductor industry for the SEMILAB Co.
- Development and manufacturing Near InfraRed LED devices for spectroscopic applications for Senop Ltd. (Finland)

Low power consumption-type nano-sensors for gas detection in harsh environment

2017-2.3.4-TéT-RU-2017-00006

F. Bíró, Z. Hajnal, I. Bársony, Cs. Dücső

The ultimate goal of the project is to develop a novel calorimetric gas sensor family what is able to detect CH_4, NH_3 and CO up to their lower explosion limits (LEL), i.e. 5, 15 and 12,5 %, respectively. The sensors can be operated in harsh environment without any risk of ignition even over LEL concentrations. Apart from the optical and electrochemical approaches and the corresponding systems, there are two viable solutions, both exploit temperature changes and read-out by:

- measuring the temperatures of a heated catalyst surface and a passive reference,
- measuring the temperatures of a filament exposed to gas environment and a perfectly sealed reference heater.

Although the catalytic device is expected to detect lower gas concentration and exhibit better sensitivity, the second, heat-conductivity type device is simpler and still in use in practice. A more sophisticated device applies both sensors, thereby extending the detection range and improves the detection reliability. Another advantage is the commonly used filament or micro-hotplate structure. Therefore, to develop a micro-hotplate meets all the mechanical, electrical and chemical requirements is essential for a reliable and commercialized device.

The geometry of the Pt filament hotplate is finalized, and the performance is tested. Almost ideal temperature uniformity could be achieved: non-uniformities at the planned 540°C (slightly below the Hüttig temperature of Pt) operation temperature is <±2.5 °C. The stability of a microheater Wheatstone-bridge pair is ~1% in one-year long operation. This is a principal requisite in the sensor operation. The hotplate can be operated even at higher temperature for a few tens of hours. The temperature non-uniformity is less than ±8 °C at 800°C. Two versions of chip and the corresponding ceramic package designs were accomplished. A Utility Model Protection was submitted to protect the device layout [Ref. 5.3]

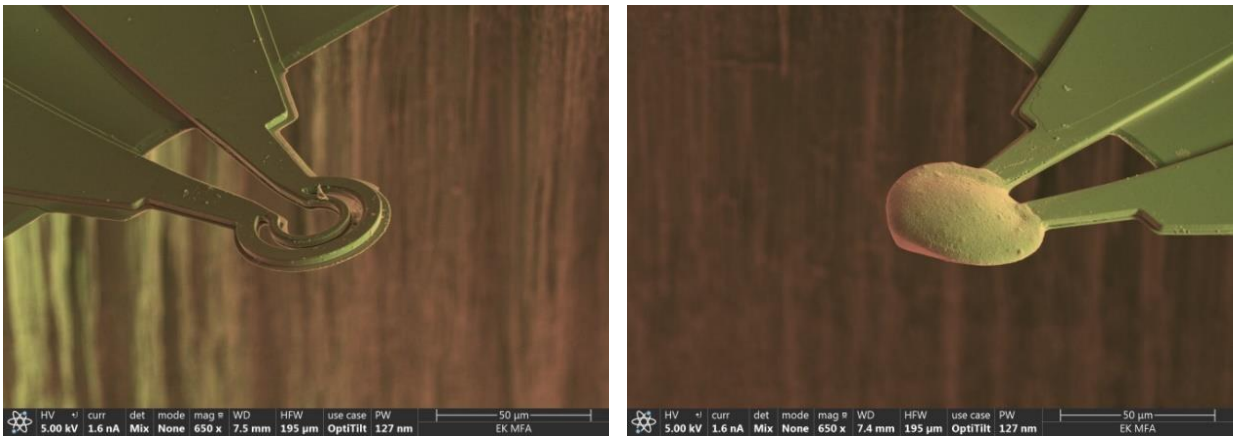

Figure 5.2. *SEM views of the bare c-Si cantilever heater (left - artificially coloured. One filament is coated with catalyst (right) to demonstrate the bead formation possibility.*

The first version of the c-Si microfilament heater was also fabricated and tested (Fig. 5.2). Contrary to the Pt filaments, the electromigration effect doesn't govern in the degradation of the c-Si heater. However in view of the long term stability its oxidation must be considered. Therefore, by coating the c-Si micro-heaters with the chemically passive suspension (Fig. 5.3) we tested the filament performance. Knowing the barrier properties of the stoichiometric silicon-nitride we have to calculate only with the back-side oxide layer for the further oxidation of the filament. The lowest temperature in the available models for Si oxidation is 700°C. At this temperature the Si consumption by the oxide growing is ca. 240nm pro year. That means a maximum 12% increase of filament resistivity. Nevertheless, the targeted operation temperature is 450-550°C only, thereby we figure on less than 3% change in resistivity. Preliminary measurements seem to confirm this expectation. Considering similar changes in the active and the passive elements of the Wheatstone-bridge configuration we think that the filament characteristics will meet the required sensor parameters. Note that the open-side chip construction facilitates the deposition of the catalyst/reference material beads. The depositions were done manually, but the process can be automated on need. The ongoing process development is aiming at the further development of the stress related issues and optimizing the resistance and passivation of the c-Si filament. [Ref. 5.1, Ref. 5.2]

Design and development of a 3D Flex-to-Rigid compatible force sensor

H2020-ECSEL-2017-2-783132 "POSITION-II", 2018-2.1.6-NEMZ-ECSEL-2018-00001

J. Radó, L. Illés, P. Fürjes, Cs. Dücső

The main objective of the POSITION-II project is the realization of a pilot line for the fabrication of the next generation of smart medical instruments. This second generation of smart medical instruments offers improved performance through better sensors and transducers combined with an improved manufacturability and lower cost. The task of our research group is to develop and demonstrate the applicability of a capacitive force sensor integrable in the tip of an electrophysiological catheter.

In the first period of the project we designed and constructed capacitive type force sensors exploit the signal of capacitances with elastic PDMS dielectric. Thereby, following the original plan to have an alternative path in the development, we adopted the Philips' surface micromachined cavity type capacitor technology (CMUT - capacitive micromachined ultrasonic transducer) to form force sensor. During the preliminary measurements, we successfully demonstrated the feasibility of the air-gap type capacitors, i.e. the Philips' CMUT elements for detecting the force (Fig. 5.3.a). On the basis of the promising results we jointly designed and fabricated a six element circular capacitor array chip. The chip was processed by the standard CMUT technology of Philips and the appropriate assembling technique was elaborated at EK-MFA. We directly mounted a semi-sphere PDMS bumper on the top of the 2.7mm diameter transducer array, containing 6 blocks of the capacitive sensing elements (Fig. 5.3.b). In functional testing we used our dedicated the semi-automatic system we had developed earlier.

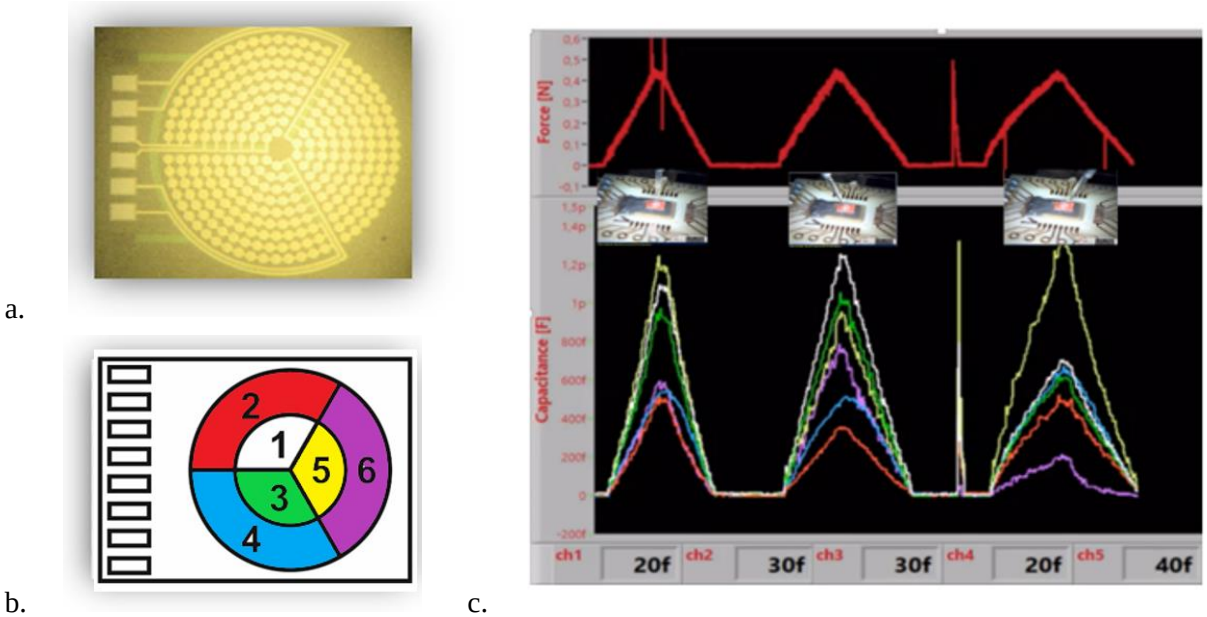

Figure 5.3. *The CMUT transducer array (a), the representation of its 6 sensing blocks (b) and the signals of the six elements (c) responding to the forces loading from three characteristic directions indicated in the insets.*

The functionality of the sensor was tested by touching the highest point, i.e. the centre of the semi-sphere bumper was loaded normally and from 12 different directions in the chip plane (with increments of 30°). In

each directions four angles, 10, 20, 30 and 45^{o} to the normal vector were applied. The first demo clearly shows how the signals of the 6 elements depend on the loading direction and the magnitude of the force. Fig. 5.3.c represents the responses of the 6 segment device for three characteristic loadings.

Practical applications require reliable and quick feedback as well as an informative representation of the loading parameters. Considering the complexity of the structure, i.e. the elasticity and the coupled force propagation inside the bumper, purely analytical retrieval of the load components is impossible. Nevertheless, the needed information can be revealed by the adaptation of a regression method or training neural networks. Consequently, a large number of the read–out signals has to be collected and processed, in our case response data of 12 x 4 + 1= 49 loading directions were collected. In each direction the responses on loads between 0-500mN were measured. A neural network was trained by teaching the network with the responses of the central three, the outer three and using the signals of all the six capacitor blocks. The signals of all the six or the outer three capacitors were considered, a perfect correlation (min. 99%) was found for all the three vector components.

Manufacturing implantable microelectrode arrays

OTKA K120143, 2017-1.2.1-NKP-2017-00002 National Brain Research Programme 2.0, OTKA NN116550

A. Zátonyi, Á. Horváth, A. Pongrácz, Z. Fekete

In collaboration with the PPKE ITK Research Group for Implantable Microsystems polymer and silicon based microdevices were fabricated using micro- and nanomachining processes. A 32-channel polyimide intracranial EEG array (Fig. 5.4.) was prepared for long-term use in pharmacological experiments in rodents. The effect of an anesthetics, ketamine on the functional connectivity of the rat cortex was revealed and related methodology was published. [Ref. 5.4]

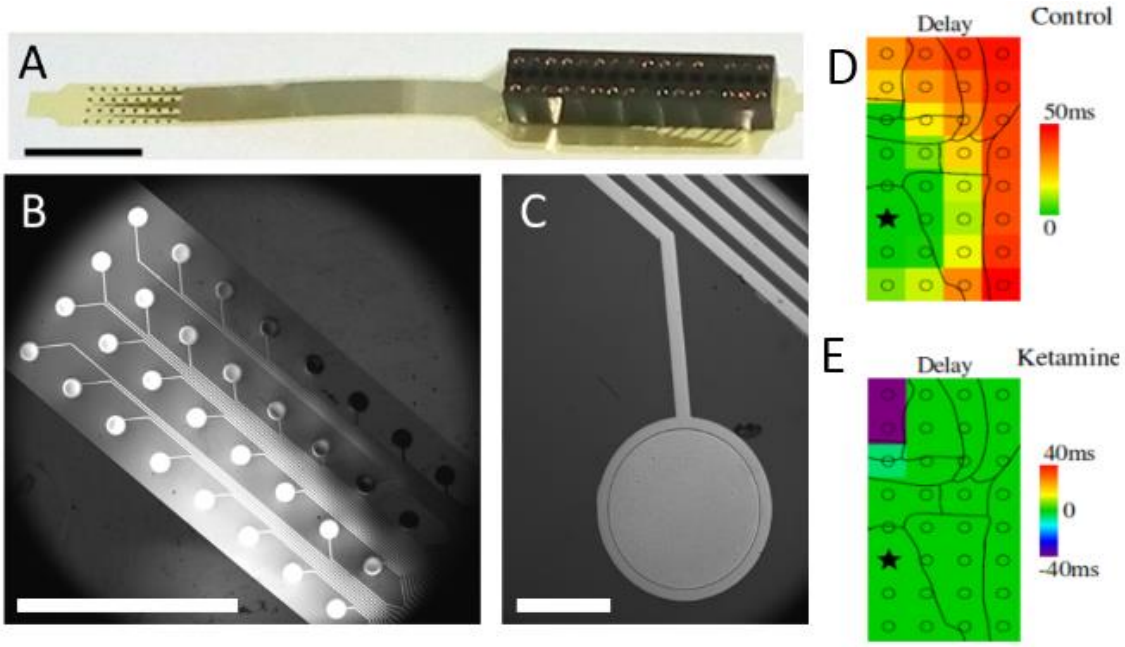

Figure 5.4. *Photo of the ready to use microECoG array. Close microscopic view on a 32-channel sensor array (a) and on a platinum recording site (b, c). Scale bars show10 mm, 0.5 mm and 150 µm, respectively. Delays in the propagation of visually evoked cortical response without ketamine (control) (d). Signs of propagation cannot be identified after ketamine treatment (e).*

The lab contributed to the characterization and in vivo testing of a multimodal implantable optical actuator (see Fig. 5.5.), which comprises of monolithically integrated infrared waveguide, a temperature sensor and electrophysiological recording sites. Artefact-free recording of the neural activity evoked through infrared excitation was demonstrated and published by the research group. [Ref. 5.5]

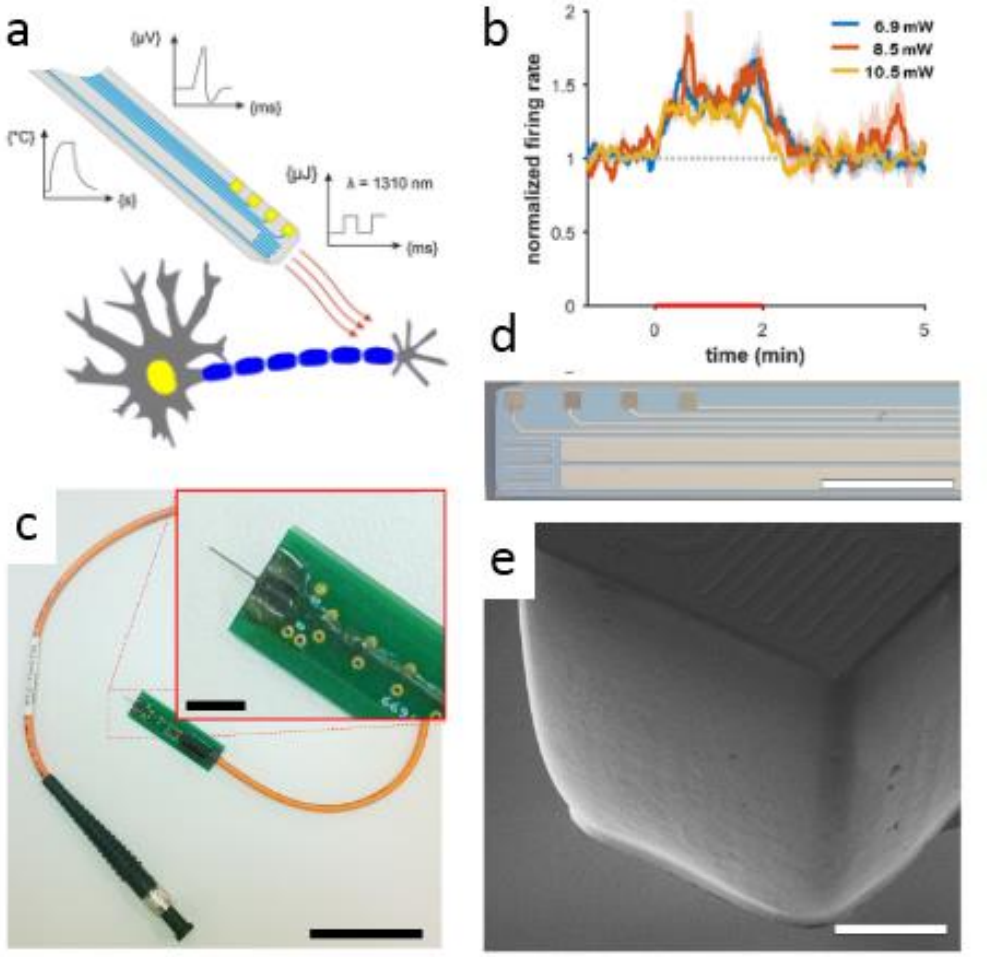

Figure 5.5. *Operation of the multifunctional probe chip designed to deliver infrared light into the neural tissue and monitor electrophysiology concurrently. (a) Representative cellular response in the cortex to IR stimulation at various input optical power. (b) Photo of the ready-to-use device and top (c-d) and SEM (e) view of device tip holding the electrical and thermal sensors.*

Polymer based autonomous microfluidic systems for medical diagnostics

GINOP-2.3.2-15 „Stratégiai K+F műhelyek kiválósága - Chiptechnológia alkalmazása a humán in vitro fertilizáció eredményességének javításában”

A. Bányai, P. Hermann, O. Hakkel, P. Fürjes

Precise and fast PoC monitoring of marker molecules or bacteria levels in body fluids or cell culture media could be crucial in effective diagnostics and choosing therapies. Due to the specific tools and novel microtechnology processes the cost-effective, complex but miniaturised analytical systems, such as Lab-on-a-Chip (LoC) and microfluidic devices have become available and applicable for implementing the overall sample analysis from the preparation to the molecular detection. The microfluidic system has to transport the sample and the washing buffer to the active area of the chip meanwhile mix and incubate the sample with the reagents. As the incubation and read-out needs a specified time, precise sample handling and flow control are crucial. The perspective of our work is to develop a polymer based microfluidic cartridge suitable to autonomously controlled sample transport or preparation for integrated bioanalytical device.

To define precise sample flow rates in the microfluidic systems adequate surface modification and macro and microscale structuring of the geometry are crucial. Accordingly the applicability of different surface modification methods were analysed with special consideration of the long term stability of the surface properties as contact angle, roughness, non-specific binding of biomolecules and labelling nanoparticles. The modified surfaces were characterised by surface contact angle measurements, FTIR (Fourier Transform Infrared Spectroscopy), AFM (Atomic Force Microscopy), spectro-ellipsometry (Fig. 5.6).

In a previous project (Multiparaméteres Point of Care in vitro diagnosztikai rendszerek fejlesztése) an autonomous microfluidic system was designed and manufactured for transporting blood or plasma by precisely controlled sample rate. These autonomous sample transport systems were integrated into Point-of-Care Lab-on-a-Chip based diagnostic devices. The developed systems are to be applied for detection cardiovascular diseases in cooperation with 77 Elektronika Ltd. Based on these results we are developing **Lab-on-a-Chip based diagnostic device** for a specific project of the University of Pécs dedicated to support **human in-vitro fertilisation** with the 77 Elektronika Kft. In the actual period the geometry of the microfluidic systems was finalised according to the additional requirements of the optical detection method and the real sample. Accordingly, a new actualised microfluidic structure was designed (see Fig. 5.7) to be compatible with the applied bioanalytical specifications (targeted detection limits, surface blocking, etc.).

The material composition of the pre-industrial / laboratory stage cartridge was optimised according to the required sample flow rate, the optical and mechanical properties. The microfluidic cartridges were fabricated in adequate volume (400pcs) for supporting the pre-clinical study of the diagnostic method. During the project a specific chip-diagnostic equipment was developed for supporting the successful classification of the embryonic viability. This cooperative research supported the establishment of the National Laboratory for Human Reproduction at PTE and assured the further improvement of the scientific and innovative results towards commercialisation. [Ref. 5.6-5.9]

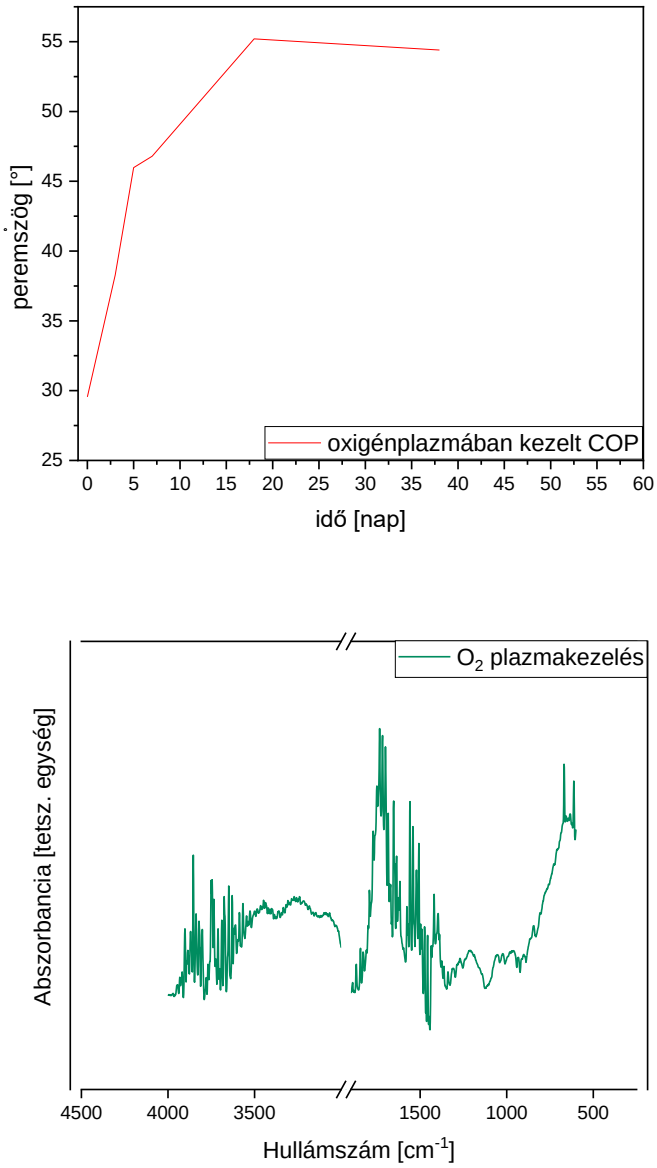

Figure 5.6. *Long-term stability of the surface contact angle (left) and FTIR spectra of oxygen plasma treated COP (cyclo-ofefin-polimer) surfaces.*

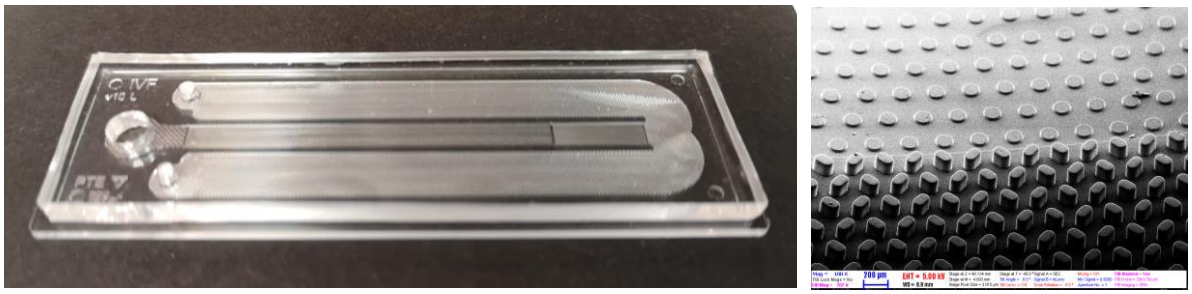

Figure 5.7. *The autonomous microfluidic cartridge proposed for transport culture media applied in human in-vitro fertilisation (left) and its microstructure (SEM image).*

Microfluidic sample preparation system for rapid urine bacteria analysis

VEKOP-2.2.1-16-2017-00001

A. Bányai, P. Hermann, Zs. B. Sik, O. Hakkel, P. Fürjes

The goal was to develop a **single-channel microfluidic cartridge** for certain subtasks of **sample preparation and handling**, which then can be integrated into a measuring instrument. During the optical measurements of bioanalytical tests, the sample handling is solved in an integrated Lab-on-a-Chip cartridge. The cartridge includes transport and filtration of the liquid sample, positioning of bacteria in the detection chamber over the sensing layer, and a microfluidic component for storage of used sample. Accordingly, we focused our attention to develop a **passive hydrodynamic unit** that is capable of filtering larger elements (>6µm in diameter) in **urine samples** and positioning permeated bacteria laterally. In order to achieve this goal, we designed and characterized such units. Simultaneously, single-channel cuvettes were made to test the optical system with the sample solution.

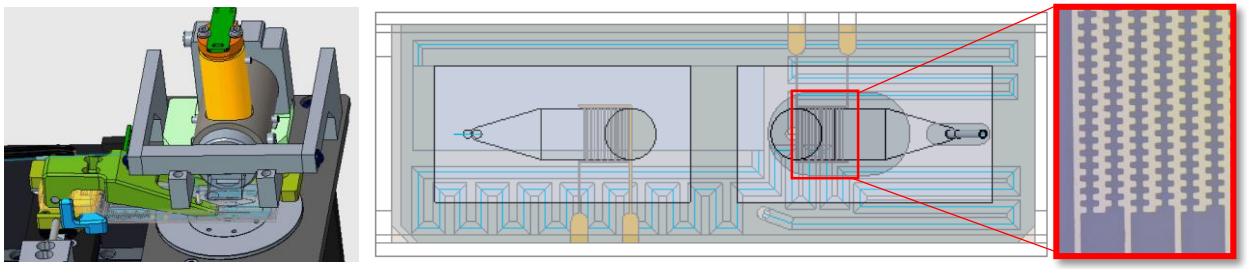

Figure 5.8. *The layout of the developed microfluidic cartridge with a high-resolution electrode network.*

As a part of a cooperative project, a complex microfluidic platform was further developed to fulfill essential functions, by making it capable for multiple target inspection, and compatible with laboratory instrument. For the proper operation of such device, a bubble-free channel upload had to be provided, by taking account the appropriate setting of the surface properties of the structural materials, and making a special design of the fluidic microstructure. At this stage of the development, the microfluidic cell was made up from the combination of two parts, and two materials, accordingly. The microfluidic channel was developed by soft lithographic method in PDMS (polydimethylsiloxane) polymer and the raw material was further modified by PDMS-b-PEO copolymer molecules, to ensure the hydrophilic properties of the walls. Development of appropriate hydrodynamic properties are also highly influenced by the microstructure of the channel; therefore, an investigation was made to study the effect of the microscopic structure of the channels on the capillary upload: different capillary structures were tested to optimize the bubble free-filling of the inlet section.

For the electrophoretic concentration of bacteria, metallization technology was used to develop a high-resolution electrode network on COP polymer film with the thickness of 100 µm. To manage the autofocus function for image processing system, the electrode design was further equipped with an additional pattern. The manufactured microfluidic compartments and COP foils the containing high-resolution gold electrodes, were then handed over to 77 Electronics for further measurements.

Hydrodynamic principle based microfluidic filters and lateral concentrating structures were developed and evaluated by their filtration efficiency for different particle sizes; and by the target loss ratio in the size range of bacteria. The development included the challenge to combine the previously separately tested fluidic units - crossflow filter and lateral focusing module into one integrated system. The implementation implicated the goal to determine the filtering and focusing efficiency, under different parameters. In addition to intensive parameterization, the behavior of the microfluidic system was tested by using artificial fluorescent beads with different sizes (diameter of 15.8 µm – 6.08 µm – 1.97 µm beads) and GFP-labeled E. coli.

Cross-flow filtration

In order to handle the liquid sample of the corresponding volume within limited time window, the application of crossflow type separation / filtration system proved to be beneficial. The crossflow system achieves a continuous mechanical filtration within a microfluidic environment. The size of the permeable particles determines the geometry of the microchannels, which then filters any particle that is larger in size. Moreover, the longitudinal arrangement allows larger sample volumes without clogging. After filtration, the composition of the filtrate was examined in a Bürker chamber and the filtration efficiency of each fluid architecture was estimated. Two type of filter arrangement were tested: the columnar-, and the weir type filtration. In case of columnar arrangement, significant filtration cake has formed on the inner surface of the filter by the reduction of the filter height. This prevented the smaller beads from passing into the filtrate, and caused a significant target beads loss (d = 1.97µm). In case of weir type arrangement, the filtration by using E.coli (conc. $3.9*10^6$ cell/ml), 94% of the target bacteria was recovered in the filtrate. By adding the target bacteria to the fluorescent bead mixture the target recovery dropped, although the formed filtration cake on the filter's surface did not completely prevent the infiltration of bacteria, merely increasing the resistance of the filter.

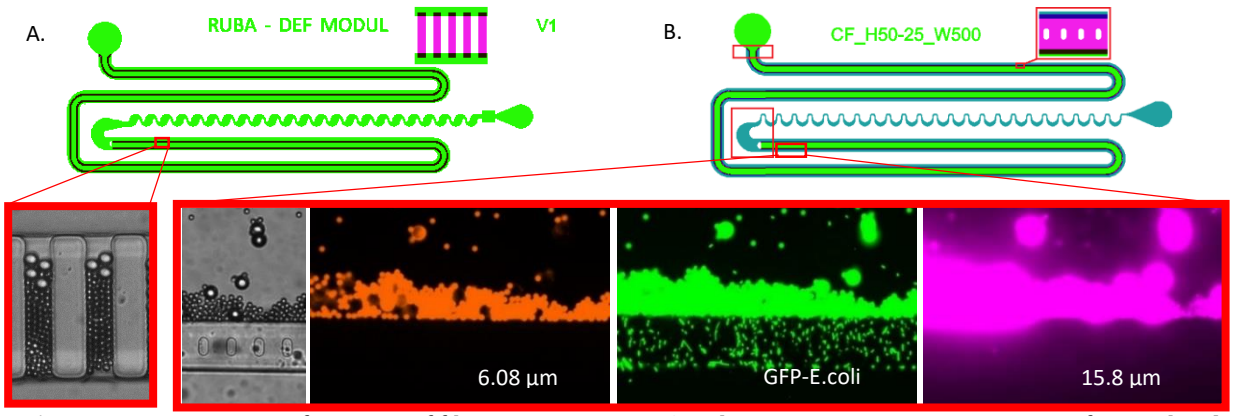

Figure 5.9. *Comparison of two type of filter arrangement: A.) Column type – microscopic picture of target bead loss (d=1.97 um). B.) Weir type – filtration of E.coli bacteria (green). Filter height – 5 µm.*

Lateral focusing

After filtering every larger component of the urine sample, the permeated bacteria must be vertically and possibly laterally focused in the detection chamber in order to achieve high trapping efficiency on the functionalized surface. The lateral focusing was achieved by a hydrodynamic method. The efficiency of the hydrodynamic focusing depends mainly on the characteristics of the fluidic system and on the particle to channel size ratio. The position of the particle within the flow profile is determined by forces acting on the particle in the fluidic system. The focusing was carried out in an asymmetric microfluidic system (see Fig. 5.9) with alternating geometric parameters. The concentration of target E.coli by flow is critical in the lateral focusing unit. By reducing the channel cross-section in the curved channel would help the lateral focusing of the bacteria, but also would enhance the required time of analyzing a given sample volume.

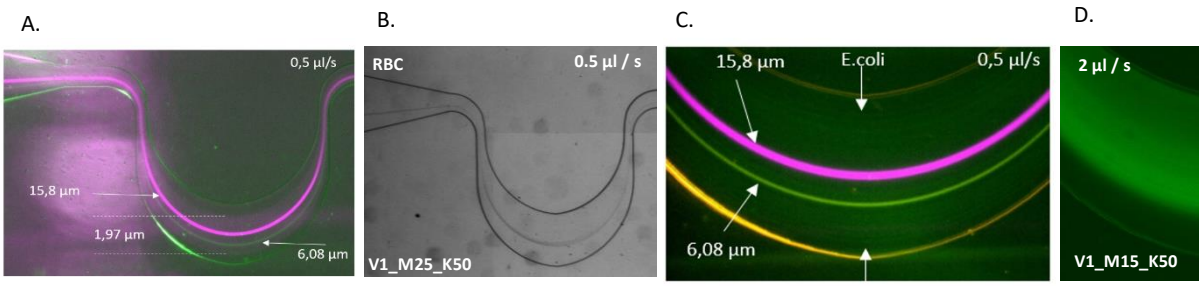

Figure 5.10. *A.) Lateral focusing of beads at 0.5 µl/s flow rate: 15.8 and 6.08 µm beads, and concentration of 1.97 µm beads at the end of the lateral focusing unit. B.) Red blood cells focused in the same structure at 0.5 µl/s flow rate. C.) E.coli could not be focused in the very same structure due to the stick shape: with 0.5 and 2 µm dimensions. D.) E.coli concentration at decreased channel height (15 µm), and increased flow rate (2µl/s).*

Hierarchically Combined Periodic SERS Active 3D Micro- and Nanostructures

R. Öcsi, Zs. Zolnai, I. Rigó (Wigner FKK), M. Veres (Wigner FKK), O. Hakkel, P. Fürjes

Raman spectroscopy is finding many applications in biology, life sciences and other areas. Raman scattering is inherently weak, but its sensitivity can be improved by implementing surface-enhanced Raman scattering (SERS). Surface Enhanced Raman Scattering (SERS) is applied to enhance the Raman signal by several orders of magnitude and significantly improve the sensitivity of the ordinary scattering method. As a result of the electromagnetic enhancement emerging in the vicinity of metallic nanostructures the sensitivity of molecule detection can achieve attomolar concentrations. This highly sensitive detection performance of SERS was utilized for analysing molecules located in the few nanometer distance or immobilised on the surface of nanoparticles trapped in a specially designed microstructure. By means of the effect efficient detection method can be developed for the analysis of low concentration biological samples assuming that sample transport and preparation system is also integrable.

To increase the local field intensity of Raman scattering, gold nanospheres were entrapped in gold coated periodic inverse pyramid structures, being SERS substrates by themselves. The applicability of this complex structure for sensitive molecule detection was proved by comparison of the detected Raman signals with and without particle entrapment. Moreover, its relevance in molecular diagnostic was also proposed considering the specific surface functionalisation of the gold nanoparticles.

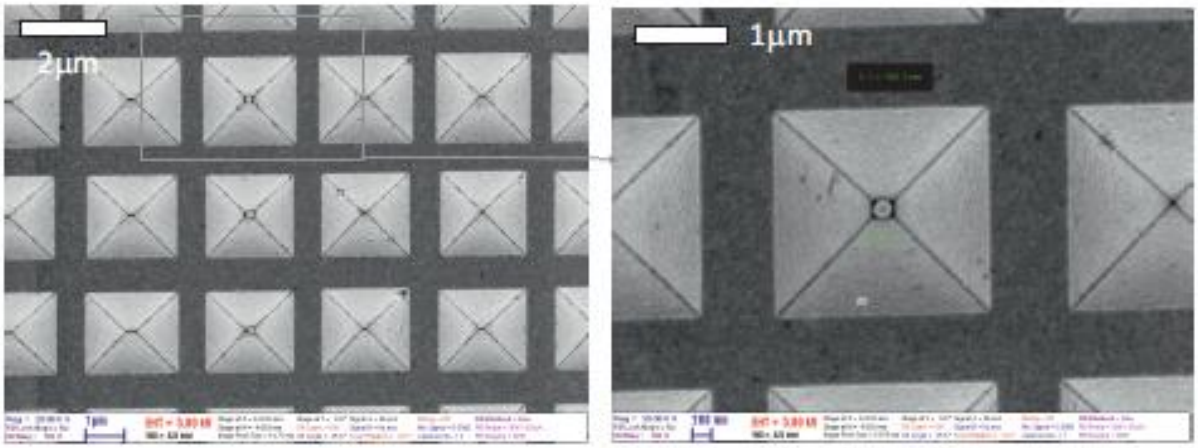

Figure 5.10. SEM images of the inverse pyramid SERS substrate with 200 nm GNPs located in some of the voids.

To understand the analytical performance, the near-field intensity distributions of inverse pyramid arrays were studied by FDTD simulations using the Lumerical FDTD Solutions v.8.15.736 software. Silicon was used as substrate material of the inverse pyramids with 150 nm gold coating, and periodically ordered gold nanospheres (50, 100, 200 and 250 nm diameter) were placed into the pyramids.

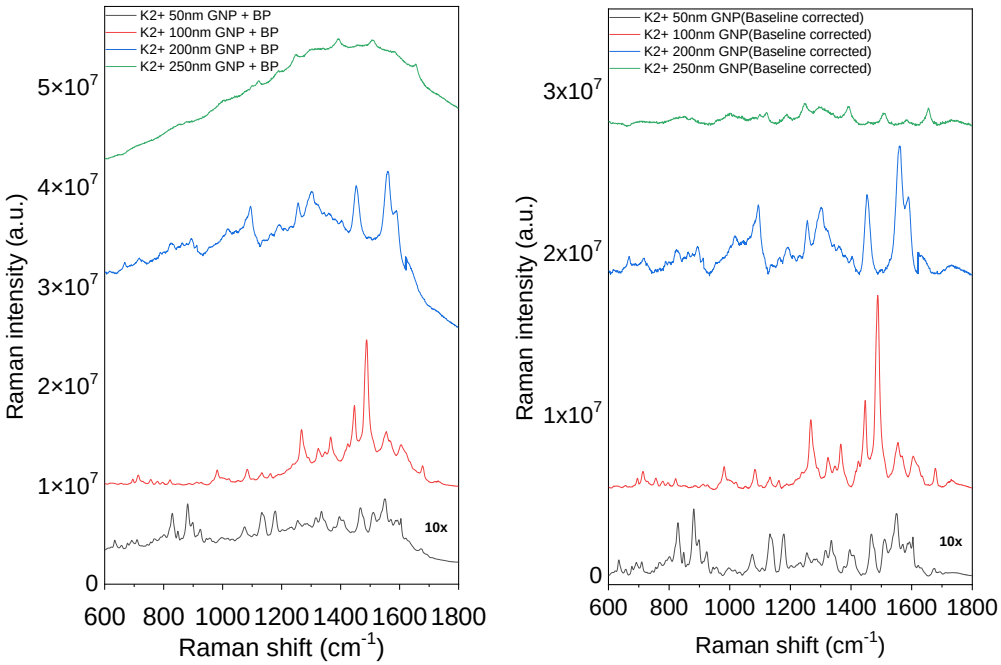

Figure 5.11. Raw (left) and baseline corrected surface enhanced Raman spectra of benzophenone solution dripped and dried onto inverse pyramid arrays entrapping a GNP of different size.

A remarkable increase of the surface enhancement has been observed in gold coated micron sized inverse pyramid after placing a gold nanosphere inside it. The amplification of both surface enhanced Raman and fluorescence signals was found to be dependent on the size of the gold nanoparticle, and the enhancement can be two orders of magnitude larger than that of the empty pyramid. The origin of the phenomenon was investigated by finite differential time domain simulations that showed that coupling of the electric field occurs when the nanosphere protrudes into the high intensity near-field region of the pyramid. The plasmon-related near-field enhancement was found to be concentrated into the gaps formed around the contact points of the curved sphere and the flat pyramid surface. [Ref. 5.10]

Development and small scale production of near infrared LEDs and LED based devices and their spectroscopic applications

ECSEL-2019-1-IA-876190 "Moore4Medical", 2019-2.1.3-NEMZ_ECSEL-2020-00005

F. Bíró, I. Réti, G. Battistig, Cs. Dücső, B. Beiler, Z. Szabó, P. Fürjes

Near infrared LEDs for spectroscopy

Infrared spectroscopy is a very popular measurement technique especially in food industry, pharmaceutical industry and agriculture for the detection and measurement of organic materials. The -OH, -NH and -CH functional groups found in organic substances can frequently be detected by spectroscopy through absorbance measurements at the resonance wavelength of valence-bond vibrations. The measured wavelengths are 4-2.5μm, while the signal to noise ratio of photon detectors is low due to thermal noise at room temperature. The 1st-3rd harmonic absorption bands are located in the range of the near infrared (NIR), where smaller signals can be measured effectively in practice. NIR LEDs have narrow range emissions; therefore, they are suitable for measurements at given wavelength. Further advantages of LEDs compared to incandescent lamps are their small dimensions, high efficiency, and low power consumption, which is critical in small handheld devices.

GaInAsP/InP is an ideal material system for the fabrication of double heterostructure devices as the emission wavelength is easily tuneable between 950-1650 nm. As InP has higher bandgap than the lattice-matched GaInAsP active layer the absorption losses inside the device structure can be minimized. In order to tune the emission wavelength of the LED, the composition of the semiconductor light-emitting layer has to be properly set. Our high quality single peak LED chips (1220nm) have a stable market with a sales value around 40kEUR in 2020. Our business partners are SENOP Oy (Fi) and Anton Paar Ltd. (At).

Marker molecule detection in Organ-on-Chip applications

The 3 year long international Moore 4 Medical project try to create the base of new open technology platforms which will accelerate innovations in various medical domains such as implantable devices, organ-on-chip, drug adherence, next generation ultrasound, towards x-ray free surgery and continuous patient monitoring. The consortium has participants from 12 countries and from around 90 companies and research institutes. One of the main task is to develop a smart multiwell plate system capable to work as an autonomous system with micropumps, microfluidic infrastructure that provide perfusion, as well as the electronics to drive the micropumps and integrated readout sensors. Our laboratory participates in designing the microfluidic layer of the smart well plate, development optical sensor module for the system with **integration of optical NIR spectral detectors**. We intend to develop near IR LED sources and spectroscopic solution for monitoring nutrient composition (e.g. lactate concentration) in microfluidic channels.

The first goal was to define system specifications and design – in our case it means we have to know the composition of the commonly used nutrient solutions, the additives and the dynamically changing measurable parameters in the targeted biological model systems. The desired parameters could be the temperature, O_2, CO_2 concentrations, pH. Commonly used components are the grow factors (EGF, bFGF, R3 IGF-1, VEGF, NGF, BDNF, GDNF, NEAA, HKGS, etc.), antibiotics (eg. penicillin-streptomycin), vitamins (mainly B-group), amino acids (eg. glutamine) ascorbic acid, carbohydrates (eg. glucose), proteins, peptides, fatty acids, lipids, cell adhesives, insulin, etc. Gaseous CO_2 is used in natural buffering systems maintaining the right pH values by CO_2 incubator. Other buffering solutions are using HEPES, inorganic salts or phenol red only as an indicator. Other molecule can appear in the live cell culture such as ATP, lactate.

We are investigating the components of the cell culture media and its additives, measuring the optical characteristics of them in the 200-2500 nm (and even in mid infrared) range. Absorbance, transmittance and fluorescence spectra are measured so far on different solutions, glucose, lactate, glutamine molecules and antibiotics such as penicillin streptomycin, streptomycin sulfate, neomycin sulphate in different concentrations. Other target molecules, various grow factors are also considered: EGF, FGF, BDNF, VEGF, GDNF, NOGGIN. DMEM/F-12 basal medium has high absorbance in UV and in the visible region (mainly due to the phenol red), and has absorbance peaks in the NIR range as well. Measuring Phenol red's colour change in the visible range can be used as a pH indicator. This basal medium has a strong fluorescence as well. Vitrolife G1 (plus) has similar rich optical characteristics. Lactate (which indicates the anaerobic glucose consumption) has high absorbance in the UV region and absorbance peaks in the NIR range (Fig. 5.12.).

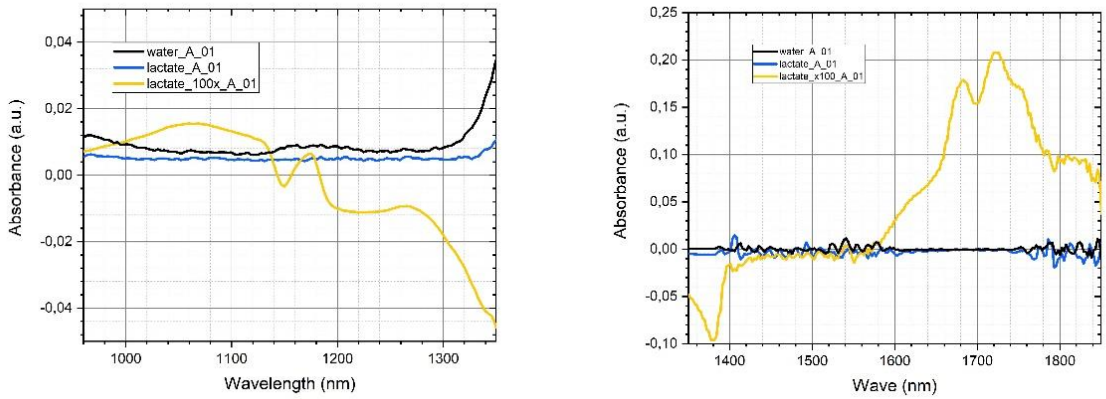

Figure 5.12. *Spectral characteristics of the lactate as being a significant marker molecule of OoC applications*.

Nanobiosensorics Momentum Goup

Head: Robert HORVATH, Ph.D., Senior Scientist

Research Staff

- Robert HORVATH, Ph.D.
- Sándor KURUNCZI, Ph.D.
- Inna SZÉKÁCS, Ph.D.
- Beatrix PÉTER, Ph.D.
- Boglárka KOVÁCS, Ph.D.
- András SAFTICS, Ph.D.
- Zoltán SZITTNER, Ph.D.
- Nicolett KANYÓ, M.Sc.
- Eleonóra HATY, M.Sc.

Ph.D. students / Diploma workers

- Enikő FARKAS, Ph.D. student
- Ágoston NAGY, Ph.D. student
- Tamás GERECSEI, Ph.D. student
- Kristóf KLIMENT, Ph.D. student
- Kinga Dóra KOVÁCS, Ph.D. student
- Milán SZTILKOVICS, M.Sc. student
- Norbert PAP, B.Sc. student
- Róbert TARR, B.Sc. student
- Péter CHRENKÓ, M.Sc. student
- Kinga TÓTH, B.Sc. student
- Barbara MAJOROS, M.Sc. student
- Beatrix MAGYARÓDI, M.Sc. student
- Bence JOÓ, M.Sc. student
- Fatime GAJNUT, M.Sc. student

The research profile of the Nanobiosensorics Group is the development and application of label-free optical biosensors, the mathematical modeling of the relevant biological and biophysical processes. Building on their broad national and international collaborative network the group conducts research in the fields of instrument development, monitoring of cell secreted extracellular vesicles, development of protein-based functional coatings, adhesion studies on human cancer and immune cells, and theoretical modeling. In 2014, the application for an ERC Consolidator Grant by the head of the research group received qualification category “A (fully meets the ERC excellence criteria and should be funded if sufficient funds are available)” after the interview in Brussels, but the funding line did not reach this proposal due to budgetary constraints. However, using this achievement the Group could successfully apply for funding from National Research, Development and Innovation Office (NKFIH) in the framework of the ERC_HU call. In the framework of this project they aim single cell manipulation and label-free sensing. Building on this expertise, in 2018 they won an Élvonal (NKFIH) research project for single cell biosensing.

Subnanoliter precision piezo pipette for single-cell isolation and droplet printing

OTKA PD124559, OTKA KH126900, OTKA KKP129936, OTKA ERC_HU117755, LP2012-26/2012 Lendület, 2018-1.1.1-MKI-2018-00073, VEKOP-2.1.7-15-2016-00146

B. Francz, R. Ungai-Salánki, É. Sautner, R. Horvath, B. Szabó

Although microliter-scale liquid handling with a handheld pipette is a routine task, pipetting nanoliter-scale volumes is challenging due to several technical difficulties including surface tension, adhesion and evaporation effects. We developed a fully automated piezoelectric micropipette with a precision of < 1 nanoliter, improving the efficiency of imaging-based single-cell isolation to above 90%. This improvement is crucial when sorting rare or precious cells, especially in medical applications. The compact piezoelectric micropipette can be integrated into various (bio)chemical workflows. It eliminates plastic tubes, valves, syringes, and pressure tanks. For high-quality phase-contrast illumination of the sample, e.g., cells or tiny droplets, we constructed rings of LEDs arranged concentrically to the micropipette. The same device can be readily used for single-cell printing and nanoliter-scale droplet printing of reagents using either fluorescent or transparent illumination on a microscope. We envision that this new technology will shortly become a standard tool for single-cell manipulations in medical diagnostics, e.g., circulating tumor cell isolation [Ref. 6.1].

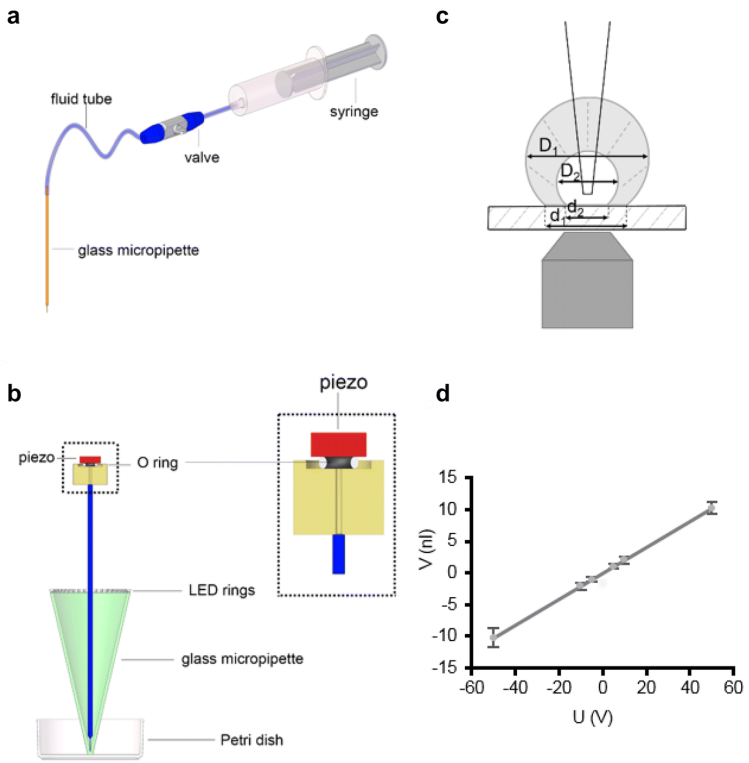

Figure 6.1. *Piezo micropipette. (a) Standard micropipette setup with an elastic tube and syringe. (b) Schematic representation of the piezo micropipette. (c)Principle of calibration. (d) Calibration curve of the nanoliter droplet printing.*

Chemical resonance, beats, and frequency locking in forced chemical oscillatory systems

OTKA NN125752, OTKA K131425, OTKA KH126900, OTKA KKP129936, LP2012-26/2012 Lendület, BME Nanotechnology FIKP grant

H. Shearer Lawson, G. Holló, R. Horvath, H. Kitahata, I. Lagzi

Resonance, beats, and synchronization are general and fundamental phenomena in physics. Their existence and their in-depth understanding in physical systems have led to several applications and technological developments shaping our world today. Here we show the existence of chemical resonance, chemical beats, and frequency locking phenomena in periodically forced pH oscillatory systems (sulfite–hydrogen peroxide and sulfite–formaldehyde–gluconolactone pH oscillatory systems (Fig.6.2)). Periodic forcing was realized by a superimposed sinusoidal modulation on the inflow rates of the reagents in the continuous-flow stirred tank reactor. The dependence of the time period of beats follows the relation known from classical physics for forced physical oscillators. Our developed numerical model describes qualitatively the resonance and beat phenomena experimentally revealed. Application of periodic forcing in autonomously oscillating systems can provide new types of oscillators with a controllable frequency and new insight into controlling irregular chemical oscillation regimes [Ref. 6.2].

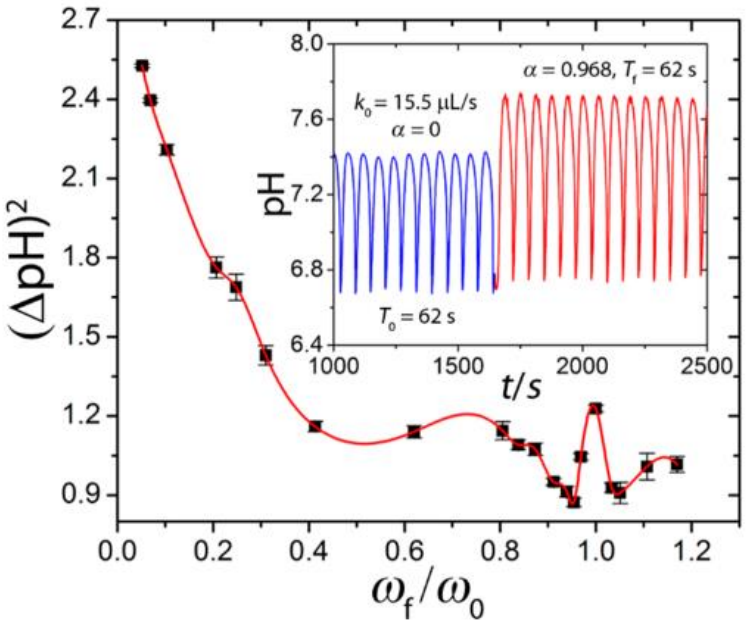

Figure 6.2. *Chemical resonance curve in the sulfite−hydrogen peroxide pH oscillatory system using a sinusoidal periodic forcing of the inflow rate of the reagents (k_0 = 15.5 μL/s, and α = 0.968). ΔpH is the peak-to-peak amplitude of the oscillation. The inset shows the oscillations in the unforced case (blue line) with a time period of 62 s, and the oscillations when a sinusoidal periodic forcing is applied (red line) with the natural frequency of the oscillatory system. Close to the natural frequency, where beat phenomena appeared, the amplitude of the oscillations was calculated as an average amplitude corresponding to the one period of beat.*

Human primary endothelial label-free biochip assay reveals unpredicted functions of plasma serine proteases

LP2012-26/2012 Lendület, OTKA ERC_HU117755, OTKA KH126900, OTKA KKP129936, OTKA K115623, MedInProt Synergy Grant

M. L. Debreczeni, I. Szekacs, B. Kovacs, A. Saftics, S. Kurunczi, P. Gál, J. Dobó, L. Cervenak, R. Horvath

Tissue-on-a-chip technologies are more and more important in the investigation of cellular function and in the development of novel drugs by allowing the direct screening of substances on human cells. Constituting the inner lining of vessel walls, endothelial cells are the key players in various physiological processes, moreover, they are the first to be exposed to most drugs currently used. However, to date, there is still no appropriate technology for the label-free, real-time and high-throughput monitoring of endothelial function. To this end, we developed an optical biosensor-based endothelial label-free biochip (EnLaB) assay that meets all the above requirements. Using our EnLaB platform, we screened a set of plasma serine proteases as possible endothelial cell activators, and first identified the endothelial cell activating function of three important serine proteases – namely kallikrein, C1r and mannan-binding lectin-associated serine-protease 2 (MASP-2) – and verified these results in well-established functional assays. EnLaB proved to be an effective tool for revealing novel cellular mechanisms as well as for the high-throughput screening of various compounds on endothelial cells (Fig.6.3) [Ref. 6.3].

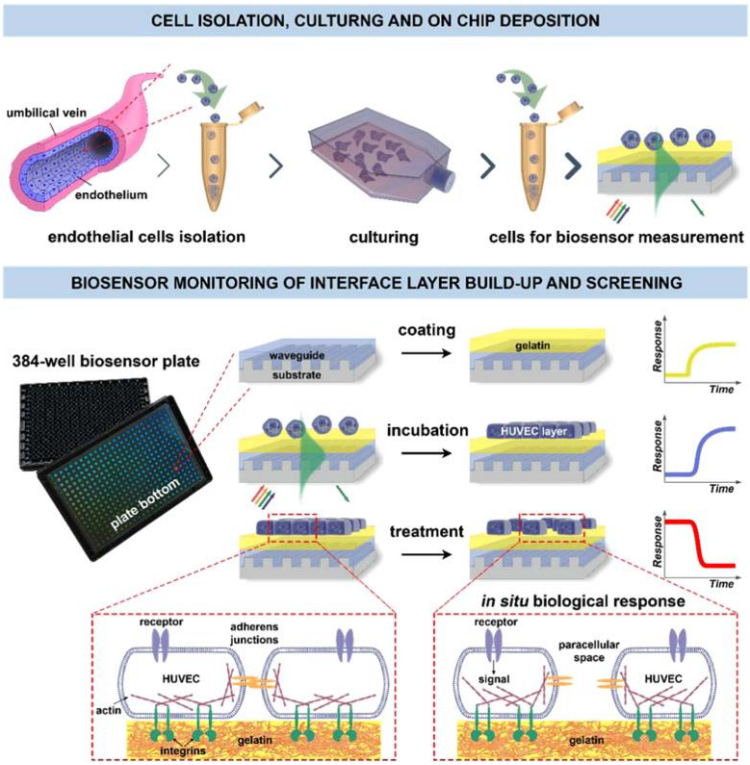

Figure 6.3*. Schematic overview of the proposed EnLaB measurement setup. Upper part: cell preparation steps (primary cell isolation, culturing, transferring onto the sensor chip surface). The lower part illustrates the steps of the biosensor measurements and typically obtained biosensor responses (the detected shifts in the resonant wavelength): coating of the chip with gelatin, following with cell attachment to the gelatin surface, and subsequent cell treatment by the studied molecular compounds (screening). Illustration of the biological effect of the treatment is highlighted in dashed boxes*

Dextran-based hydrogel layers for biosensors

LP2012-26/2012 Lendület, OTKA KKP129936, OTKA KH126900, OTKA ERC_HU117755, OTKA FK128901, János Bolyai Research Scholarship

A. Saftics, B. Türk, A. Sulyok, N. Nagy, E. Agócs, B. Kalas, P. Petrik, M. Fried, N. Q. Khánh, A. Prósz, K. Kamarás, I. Szekacs, R. Horvath, S. Kurunczi

Biofunctional coatings are key elements of biosensors regulating interactions between the sensing surface and analytes as well as matrix components of the sample. These coatings can improve sensing capabilities both by amplifying the target signal and attenuating interfering signals originating from surface fouling (non-specific binding). Considering the tested materials so far, hydrogel-based layers have been verified to be among the most effective layers in improving biochip performance. The polysaccharide dextran can be efficiently used to form hydrogel layers displaying extended three-dimensional structure on biosensor surfaces. Owing to their high water content and flexible structure, dextran coatings present advanced antifouling abilities, which can be exploited in classic bioanalytical measurements as well as in the development of cell-on-a-chip type biosensors. However, in spite of the numerous applications, the deep characterization of dextran layers has been missing from the literature. This phenomenon can be attributed to the challenging analysis of few nanometer-thick layers with high water content. The lack of available data is more pronounced regarding the layer behaviors under aqueous conditions. In this chapter we present various surface analytical methods (including biosensor-type techniques) suitable for the complex characterization of hydrogel coatings whose thickness ranges from few to several ten nanometers. As a case study, we focus on the analysis of carboxymethyl dextran (CMD) layers developed for waveguide-based label-free optical biosensor applications (Fig. 6.4). Examination methodologies both under dry and aqueous conditions as well as testing of antifouling abilities are also presented [Ref. 6.4].

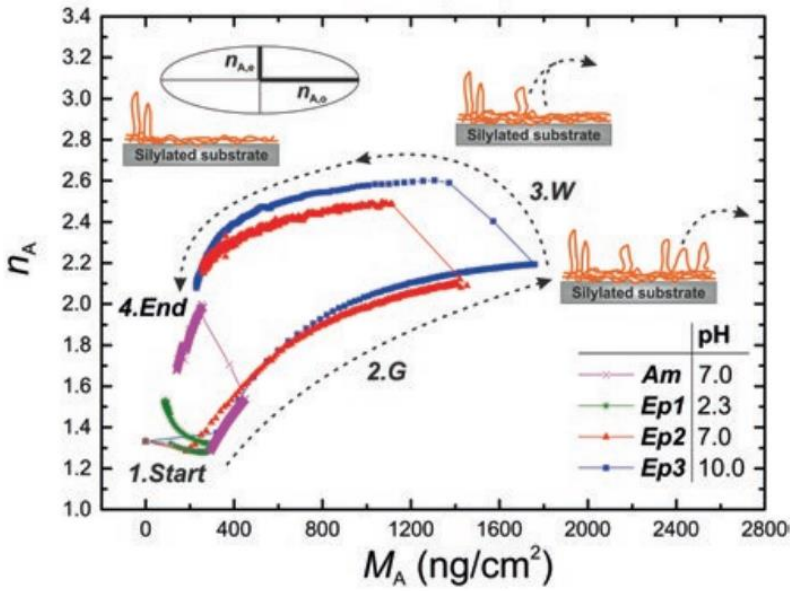

Figure 6.4. *Refractive index of an ultrathin CMD layer as a function of deposited surface mass density. The curves represent different experimental conditions revealing the dependence of CMD layer structure during its formation on the applied silane precoating and pH of the grafting solution. The time-related direction of the measurements is indicated by the dashed arrows (G indicates the grafting, W the washing section of experiments). The inset table represents the different experimental conditions (Am, aminosilylated; Ep, epoxysilylated surfaces). The schemes above the curves illustrate the alteration of CMD layer nanostructure at the different experimental phases.*

Oxidization increases the binding of EGCG to serum albumin revealed by kinetic data from label-free optical biosensor with reference channel

LP2012-26/2012 Lendület, OTKA KKP129936, OTKA KH126900, OTKA ERC_HU117755

B. Peter, A. Saftics, B. Kovacs, S. Kurunczi, R. Horvath

Epigallocatechin-gallate (EGCG) is the main polyphenol ingredient of green tea. This compound is a strong antioxidant and oxidizes easily. Numerous studies demonstrated its beneficial effects on the human health, for example its anticancer and anti-inflammatory activity. In the body, EGCG is transported by serum albumin. EGCG easily oxidizes and the interactions of the oxidized form presumably present significant differences. However, the presence of oxidized EGCG is usually neglected in the literature and its effects have not been investigated in detail. Here, we applied the label-free grating coupled interferometry method that performs dual-channel measurements. The measured kinetic signal can be compensated with a signal of a reference channel at each measurement time (Fig. 6.5). By testing both hydrophilic and hydrophobic platforms, we found that EGCG can bind to a wide range of surfaces. Exploiting the dual-channel referencing ability as well as the unique sensitivity and throughput of the employed label-free technique, the experiments revealed the specific interactions between bovine serum albumin (BSA) and EGCG and determined the characteristic dissociation constant (K_d) of the binding equilibrium. The obtained binding constants were compared to literature values, showing reasonable agreement with NMR data. Besides the native EGCG, the oxidized form of EGCG was also examined, whose binding behaviors to serum albumins have never been studied. Overstoichiometric binding was obtained: BSA has stronger and weaker binding sites, which could be characterized by two separate K_d values. Furthermore, EGCG oxidization increased the bound amount [Ref. 6.5].

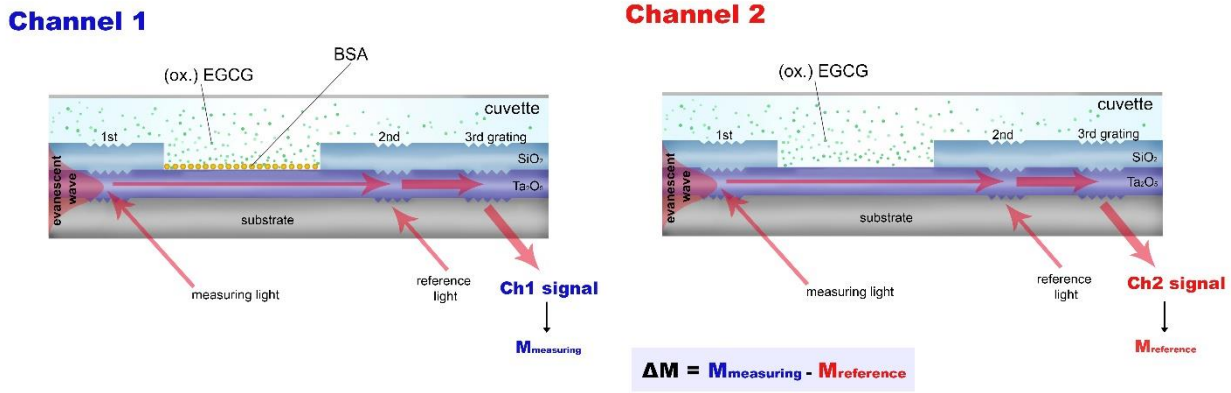

***Figure 6.5**. The sensor chips used in the WAVE instrument have two channels; one for measuring the interaction between the immobilized bioreceptor and the analyte (measuring channel, channel 1) and one for subtracting the channel 1 signal by a reference signal (reference channel, channel 2). In our case, BSA was immobilized on channel 1 surface, while channel 2 remained unmodified.*

Assembly of epithelial monolayers and transmigration of cancer cells captured with phase holographic imaging

LP2012-26/2012 Lendület, OTKA KKP129936, OTKA KH126900, BME FIKP BIO Grant

Á. G. Nagy, I. Székács, A. Bonyár, R. Horvath

Cellular monolayers have a fundamental role in the development of embryos, vascularization, organ formation, attachment to artificial implants, and metastasis of cancerous cells. Phase holographic imaging was used to monitor the time-dependent behavior of cancerous HeLa cells. After monitoring the assembly of epithelial Vero monolayer on a gelatin-coated surface, HeLa cells were seeded on top of the monolayer, and their transmigration was observed. This method is label-free and non-toxic to cells and enables the visualization of living cells in real-time and analyze their parameters such as motility and morphology. HeLa cells seeded on the tight Vero monolayer (100% confluency) were observed for 24 hours, and a 60-minute time period has been selected for further analysis that showed the difference in cellular parameters between non-invasive and invasive HeLa cells in the observed time frame (Fig.6.6). Our investigations revealed that invasive HeLa cells have reduced area and optical volume compared to noninvasive HeLa cells, corresponding to the phase shift detected in transmigration events. [Ref. 6.6].

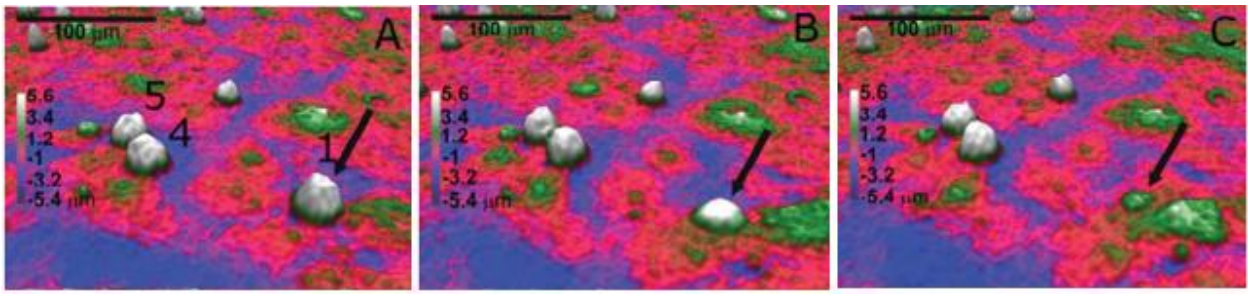

Figure 6.6. *Intravasation of a HeLa cell seeded on top of the Vero monolayer. (A, B, C) The invasive Hela cell (1) marked with black arrow embedded itself into the underlying Vero monolayer. The 4 and 5 are non-invasive HeLa cells.*

Grating-coupled interferometry reveals binding kinetics and affinities of Ni ions to genetically engineered protein layers

LP2012-26/2012 Lendület, OTKA KKP129936, OTKA KH126900, OTKA ERC_HU117755, BIONANO_GINOP-2.3.2-15-2016-00017 project, TKP2020-IKA-07 project financed under the 2020-4.1.1-TKP2020 Thematic Excellence Programme

H. Jankovics, B. Kovacs, A. Saftics, T. Gerecsei, É. Tóth, I. Szekacs, F. Vonderviszt, R. Horvath

Reliable measurement of the binding kinetics of low molecular weight analytes to their targets is still a challenging task. Often, the introduction of labels is simply impossible in such measurements, and the application of label-free methods is the only reliable choice. By measuring the binding kinetics of Ni(II) ions to genetically modified flagellin layers, we demonstrate that: (1) Grating-Coupled Interferometry (GCI) is well suited to resolve the binding of ions, even at very low protein immobilization levels; (2) it supplies high quality kinetic data from which the number and strength of available binding sites can be determined, and (3) the rate constants of the binding events can also be obtained with high accuracy.

Experiments were performed using a flagellin variant incorporating the C-terminal domain of the nickel-responsive transcription factor NikR. GCI results were compared to affinity data from titration calorimetry. We found that besides the low-affinity binding sites characterized by a micromolar dissociation constant (Kd), tetrameric FliC-NikR_C molecules possess high-affinity binding sites with Kd values in the nanomolar range. GCI enabled us to obtain real-time kinetic data for the specific binding of an analyte with molar mass as low as 59 Da, even at signals lower than 1 pg/mm^2 [Ref. 6.7].

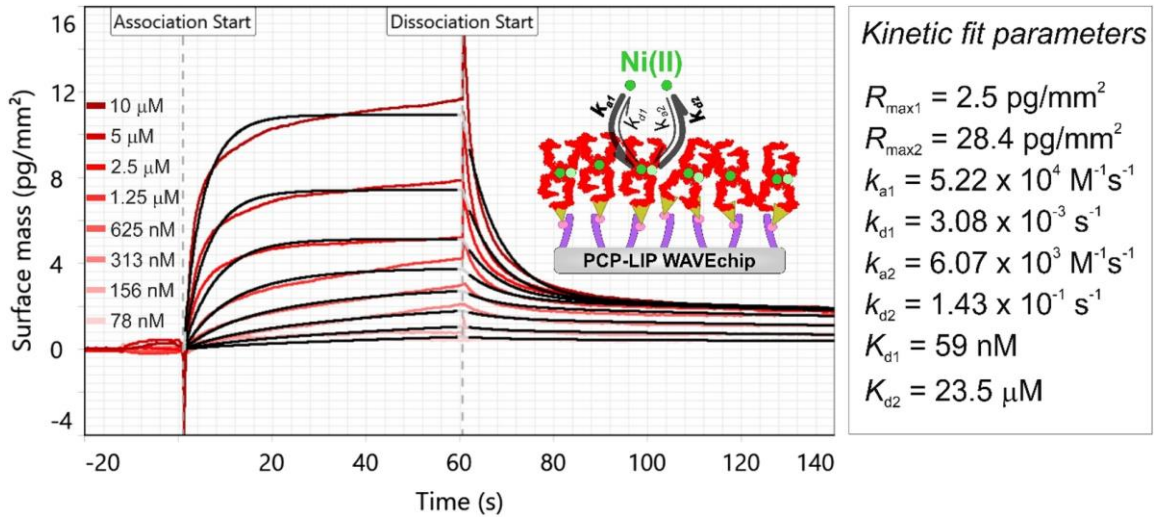

Figure 6.7*. Measured kinetic data of Ni(II) binding obtained at high FliC-NikR_C coverage on a PCP-LIP WAVEchip (red curves). The shown measurement curves represent Ch1-Ch2 reference corrected data. The data were fitted using the heterogeneous ligand kinetic model (black curves). The spikes at association start and dissociation start annotations were originated from solution exchange effect. The inset scheme illustrates the binding of Ni to the FliC-NikR_C tetramers which were immobilized on the quasi-planar lipophilic coating of the PCP-LIP chip.*

Single-cell adhesion force kinetics of cell populations from combined label-free optical biosensor and robotic fluidic force microscopy

LP2012-26/2012 Lendület, OTKA KKP129936, OTKA KH126900, OTKA ERC_HU117755, OTKA PD131543, ÚNKP-19-3

M. Sztilkovics, T. Gerecsei, B. Peter, A. Saftics, S. Kurunczi, I. Szekacs, B. Szabo, R. Horvath

Single-cell adhesion force plays a crucial role in biological sciences, however its in-depth investigation is hindered by the extremely low throughput and the lack of temporal resolution of present techniques. While atomic force microcopy (AFM) based methods are capable of directly measuring the detachment force values between individual cells and a substrate, their throughput is limited to few cells per day, and cannot provide the kinetic evaluation of the adhesion force over the timescale of several hours.

In this study, a high spatial and temporal resolution resonant waveguide grating based label-free optical biosensor (Fig. 6.8) was combined with robotic fluidic force microscopy to monitor the adhesion of living cancer cells. In contrast to traditional fluidic force microscopy methods with a manipulation range in the order of 300–400 micrometers, the robotic device employed here can address single cells over mm-cm scale areas. This feature significantly increased measurement throughput, and opened the way to combine the technology with the employed microplate-based, large area biosensor. After calibrating the biosensor signals with the direct force measuring technology on 30 individual cells, the kinetic evaluation of the adhesion force and energy of large cell populations was performed for the first time.

We concluded that the distribution of the single-cell adhesion force and energy can be fitted by log-normal functions as cells are spreading on the surface and revealed the dynamic changes in these distributions. The present methodology opens the way for the quantitative assessment of the kinetics of single-cell adhesion force and energy with an unprecedented throughput and time resolution, in a completely non-invasive manner [Ref. 6.8].

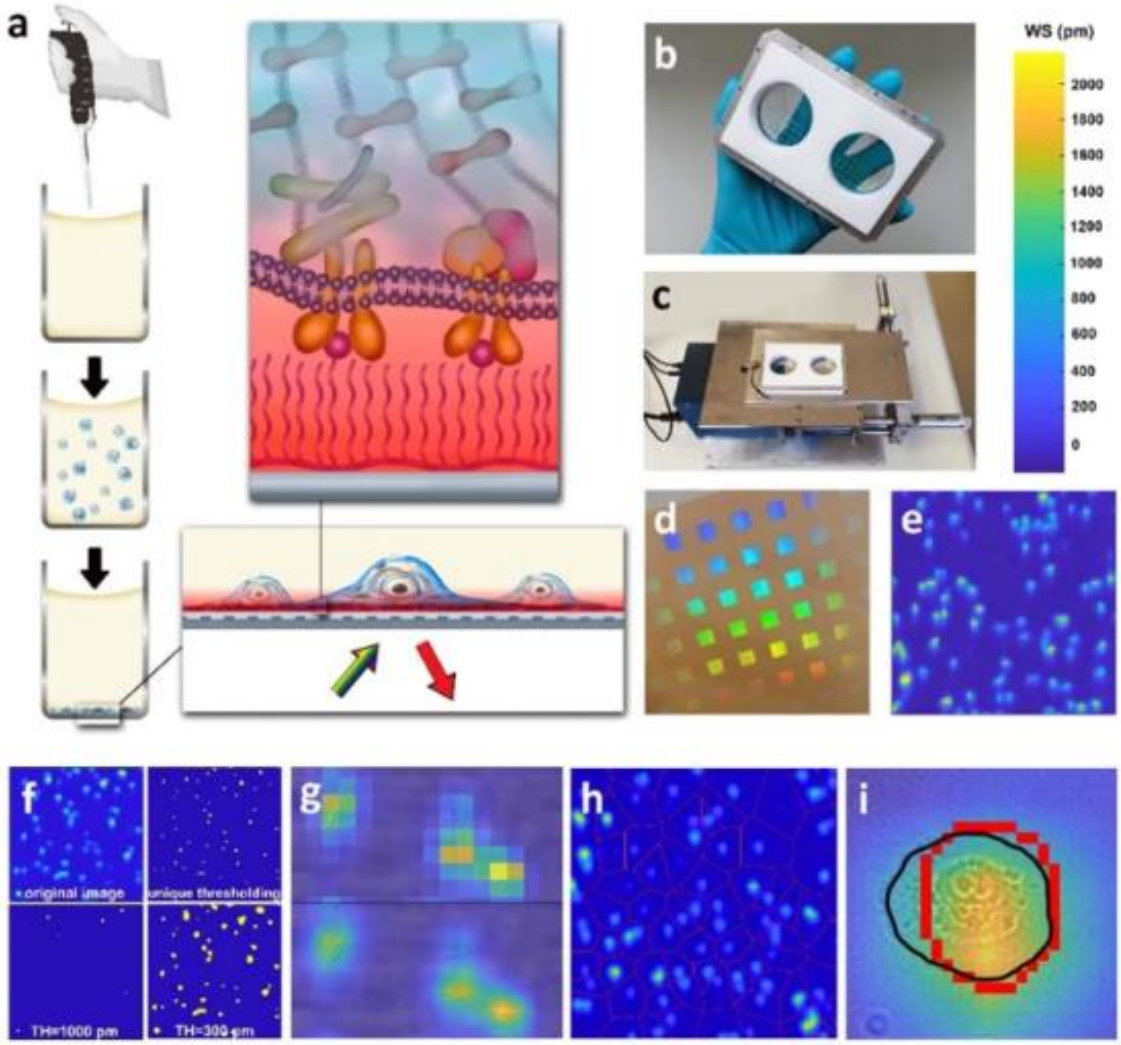

Figure 6.8. *The optical biosensor measurement workflow and results. (a) Schematic of the measurement workflow. (b,c) Photographs showing the custom-made biosensor insert holder (in a hand, and placed into the Epic Cardio device) with two circular wells optimized for subsequent FluidFM BOT measurements. (d) Photograph of the Epic Cardio biosensor insert. (e) Raw WS signal image of a single sensor area at t = 90 min. (f) Comparison of different thresholding strategies of recorded biosensor images. (g) Fused image of the biosensor signal and the brightfield picture, showing a clear correspondence between the two overlapping modalities. (h) The Voronoi tessellation of a sensor area. (i) Area matching segmentation: the combined optical biosensor and brightfield picture shows how the segmented cell perimeter (red) approximates the actual cell perimeter measured on the microscope image (black) after setting the optimal threshold.*

Glycocalyx regulates the strength and kinetics of cancer cell adhesion revealed by biophysical models based on high resolution label-free optical data

LP2012-26/2012 Lendület, OTKA ERC_HU117755, OTKA PD131543, OTKA KKP129936, GINOP-2.3.2-15-2016-00037, OTKA PD128480, János Bolyai Research Fellowship, UNKP-19-4-SZTE-42, UNKP-20-5-SZTE-672, H2020- MSCA-ITN-2015-675619, UNKP-20-4-SZTE-593.

N. Kanyo, K. D. Kovacs, A. Saftics, I. Szekacs, B. Peter, A. R. Santa-Maria, F. R. Walter, A. Dér, M. A. Deli, R. Horvath

In the present work, we investigated the effect of enzymatic digestion of specific glycocalyx components on cancer cell adhesion to RGD (arginine–glycine–aspartic acid) peptide motif displaying surfaces. High resolution kinetic data of cell adhesion was recorded by the surface sensitive label-free resonant waveguide grating (RWG) biosensor (Fig. 6.9), supported by fluorescent staining of the cells and cell surface charge measurements. We found that intense removal of chondroitin sulfate (CS) and dermatan sulfate chains by chondroitinase ABC reduced the speed and decreased the strength of adhesion of HeLa cells. In contrast, mild digestion of glycocalyx resulted in faster and stronger adhesion. Control experiments on a healthy and another cancer cell line were also conducted, and the discrepancies were analysed.

We developed a biophysical model which was fitted to the kinetic data of HeLa cells. Our analysis suggests that the rate of integrin receptor transport to the adhesion zone and integrin-RGD binding is strongly influenced by the presence of glycocalyx components, but the integrin-RGD dissociation is not. Moreover, based on the kinetic data we calculated the dependence of the dissociation constant of integrin-RGD binding on the enzyme concentration. We also determined the dissociation constant using a 2D receptor binding model based on saturation level static data recorded at surfaces with tuned RGD densities. We analyzed the discrepancies of the kinetic and static dissociation constants, further illuminating the role of cancer cell glycocalyx during the adhesion process.

Altogether, our experimental results and modelling demonstrated that the chondroitin sulfate and dermatan sulfate chains of glycocalyx have an important regulatory function during the cellular adhesion process, mainly controlling the kinetics of integrin transport and integrin assembly into mature adhesion sites. Our results potentially open the way for novel type of cancer treatments affecting these regulatory mechanisms of cellular glycocalyx [Ref. 6.9].

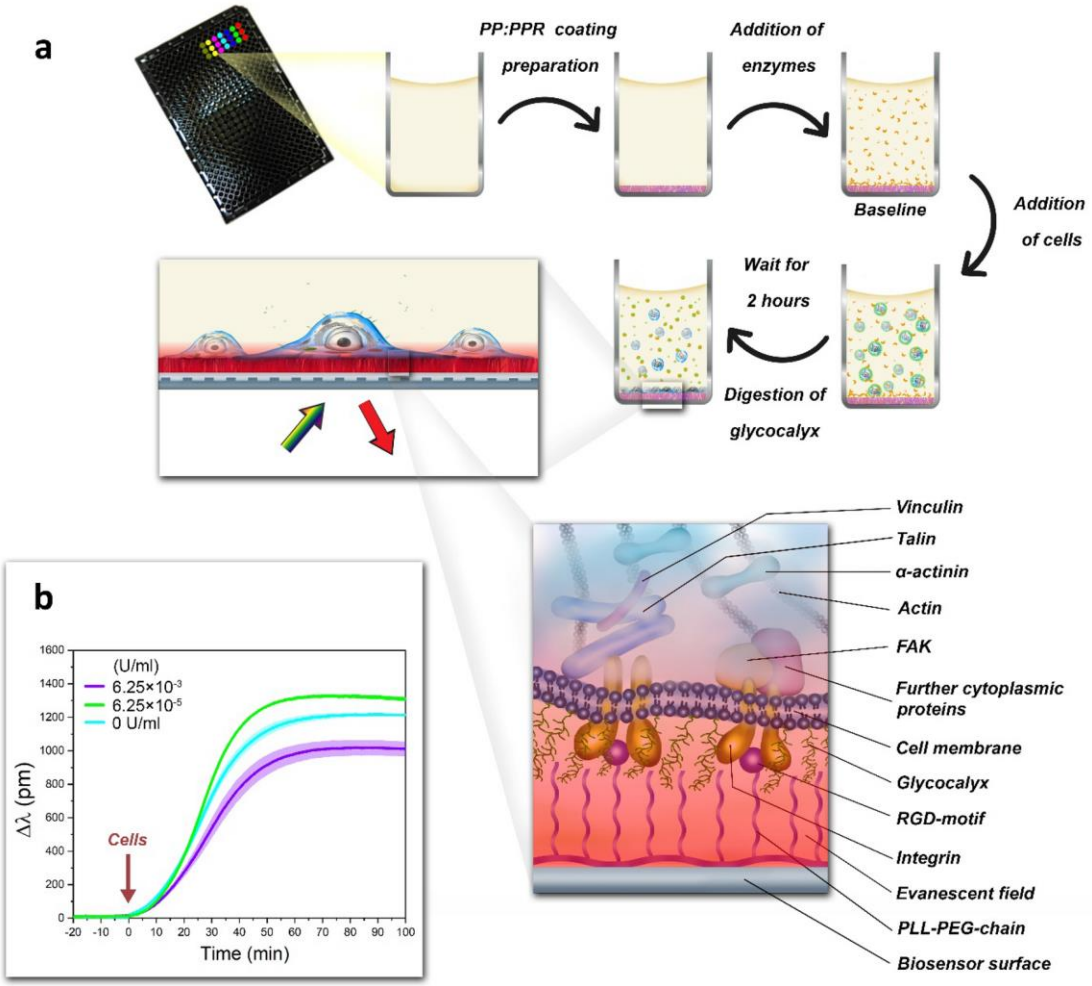

Figure 6.9. *Schematics of RWG measurements of cell adhesion kinetics on the polymer coated biosensor surfaces. (a) The adhesion kinetics of cells were real-time monitored using the label-free optical biosensor. First, the PP: PPR copolymer coating was prepared on the sensor surfaces, and the ChrABC enzyme at different concentrations was added to the wells. After recording a baseline, HeLa cells were pipetted into the biosensor wells (0 min). The cell adhesion was monitored for 100 min. The schematic illustration of the adhered cells in the biosensor wells and the cellular components are also shown in the magnified parts. The surface localized evanescent optical field is illustrated as red shadow. (b) Representative cell adhesion kinetic curves on 50% PP: PPR copolymer surface.*

Complex Systems Department

Head: Dr. Géza Ódor D.Sc., scientific advisor

Research Staff

- Balázs KIRÁLY, Ph.D.
- István BORSOS
- Zoltán JUHÁSZ, Ph.D.
- György SZABÓ, D.Sc., scientific advisor
- Attila SZOLNOKI, D.Sc., scientific advisor

Ph.D. students / Diploma workers

- István HEGEDŰS LFZE diploma
- Béla SZERÉNYI LFZE diploma
- Beatriz DE SIMONI BME, B.Sc. student
- Bendegúz SULYOK, BME M.Sc.
- Attila KAZSOKI BME Ph.D. student

The research field of the group is the investigation of complex systems by the methods of statistical physics in equilibrium as well as non-equilibrium states.

The theoretical investigation of multi-agent evolutionary game models studies processes supporting fair behavior of individuals by numerically analyzing mathematical models when a player's own interest opposes that of the community. Mathematical models have been used to investigate the effect of one kind of penalties, the combinations of the rules of strategy updates, and systems in which the income of the players is obtained from two or three interconnection systems (communities).

Decomposing matrices into elementary (orthogonal) components allows the identification and frequency analysis of elementary interactions causing social dilemmas in potential games. The systematic examination of elementary interactions of evolutionary matrix games unearthed two newer versions of social dilemmas. In the first case the macroscopic system to develop into a state of higher average income, because of the greater number of possible microscopic states. In the second case the anomalous consequence of cyclic symmetry-breaking forces the system develops into the state of lower average income. Because of the cyclic dominance, however, this system returns to the initial state, where newer and newer similar avalanche phenomena cause huge fluctuations both in the proportions of the strategies and in the incomes. The applicability of matrix decomposition is also being investigated in other related fields. In population ecology, the nature and intensity of pairwise interactions between different species can be gauged in biological growth experiments conducted in bicultures, but the specifics of the interplay between these interspecific interactions and how they determine outcomes in mixtures of multiple species are unclear as yet. The ongoing decomposition analysis of the elementary game content of empirical pair interaction matrices found in the literature has revealed a positive correlation between the coordination component of the matrix and the mean relative yield of the whole mixed community and anticorrelations of its biodiversity with both the asymmetric and the external benefit components.

Using traditional concepts and methods of statistical physics the universal properties of avalanche phenomena were analyzed in human brain models. Similarly, catastrophe analyses were performed in models appearing in the interconnected network of electric plants. They extended the investigation of the general characteristics of the Griffiths phase to inhomogeneous networks of modular structure.

The increase of data in folk music and genetic data sets implies the continuous improvement of algorithms to analyze them. The newly developed algorithms are able both to identify clusters and to follow the evolutionary inheritance of clusters, both in genetic (haplogroup) features and in popular characteristics of folk music tunes.

Blocking defector invasion by focusing on the most successful partner

A. Szolnoki and X. Chen

According to the standard protocol of spatial public goods game a cooperator player invests not only into his own game but also into the games organized by neighboring partners. In this work we relax this assumption and allow cooperators to decide which neighboring group to prefer instead of supporting them uniformly. In particular, we assume that they select their most successful neighbor and focus their investments exclusively into the related group. We show that this very simple alteration of the dynamical rule results in a surprisingly positive evolutionary outcome – cooperators prevail even at harsh environment represented by small values of synergy factor. The microscopic mechanism behind the reported success of cooperator strategy can be explained by a blocking mechanism which affects the propagations of competing strategies in a biased way. Our results, which remain intact by using different interaction topologies, reveal that it could be beneficial to concentrate individual efforts to reach a higher global wellbeing.

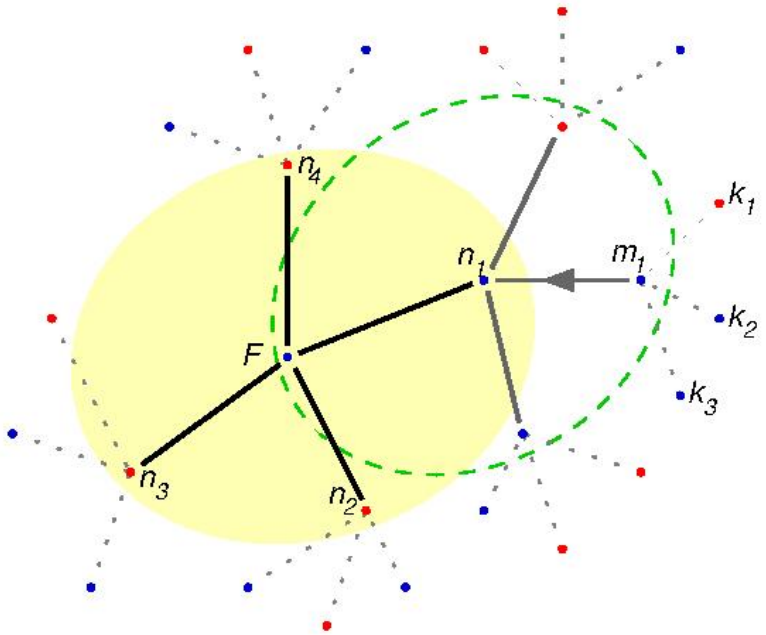

Figure 7.1. *The focal F player collects income from not only his own game, marked by yellow set, but also from the game organized by his neighbor n_1. The group of the latter game is marked by a dashed green ellipse. If cooperator m_1 is focusing on the best neighbor, which happens with probability alpha then he invests contribution to n_1's game only if the payoff of n_1 player is higher than the payoff of $k_1, \ldots, k_3$ players. If this is the case then m_1 player invests all his external $(G - 1) \cdot c = 4$ contribution here. The latter act is marked by an arrow. Similarly, focal F always contributes his own game, but his external investment depends on its own state. In normal case regular cooperator F contributes to n_1's game by $c = 1$. But if F focuses on the best neighbor then he invests into n_1's game only if the payoff of n_1 exceeds the payoff of $n_2, \ldots, n_4$ players. Otherwise F contributes nothing no matter he is in a cooperator state.*

The microscopic mechanism which explains the success of the suggested protocol is based not on the usual reciprocity-based arguments. In our present case the introduced investment policy weaken those who are in the front line separating the competing domains independently of their actual strategies. But this weakening effect is biased and defectors suffer more from it. As a consequence, they are unable to exploit the vicinity of cooperators hence they lose their success. They become less attractive and their invasion is

completely blocked. The mentioned weakened cooperators, however, still have a chance to enjoy the vicinity of successful cooperators, hence they benefit from the success of their neighbor. In sum weakened cooperators still do better than weakened defectors, hence the direction of strategy propagation can be reversed. [Ref.7.1]

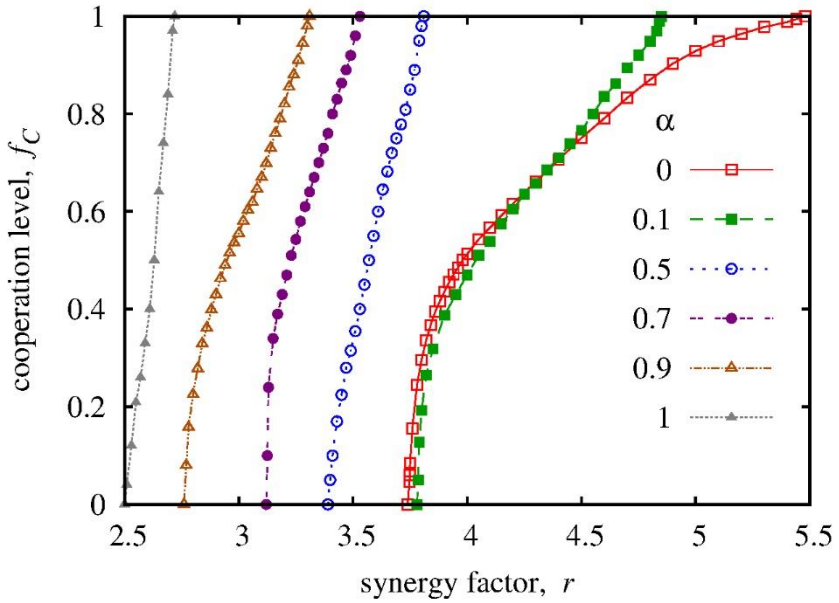

Figure 7.2. *Cooperation level in dependence on synergy factor for different values of α parameter as indicated in the figure legend. This plot suggests that cooperation is largely supported if cooperator players prefer to support exclusively the best neighbor independently of the latter strategy.*

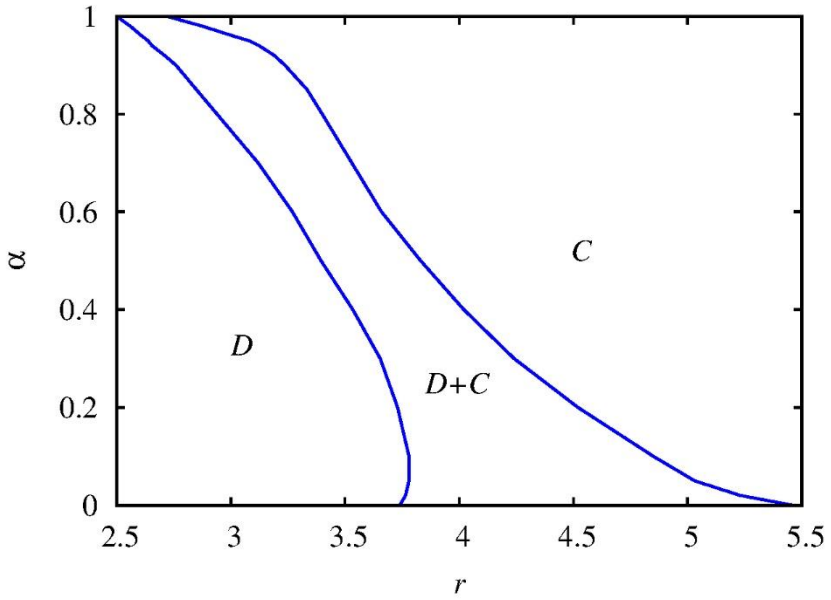

Figure 7.3. *Phase diagram, depicting the stable solutions (C-full cooperator state, D-full defector state and D + C-mixed state) on the α−r parameter plane. In agreement with previous plot cooperators can fight more efficiently against defection at high α values where they focus their external contributions on a single neighbor who does the best in their neighborhood.*

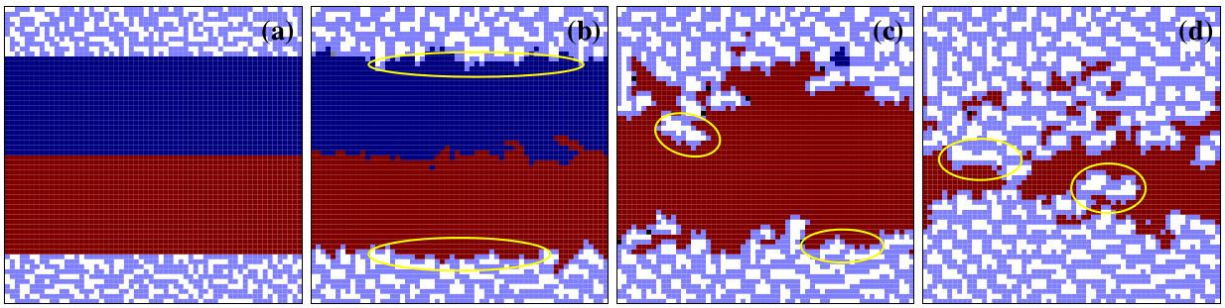

Figure 7.4. *Pattern formation starting from a prepared initial state. Here we used a special coloring to mark those players who have the highest payoff in a group and enjoy the support of a neighboring selective cooperator player. We mark those defectors, unconditional cooperators, and selective cooperators by black, gray, and white color respectively. The mentioned supported players are not present in the borderline between competing domains, but they are generally behind it in the next lines. Their typical positions during the evolution are highlighted by yellow ellipses in panels (b-d).*

A new linear combination method of Haplogroup distribution Central Vectors to model population admixtures

*Z. Juhász, K. Maár (*University of Szeged*), I. G. Varga (*Institute of Hungarian Research*), T. Török (*University of Szeged*)*

We show a new method for analyzing relationships of populations represented by haplogroup (Hg) frequency distributions that are generated from Hg labels and population identifiers of individuals. Our database contains data of 16 019 female individuals belonging to 62 modern and 117 ancient populations. The method has 3 main parts.

1. Extraction a universal Hg basis from the complete set of Hgs, for describing the Hg frequency distributions in a common vector space. The method is based on the assumption that Hgs playing significant roles in ancient migration, admixture and disunion processes construct associations having correlated frequencies in certain subsets of the populations studied.
2. Determining the central vectors (CVs) of the local condensations in the multidimensional point system constructed by the Hg distribution vectors using an unsupervised artificial intelligence described in previous articles (Self Organizing Cloud, SOC). The resulting CVs can be identified from archaeological point of view as ancient ancestral populations strongly influencing the genetic contents of the most ancient and modern populations.
3. The populations are modeled as weighted linear combinations of the CVs using a new linear combination algorithm based on a gradient search for the weights.

The method is applied for analyzing the peopling of Hungary between the Copper Age and the early Middle Ages.

Fig. 7.5 shows the Hg frequency distributions of CVs 25 and 34. The frequencies were learned by the SOC algorithm as the coordinates of the CVs of local condensations constructed by the 179 populations studied. The curves show significant overlaps of the dominant Hgs, referring to the relationship of the assumable ancient populations standing in the background of CVs 25 and 34.

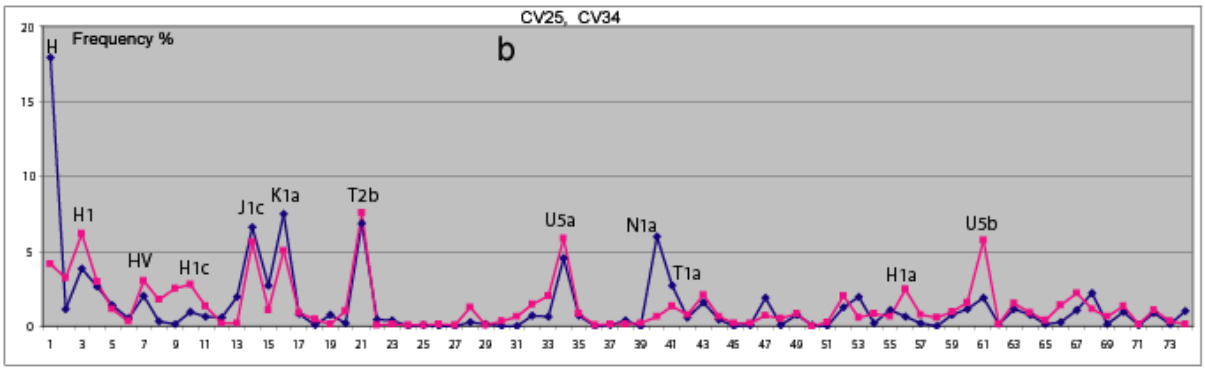

Figure 7.5. *Hg distributions of CV25 (red), and CV34 (blue). Horizontal axis shows Hg serial numbers. Vertical axis shows Hg frequencies. Most frequent Hgs are labeled at the peaks.*

Although the above approach attributes each Hg-distribution to one cluster unambiguously, the fuzzy structure of the point system makes it possible to relate a Hg-distribution to more CVs simultaneously, with different weights depending on the distances of the CVs from the given Hg-distribution.

The mathematical problem can be formulated as follows: We want to approximate the given D-dimensional vector $\underline{h}$ as a weighted sum of the set of *N* given D-dimensional vectors $\underline{v}_1 \ldots \underline{v}_N$:

$$\underline{h} = a_1\underline{v}_1 + a_2\underline{v}_2 + \ldots + a_N\underline{v}_N + \underline{\varepsilon}\,. \qquad 1.$$

Where $\underline{h}$ is the Hg-distribution vector to be approximated by the CVs $\underline{v}_1 \cdots \underline{v}_N$, $N = 74$ is the number of the CVs and $\underline{\varepsilon}$ is the error vector of the approximation. Our aim is to find the optimal set of the weights $a_1 \cdots a_N$, minimizing the power of the error vector $\underline{\varepsilon}$ (the squared sum of the *D* error components):

$$H = \varepsilon_1^2 + \varepsilon_2^2 + \ldots + \varepsilon_D^2 = \sum_{k=1}^{D} \varepsilon_k^2 = \min \quad , \qquad 2.$$

where *H* is the power of the error to be minimized and $\varepsilon_1 \cdots \varepsilon_D$ are the coordinates of the D-dimensional error vector $\underline{\varepsilon}$. Note that the CVs $\underline{v}_1 \cdots \underline{v}_N$ are usually not orthogonal, therefore the weights $a_1 \cdots a_N$ cannot be interpreted as independent coordinates.

As the partial derivatives of the error power can be analytically formulated as

$$\frac{\partial H}{\partial a_m} = \sum_{k=1}^{D} 2\,\varepsilon_k \frac{\partial \varepsilon_k}{\partial a_m} = 2\sum_{k=1}^{D} \varepsilon_k(-v_{m,k}) \quad , \qquad 3.$$

the solution could be determined by a gradient search algorithm.

Red curves in Fig.7.6 show original Hg-distributions of populations living in Hungary in the Copper Age, in the 6-9th and 9-11th centuries, as well as modern Hungarians. Blue lines show the linear combination models of these populations based on the 35 CVs determined by the SOC algorithm. The significant overlaps of the dominant Hg-s refer to a clear genetic continuity of the populations peopling the Carpathian Basin in this wide historical period. The close relationship of 9th century and recent Hungarians is particularly clear in the corresponding distributions in Fig.7.6.c and Fig.7.6.d.

The weights of the CV-based linear combination models of these four populations provide more insight into the history of the human populations of the Carpathian basin. Fig. 7.7 shows a gradual decrease of the weights of CV25 in contrast with the gradual increase of those of CV34. As we have shown the close genetic relationship of these CVs in Fig. 7.5., this gradual transition can be interpreted as a genetic drift of a continuous substrate population of the Carpathian Basin.

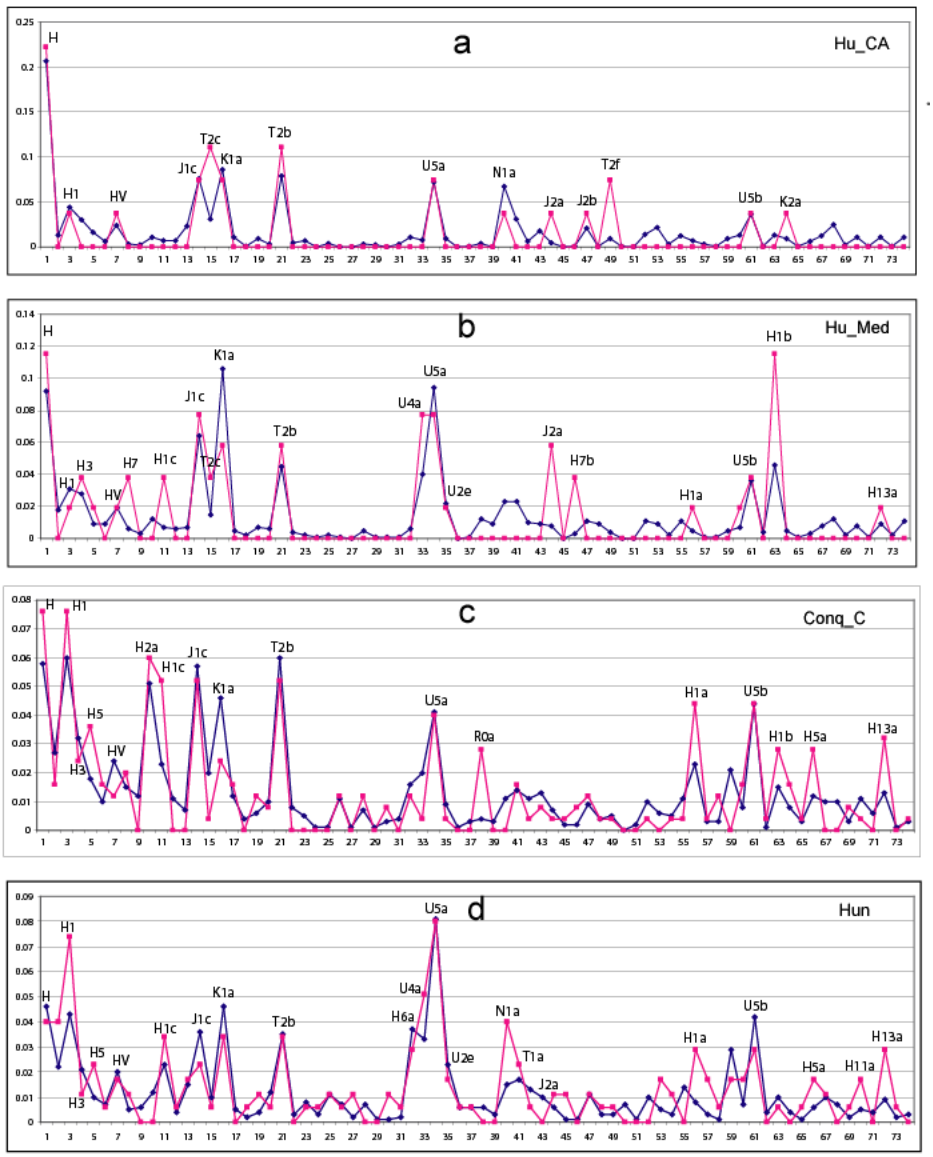

Figure 7.6. *Hg distributions of a: Hungarian Copper Age (Hu_CA), b: 5-9th century population in Hungary, c: Hungarian conqueror commoner of Steppe origin (9-11th century, ConqC) and d: modern Hungarian (Hun) populations. Red lines indicate original Hg distributions while blue lines show CV-modeled distributions.*

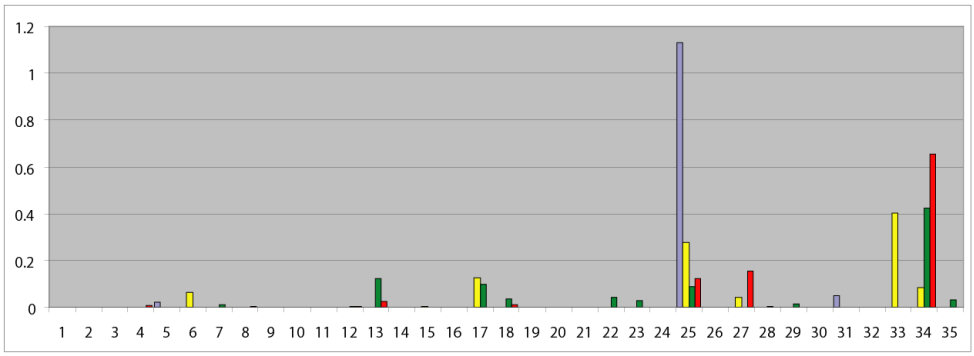

Figure 7.7. *35-dimensional weight vectors of populations in Hungary in the Copper-age (blue), the 6th-9th centuries (yellow), the 9-11th centuries (green), as well as modern Hungarians (red). Horizontal axis: serial numbers of CVs. Vertical axis: weights of Cvs.*

Heterogeneities in Brain models

G.Ódor, B.de Simoni

In $d > 2$ dimensional, homogeneous threshold models discontinuous transition occur, but the mean-field solution provides $1/t$ power-law activity decay and other power laws, and thus it is called mixed-order or hybrid type. It has recently been shown that the introduction of disorder rounds the discontinuity and second-order phase transition and Griffiths phases appear. Here we provide numerical evidence that even in case of high graph dimensional hierarchical modular networks a Griffiths phase in the $K=2$ threshold model is present below the hybrid phase transition.

Discrete threshold models can be defined as two-state systems: $x_i = 0, 1$ (inactive, active) at sites i, with a conditional activation rule, depending on the sum of activity of neighbors compared to the threshold value $\sum_j x_j w_{i,j} > K$, where $w_{i,j}$ is the weight of the link connecting site j to i. In interacting homogeneous systems $w_{i,j}$ is just the adjacency matrix element, $A_{i,j}$, which is 1 if nodes are connected or 0 otherwise. To describe stochasticity this activity creation can be accepted with probability λ, competing with an activity removal process of probability ν.

This is due to the fragmentation of the activity propagation by modules, which are connected via single links. This provides a widespread mechanism in the case of the threshold type of heterogeneous systems, modeling the brain, or epidemics for the occurrence of dynamical criticality in extended Griffiths phase parameter spaces. We have investigated this in synthetic modular networks with and without inhibitory links as well as in the presence of refractory states. For neural systems our results imply that the functional and structural connectivity can be different. [Ref. 7.2]

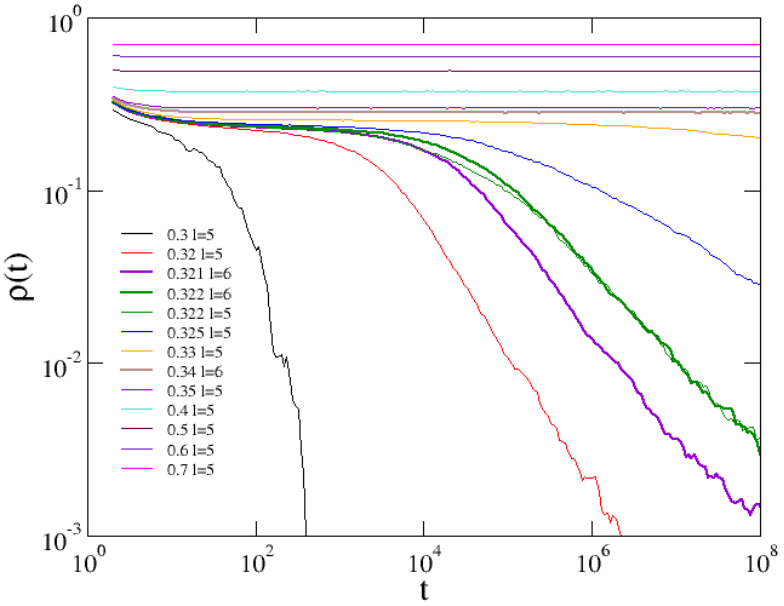

Figure 7.8. *Evolution of ρ(t) for different λ in case of starting from fully active state in the excitatory model with levels: l = 5, 6. From bottom to top symbols: λ = 0.30, 0.32, 0.321 (l = 6), 0.322, 0.322 (l = 6), 0.325, 0.33, 0.34 (l = 6), 0.35, 0.4, 0.5, 0.6, 0.7.*

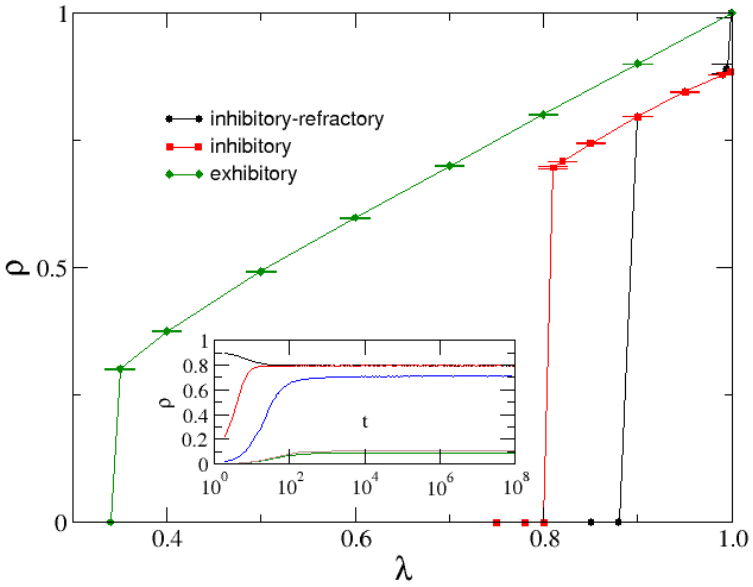

Figure 7.9. *Steady-state behavior for the excitatory, inhibitory, and refractory-inhibitory cases. Inset: evolution of ρ in an inhibitory HMN2d with N = 4096 for different initial activity densities: ρ(0) = 0.0005, 0.001, 0.01, 0.1, 1 (bottom to top curves).*

Power-Law Distributions of Dynamic Cascade Failures in Power-Grid Models

Géza Ódor, Bálint Hartmann

Power-law distributed cascade failures are well known in power-grid systems. Understanding this phenomena has been done by various DC threshold models, self-tuned at their critical point. Here, we attempt to describe it using an AC threshold model, with a second-order Kuramoto type equation of motion of the power-flow. We have focused on the exploration of network heterogeneity effects, starting from homogeneous two-dimensional (2D) square lattices to the US power-grid, possessing identical nodes and links, to a realistic electric power-grid obtained from the Hungarian electrical database. The last one exhibits node dependent parameters, topologically marginally on the verge of robust networks. We show that too weak quenched heterogeneity, coming solely from the probabilistic self-frequencies of nodes (2D square lattice), is not sufficient for finding power-law distributed cascades. On the other hand, too strong heterogeneity destroys the synchronization of the system. We found agreement with the empirically observed power-law failure size distributions on the US grid, as well as on the Hungarian networks near the synchronization transition point. We have also investigated the consequence of replacing the usual Gaussian self-frequencies to exponential distributed ones, describing renewable energy sources. We found a drop in the steady state synchronization averages, but the cascade size distribution, both for the US and Hungarian systems, remained insensitive and have kept the universal tails, being characterized by the exponent $\tau \sim 1.8$. We have also investigated the effect of an instantaneous feedback mechanism in case of the Hungarian power-grid. [Ref. 7.3.]

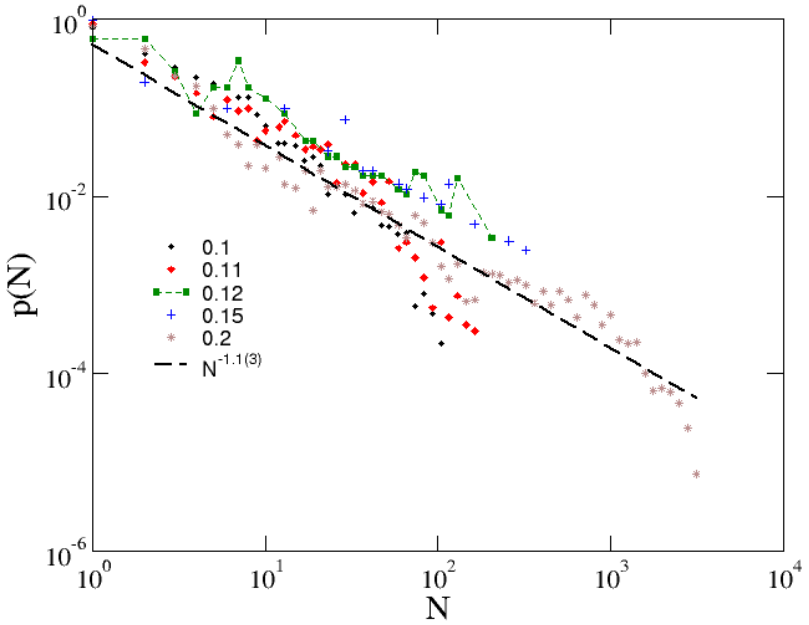

Figure 7.10. *Probability distribution of line failures for different thresholds, as shown in the legends in case of the HU-HV power-grid. The dashed line shows a power-law fit for scaling region of the T = 0.43 results.*

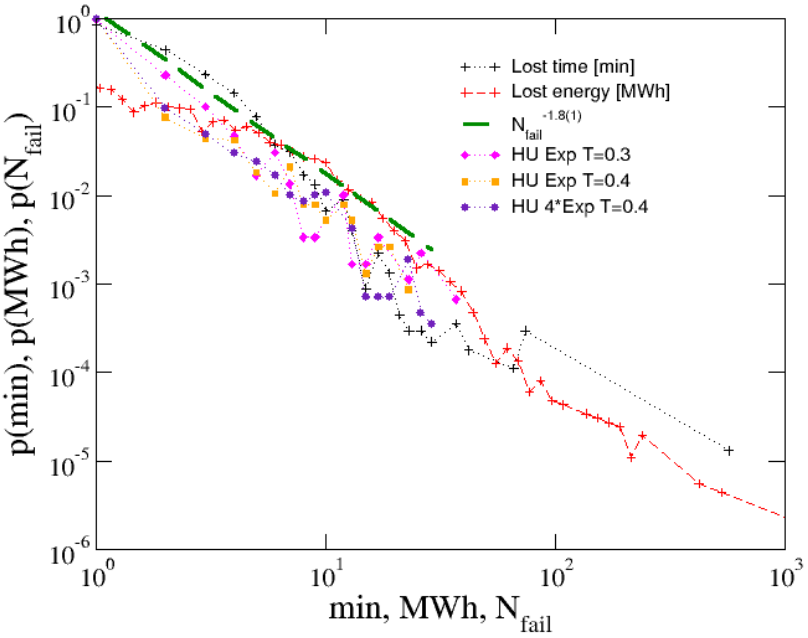

Figure 7.11. *The same as in Fig. 7.10, in the case of exponential tailed self-frequency fluctuations. The green dashed line shows a power-law fit for the scaling region of the T = 0.4 threshold result shifted up for better visibility. For comparison, we also show empirical distributions for the lost time (black dots) and lost energy (orange dashed line) obtained from the MAVIR database.*

REFERENCES AND PUBLICATIONS

Full list of MFA publications in 2020

[1] A. Ábrahám, L. Kócs, E. Albert, B. Tegze, B. Szolnoki, N. Nagy, G. Sáfrán, P. Basa, and Z. Hórvölgyi, "Durability of microporous hybrid silica coatings: Optical and wetting properties," *THIN SOLID FILMS*, vol. 699, 2020., DOI link

[2] Á. C. Horváth, S. Borbély, C. Ö. Boros, L., Komáromi, P. Koppa, P. Barthó, Z. Fekete, "Infrared neural stimulation and inhibition using an implantable silicon photonic microdevice," *MICROSYSTEMS & NANOENGINEERING*, vol. 6, no. 1, 2020., DOI link

[3] I. A. Aleksandrov, T. V. Malin, K. S. Zhuravlev, S. V. Trubina, S. B. Erenburg, B. Pecz, and Y. V. Lebiadok, "Diffusion in GaN/AlN superlattices: DFT and EXAFS study," *APPLIED SURFACE SCIENCE*, vol. 515, 2020., DOI link

[4] I. V. Alenkina, V. K. Kis, I. Felner, E. Kuzmann, Z. Klencsár, and M. I. Oshtrakh, "Structural and magnetic study of the iron cores in iron(III)-polymaltose pharmaceutical ferritin analogue Ferrifol (R)," *JOURNAL OF INORGANIC BIOCHEMISTRY*, vol. 213, 2020., DOI link

[5] S. Al-Zuraiji, D. Lukács, M. Németh, K. Frey, T. Benkó, L. Illés, and J. Pap, "An Iron(III) Complex with Pincer Ligand—Catalytic Water Oxidation through Controllable Ligand Exchange," *REACTIONS*, vol. 1, no. 1, pp. 16–36, 2020., DOI link

[6] S. M. Al-Zuraiji, T. Benkó, L. Illés, M. Németh, K. Frey, A. Sulyok, and J. S. Pap, "Utilization of hydrophobic ligands for water-insoluble Fe(II) water oxidation catalysts – Immobilization and characterization," *JOURNAL OF CATALYSIS*, vol. 381, pp. 615–625, 2020., DOI link

[7] M. Arfaoui, G. Radnóczi, and K. V. Kovács, "Transformations in CrFeCoNiCu High Entropy Alloy Thin Films during In-Situ Annealing in TEM," *COATINGS*, vol. 10, no. 1, 2020., DOI link

[8] G. Attolini, M. Negri, T. Besagni, B. Pecz, and I. Cora, "CVT and PVT growth and characterization of GaS crystals," *MATERIALS SCIENCE AND ENGINEERING B - SOLID STATE MATERIALS FOR ADVANCED TECHNOLOGY*, vol. 261, 2020., DOI link

[9] Q. Awais, B. Katalin, B. Csaba, I. Michal, and D. Jan, "Properties of MWCNTs added Si3N4composites processed fromoxidized silicon nitride powders," *PROCESSING AND APPLICATION OF CERAMICS*, vol. 14, no. 1, pp. 25–31, 2020., DOI link

[10] L. P. Bakos, J. Mensah, K. László, B. Parditka, Z. Erdélyi, E. Székely, I. Lukács, Z. Kónya, C. Cserháti, C. Zhou, J. W. Seo, G. Halasi, and I. M. Szilágyi, "Nitrogen doped carbon aerogel composites with TiO 2 and ZnO prepared by atomic layer deposition," *JOURNAL OF MATERIALS CHEMISTRY C*, vol. 8, no. 20, pp. 6891–6899, 2020., DOI link

[11] L. P. Bakos, N. Justh, U. C. Moura da Silva Bezerra da Costa, K. László, J. L. Lábár, T. Igricz, K. Varga-Josepovits, P. Pasierb, E. Färm, M. Ritala, M. Leskelä, and I. M. Szilágyi, "Photocatalytic and Gas Sensitive Multiwalled Carbon Nanotube/TiO2-ZnO and ZnO-TiO2 Composites Prepared by Atomic Layer Deposition," *NANOMATERIALS*, vol. 10, no. 2, 2020., DOI link

[12] C. Balázsi and K. Balázsi, "A sokoldalú grafén: Kerámiaipari trendek," *GYÁRTÁSTREND*, vol. 13, no. 7–8, pp. 18–20, 2020.

[13] K. Balázsi, M. Furkó, Z. Liao, J. Gluch, D. Medved, R. Sedlák, J. Dusza, E. Zschech, and C. Balázsi, "Porous sandwich ceramic of layered silicon nitride-zirconia composite with various multilayered graphene content," *JOURNAL OF ALLOYS AND COMPOUNDS*, vol. 832, 2020., DOI link

[14] K. Balázsi, M. Furkó, Z. Liao, Z. Fogarassy, D. Medved, E. Zschech, J. Dusza, and C. Balázsi, "Graphene added multilayer ceramic sandwich (GMCS) composites: Structure, preparation and properties," *JOURNAL OF THE EUROPEAN CERAMIC SOCIETY*, vol. 40, no. 14, pp. 4792–4798, 2020., DOI link

[15] K. Balazsi, M. Furkó, P. Klimczyk, and C. Balázsi, "Influence of Graphene and Graphene Oxide on Properties of Spark Plasma Sintered Si3N4 Ceramic Matrix," *CERAMICS*, vol. 3, no. 1, pp. 40–50, 2020., DOI link

[16] K. Balazsi, M. Furko, and C. Balazsi, “Nitrid kerámiák környezetkímélő előállítása és vizsgálata,” in *XXVIII. Nemzetközi Gépészeti Konferencia – OGÉT 2020*, 2020, pp. 33–36.

[17] J. Balogh, L. Bujdosó, Z. Horváth, D. Kaptás, L. Kiss, A. Nakanishi, S. Sajti, and E. Szilágyi, “Alloy formation at the Fe-on-Nb and Nb-on-Fe interfaces,” *VACUUM*, vol. 171, 2020., DOI link

[18] I. Bársony, S. Misák, F. Kun, and G. Battistig, “20 éves a villamosmérnök-képzés a Debreceni Egyetemen,” *ELEKTROTECHNIKA*, vol. 113, no. 5–6, pp. 42–44, 2020.

[19] I. Bársony, “Fenntarthatóság – fenntartásokkal,” *MAGYAR TUDOMÁNY*, vol. 181, no. 7, pp. 948–967, 2020., DOI link

[20] Z. Bay, I. Almár, and G. Kádár, “A világűrkísérletek jövője,” *FIZIKAI SZEMLE*, vol. 70, no. 6, pp. 183–191, 2020.

[21] D. Bazeia, B. F. de Oliveira, J. V. O. Silva, and A. Szolnoki, “Breaking unidirectional invasions jeopardizes biodiversity in spatial May-Leonard systems,” *CHAOS SOLITONS & FRACTALS*, vol. 141, 2020., DOI link

[22] D. Beke, J. Valenta, G. Károlyházy, S. Lenk, Z. Czigány, B. Márkus, K. Kamarás, F. Simon, and A. Gali, “Room-Temperature Defect Qubits in Ultrasmall Nanocrystals,” *JOURNAL OF PHYSICAL CHEMISTRY LETTERS*, vol. 11, no. 5, pp. 1675–1681, 2020., DOI link

[23] S. Bensalem, E. Ghegin, F. Boyer, J. L. Lábár, M. Menyhárd, P. Gergaud, F. Nemouchi, and P. Rodriguez, “Study of the Ti/InGaAs solid-state reactions: Phase formation sequence and diffusion schemes,” *MATERIALS SCIENCE IN SEMICONDUCTOR PROCESSING*, vol. 113, 2020., DOI link

[24] F. Biro, I. Barsony, C. Ducso, N. Samotaev, A. Pisliakov, D. Filipchuk, and K. Oblov, “SOI Based Low Power Thermocatalytic Sensor with Nanostructured Gas Sensitive Material,” *ECS MEETING ABSTRACTS*, vol. MA2020-01, no. 28, 2020., DOI link

[25] M. Blahota, I. Blahota, and A. Szolnoki, “Equal partners do better in defensive alliances,” *EUROPHYSICS LETTERS*, vol. 131, no. 5, 2020., DOI link

[26] M. Chelu, H. Stroescu, M. Anastasescu, J. M. Calderon-Moreno, S. Preda, M. Stoica, Z. Fogarassy, P. Petrik, M. Gheorghe, C. Parvulescu, C. Brasoveanu, A. Dinescu, C. Moldovan, and M. Gartner, “High-quality PMMA/ZnO NWs piezoelectric coating on rigid and flexible metallic substrates,” *APPLIED SURFACE SCIENCE*, vol. 529, 2020., DOI link

[27] I. Chepkasov, V. Baidyshev, E. Sukhanova, M. Visotin, P. Süle, and Z. Popov, “Iron silicides formation on Si (100) and (111) surfaces through theoretical modeling of sputtering and annealing,” *APPLIED SURFACE SCIENCE*, vol. 527, 2020., DOI link

[28] I. Cora, Z. Fogarassy, R. Fornari, M. Bosi, A. Rečnik, and B. Pécz, “In situ TEM study of κ→β and κ→γ phase transformations in Ga2O3,” *ACTA MATERIALIA*, vol. 183, pp. 216–227, 2020., DOI link

[29] B. Csernyus, Á. Szabó, A. Zátonyi, R. Hodován, C. Lázár, Z. Fekete, L. Erőss, and A. Pongrácz, “Recent antiepileptic and neuroprotective applications of brain cooling,” *SEIZURE-EUROPEAN JOURNAL OF EPILEPSY*, vol. 82, pp. 80–90, 2020., DOI link

[30] Z. Dallos, V. K. Kis, F. Kristály, and I. Dódony, “Leaching mechanism of bioapatite in carbonate-saturated water,” *CRYSTENGCOMM*, vol. 22, no. 16, pp. 2788–2794, 2020., DOI link

[31] P. S. Dániel, P. Szilárd, Z. Dániel, N. Norbert, H. Zoltán, O. Zoltán, Z. Zsolt, and D. András, “Single-nanoparticle spectroscopy in colloid chemistry,” in *Proceedings of Anyagtudományi Szimpózium*, 2020, pp. 18–21.

[32] P. S. Dániel, Z. Dániel, Z. Zsolt, N. Norbert, and D. Andras, “Detecting short-chain thiol binding on CTAB-stabilised gold nanorods at single particle level,” in *Proceedings of Anyagtudományi Szimpózium*, 2020, pp. 34–36.

[33] M. L. Debreczeni, I. Szekacs, B. Kovacs, A. Saftics, S. Kurunczi, P. Gál, J. Dobó, L. Cervenak, and R. Horvath, “Human primary endothelial label-free biochip assay reveals unpredicted functions of plasma serine proteases,” *SCIENTIFIC REPORTS*, vol. 10, no. 1, 2020., DOI link

[34] V. A. Demin, D. G. Kvashnin, P. Vancsó, G. I. Márk, and L. A. Chernozatonskii, “Wave-Packet Dynamics Study of the Transport Characteristics of Perforated Bilayer Graphene Nanoribbons,” *JETP LETTERS*, vol. 112, no. 5, pp. 305–309, 2020., DOI link

[35] A. Domán, S. Klébert, J. Madarász, G. Sáfrán, Y. Wang, and K. László, “Graphene Oxide Protected Copper Benzene-1,3,5-Tricarboxylate for Clean Energy Gas Adsorption,” *NANOMATERIALS*, vol. 10, no. 6, 2020., DOI link

[36] O. Dugerjav, G. Duvjir, L. Tapaszto, and C. Hwang, “Growth of Graphene on the Cu(110) Surface,” *JOURNAL OF PHYSICAL CHEMISTRY C*, vol. 124, no. 22, pp. 12106–12111, 2020., DOI link

[37] E. Albert, B. Tegze, Z. Hajnal, D. Zámbó, D.P. Szekrényes, A. Deák, Z. Hórvölgyi, N. Nagy., “How to overcome the uncertainties of polynomial fitting in contact angle determination?,” in *Proceedings of Anyagtudományi Szimpózium*, 2020, pp. 37–38.

[38] D. Erzsébet, Z. R. György, and D. István, “Reactions between amporphous thin films of silicon with nickel on heating.” 2020.

[39] M. Fábián, Z. Kovács, J. L. Lábár, A. Sulyok, Z. E. Horváth, I. Székács, and K. V. Kovács, “Network structure and thermal properties of bioactive (SiO2–CaO–Na2O–P2O5) glasses,” *JOURNAL OF MATERIALS SCIENCE*, vol. 55, no. 6, pp. 2303–2320, 2020., DOI link

[40] F. Z. Fedor, A. Zátonyi, D. Cserpán, Z. Somogyvári, Z. Borhegyi, G. Juhász, and Z. Fekete, “Application of a flexible polymer microECoG array to map functional coherence in schizophrenia model,” *METHODSX*, vol. 7, 2020., DOI link

[41] B. Francz, R. Ungai-Salánki, É. Sautner, R. Horvath, and B. Szabó, “Subnanoliter precision piezo pipette for single-cell isolation and droplet printing,” *MICROFLUIDICS AND NANOFLUIDICS*, vol. 24, no. 2, 2020., DOI link

[42] M. Furko and C. Balázsi, “Morphological, Chemical, and Biological Investigation of Ionic Substituted, Pulse Current Deposited Calcium Phosphate Coatings,” *MATERIALS*, vol. 13, no. 20, 2020., DOI link

[43] M. Furko and C. Balázsi, “Calcium Phosphate Based Bioactive Ceramic Layers on Implant Materials Preparation, Properties, and Biological Performance,” *COATINGS*, vol. 10, no. 9, 2020., DOI link

[44] M. Gajdics, T. Spassov, V. Kovács Kis, F. Béke, Z. Novák, E. Schafler, and Á. Révész, “Microstructural Investigation of Nanocrystalline Hydrogen-Storing Mg-Titanate Nanotube Composites Processed by High-Pressure Torsion,” *ENERGIES*, vol. 13, no. 3, 2020., DOI link

[45] M. Gajdics, T. Spassov, V. K. Kis, E. Schafler, and Á. Révész, “Microstructural and morphological investigations on Mg-Nb2O5-CNT nanocomposites processed by high-pressure torsion for hydrogen storage applications,” *INTERNATIONAL JOURNAL OF HYDROGEN ENERGY*, vol. 45, no. 14, pp. 7917–7928, 2020., DOI link

[46] N. G. Galkin, K. N. Galkin, S. A. Dotsenko, D. L. Goroshko, Z. Fogarassy, and B. Pécz, “The growth processes and crystal structure of Ca silicides films grown by MBE at 500 °C on a Si(001) substrate,” *MATERIALS CHEMISTRY AND PHYSICS*, vol. 253, 2020., DOI link

[47] N. G. Galkin, K. N. Galkin, A. V. Tupkalo, Z. Fogarassy, and B. Pécz, “A low temperature growth of Ca silicides on Si(100) and Si(111) substrates: Formation, structure, optical properties and energy band structure parameters,” *JOURNAL OF ALLOYS AND COMPOUNDS*, vol. 813, 2020., DOI link

[48] N. G. Galkin, K. N. Galkin, A. V. Tupkalo, E. A. Chusovitin, D. L. Goroshko, Z. Fogarassi, and B. Pecz, “Semitransparent and conductive CaSi 2 films for silicon device applications,” *JAPANESE JOURNAL OF APPLIED PHYSICS*, vol. 59, no. SF, 2020., DOI link

[49] J. Gubicza, G. Kapoor, D. Ugi, L. Péter, J. L. Lábár, and G. Radnóczi, “Micropillar compression study on the deformation behavior of electrodeposited Ni-Mo films,” *COATINGS*, vol. 10, no. 3, 2020., DOI link

[50] J. Gubicza, M. El-Tahawy, J. L. Lábár, E. V. Bobruk, M. Y. Murashkin, R. Z. Valiev, and N. Q. Chinh, “Evolution of microstructure and hardness during artificial aging of an ultrafine-grained Al-Zn-Mg-Zr alloy processed by high pressure torsion,” *JOURNAL OF MATERIALS SCIENCE*, vol. 55, pp. 16791–16805, 2020., DOI link

[51] S. György, S. Noémi, D. Gergely, K. Benjámin, and S. Miklós, “Self-regulating gas dosage for reactive RF sputtering of composition spread Hf oxy-nitride combinatorial layers,” in *Proceedings of Anyagtudományi Szimpózium*, 2020, pp. 41–44.

[52] J. Gyulai, “Nagy Elemér (1920–2000),” *FIZIKAI SZEMLE*, vol. 70, no. 7–8, pp. 226–227, 2020.

[53] M. Hans, H. Ruess, Z. Czigany, J. Krause, P. Ondracka, D. Music, S. Evertz, D. M. Holzapfel, D. Primetzhofer, and J. M. Schneider, “Spinodal decomposition of reactively sputtered (V0.64Al0.36)(0.49)N-0.51 thin films,” *SURFACE AND COATINGS TECHNOLOGY*, vol. 389, 2020., DOI link

[54] J. Hlinka, Z. Fogarassy, Á. Cziráki, and Z. Weltsch, “Wetting Properties, Recrystallization Phenomena and Interfacial Reactions between Laser Treated Cu Substrate and SAC305 Solder,” *APPLIED SURFACE SCIENCE*, vol. 501, 2020., DOI link

[55] Á. Horváth, N. Nagy, G. Vértesy, and R. Schiller, “Phenomenology of the effect of ion irradiation on the work function of metals,” *NUCLEAR INSTRUMENTS & METHODS IN PHYSICS RESEARCH SECTION B-BEAM INTERACTIONS WITH MATERIALS AND ATOMS*, vol. 466, pp. 12–16, 2020., DOI link

[56] Z. G. Horváth, G. Juhász, M. Fried, C. Major, and P. Petrik, “Imaging optical inspection device with a pinhole camera,” 2020.

[57] P. T. Hung, M. Kawasaki, J.-K. Han, J. L. Lábár, and J. Gubicza, “Thermal stability of a nanocrystalline HfNbTiZr multi-principal element alloy processed by high-pressure torsion,” *MATERIALS CHARACTERIZATION*, vol. 168, 2020., DOI link

[58] C. Ildikó, L. L. János, and S. György, “Concentration dependent pair-correlation in amorphous Si1−xGex layers revealed by micro-combinatorial TEM,” in *Proceedings of Anyagtudományi Szimpózium*, 2020, pp. 26–30.

[59] V. Isnaini, T. Kolonits, Z. Czigány, J. Gubicza, S. Zsurzsa, L. Varga, E. Tóth-Kádár, L. Pogány, L. Péter, and I. Bakonyi, “Room-temperature magnetoresistance of nanocrystalline Ni metal with various grain sizes,” *EUROPEAN PHYSICAL JOURNAL PLUS*, vol. 135, no. 1, 2020., DOI link

[60] H. Jankovics, B. Kovacs, A. Saftics, T. Gerecsei, É. Tóth, I. Szekacs, F. Vonderviszt, and R. Horvath, “Grating-coupled interferometry reveals binding kinetics and affinities of Ni ions to genetically engineered protein layers,” *SCIENTIFIC REPORTS*, vol. 10, no. 1, 2020., DOI link

[61] L. Juhász, B. Parditka, P. Petrik, Z. Erdélyi, and C. Cserháti, “Porózus arany nanorészecskék optikai tulajdonságainak kevert fém-oxidrétegekkel történő hangolása,” *FIZIKAI SZEMLE*, vol. 70, no. 9, pp. 309–313, 2020.

[62] L. Juhász, B. Parditka, P. Petrik, C. Cserháti, and Z. Erdélyi, “Continuous tuning of the plasmon resonance frequency of porous gold nanoparticles by mixed oxide layers,” *JOURNAL OF POROUS MATERIALS*, vol. 27, pp. 1583–1588, 2020., DOI link

[63] Z. Juhász and J. Sipos, “A magyar népzene őstörténetének kutatása korreláló zenei és genetikai típusok alapján,” in *Magyar őstörténeti műhelybeszélgetés*, 2020, pp. 55–78.

[64] A. Kakanakova-Georgieva, G. K. Gueorguiev, D. G. Sangiovanni, N. Suwannaharn, I. G. Ivanov, I. Cora, B. Pécz, G. Nicotra, and F. Giannazzo, “Nanoscale phenomena ruling deposition and intercalation of AlN at the graphene/SiC interface,” *NANOSCALE*, vol. 12, no. 37, pp. 19470–19476, 2020., DOI link

[65] B. Kalas, Z. Zolnai, G. Safran, M. Serenyi, E. Agocs, T. Lohner, A. Nemeth, N. Khanh, M. Fried, and P. Petrik, “Micro-combinatorial sampling of the optical properties of hydrogenated amorphous Si (1-x) Ge (x) for the entire range of compositions towards a database for optoelectronics,” *SCIENTIFIC REPORTS*, vol. 10, no. 1, 2020., DOI link

[66] B. Kalas, K. Ferencz, A. Saftics, Z. Czigány, M. Fried, and P. Petrik, “Biosensing in the ultraviolet wavelength range by Kretschmann-Raether ellipsometry,” in *Proceedings of Anyagtudományi Szimpózium*, 2020, pp. 16–17.

[67] K. Kandrai, P. Vancso, G. Kukucska, J. Koltai, G. Baranka, A. Hoffmann, A. Pekker, K. Kamaras, Z. Horvath, A. Vymazalova, L. Tapaszto, and P. Nemes-Incze, “Signature of Large-Gap Quantum Spin Hall State in the Layered Mineral Jacutingaite,” *NANO LETTERS*, vol. 20, no. 7, pp. 5207–5213, 2020., DOI link

[68] N. Kanyo, K. D. Kovacs, A. Saftics, I. Szekacs, B. Peter, A. R. Santa-Maria, F. R. Walter, A. Dér, M. A. Deli, and R. Horvath, “Glycocalyx regulates the strength and kinetics of cancer cell adhesion revealed by biophysical models based on high resolution label-free optical data,” *SCIENTIFIC REPORTS*, vol. 10, 2020., DOI link

[69] G. Kapoor, T. Kvackaj, A. Heczel, J. Bidulská, R. Kočiško, Z. Fogarassy, D. Simcak, and J. Gubicza, “The Influence of Severe Plastic Deformation and Subsequent Annealing on the Microstructure and Hardness of a Cu–Cr–Zr Alloy,” *MATERIALS*, vol. 13, no. 10, 2020.

[70] K. Bán, M. Nagy, Zs. Fogarassy, A. Szabó, “Comparison of direct and indirect structural analysis of HAZ after laser cutting in amorphous alloys,” *ACTA PHYSICA POLONICA A*, vol. 137, no. 5, pp. 861–863, 2020., DOI link

[71] N. Q. Khánh, J. Radó, Z. E. Horváth, S. Soleimani, B. Oyunbolor, and J. Volk, “The effect of substrate bias on the piezoelectric properties of pulse DC magnetron sputtered AlN thin films,” *JOURNAL OF MATERIALS SCIENCE: MATERIALS IN ELECTRONICS*, vol. 31, no. 24, pp. 22833–22843, 2020., DOI link

[72] L. Khomenkova, K. Makasheva, P. Petrik, Z. Tsybrii, O. Melnichuk, L. Melnichuk, I. Balberg, F. Gourbilleau, and N. Korsunska, “Spectroscopic characterization of phase transformation in Ge-rich Al2O3 films grown by magnetron co-sputtering,” *MATERIALS LETTERS*, vol. 277, 2020., DOI link

[73] L. Khomenkova, K. Makasheva, P. Petrik, C. Bonafos, N. Ratel-Ramond, O. Melnichuk, L. Melnichuk, I. Balberg, F. Gourbilleau, and N. Korsunska, “Thermally stimulated evolution of optical and structural properties of germanium-doped alumina films,” *ECS TRANSACTIONS*, vol. 97, no. 2, pp. 81–90, 2020., DOI link

[74] L. Khomenkova, D. Lehninger, E. Agocs, P. Petrik, X. Portier, N. Korsunska, O. Melnichuk, F. Gourbilleau, and J. Heitmann, “Whether Ge-Rich ZrO2 and Ge-Rich HfO2 Materials Have Similar Reaction on Annealing Treatment?,” *ECS TRANSACTIONS*, vol. 97, no. 1, pp. 49–60, 2020., DOI link

[75] L. Khouchaf, K. Boulahya, P. P. Das, S. Nicolopoulos, V. K. Kis, and J. L. Lábár, “Study of the Microstructure of Amorphous Silica Nanostructures Using High-Resolution Electron Microscopy, Electron Energy Loss Spectroscopy, X-ray Powder Diffraction, and Electron Pair Distribution Function,” *MATERIALS*, vol. 13, no. 19, 2020., DOI link

[76] B. Király and G. Szabó, “Interplay of Elementary Interactions Causing Social Traps in Evolutionary Games,” *FRONTIERS IN PHYSICS*, vol. 8, 2020., DOI link

[77] S. Kollarics, A. Bojtor, K. Koltai, B. G. Márkus, K. Holczer, J. Volk, G. Klujber, M. Szieberth, and F. Simon, “Optical–Microwave Pump–Probe Studies of Electronic Properties in Novel Materials,” *PHYSICA STATUS SOLIDI B-BASIC RESEARCH*, vol. 257, no. 12, 2020., DOI link

[78] T. Kolonits, Z. Czigány, L. Péter, I. Bakonyi, and J. Gubicza, “Improved hardness and thermal stability of nanocrystalline nickel electrodeposited with the addition of cysteine,” *NANOMATERIALS*, vol. 10, no. 11, 2020., DOI link

[79] M. Kroker, P. Souček, P. Matej, L. Zábranský, Z. Czigány, K. Balázsi, and P. Vašina, “Composition, Structure and Mechanical Properties of Industrially Sputtered Ta–B–C Coatings,” *COATINGS*, vol. 10, no. 9, 2020., DOI link

[80] P. Kun, B. Fülöp, G. Dobrik, P. Nemes-Incze, I. E. Lukács, S. Csonka, C. Hwang, and L. Tapasztó, “Robust quantum point contact operation of narrow graphene constrictions patterned by AFM cleavage lithography,” *NPJ 2D MATERIALS AND APPLICATIONS*, vol. 4, no. 1, 2020., DOI link

[81] Z. Labadi, B. Kalas, A. Saftics, L. Illes, H. Jankovics, E. Bereczk-Tompa, A. Sebestyen, E. Toth, B. Kakasi, C. Moldovan, B. Firtat, M. Gartner, M. Gheorghe, F. Vonderviszt, M. Fried, and P. Petrik, “Sensing Layer for Ni Detection in Water Created by Immobilization of Bioengineered Flagellar Nanotubes on Gold Surfaces,” *ACS BIOMATERIALS-SCIENCE & ENGINEERING*, vol. 6, no. 7, pp. 3811–3820, 2020., DOI link

[82] S. Lamnini, “Synthesis and characterization of multiwall carbon nanotube reinforced yttria stabilized zirconia composites,” Ph.D thesis, Óbudai Egyetem, 2020.

[83] H. S. Lawson, G. Holló, R. Horvath, H. Kitahata, and I. Lagzi, “Chemical Resonance, Beats, and Frequency Locking in Forced Chemical Oscillatory Systems,” *JOURNAL OF PHYSICAL CHEMISTRY LETTERS*, vol. 11, no. 8, pp. 3014–3019, 2020., DOI link

[84] T. Lohner, E. Szilágyi, Z. Zolnai, A. Németh, Z. Fogarassy, L. Illés, E. Kótai, P. Petrik, and M. Fried, “Determination of the Complex Dielectric Function of Ion-Implanted Amorphous Germanium by Spectroscopic Ellipsometry,” *COATINGS*, vol. 10, no. 5, 2020., DOI link

[85] S. Lukácsi, T. Gerecsei, K. Balázs, B. Francz, B. Szabó, A. Erdei, and Z. Bajtay, “The differential role of CR3 (CD11b/CD18) and CR4 (CD11c/CD18) in the adherence, migration and podosome formation of human macrophages and dendritic cells under inflammatory conditions.,” *PLOS ONE*, vol. 15, no. 5, 2020., DOI link

[86] S. Lukácsi, B. Mácsik-Valent, Z. Nagy-Baló, K. G. Kovács, K. Kliment, Z. Bajtay, and A. Erdei, “Utilization of complement receptors in immune cell-microbe interaction,” *FEBS LETTERS*, vol. 594, no. 16, pp. 2695–2713, 2020., DOI link

[87] G. Márton, E. Z. Tóth, L. Wittner, R. Fiáth, D. Pinke, G. Orbán, D. Meszéna, I. Pál, E. L. Győri, Z. Bereczki, Á. Kandrács, K. T. Hofer, A. Pongrácz, I. Ulbert, and K. Tóth, “The neural tissue around SU-8 implants: A quantitative in vivo biocompatibility study,” *MATERIALS SCIENCE & ENGINEERING C-MATERIALS FOR BIOLOGICAL APPLICATIONS*, vol. 112, 2020., DOI link

[88] P. Márton, E. Albert, N. Nagy, B. Tegze, G. S. Szabó, and Z. Hórvölgyi, “Chemically modified chitosan coatings: wetting and electrochemical studies,” *STUDIA UNIVERSITATIS BABES-BOLYAI CHEMIA*, vol. 65, no. 3, pp. 63–79, 2020., DOI link

[89] D. Merkel, A. Lengyel, D. Nagy, A. Németh, Z. Horváth, C. Bogdán, M. Gracheva, G. Hegedűs, S. Sajti, G. Radnóczi, and E. Szilágyi, “Reversible control of magnetism in FeRh thin films,” *SCIENTIFIC REPORTS*, vol. 10, no. 1, 2020., DOI link

[90] M. Fried, R. Bogar, Z. Lábadi, Z. E. Horvath, Z. Zolnai "Combinatorial Investigation of WO3-MoO3 Mixed Layers by Spectroscopic Ellipsometry to assess Effective Medium Approximation," in *Proceedings of Anyagtudományi Szimpózium*, 2020, pp. 3–10.

[91] M.Fried, *Proceedings of Anyagtudományi Szimpózium*. Budapest: Óbudai Egyetem, 2020.

[92] S. Mirzaei, M. Alishahi, P. Souček, J. Ženíšek, D. Holec, N. Koutná, V. Buršíková, M. Stupavská, L. Zábranský, F. Burmeister, B. Blug, Z. Czigány, K. Balázsi, R. Mikšová, and P. Vašina, "The effect of chemical composition on the structure, chemistry and mechanical properties of magnetron sputtered W-B-C coatings: Modeling and experiments," *SURFACE AND COATINGS TECHNOLOGY*, vol. 383, 2020., DOI link

[93] A. G. Nagy, A. Bonyár, I. Szekacs, and R. Horvath, "Analysis of single-cell force-spectroscopy data of Vero cells recorded by FluidFM BOT," in *2020 IEEE 26th International Symposium for Design and Technology in Electronic Packaging (SIITME)*, 2020, pp. 21–25., DOI link

[94] A. G. Nagy, I. Szekacs, A. Bonyar, and R. Horvath, "Assembly of Epithelial Monolayers and Transmigration of Cancer Cells Captured with Phase Holographic Imaging," *INTERNATIONAL SPRING SEMINAR ON ELECTRONICS TECHNOLOGY*, vol. 43, 2020., DOI link

[95] G. Nagy, T. Gál, D. F. Srankó, G. Sáfrán, B. Maróti, I. E. Sajó, F.-P. Schmidt, and A. Beck, "Selective aerobic oxidation of benzyl alcohol on alumina supported Au-Ru and Au-Ir catalysts," *MOLECULAR CATALYSIS*, vol. 492, 2020., DOI link

[96] M. Nagy, K. Bán, Z. Fogarassy, and R. Berényi, "Amorf és nanokristályos lágymágneses anyagok bevezethetőségének vizsgálata gépjármű elektromotorok gyártásába," *BÁNYÁSZATI ÉS KOHÁSZATI LAPOK-KOHÁSZAT*, vol. 153, no. 1, pp. 40–43, 2020.

[97] T. Nagyné-Kovács, L. Studnicka, I. Lukács, K. László, P. Pasierb, I. Szilágyi, and G. Pokol, "Hydrothermal Synthesis and Gas Sensing of Monoclinic MoO3 Nanosheets," *NANOMATERIALS*, vol. 10, no. 5, 2020., DOI link

[98] T. Nagyné-Kovács, I. E. Lukács, A. Szabó, K. Hernadi, T. Igricz, K. László, I. M. Szilágyi, and G. Pokol, "Effect of pH in the hydrothermal preparation of monoclinic tungsten oxide," *JOURNAL OF SOLID STATE CHEMISTRY*, vol. 281, 2020., DOI link

[99] P. Nagy, N. Rohbeck, G. Roussely, P. Sortais, J. L. Lábár, J. Gubicza, J. Michler, and L. Pethö, "Processing and characterization of a multibeam sputtered nanocrystalline CoCrFeNi high-entropy alloy film," *SURFACE AND COATINGS TECHNOLOGY*, vol. 386, 2020., DOI link

[100] R. Nagy, M. Király, P. Petrik, and Z. Hózer, "Infrared observation of ballooning and burst of nuclear fuel cladding tubes," *NUCLEAR ENGINEERING AND DESIGN*, vol. 371, 2020., DOI link

[101] P. Németh, K. McColl, R. Smith, M. Murri, L. Garvie, M. Alvaro, B. Pécz, A. Jones, F. Corà, C. Salzmann, and P. McMillan, "Diamond-Graphene Composite Nanostructures," *NANO LETTERS*, vol. 20, no. 5, pp. 3611–3619, 2020., DOI link

[102] N. Nagy, "A new effect observed on superhydrophilic surfaces using the capillary bridge probe method," in *Proceedings of Anyagtudományi Szimpózium*, 2020, pp. 39–40.

[103] A. Nyáry, A. Gubicza, J. Overbeck, L. Pósa, P. Makk, M. Calame, A. Halbritter, and M. Csontos, "A non-oxidizing fabrication method for lithographic break junctions of sensitive metals," *NANOSCALE ADVANCES*, vol. 2, no. 9, pp. 3829–3833, 2020., DOI link

[104] G. Ódor and B. Hartmann, "Power-Law Distributions of Dynamic Cascade Failures in Power-Grid Models," *ENTROPY*, vol. 22, no. 6, 2020., DOI link

[105] Z. Osváth, A. Pálinkás, G. Piszter, and G. Molnár, "Synthesis and Characterization of Graphene–Silver Nanoparticle Hybrid Materials," *MATERIALS*, vol. 13, no. 20, 2020., DOI link

[106] A. Palinkas, "Grafén-nanorészecske hibrid szerkezetek előállítása és vizsgálata pásztázószondás módszerekkel," Ph.D. thesis BME, 2020.

[107] Z. Pápa, J. Kasza, J. Budai, Z. Márton, G. Molnár, and P. Dombi, "Tuning plasmonic field enhancement and transients by far-field coupling between nanostructures," *APPLIED PHYSICS LETTERS*, vol. 117, no. 8, 2020., DOI link

[108] B. Pécz, G. Nicotra, F. Giannazzo, R. Yakimova, A. Koos, and A. Kakanakova-Georgieva, "Indium Nitride at the 2D Limit," *ADVANCED MATERIALS*, vol. 33, no. 1, 2020., DOI link

[109] S. Pelli, I. Bányász, E. Szilágyi, I. Rajta, G. Nagy, G. Conti, S. Berneschi, V. Havránek, V. Vosecek, N. Nagy, Z. Szabó, M. Veres, A. Speghini, and G. Righini, "Carbon ion microbeam fabrication of channel waveguide in tellurite glass (Conference Presentation)," *PROCEEDINGS OF SPIE - THE INTERNATIONAL SOCIETY FOR OPTICAL ENGINEERING*, vol. 11357, 2020., DOI link

[110] B. Peter, A. Saftics, B. Kovacs, S. Kurunczi, and R. Horvath, "Oxidization increases the binding of EGCG to serum albumin revealed by kinetic data from label-free optical biosensor with reference channel," *ANALYST*, vol. 145, no. 2, pp. 588–595, 2020., DOI link

[111] G. Peto, I. Dézsi, L. F. Kiss, Z. E. Horváth, D. Oszetzky, A. Nagy, G. Molnár, C. S. Daróczi, K. Frey, and A. Horváth, "Tracing fcc iron in oxide dispersion strengthened steel by photoelectron emission, Mössbauer spectroscopy, and X-ray diffraction," *VACUUM*, vol. 175, 2020. DOI link

[112] P. Petrik, A. S. Racz, and M. Menyhard, "Complementary physicochemical analysis by ellipsometry and Auger spectroscopy of nano-sized protective coating layers," *APPLIED SURFACE SCIENCE*, vol. 534, 2020., DOI link

[113] P. Petrik, "Optical Characterization of Oxide-Based Materials Using Ellipsometry," in *Oxide-Based Materials and Structures*, 2020, pp. 5–29.

[114] G. Piszter, K. Kertész, Z. Bálint, and L. P. Biró, "Stability and Selective Vapor Sensing of Structurally Colored Lepidopteran Wings Under Humid Conditions," *SENSORS*, vol. 20, no. 11, 2020., DOI link

[115] O. Pohorelec, M. Ťapajna, D. Gregušová, F. Gucmann, S. Hasenöhrl, Š. Haščík, R. Stoklas, A. Seifertová, B. Pécz, L. Tóth, and J. Kuzmík, "Investigation of interfaces and threshold voltage instabilities in normally-off MOS-gated InGaN/AlGaN/GaN HEMTs," *APPLIED SURFACE SCIENCE*, vol. 528, 2020., DOI link

[116] A. Policicchio, G. Conte, S. Stelitano, C. Bonaventura, A. Putz, C. Ianasi, L. Almasy, Z. Horvath, and R. Agostino, "Hydrogen storage performances for mesoporous silica synthesized with mixed tetraethoxysilane and methyltriethoxysilane precursors in acidic condition," *COLLOIDS AND SURFACES A : PHYSICOCHEMICAL AND ENGINEERING ASPECTS*, vol. 601, 2020., DOI link

[117] A. S. Racz, D. Dworschak, M. Valtiner, and M. Menyhard, "Scratching resistance of SiC-rich nano-coatings produced by noble gas ion mixing," *SURFACE AND COATINGS TECHNOLOGY*, vol. 386, 2020., DOI link

[118] J. Radó, J. Volk, and A. Nagy, "Jármű gumiabroncs menetdinamikai állapotát mérő eszköz," 2020.

[119] J. Radó, C. Dücső, G. Szebényi, N. Zbigniew, and P. Fürjes, "ERŐVISSZAJELZÉS ÉS MESTERSÉGES TAPINTÁS A MINIMÁLISAN INVAZÍV SEBÉSZETBEN," *FIZIKAI SZEMLE*, vol. 70, no. 4, pp. 134–140, 2020.

[120] A. Revesz, T. Spassov, V. Kis, E. Schafler, and M. Gajdics, "The Influence of Preparation Conditions on the Hydrogen Sorption of Mg-Nb2O5-CNT Produced by Ball Milling and Subsequent High-Pressure Torsion," *JOURNAL OF NANOSCIENCE AND NANOTECHNOLOGY*, vol. 20, no. 7, pp. 4587–4590, 2020., DOI link

[121] I. Rigó, M. Veres, Z. Pápa, L. Himics, R. Öcsi, O. Hakkel, and P. Fürjes, "Plasmonic enhancement in gold coated inverse pyramid substrates with entrapped gold nanoparticles," *JOURNAL OF QUANTITATIVE SPECTROSCOPY & RADIATIVE TRANSFER*, vol. 253, 2020., DOI link

[122] M.-H. Rim, E. Agocs, R. Dixson, P. Kavuri, A. E. Vladár, and R. K. Attota, "Detecting nanoscale contamination in semiconductor fabrication using through-focus scanning optical microscopy," *JOURNAL OF VACUUM SCIENCE AND TECHNOLOGY B: NANOTECHNOLOGY AND MICROELECTRONICS*, vol. 38, no. 5, 2020., https://doi.org/10.1116%2F6.0000352

[123] G. Sáfrán, N. Szász, G. Dobrik, B. Kalas, and M. Serényi, "Smart gas dosage by a peristaltic pump for reactive RF sputtering of composition spread combinatorial hafnium-oxy-nitride layers," *VACUUM*, vol. 182, 2020., DOI link

[124] A. Saftics, B. Türk, A. Sulyok, N. Nagy, E. Agócs, B. Kalas, P. Petrik, M. Fried, N. Khánh, A. Prósz, K. Kamarás, I. Szekacs, R. Horvath, and S. Kurunczi, "Dextran-based Hydrogel Layers for Biosensors," in *Nanobiomaterial Engineering*, 2020, pp. 139–164., DOI link

[125] N. Samotaev, K. Oblov, P. Dzhumaev, D. Filipchuk, and C. Ducso, "Micro-catalytic gas sensor operating modes for extended life service, increasing sensitivity to target gases and power consumption reduction," *JOURNAL OF PHYSICS-CONFERENCE SERIES*, vol. 1681, no. 1, 2020., DOI link

[126] N. Samotaev, A. Pisliakov, A. Gorshkova, P. Dzhumaev, I. Barsony, C. Ducso, and F. Biro, "Al2O3 nanostructured gas sensitive material for silicon based low power thermocatalytic sensor," *MATERIALS TODAY: PROCEEDINGS*, vol. 30, pp. 443–447, 2020., DOI link

[127] B. Sánta, D. Molnár, P. Haiber, A. Gubicza, E. Szilágyi, Z. Zolnai, A. Halbritter, and M. Csontos, “Nanosecond resistive switching in Ag/AgI/PtIr nanojunctions,” *BEILSTEIN JOURNAL OF NANOTECHNOLOGY*, vol. 11, pp. 92–100, 2020., DOI link

[128] S. Soleimani, B. Kalas, Z. E. Horváth, Z. Zolnai, Z. Czigány, A. Németh, P. Petrik, and J. Volk, “Optimization of co-sputtered CrxAl1−xN thin films for piezoelectric MEMS devices,” *JOURNAL OF MATERIALS SCIENCE: MATERIALS IN ELECTRONICS*, vol. 31, no. 11, pp. 8136–8143, 2020., DOI link

[129] J. Stoever, J. E. Boschker, A. S. Bin, M. Schmidbauer, P. Petrik, J. Schwarzkopf, M. Albrecht, and K. Irmscher, “Approaching the high intrinsic electrical resistivity of NbO2 in epitaxially grown films,” *APPLIED PHYSICS LETTERS*, vol. 116, no. 18, 2020., DOI link

[130] M. Stucchi, S. Capelli, S. Cardaci, S. Cattaneo, A. Jouve, A. Beck, G. Sáfrán, C. Evangelisti, A. Villa, and L. Prati, “Synergistic effect in Au-Cu bimetallic catalysts for the valorization of Lignin-Derived compounds,” *CATALYSTS*, vol. 10, no. 3, 2020., DOI link

[131] D. P. Szekrényes, D. Kovács, Z. Zolnai, and A. Deák, “Chemical Interface Damping as an Indicator for Hexadecyltrimethylammonium Bromide Replacement by Short-Chain Thiols on Gold Nanorods,” *JOURNAL OF PHYSICAL CHEMISTRY C*, vol. 124, no. 36, pp. 19736–19742, 2020., DOI link

[132] D. P. Szekrényes, “Az arany a nanotechnológia szolgálatában. Trükkös színektől a rákgyógyításig,” *ÉLET ÉS TUDOMÁNY*, vol. 75, no. 38, pp. 1196–1198, 2020.

[133] M. Szendro, P. Sule, G. Dobrik, and L. Tapaszto, “Ultra-flat twisted superlattices in 2D heterostructures,” *NPJ COMPUTATIONAL MATERIALS*, vol. 6, no. 1, 2020., DOI link

[134] A. Szolnoki, B. F. de Oliveira, and D. Bazeia, “Pattern formations driven by cyclic interactions: A brief review of recent developments,” *EUROPHYSICS LETTERS*, vol. 131, no. 6, 2020., DOI link

[135] A. Szolnoki and X. Chen, “Blocking defector invasion by focusing on the most successful partner,” *APPLIED MATHEMATICS AND COMPUTATION*, vol. 385, 2020., DOI link

[136] A. Szolnoki and X. Chen, “Strategy dependent learning activity in cyclic dominant systems,” *CHAOS SOLITONS & FRACTALS*, vol. 138, 2020., DOI link

[137] A. Szolnoki and X. Chen, “Gradual learning supports cooperation in spatial prisoner’s dilemma game,” *CHAOS SOLITONS & FRACTALS*, vol. 130, 2020., DOI link

[138] M. Sztilkovics, T. Gerecsei, B. Peter, A. Saftics, S. Kurunczi, I. Szekacs, B. Szabo, and R. Horvath, “Single-cell adhesion force kinetics of cell populations from combined label-free optical biosensor and robotic fluidic force microscopy,” *SCIENTIFIC REPORTS*, vol. 10, no. 1, 2020., DOI link

[139] M. Tkalčević, L. Basioli, K. Salamon, I. Šarić, J. S. Parramon, M. Bubaš, I. Bogdanović-Radović, S. Bernstorff, Z. Fogarassy, K. Balázsi, M. Petravić, and M. Mičetić, “Ge quantum dot lattices in alumina prepared by nitrogen assisted deposition: Structure and photoelectric conversion efficiency,” *SOLAR ENERGY MATERIALS AND SOLAR CELLS*, vol. 218, 2020., DOI link

[140] G. Varga, A. Sápi, T. Varga, K. Baán, I. Szenti, G. Halasi, R. Mucsi, L. Óvári, J. Kiss, Z. Fogarassy, B. Pécz, Á. Kukovecz, and Z. Kónya, “Ambient pressure CO2 hydrogenation over a cobalt/manganese-oxide nanostructured interface,” *JOURNAL OF CATALYSIS*, vol. 386, pp. 70–80, 2020., DOI link

[141] G. Vértesy, A. Gasparics, I. Uytdenhouwen, I. Szenthe, F. Gillemot, and R. Chaouadi, “Detection of neutron irradiaton induced degradation of reactor steel by magnetic method,” *IOP CONFERENCE SERIES: MATERIALS SCIENCE AND ENGINEERING*, vol. 903, 2020., DOI link

[142] G. Vértesy, A. Gasparics, J. M. Griffin, J. Mathew, M. E. Fitzpatrick, and I. Uytdenhouwen, “Analysis of surface roughness influence in non-destructive magnetic measurements applied to reactor pressure vessel steels,” *APPLIED SCIENCES-BASEL*, vol. 10, no. 24, 2020., DOI link

[143] G. Vértesy, A. Gasparics, I. Uytdenhouwen, I. Szenthe, F. Gillemot, and R. Chaouadi, “Nondestructive Investigation of Neutron Irradiation Generated Structural Changes of Reactor Steel Material by Magnetic Hysteresis Method,” *METALS*, vol. 10, no. 5, 2020., DOI link

[144] A. Zátonyi, M. Madarász, Á. Szabó, T. Lőrincz, R. Hodován, B. Rózsa, and Z. Fekete, “Transparent, low-autofluorescence microECoG device for simultaneous Ca 2+ imaging and cortical electrophysiology in vivo,” *JOURNAL OF NEURAL ENGINEERING*, vol. 17, no. 1, 2020. , DOI link

[145] X. Zhilong, C. Xiaojie, and S. Attila, “Leaving bads provides better outcome than approaching goods in a social dilemma,” *NEW JOURNAL OF PHYSICS*, vol. 22, no. 2, 2020., DOI link

[146] Z. Labadi, P. Petrik, M. George, C. Moldovan, M. Fried, “Preparation and Characterization of Mixed Metal Oxide Layers using Reactive Combinatorial Sputtering,” in *Proceedings of Anyagtudományi Szimpózium*, 2020, pp. 31–33.

[147] J. Zoltán, “A new approach in the research of ethnomusicology with intercontinental prehistoric perspectives,” *PRAEHISTORIA*, vol. 1–2, pp. 329–339, 2020.

References

[Ref. 1.1] Balents, L., et al. Nat. Phys. 16, 725–733 (2020).
[Ref. 1.2] Slizovskiy, S., et al. Communications Physics 2, 164 (2019).
[Ref. 1.3] Dagotto, E. Science 309, 257–262 (2005).
[Ref. 1.4] Z. Osváth, A. Pálinkás, G. Piszter, and G. Molnár, "Synthesis and Characterization of Graphene–Silver Nanoparticle Hybrid Materials," MATERIALS, vol. 13, no. 20, 2020.,
[Ref 2.1] Alekszej Romanenko, Benjamin Kalas, Petra Hermann, Orsolya Hakkel, Levente Illés, Miklós Fried, Péter Fürjes, Gergő Gyulai, and Péter Petrik, „Membrane-based *in situ* mid infrared spectroscopic ellipsometry – a study on the membrane affinity of polylactide-co-glycolidenanoparticulate systems", Anal. Chem., 93, 2, 981–991, 2021.
[Ref 2.2] Szekrényes, D. P.; Kovács, D.; Zolnai, Z.; Deák, A. Chemical Interface Damping as an Indicator for Hexadecyltrimethylammonium Bromide Replacement by Short-Chain Thiols on Gold Nanorods. J. Phys. Chem. C 2020, 124 (36), 19736–19742. https://doi.org/10.1021/acs.jpcc.0c04629
[Ref 2.3] Vértesy, Gábor; Gasparics, Antal; Griffin, James M.; Mathew, Jino; Fitzpatrick, Michael; Uytdenhouwen, Inge: Analysis of surface roughness influence in non-destructive magnetic measurements applied to reactor pressure vessel steels" APPLIED SCIENCES-BASEL 10 : 24 Paper: 8938 , 11 p. (2020)
[Ref. 2.4] Vértesy, Gábor; Gasparics, Antal; Uytdenhouwen, Inge; Szenthe, Ildikó; Gillemot, Ferenc; Chaouadi, Rachid: Nondestructive Investigation of Neutron Irradiation Generated Structural Changes of Reactor Steel Material by Magnetic Hysteresis Method METALS 10 : 5 Paper: 642 , 11 p. (2020)
[Ref. 2.5] N. Nagy, "Contact Angle Determination on Hydrophilic and Superhydrophilic Surfaces by Using r–θ-Type Capillary Bridges" LANGMUIR, vol. 35, iss. 15, 5202-5212, 2019.
[Ref. 2.6] Z. Labadi, B. Kalas, A. Saftics, L. Illes, H. Jankovics, É. Bereczk-Tompa, A. Sebestyén, É. Tóth, B. Kakasi, C. Moldovan, B. Firtat, M. Gartner, M. Gheorghe, F. Vonderviszt, M. Fried, P. Petrik; „Sensing Layer for Ni Detection in Water Created by Immobilization of Bioengineered Flagellar Nanotubes on Gold Surfaces" ACS BIOMATERIALS-SCIENCE & ENGINEERING 6 : 7 pp. 3811-3820. , 10 p. (2020) https://doi.org/10.1021/acsbiomaterials.0c00280
[Ref. 2.7] P. Kozma, F. Kehl, E. Ehrentreich-Förster, C. Stamm, F. Bier, Biosensors and Bioelectronics 58 (2014) 287–307.
[Ref. 2.8] K. Hinrichs, K.-J. Eichhorn, Ellipsometry of Functional Organic Surfaces and Films, Springer Series in Surface Sciences 52, 2nd ed. Springer International Publishing, 2018
[Ref. 2.9] J. Homola, Chemical reviews 108 (2008) 462–93.
[Ref. 2.10] E. Wijaya, C. Lenaerts, S. Maricot, J. Hastanin, S. Habraken, J. Vilcot,R. Boukherroub, S. Szunerits, Current Opinion in Solid State and Materials Science - CURR OPIN SOLID STATE MAT SCI 15 (2011) 208–224.
[Ref. 2.11] P. Yeh, A. Yariv, A. Cho, Applied Physics Letters 32 (1978).
[Ref. 2.12] F. Villa, L. E. Regalado, F. Ramos-Mendieta, J. Gaspar, T. Lopez-Ríos,Optics letters 27 (2002) 646–8.
[Ref. 2.13] A. Sinibaldi, A. Anopchenko, R. Rizzo, N. Danz, P. Munzert, P. Rivolo,485F. Frascella, S. Ricciardi, F. Michelotti, Analytical and bioanalytical chemistry 407 (2015).
[Ref. 2.14] A. Sinibaldi, C. Sampaoli, N. Danz, P. Munzert, L. Sibilio, F. Sonntag,A. Occhicone, E. Falvo, E. Tremante, P. Giacomini, F. Michelotti, Biosensors and Bioelectronics 92 (2017)
[Ref. 2.15] M., Fried ; R., Bogar ; Z., Lábadi ; Z. E., Horvath ; Z., Zolnai Combinatorial Investigation of WO3-MoO3 Mixed Layers by Spectroscopic Ellipsometry to assess Effective Medium Approximation In: Miklós, Fried (szerk.) Proceedings of Anyagtudományi Szimpózium. Budapest, Magyarország : Óbudai Egyetem (2020) 44 p. pp. 3-10. , 8 p.
References:
[Ref. 3.1] B. Pécz, G. Nicotra, F. Giannazzo, R. Yakimova, A. Koos, A. Kakanakova -Georgieva, Indium Nitride at the 2D Limit Adv. Mater. (2021)33, 2006660.
[Ref. 3.2] Racz, A. S.; Dworschak, D.; Valtiner, M.; Menyhard, M. Scratching Resistance of SiC-Rich Nano-Coatings Produced by Noble Gas Ion Mixing. Surface and Coatings Technology 2020, 386, 125475. https://doi.org/10.1016/j.surfcoat.2020.125475
[Ref. 3.3] M. Hans, H. Rueß, Zs. Czigány, J. Krause, P. Ondračka, D. Music, S. Evertz, D. M. Holzapfel, D. Primetzhofer, J. M. Schneider Spinodal decomposition of reactively sputtered VAlN thin films, Surface and Coatings Technology 389 (2020) 125641

[Ref. 3.4] D. M. Holzapfel, Zs. Czigány, A. O. Eriksson, M. Arndt and J. M. Schneider Thermal stability of macroparticles in $Ti_{0.27}Al_{0.21}N_{0.52}$, Appl. Surf. Sci. 2020, in press
[Ref. 3.5] T. Kolonits, Zs. Czigány, L. Péter, I. Bakonyi, J, Gubicza, Improved Hardness and Thermal Stability of Nanocrystalline Nickel Electrodeposited with the Addition of Cysteine, Nanomaterials, (2020) 10, 2254. https://doi.org/10.3390/nano10112254
[Ref. 3.6] B.A. Movchan, A.V. Demchishin, Phys. Met. Metallogr. 28/4 (1969) 83.
[Ref. 3.7] P.B. Barna, M. Adamik, Thin Solid Films 317 (1998) 27.
[Ref. 3.8] M. Arfaoui, G. Radnóczi, VK. Kis, Transformations in CrFeCoNiCu High Entropy Alloy Thin Films during In-Situ Annealing in TEM. Coatings 2020, 10, 60; doi:10.3390/coatings10010060.
[Ref. 3.9] M. Arfaoui, VK. Kis, G, Radnóczi, Diffusionless FCC to BCC phase transformation in CoCrCuFeNi MPEA thin films. Journal of Alloys and Compounds 863 (2021) 158712.
[Ref. 3.10]. Q. Zhang et al. Mater Lett 179 (2016) 126–129 .
[Ref. 3.11].E. Beniash, et al. Nat. Communications 10 (2019) 4383
[Ref. 3.12].V.K. Kis et al. Acta Biomat. 120 (2021) 104-115. doi: 10.1016/j.actbio.2020.08.035
[Ref. 3.13].J.P. Sun et al. Mater. Sci. Eng. C 33 (2013) 1109–1115.
[Ref. 3.14] N. Hegedus, R. Lovics, M. Serényi, Zs. Zolnai, P. Petrik, J. Mihály, Zs. Fogarassy, C. Balázsi, K. Balázsi, Examination of the Hydrogen Incorporation into RadioFrequency - Sputtered Hydrogenated SiNx Thin Films, COATINGS 11 : 1 P: 54 , 13 (2021)
[Ref. 3.15] K. Balázsi, M. Furkó, Z. Liao, J. Gluch, D. Medved, R. Sedlák, J. Dusza, E. Zschech, C. Balázsi, Porous sandwich ceramic of layered silicon nitride-zirconia composite with various multilayered graphene content JOURNAL OF ALLOYS AND COMPOUNDS 2020, 832 Paper: 154984 .
[Ref. 3.16] K. Balázsi, M. Furkó, Z. Liao, Z. Fogarassy, D. Medved, E. Zschech, J. Dusza, C. Balázsi, Graphene added multilayer ceramic sandwich (GMCS) composites: Structure, preparation and properties JOURNAL OF THE EUROPEAN CERAMIC SOCIETY 2020, 40 (4), 4792-4798.
[Ref. 3.17] K. Balazsi, M. Furkó, P. Klimczyk, C. Balázsi, Influence of Graphene and Graphene Oxide on Properties of Spark Plasma Sintered Si3N4 Ceramic Matrix CERAMICS 3 : 1 pp. 40-50. , 11 p. (2020)
[Ref. 3.18] K. Balázsi, M. Furkó, C. Balázssi, Nitrid kerámiák környezetkímélő előállítása és vizsgálata, OGÉT (2020) 354 pp. 33-36.
[Ref. 3.19] M. Serényi, M. Rácz, T. Lohner, Vacuum 61(2-4) (2001) 245–249.
[Ref. 3.20] D.A.G. Bruggeman, Ann. Phys. 416(8) (1935) 665–674.
[Ref. 3.21] T.N. Nunley, et al, J. Vac. Sci. Technol. B 34, (2016) 061205
[Ref. 3.22] https://refractiveindex.info/?shelf=main&book=HfO2&page=Wood
[Ref. 3.23] J. Sancho-Parramon, et. al. Thin Solid Films, 516(22), (2008) 7990–7995.
[Ref. 3.24] https://ntrs.nasa.gov/archive/nasa/casi.ntrs.nasa.gov/19820013457.pdf
[Ref. 3.25] H. Gueddaoui, et.al , The European Physical Journal B, 60(3), (2007) 305–312.
[Ref. 3.26] G. Sáfrán, N. Szász, G. Dobrik, B. Kalas M. Serényi VACUUM 182: 109675. (2020)
[Ref. 4.1] Pósa, L.; Molnár, G.; Kalas, B.; Baji, Z.; Czigány, Z.; Petrik, P.; Volk, J. A Rational Fabrication Method for Low Switching-Temperature VO2. Nanomaterials 11, 212, (2021). https://doi.org/10.3390/nano11010212
[Ref. 5.1] Samotaev, N., Pisliakov, A, Filipchuk, D., Etrekova, M, SOI Based Micro-Bead Catalytic Gas Sensor, Volume 255, 2021, Pages 105-111International Youth Conference on Electronics, Telecommunications and Information Technologies, YETI 2020; St. Petersburg; Russian Federation; 10 July 2020 through 11 July 2020;
[Ref. 5.2] Samotaev, N., Oblov, K., Dzhumaev, P., Filipchuk, D., and Ducso, C., Micro-catalytic gas sensor operating modes for extended life service, increasing sensitivity to target gases and power consumption reduction, Journal of Physics: Conference Series Volume 1681, Issue 1, 18 November 2020, Article number 0120076th International Conference on Chemical Materials and Process, ICCMP 2020; Warsaw University of Technology Warsaw, Virtual; Poland; 2 July 2020 through 4 July 2020
[Ref. 5.3] Utility model protection: Microheater ensuring homogenous surface temperature, Submitted to the Hungarian Intellectual Property Office, Nr. 22861, 02-09-2020
[Ref. 5.4] F.Z. Fedor, A. Zátonyi, D. Cserpán, Z. Somogyvári, Z. Borhegyi, G. Juhász, Z. Fekete, Application of a flexible polymer microECoG array to map functional coherence in schizophrenia model, METHODSX 7 (2020) 101117
[Ref. 5.5] Á. C. Horváth, Ö. C. Boros, L. Komáromi, S. Borbély, P. Koppa, P. Barthó, Z. Fekete, Infrared neural stimulation and inhibition using an implantable silicon photonic microdevice, MICROSYSTEMS & NANOENGINEERING 6 (2020) 44
[Ref. 5.6] https://index.hu/techtud/2020/11/10/magyar_chiplaboratorium_segiti_a_mesterseges_megtermekenyitest/
[Ref. 5.7] https://www.innoteka.hu/cikk/chip_technologiaval_a_szuletendo_gyermekert.2117.html

[Ref. 5.8] https://www.origo.hu/tudomany/20200606-chip-technologiaval-teszik-eredmenyesebbe-a-mesterseges-megtermekenyitest.html
[Ref. 5.9] http://gazdasagfejlesztes.gov.hu/hirek/az-embrio-furdovize
[Ref. 5.10] I. Rigó, M. Veres, Zs. Pápa, L. Himics, R. Öcsi, O. Hakkel, P. Fürjes, Plasmonic enhancement in gold coated inverse pyramid substrates with entrapped gold nanoparticles, JOURNAL OF QUANTITATIVE SPECTROSCOPY & RADIATIVE TRANSFER 253 Paper: 107128 , 8 p. (2020) (IF: 3.047)
[Ref. 6.1] B. Francz, R. Ungai-Salánki, É. Sautner, R. Horvath, B. Szabó, "Subnanoliter precision piezo pipette for single-cell isolation and droplet printing "MICROFLUIDICS AND NANOFLUIDICS, vol. 24, 2020.
[Ref. 6.2] H. Shearer Lawson, G. Holló, R. Horvath, H. Kitahata, I. Lagzi, "Chemical resonance, beats, and frequency locking in forced chemical oscillatory systems", THE JOURNAL OF PHISYCAL CHEMISTRY LETTERS, vol. 11, 2020.
[Ref. 6.3] M. L. Debreczeni, I. Szekacs, B. Kovacs, A. Saftics, S. Kurunczi, P. Gál, J. Dobó, L. Cervenak, R. Horvath, "Human primary endothelial label-free biochip assay reveals unpredicted functions of plasma serine proteases", SCIENTIFIC REPORTS vol. 10, 3303, 2020.
[Ref. 6.4] A. Saftics, B. Türk, A. Sulyok, N. Nagy, E. Agócs, B. Kalas, P. Petrik, M. Fried, N. Q. Khánh, A. Prósz, K. Kamarás, I. Szekacs, R. Horvath, S. Kuruncz,"Dextran-based hydrogel layers for biosensors", NANOBIOMATERIAL ENGINEERING (book chapter), 2020.
[Ref. 6.5] B. Peter, A. Saftics, B. Kovacs, S. Kurunczi and R. Horvath, „Oxidization increases the binding of EGCG to serum albumin revealed by kinetic data from label-free optical biosensor with reference channel", ANALYST, 145, 588-595, 2020.
[Ref. 6.6] Á. G. Nagy, I. Székács, A. Bonyár, R. Horvath,"Assembly of epithelial monolayers and transmigration of cancer cells captured with phase holographic imaging", IEEE XPLORE, 2020.
[Ref. 6.7] H. Jankovics, B. Kovacs, A. Saftics, T. Gerecsei, É. Tóth, I. Szekacs, F. Vonderviszt, R. Horvath, "Grating-coupled interferometry reveals binding kinetics and affinities of Ni ions to genetically engineered protein layers", SCIENTIFIC REPORTS, vol. 10, 22253, 2020.
[Ref. 6.8] M. Sztilkovics, T. Gerecsei, B. Peter, A. Saftics, S. Kurunczi, I. Szekacs, B. Szabo, R. Horvath, "Single-cell adhesion force kinetics of cell populations from combined label-free optical biosensor and robotic fluidic force microscopy", SCIENTIFIC REPORTS, vol. 10, 61, 2020.
[Ref. 6.9] N. Kanyo, K. D. Kovacs, A. Saftics, I. Szekacs, B. Peter, A. R. Santa-Maria, F. R. Walter, A. Dér, M. A. Deli, R. Horvath, "Glycocalyx regulates the strength and kinetics of cancer cell adhesion revealed by biophysical models based on high resolution label-free optical data", SCIENTIFIC REPORTS, vol. 10, 22422, 2020.
[Ref. 7.1] A. Szolnoki, X. Chen: "Blocking defector invasion by focusing on the most successful partner", Appl. Math. Comput. 385 (2020) 125430
[Ref. 7.2] Géza Ódor and Beatriz de Simoni: Heterogeneous excitable systems exhibit Griffiths phases below hybrid phase transitions Phys. Rev. Research 3 (2021) 013106.
[Ref. 7.3] Géza Ódor and Bálint Hartmann Power-Law Distributions of Dynamic Cascade Failures in Power-Grid Models Entropy 22 (2020) 666